SCATTERING OF LIGHT
FROM LARGE CYLINDERS

Thesis by

Mustafa A.G. Abushagur

In Partial Fulfillment of the Requirements

for the Degree of

Doctor of Philosophy

California Institute of Technology

Pasadena, California

1984

(Submitted October 27, 1983)

ACKNOWLEDGEMENTS

It is with great pleasure that I express my gratitude to my advisor, Professor Nicholas George who suggested the investigation of this problem, for his support, guidance and encouragement throughout the course of my studies. As a teacher, scientist and friend his patience, enthusiasm, and vast knowledge set an example that few equal.

I also gratefully acknowledge Professor W.B. Bridges for being my official advisor at Caltech while I am in residence at the University of Rochester.

In addition I would like to thank all the faculty of the Institute of Optics for enriching educational experiences while in residence at the University of Rochester.

My thanks are extended to the staff of Computype of Rochester for the word processing of the manuscript.

Finally, a special degree of appreciation is expressed to my wife Fatma and my parents. Their support, encouragement, and understanding were invaluable throughout the course of this work.

The scholarship from Al-Fatih University and the partial support of this research by the Air Force Office of Scientific Research is gratefully acknowledged.

ABSTRACT

Scattering of a plane electromagnetic wave from circular conducting and dielectric cylinders is analyzed. Both polarizations of the incident electric field, parallel and normal to the axis of the cylinder, are considered. The study of the rigorous solutions gives an insightful understanding of the scattered field and its dependence on the material of the cylinder, the polarizations of the incident field, and the three dimensionality of the object which usually are not considered in Fourier optics. It is shown that a combination of Fourier optics and ray theory can give good approximations for the scattered field from both conducting and dielectric cylinders. It is shown that the scattered pattern from a conducting cylinder consists of a main lobe and a number of side lobes. The spacing between the side lobes decreases as ka increases, where k is the wave number of the incident field and a the radius of the cylinder. It is found that for a certain conducting cylinder the side lobes terminate in a smaller scattering angle when the incident field is polarized parallel to the axis than when the incident field is polarized normal to the axis of the cylinder. The surface current density in the shadow region is found to be larger for the normal polarization case than for the parallel polarization case. The pattern of the scattered field from a dielectric cylinder has fringes all around the cylinder. The contrast of the fringes for the dielectric cylinder is much

larger when the polarization of the incident field is parallel to the axis than that when the polarization is normal to the axis. The backscattered field of the dielectric cylinder has a peak which depends in its position on the refractive-index of the cylinder for the parallel polarization case. The fine structure of the scattering by a dielectric cylinder is studied. It is shown that the dielectric cylinder has resonant frequencies which depend on the radius and refractive-index of the cylinder. It is found that there are significant differences in the shape of the scattered pattern depending on whether the cylinder is at-resonance or at off-resonance. Experimental investigations are carried out to verify the theory derived in this study and it is found that both theory and experiments are in good agreement.

TABLE OF CONTENTS

CHAPTER I

INTRODUCTION

The scattering of electromagnetic waves by circular cylinders is a fundamental problem in scattering theory. This problem is one of the few scattering problems for which a rigorous solution can be derived. Many authors have treated this problem[1-4]. The solution of Maxwell's equations for a dielectric cylinder goes back to Lord Rayleigh,[5,6] who derived the solutions for arbitrary radius, arbitrary refractive index, and perpendicular incidence. The solutions for metallic wires in the microwave region were reported by Ignatowsky[7,8] and Seitz[9]. The method for finding the asymptotic behavior for large sizes was reported by Debye[10]. A detailed study of the scattering of electromagnetic waves by conducting cylinders is reported by King and Wu[11] for $ka \leqq 12$. The asymptotic solutions for the scattering cross section using perturbation theory were reported by Papas[12], and Borgnis and Papas[13]. Keller reported a ray-theory approach to construct the leading term in the asymptotic expansion of the field scattered from large convex cylinders.[14] Interest in the study of the scattering of light by dielectric cylinders has increased greatly since optical fibers started to be used in the field of optical communications. Recently there are many writers working on problems relating to scattering from dielectric cylinders. The scattering of light from cylinders with arbitrary

refractive-index distributions is reported by few authors[15-17]. Determination of the diameter of the cylinders and profiling the refractive-index of the cylinders are reported by many authors[18-21]. It is quite important to refer to the work done by Fock in the treatment of the problem of scattering from large bodies; he derived approximate solutions for the surface currents at the shadow boundary[22,23].

In this work, we are interested in studying the problem of scattering of light from large circular cylinders, both conducting and dielectric. Solutions are derived for a linearly polarized plane wave incident normal to the axis of symmetry of the cylinder. The major emphasis in this work has been to study the fields scattered by large conducting and dielectric cylinders ($ka >> 1$) when they are illuminated with a plane electromagnetic wave. The scattered field has been studied for different cylinder parameters, and for different polarizations of the incident plane wave.

In Chapter II, the scattering of light from conducting cylinders is reported. Rigorous solutions of the scattered field are derived from Maxwell's equations, using appropriate boundary conditions, for both polarizations of the incident field. The surface current density induced by the fields on the surface of the cylinder is derived and plotted for the two different polarizations, and it is shown that the currents for the normal polarization case are very large in the shadow region in comparison to those for the case of parallel polarization. The amplitude of the scattered field is plotted as a function of the scattering angle (ϕ) and the factor ka.

The fringe spacings of the scattered field are deduced and plotted for various values of ka. The main differences between the scattered fields resulting from the parallel and normal incident field polarizations are pointed out.

The scattering of light from large dielectric cylinders is reported in Chapter III. Rigorous solutions of the scattered field are derived from Maxwell's equations for the two different polarizations of the incident field. The scattered field patterns outside of the cylinder are plotted as a function of ϕ for a set of values of ka. The fringe spacings of the field are plotted as a function of ϕ and ka, and their dependences on ϕ and ka are studied. A very interesting result is obtained concerning the effect of the index of refraction on the scattered field. It is found that the backscattered field ($90° < \phi < 180°$) has a peak with a position increasing in ϕ by the increase of the index of refraction, and also it is found that this position is not sensitive to the change of ka.

In Chapter IV, approximate solutions for the scattering of light from circular conducting and dielectric cylinders are reported. It is shown that the scattered field from a conducting cylinder can be approximated very closely by the superposition of the diffracted field from a variable width strip and the backscattered field generated by the surface current density. The fields scattered by the dielectric cylinder can be approximated by the superposition of the diffracted, reflected and refracted fields. The approximate solutions are compared to the rigorous solution and they are shown to

give very good agreements. A closed form is derived for the fringe spacings of the scattered fields.

In Chapter V, the fine structure of the scattering from dielectric cylinders is presented. The effect of the change in the wavelength of the incident field is studied. It is found that the cylinder behaves like a cavity resonator. The effect of the resonances on the scattered field is studied, and it is found that at-resonance the fields tend to concentrate around the main-lobe, while at off-resonance the fields spreads more in all around the cylinder. It is shown also that the resonanance effect the shape of the modulating function of the scattered pattern.

In Chapter VI, an experimental study of the scattering of light from cylinders is reported. The scattered intensity has been detected by two different methods. In the first method a photodetector is rotated around the cylinder in precise steps, and a record of the intensity is collected using a data acquisition system. In the second method the radiation patterns are recorded photographically with precise alignment controlled by registery pins. Then, a microdensitometer is used to obtain a density vs. angle plot which is later digitized and converted to read optical intensity. The experimental results are compared with the theoretical results and they are in good agreement.

A recaptulation of the major results of the research is contained in Chapter VII.

CHAPTER I

REFERENCES

1. J.A. Stratton, Electromagnetic Theory (McGraw-Hill, New York, 1941).
2. H.C. Van de Hulst, Light Scattering by a Small Particles (Wiley, New York, 1957).
3. M. Kerker, The Scattering of Light and Other Electromagnetic Radiation (Academic, New York, 1969).
4. J.J. Bowman, T.B.A. Senior, and P.L.E. Vslenghi, Electromagnetic and Acoustic Scattering by Simple Shapes (North-Holland, Amsterdam, 1969).
5. Lord Rayleigh, "On the Electromagnetic Theory of Light," Phil. Mag. 12, 81 (1881).
6. Lord Rayleigh, "The Dispersal of Light by a Dielectric Cylinder," Phil. Mag. 36, 365 (1918).
7. W. von Ignatowsky, "Reflection of Electric Waves at a Wire," Ann. de Physik, 18, 495 (1905).
8. W. von Ignatowsky, "Diffraction and Reflection on Maxwell's Theory," Ann. de Physik 23, 875 (1907).
9. W. Seitz, "Infinite Metal Cylinder and Hertz Waves," Ann. de Physik 19, 554 (1906).
10. P. Debye, "Electromagnetic Field Surrounding a Cylinder, and the Theory of Rainbow," Phys. Z. 9, 775 (1908).
11. R.W.P. King and T.T. Wu, The Scattering and Diffraction of Waves (Harvard University Press, Cambridge, 1959).

12. C.H. Papas, "Diffraction by a Cylindrical Obstacle," J. Appl. Phys. 21, 318 (1950).

13. F.E. Borgnis, and C.H. Papas, Randwerprobleme der Mikrowellen physik (Springer Verlag, Berlin, 1955).

14. J.B. Keller, "Diffraction by a Convex Cylinder," Trans. I.R.E. AP-4, 312 (1956).

15. D. Marcuse and H.M. Presby, "Light Scattering from Optical Fibers with Arbitrary Refractive-Index Distributions," J. Opt. Soc. Am. 65, p. 367 (1975).

16. C. Saekeang and P.L. Chu, "Backscattering of Light from Optical Fibers with Arbitrary Refractive-Index distributions: Uniform Approximations Approach," J. Opt. Soc. Am. 68, p. 1296 (1978).

17. D. Marcuse, "Light Scattering from Unclad Fibers: Ray Theory," Appl. Opt. 14, 1528 (1975).

18. D. Marcuse and H.M. Presby, "Index Profile Measurements of Fibers and Their Evaluations," Proc. IEEE 68, p. 666 (1980).

19. L.S. Watkins and R.E. Frazee, Jr.," High Speed Measurement of the Core Diameter of a Step-Index Optical Fiber," App-Opt. 19, p. 3756 (1980).

20. Mustafa A.G. Abushagur and Nicholas George, "Measurement of Optical Fiber Diameter Using the Fast Fourier Transform," Appl. Opt. 19, 2031 (1980).

21. L.S. Watkins, "Scattering from Side-Illuminated Clad Glass Fibers for Determination of Fiber Parameters," J. Opt. Soc. Am. 64, p. 767 (1974).

22. V.A. Fock, "Distribution of Currents Induced by a Plane Wave on the Surface of a Conductor," J. Phys. U.S.S.R. 10, 130 (1946).

23. V.A. Fock, "Diffraction of Radio Waves around the Earth's Surface," J. Phys. U.S.S.R. 9, 256 (1945).

CHAPTER II

SCATTERING OF LIGHT FROM LARGE CONDUCTING CYLINDERS

2.1 Introduction

The problem we are considering in this chapter is the scattering of a plane electromagnetic wave by a perfectly conducting circular cylinder. The problem will be studied for the two different polarizations of the incident electric field, parallel to the axis of symmetry of the cylinder (TM), and normal to the axis (TE). Fig. 2.1 shows the coordinate system used in this study.

At the beginning we will introduce some general formulations concerning the field theory, as a necessary starting point, which will lead to the solution of Maxwell's equations. We are concerned with finding the solution of Maxwell's equations which describe the field arising from a plane electromagnetic wave incident upon a cylindrical surface, across which the properties of the medium change abruptly. An appropriate system of curvilinear coordinates (cylindrical coordinates) is introduced. In the cylindrical coordinates Maxwell's equations will separate into a set of ordinary differential equations, which are then solved for the scattered fields. This method is the standard method for solving this class of scattering problems[1-4]. In Section 2.3 rigorous solutions of Maxwell's equation are derived for both parallel and normal polarizations of the

incident field. The solutions are expressed in infinite series, and the number of terms needed to get accurate values for the fields are shown. The scattered field amplitude is plotted as a function of the scattering angle, ϕ, for a set of values of ka. The surface current density is derived and plotted in Section 2.4, and a comparison between currents induced on the surface of the cylinder is made for the two polarizations of the incident field. In Section 2.5 the fringe spacings of the scattered field pattern are plotted as a function of ϕ for a set of values of ka. The cutoff angle of the fringes is studied for both polarizations as a function of the factor ka.

2.2 General Formulations

The solution of this scattering problem will be derived from the Helmholtz wave equation using the proper boundary conditions. We will start by introducing Maxwell's equations from which we will derive the Helmholtz wave equation. Maxwell's equations for a source free media are given by[5]

$$\nabla\times\underline{E}(\underline{r},t) = -\partial\underline{B}(\underline{r},t)/\partial t, \tag{2.1}$$

$$\nabla\times\underline{H}(\underline{r},t) = \partial\underline{D}(r,t)/\partial t, \tag{2.2}$$

$$\nabla\cdot\underline{D}(\underline{r},t) = 0, \tag{2.3}$$

$$\nabla\cdot\underline{B}(\underline{r},t) = 0. \tag{2.4}$$

If we assume time harmonic fields, i.e.

$$\underline{E}(\underline{r},t) = \text{Re } \underline{E}(\underline{r})\ e^{-i\omega t}, \tag{2.5}$$

$$\underline{B}(\underline{r},t) = \text{Re } \underline{B}(\underline{r})\ e^{-i\omega t}, \tag{2.6}$$

$$\underline{D}(\underline{r},t) = \text{Re } \underline{D}(\underline{r})\ e^{-i\omega t}, \tag{2.7}$$

$$\underline{H}(\underline{r},t) = \text{Re } \underline{H}(\underline{r})\ e^{-i\omega t}. \tag{2.7}$$

Maxwell's equations for the time harmonic fields will reduce to

$$\nabla\times\underline{E}(\underline{r}) = i\omega\underline{B}(\underline{r}), \tag{2.9}$$

$$\nabla\times\underline{H}(\underline{r}) = -i\omega\underline{D}(\underline{r}), \tag{2.10}$$

$$\nabla\cdot\underline{D}(\underline{r}) = 0, \tag{2.11}$$

$$\nabla\cdot\underline{B}(\underline{r}) = 0. \tag{2.12}$$

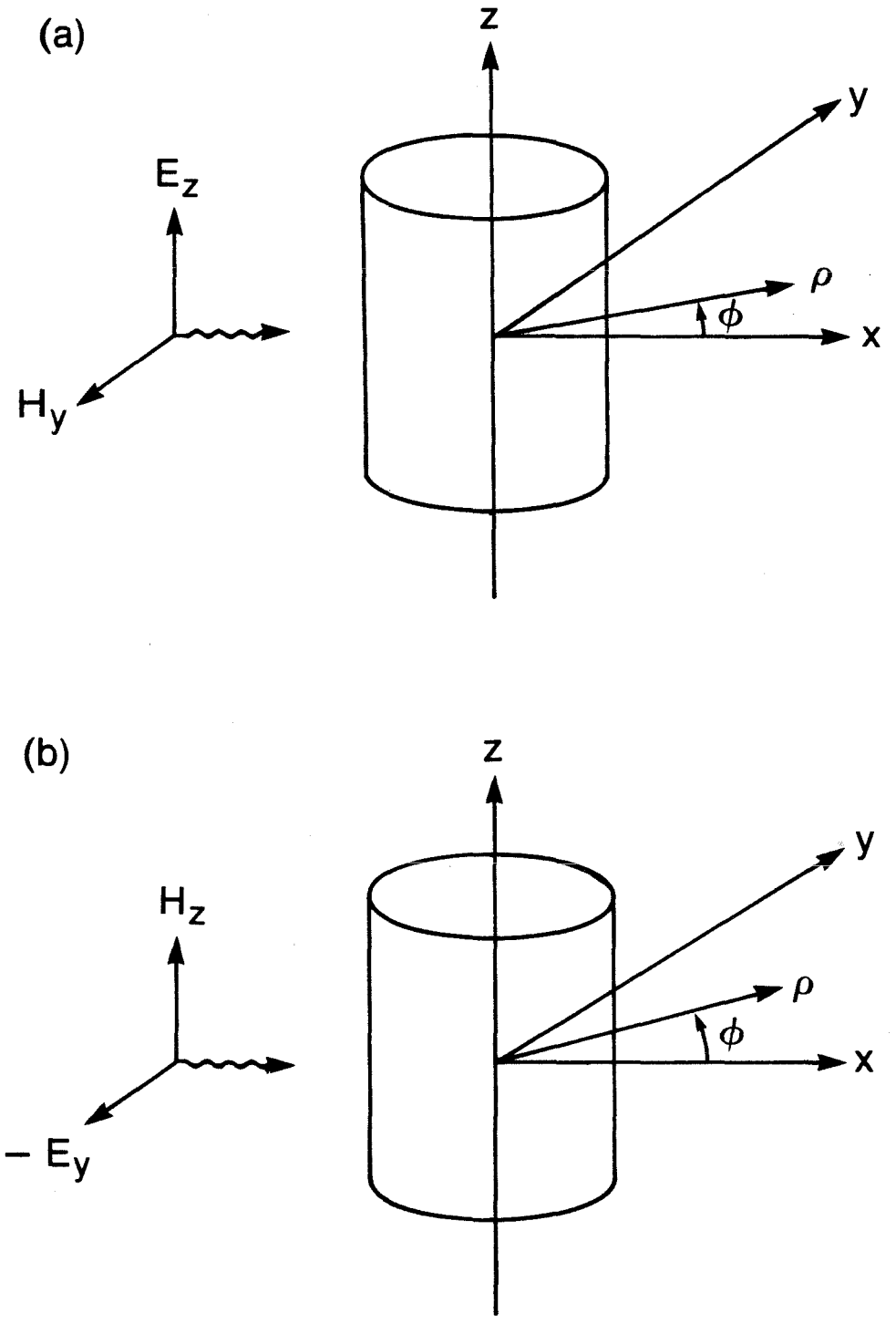

Fig. 2.1 The incident field as it illuminates the cylinder.

For an isotropic medium, where the physical properties of two neighboring points are the same in all directions, the relations between $\underline{D},\underline{E},\underline{H}$ and $\underline{B}$ are given by

$$\underline{D}(\underline{r}) = \varepsilon\, \underline{E}(\underline{r}), \tag{2.13}$$

$$\underline{B}(\underline{r}) = \mu\, \underline{H}(\underline{r}). \tag{2.14}$$

From Eqs. (2.9), (2.10), (2.13), (2.14) and some vector identities we get

$$\nabla^2\underline{E}(\underline{r})+k^2\underline{E}(\underline{r}) = 0. \tag{2.15}$$

Which is the Helmholtz wave equation for a source free medium, where

$$k^2 = \omega^2\mu\varepsilon, \qquad k = 2\pi/\lambda. \tag{2.16}$$

2.3 Rigorous Solution of the Scattering Problem

To solve the Helmholtz wave equation for the scattered field from a circular cylinder, we need to write the wave equation in cylindrical coordinates (ρ,ϕ,z). The wave equation (2.15) in cylindrical coordinates is given by

$$\frac{1}{\rho}\frac{\partial}{\partial\rho}\left(\rho\frac{\partial U_z}{\partial\rho}\right)+\frac{1}{\rho^2}\frac{\partial^2 U_z}{\partial\phi^2}+\frac{\partial^2 U_z}{\partial z^2}+k^2U_z=0, \tag{2.17}$$

where U_z is the field component parallel to the axis of symmetry of the cylinder. Eq. (2.17) is a second order partial differential equation and can be solved using separation of variables. Let U_z expressed as:

$$U_z(\rho,\phi,z)=R(\rho)\Phi(\phi)Z(z). \tag{2.18}$$

By substituting Eq. (2.18) into Eq. (2.17) and following the standard procedure of separation of variables, Eq. (2.17) will reduce to the following three differential equations:

$$\frac{\partial^2 Z(z)}{\partial z^2}+h^2Z(z)=0, \tag{2.19}$$

$$\frac{\partial^2\Phi(\phi)}{\partial\phi 2}+m^2\,\Phi(\phi)=0, \tag{2.20}$$

and

$$\rho^2\frac{\partial^2 R(\rho)}{\partial\rho^2}+\rho\frac{\partial R(\rho)}{\partial\rho}+[(k^2-h^2)\rho^2-m^2]R(\rho)=0, \tag{2.21}$$

where h is a constant, and m is an integer because the field is periodic in ϕ. Eqs. (2.19) and (2.20) are ordinary second order differential equations, and they have the following solutions:

$$Z(z) = e^{\pm ihz}, \tag{2.22}$$

and

$$\Phi(\phi) = e^{\pm im\phi}. \tag{2.23}$$

Eq. (2.21) is in the form of Bessel's differential equation and in solving it we have to keep in mind that the solution for the scattered wave should satisfy the radiation condition. The radiation condition for such problem is that the scattered field should be an outgoing wave at large ρ. So the solution of Eq. (2.21) will be given by the Hankel function of the first kind[6]

$$R(\rho) = H_m^{(1)}(\rho\sqrt{k^2-h^2}\ ). \tag{2.24}$$

From Eqs. (2.22), (2.23) and (2.24) the scattered field from a cylinder is given by

$$U_z(\rho,\phi,z) = e^{\pm ihz} \sum_{m=-\infty}^{\infty} b_m H_m^{(1)}\ (\rho\sqrt{k^2-h^2})e^{im\phi}. \tag{2.25}$$

In the case when the incident wave is propagating perpendicular to the symmetry axis of the cylinder, the scattered field will be independent of z, i.e., h = 0, then the scattered field will be given by

$$U_z(\rho,\phi) = \sum_{m=-\infty}^{\infty} b_m e^{im\phi} H_m^{(1)}(k\rho). \tag{2.26}$$

The coefficient b_m will be determined using the boundary conditions. If we illuminate the cylinder with a plane wave, $U_z^{inc}(x)$ of unit amplitude traveling in the x direction, then

$$U_z^{inc}(x) = e^{ikx} = e^{ik\rho\cos\phi}, \tag{2.27}$$

which can be expressed in terms of Bessel functions as[7]

$$U_z^{inc}(\rho,\phi) = e^{ik\rho\cos\phi} = \sum_{m=-\infty}^{\infty} (i)^m J_m(k\rho) e^{im\phi}, \tag{2.28}$$

then the total field will be the superposition of the incident and scattered fields.

$$U_z^{tot}(\rho,\phi) = U_z^{inc}(\rho,\phi) + U_z^{scat}(\rho,\phi), \tag{2.29}$$

from Eqns. (2.26), (2.28) and (2.29) the total field can be expressed as

$$U_z^{tot}(\rho,\phi) = \sum_{m=-\infty}^{\infty} [(i)^m J_m(k\rho) + b_m H_m^{(1)}(k\rho)] e^{im\phi}. \tag{2.30}$$

2.3.1 Parallel Polarization Case

When the incident electric field is linearly polarized along the z-axis, the total electric field from Eq. (2.30) is written as

$$E_z^{tot}(\rho,\phi) = \sum_{m=-\infty}^{\infty} [(i)^m J_m(k\rho) + b_m H_m^{(1)}(k_m\rho)] e^{im\phi}. \tag{2.31}$$

To evaluate the arbitrary constant b_m we need to apply the boundary condition for the electric field. This condition for the perfect conducting cylinder is that the tangential component of the electric field vanishes on the surface[1,5], i.e.,

$$E^{tot}(\rho,\phi) = 0, \qquad \text{at } \rho = a.$$

From Eqn. (2.34) with $\rho = a$, we obtain relations for b_m:

$$E_z^{tot}(a,\phi) = \sum_{m=-\infty}^{\infty} [(i)^m J_m(ka) + b_m H_m^{(1)}(ka)]e^{im\phi} = 0. \tag{2.32}$$

From the orthogonality of functions $e^{im\phi}$, we can set the individual terms in Eq. (2.32) to zero. The result is

$$b_m = - \frac{(i)^m J_m(ka)}{H_m^{(1)}(ka)} . \tag{2.33}$$

By substituting Eq. (2.33) into Eq. (2.26) we get

$$E_z^s(\rho,\phi) = - \sum_{m=-\infty}^{\infty} (i)^m \frac{J_m(ka)}{H_m^{(1)}(ka)} H_m(k\rho)e^{im\phi} . \tag{2.34}$$

This expression for the scattered field agrees with that given by Papas[8], and then by King and Wu[9].

The scattered electric field given by Eq. (2.34) is represented by an infinite series. Its coefficients are function of the wavelength (λ), the radius of the cylinder (a), the scattering angle (ϕ) and the distance ρ.

Now we consider the ρ dependence of this solution, the only parameter which is a function of ρ is the Hankel function $H_m^{(1)}(k\rho)$, and its asymptotic expansion can be given by[10]

$$H_m^{(1)}(k\rho) \sim \sqrt{2\pi/k\rho}\, e^{i\{k\rho-(m\pi/2)-(\pi/4)\}} \text{ for large } \rho,$$

so the field will have the component $e^{ik\rho}/\sqrt{\rho}$ which is a cylindrical wave propagating in the postive ρ-direction. The factor $e^{im\phi}$ will give the dependence on ϕ of the field which will have a period of 2π. From these parameters of the series, we can describe the behavior of the field. The scattered field will be propagated as an outgoing cylindrical wave, with amplitude and phase depending on the factor ka, the scattering angle ϕ and the distance ρ from the cylinder, and the field will be periodic in ϕ with a period of 2π.

In the following subsection we will study the effect of these parameters on the scattered field.

Graphical Representation of the Scattered Field

The scattered field given by Eq. (2.34) depends on three parameters: the scattering angle ϕ, the radius of the cylinder a, and the wavelength of the illuminating field λ. To study the effect of these parameters on the scattered field, we need to plot the amplitude of the scattered field as a function of each of them.

The scattered field can be written as

$$E_z^s(\rho,\phi) = -\sum_{m=-\infty}^{\infty} C_m(ka,k\rho)e^{im\phi} . \qquad (2.35)$$

Hence,

$$E_z^s(\rho,\phi) = - C_0(ka,k\rho) - 2 \sum_{m=1}^{\infty} C_m(ka,k\rho)\cos m\phi, \tag{2.36}$$

where $$C_m(ka,k\rho) = (i)^m \frac{J_m(ka)}{H_m^{(1)}(ka)} H_m^{(1)}(k\rho) \ . \tag{2.37}$$

To plot $E_z^s(\rho,\phi)$, which is represented by an infinite series, we need to use the digital computer to compute the amplitude of the scattered field. Using the digital computer will enable us to evaluate a finite number of terms of the series, and so it is important to know how many terms of the series are required to give us an accurate value of the solution. It has been stated by King and Wu[9] that the number of terms needed to make the series converge is approximately the value of ka. In Appendix A we derived analytically, in an approximate form, the number of terms of the series needed to make the sum of the series accurate enough; and they are indeed around the value of ka.

The calculations we made in Appendix A shows that we need to sum $m > ka$. To see how many terms we need to sum more than ka to get an accurate sum of the series we need to study the dependence of the coefficient $C_m(ka,k\rho)$ of the series on the different values of ka. In Fig. 2.2 we plotted the amplitude of $\mathrm{Log}\{|C_m(ka,k\rho)|\}$ vs. the number of terms m. From the curves in Fig. 2.2 we can see that $|C_m|$ fluctuates around certain values, then when $m \cong ka(1+\alpha)$ the coefficient decreases very rapidly. The value of α decreases by the

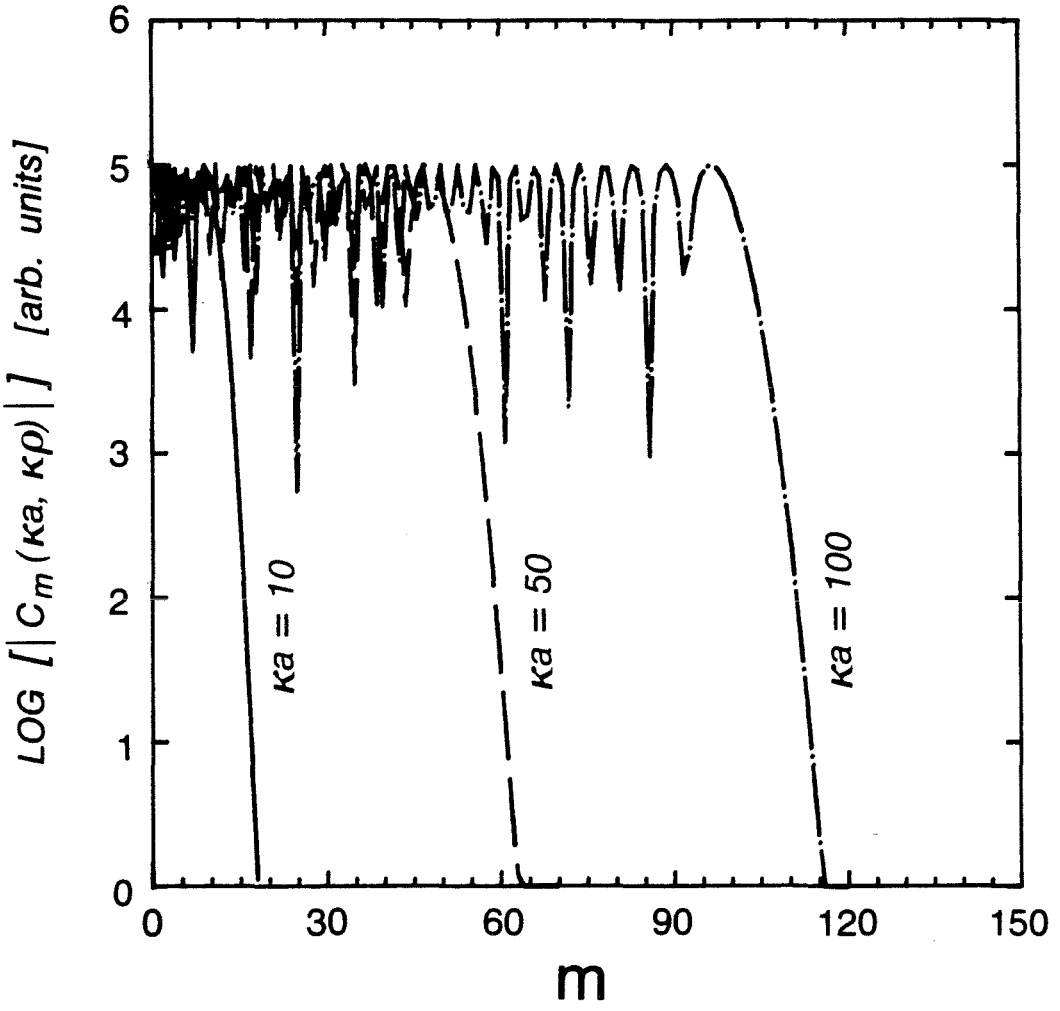

Fig. 2.2 Logarithm of the normalized coefficient $|C_m(ka,k\rho)|$ given by Eq. (2.37) plotted vs. the order m, for ka = 10, 50 and 100. Note that the coefficient tends to a negligible value at $m \cong ka + 10$.

increase of ka, e.g., α = 1.4, and 0.16 for ka = 5, and 100, respectively. So to plot the scattered field $E_z^s(\rho,\phi)$, we need to take the number of terms of the series which will make the coefficient $|C_m|$ drop by at least 60 dB.

In Figs. 2.3(a) and (b) the scattered field is plotted as a function of the scattering angle for a set of ka values in polar coordinates. The amplitude of the field is plotted at ρ = 10 cm. From Fig. 2.3 it is clear that the amplitude of the field has a main lobe and a number of side lobes. The width of the main lobe is decreasing by the increase of ka, and the number of side lobes increases by the increase of ka. In Figs. 2.3(c) and (d) a set of curves for the amplitude of the scattered field for ka = 10 and ka = 50 in linear coordinates are plotted. This will give us a more sense of the dependence of the amplitude of the field on ka and ϕ. The ratio of the amplitude of the field at $\phi = 0^o$ to that at $\phi = 180^o$ is decreasing by the increase of ka. The spacing between the nulls is decreasing as ka increases, and the amplitude of the $E_z^s(\rho,0^o)$ is increasing as ka increases.

2.3.2 Normal Polarization Case

When the incident electric field is linearly polarized in the y-axis, i.e. perpendicular to the axis of the cylinder then the incident magnetic field will be parallel to the axis of symmetry of the cylinder. From Eq. (2.30) the total magnetic field will be given by

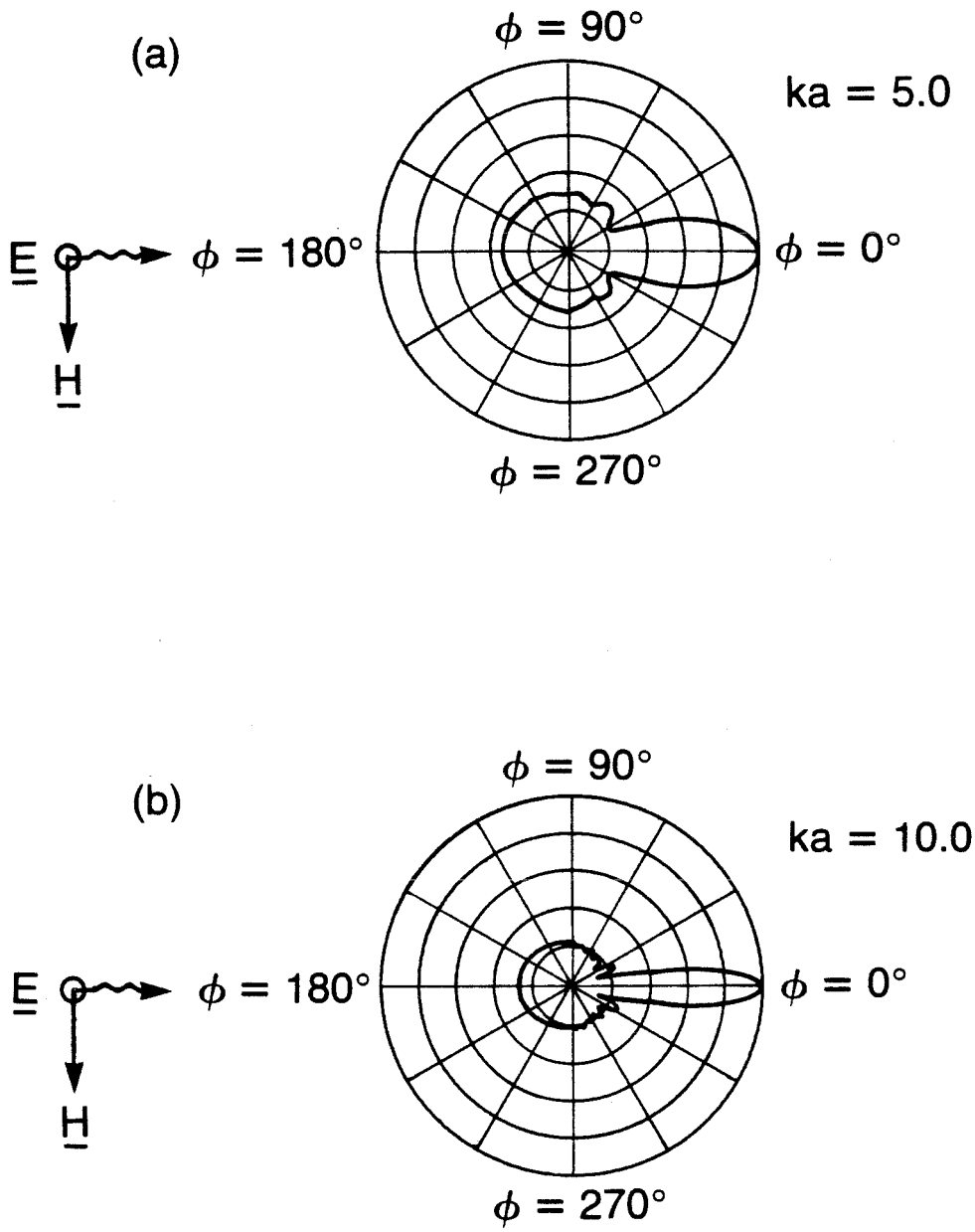

Fig. 2.3 The normalized scattered field $|E^s(\rho,\phi)/E^s(\rho,0°)|$ given by Eq. (2.34) plotted vs. the scattering angle ϕ. (a) and (b) are plotted in polar coordinates for ka = 5 and ka = 10, respectively; (continued on next page).

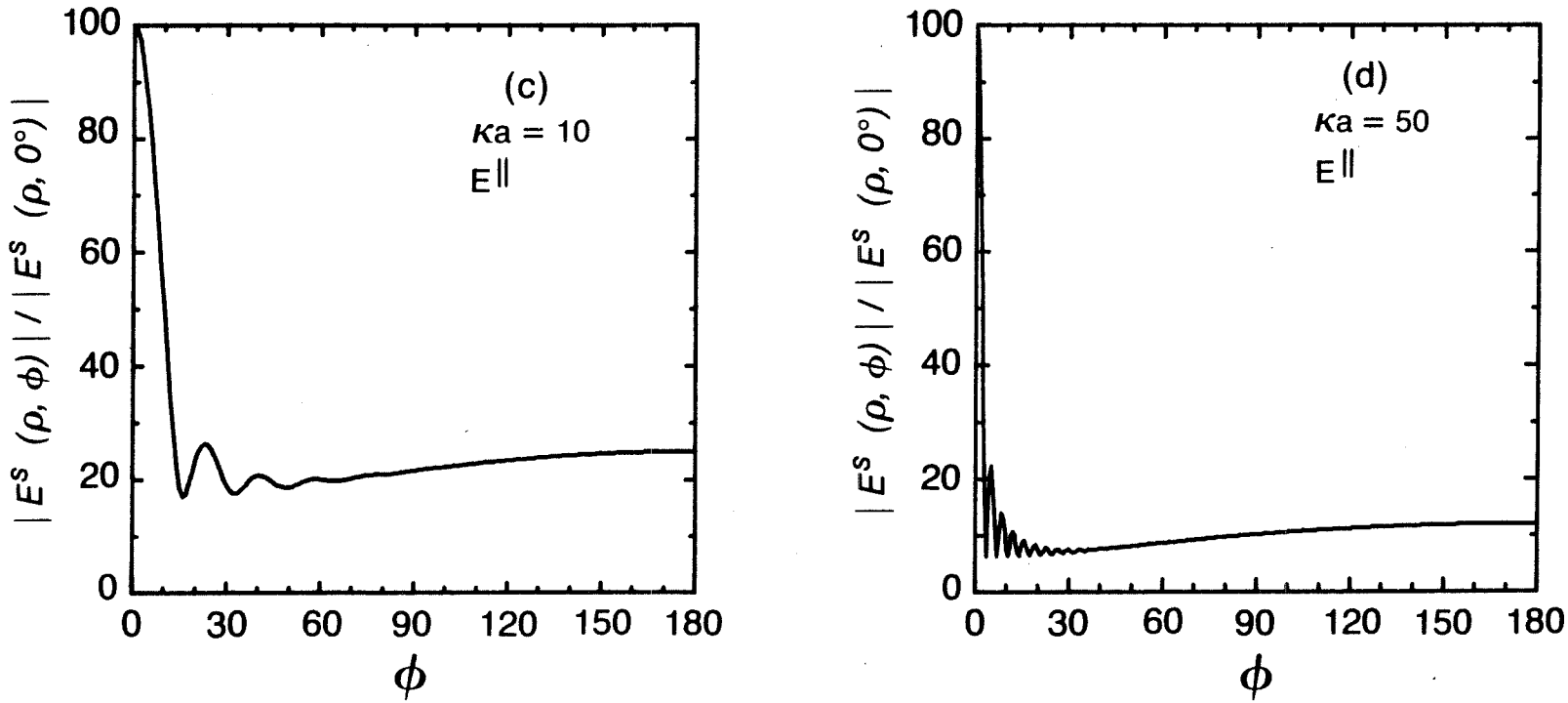

Fig. 2.3 Continued (c) and (d) show the scattered field plotted in linear coordinates for ka = 10 and 50 respectively. Note that the width of the main lobe decreases as ka increases, and the number of side lobes for ka = 50 are more than those for ka = 10.

$$H_z^{tot}(\rho,\phi) = \sum_{m=-\infty}^{\infty} [(i)^m J_m(k\rho) + d_m H_m^{(1)}(k\rho)] e^{im\phi} \quad . \tag{2.38}$$

To evaluate the arbitrary constant d_m we need to apply the boundary condition for the magnetic field. The boundary condition applicable to this case is[1,5]

$$\frac{\partial H_z^{tang}}{\partial \rho} = 0, \qquad \text{at } \rho = a \ , \tag{2.39}$$

i.e., the derivative of the tangential component of the magnetic field w.r.t ρ vanishes on the surface of the cylinder. By applying this condition to Eq. (2.38) we get

$$k \sum_{m=-\infty}^{\infty} (i)^m J_m'(k\rho)\Big|_{\rho=a} e^{im\phi} + k \sum_{m=-\infty}^{\infty} d_m H_m'^{(1)}(k\rho)\Big|_{\rho=a} e^{im\phi} = 0. \tag{2.40}$$

From the orthogonality of functions $e^{im\phi}$, we can set the individual terms in Eq. (2.40) to zero. The result is

$$d_m = -(i)^m \frac{J_m'(ka)}{H_m'^{(1)}(ka)}, \tag{2.41}$$

where the primes denote differentiation with respect to the variable ρ. Then the scattered field can be written as

$$H_z^s(\rho,\phi) = - \sum_{m=-\infty}^{\infty} (i)^m \frac{J_m'(ka)}{H_m'^{(1)}(ka)} H_m^{(1)}(k\rho) e^{im\phi} \quad . \tag{2.42}$$

The scattered magnetic field has the same form as of the scattered electric field in the parallel polarization case except that the coefficient $d_m = \partial b_m/\partial\rho$. So the main characteristic of the field are the same, i.e., the scattered field will be propagating as a cylindrical wave with amplitude and phase depending on the radius of the cylinder, the wavelength, and the distance of the observation point from the axis of the cylinder. The effect of these parameters on the scattered field will be shown in the following subsection.

Graphical Representations of the Scattered Field

The scattered field given by Eq. (2.42) can be rewritten as

$$H_z^s(\rho,\phi) = -\sum_{m=-\infty}^{\infty} F_m e^{im\phi},$$

$$H_z^s(\rho,\phi) = -F_0 - 2\sum_{m=1}^{\infty} F_m \cos m\phi, \tag{2.43}$$

where $$F_m = (i)^m \frac{J_m'(ka)}{H_m'^{(1)}(ka)} H_m^{(1)}(k\rho). \tag{2.44}$$

To plot $H_z^s(\rho,\phi)$ we need to sum up enough terms of the series to get an accurate value for the field, i.e., until the remainder of the terms of the series can be neglected without affecting the value of the field significantly. As shown in Appendix A, the number of terms which will give such a sum is slightly larger than ka.

In Fig. 2.4 a plot for $\mathrm{Log}\{|F_m|\}$ as a function of the number of terms m is shown for ρ = 10 cm. From these curves, it is clear that

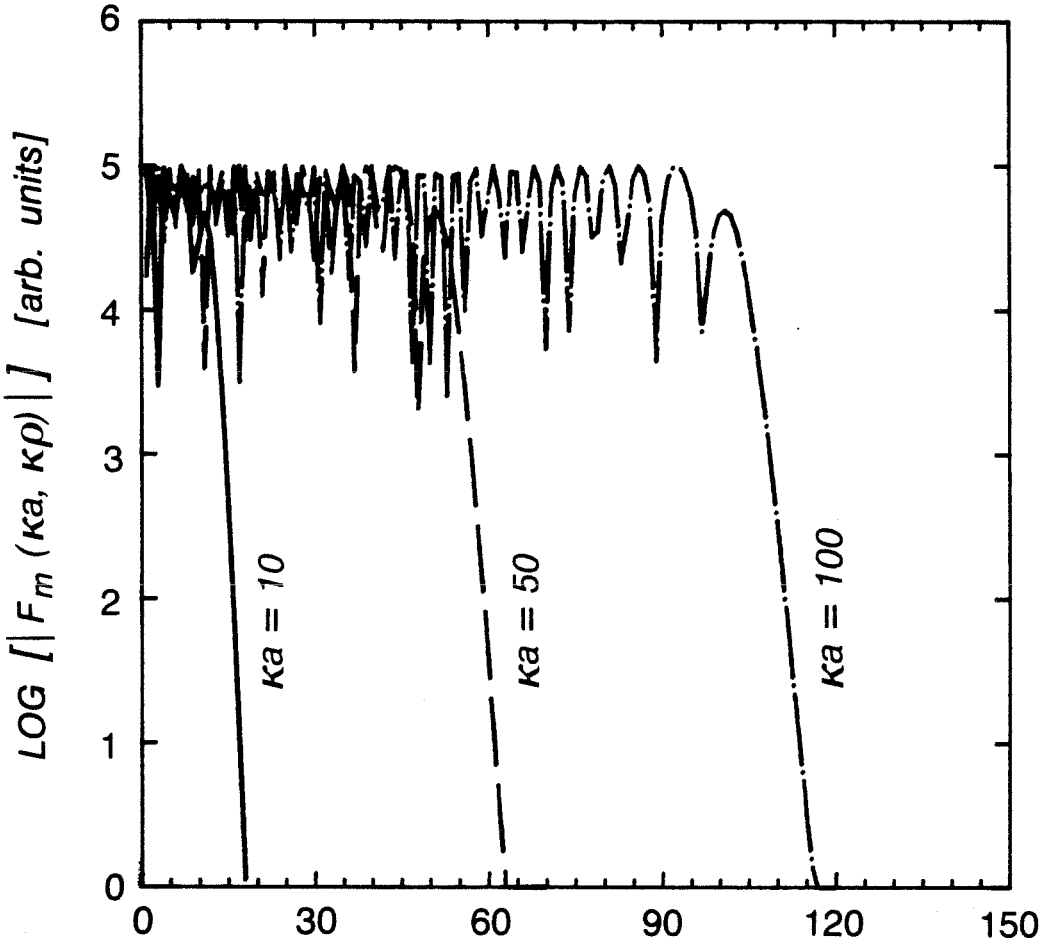

Fig. 2.4 Logarithm of the normalized coefficient $|F_m|$ in Eq. (2.44) is plotted vs. the order m.

when $m \cong ka(1+\beta)$, the value of the coefficient $|F_m|$ will become negligible. The value of β is decreasing by the increase of ka, e.g., $\beta = 1.4$ for $ka = 5$, and $\beta = 0.16$ for $ka = 100$.

In Figs. 2.5(a) and (b) a plot for the amplitude of the scattered field $|H_z^2(\rho,\phi)|/|H_z^s(\rho,0)|$ in polar coordinates is shown for $ka = 5$ and $ka = 10$. The amplitude of the field has a maximum at $\phi = 0^\circ$. The width of the main lobe decreases by the increase of ka, and the number of nulls increase by the increase of ka. Figs. 2.5(c) and (d) shows a plot for the normalized amplitude of the scattered field for $ka = 10$ and 50. The main characteristic of the field that we can recognize from these plots is that the nulls extend on a wider range of ϕ more than that for the parallel polarization case. The angle at which the nulls begin to disappear decreases by the increase of ka. The reason for the difference in the pattern structure of the scattered field for the two different polarizations of the incident field is because of the value of the surface current density generated in each case. When H_z^{inc} is parallel to the axis of the cylinder, it will induce a current flowing in the ϕ-direction which will enable it to go more deeply in the shadow region. While when E_z^{inc} is parallel to the axis of the cylinder it will induce a current in the z-direction which will die very close to the shadow boundary. This will become clear when we study the surface current density for the two different polarizations in the next section.

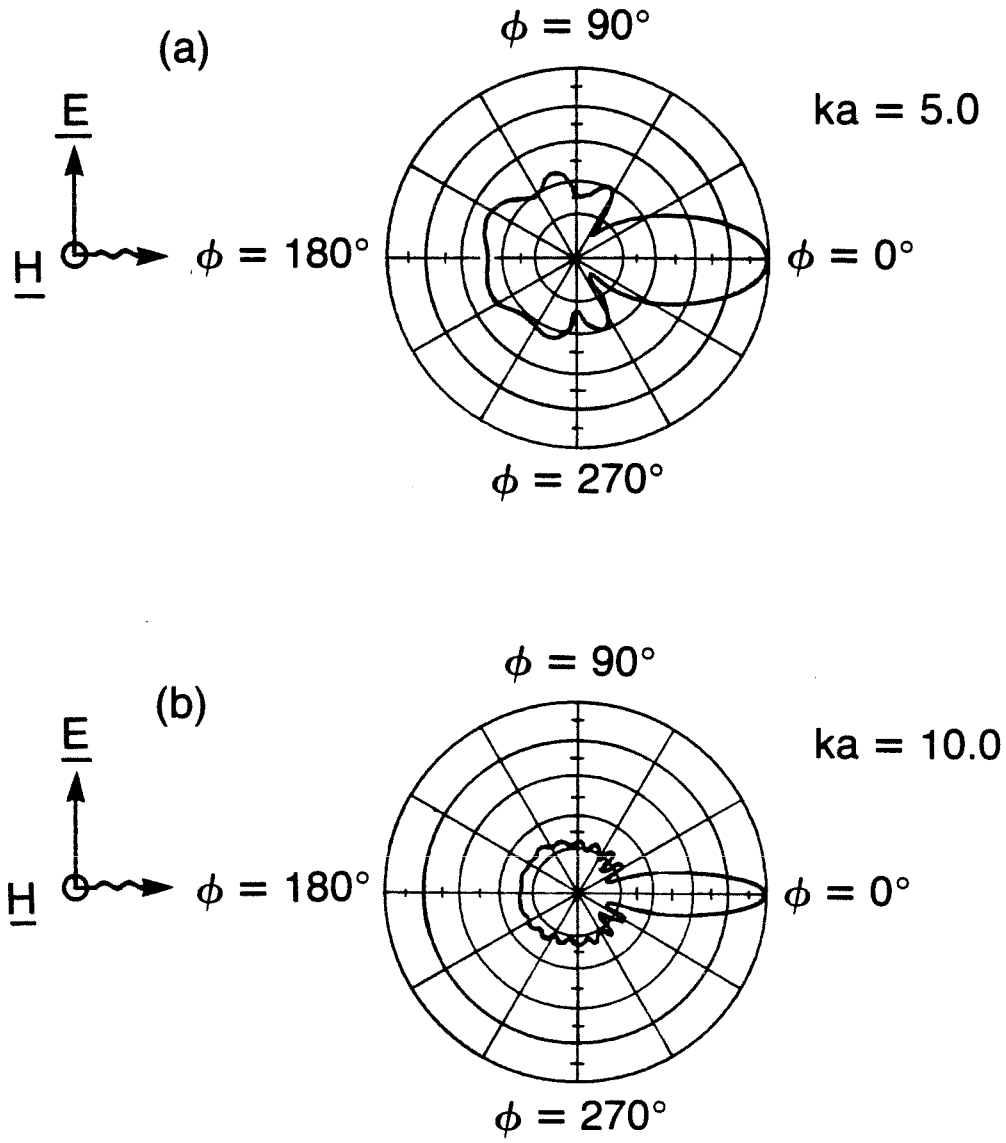

Fig. 2.5 The normalized scattered field $|H^s(\rho,\phi)/H^s(\rho,0°)|$ for the normal incidence case, in Eq. (2.42), is plotted vs. the scattering angle ϕ. (a) and (b) are plotted in polar coordinates for ka = 5, and 10; (continued on next page)

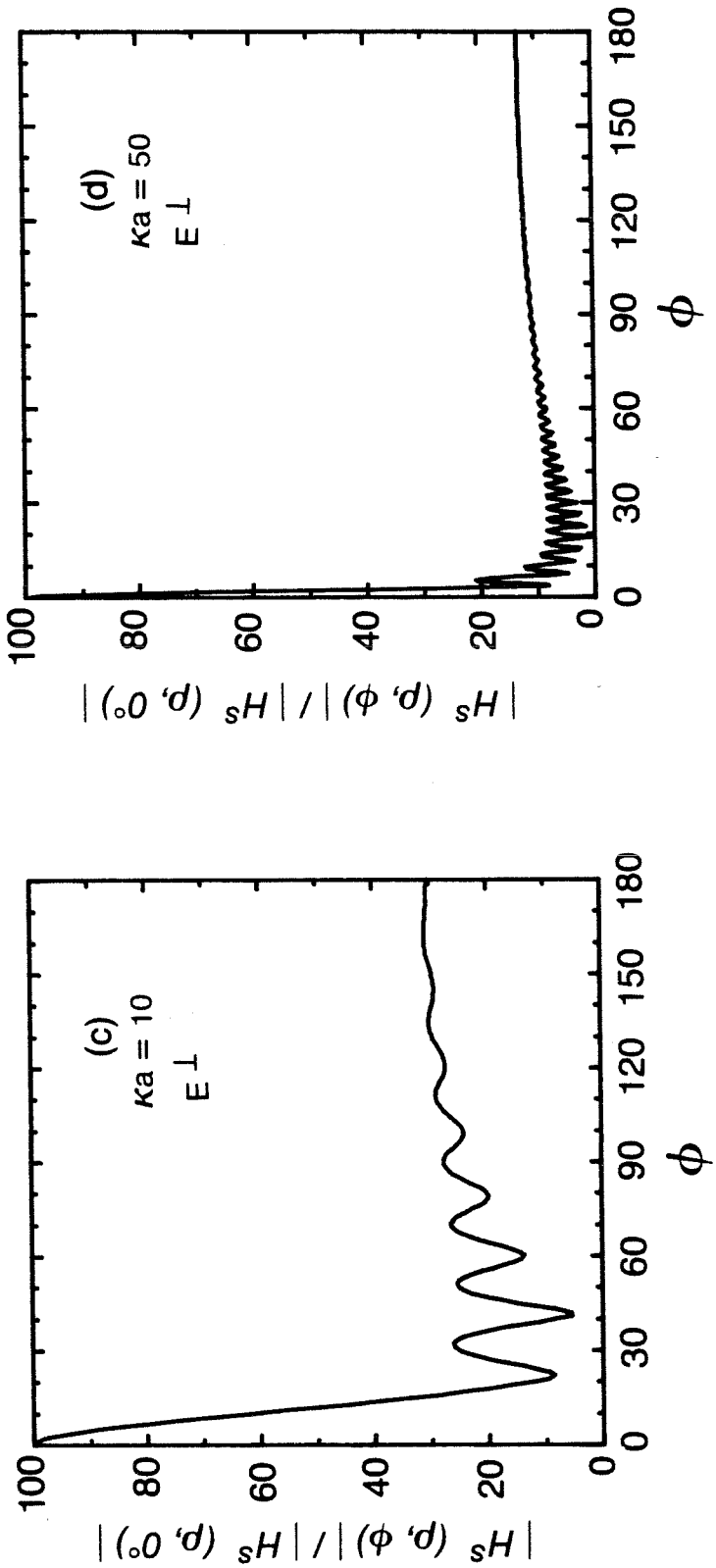

Fig. 2.5 Continued. (c) and (d) show the normalized scattered field plotted in linear coordinates for ka = 10 and 50.

2.4 Surface Current Density

According to Maxwell's equations the electric and magnetic fields illuminating a perfectly conducting cylinder will induce a surface current in a very tiny shell on the surface of the cylinder. The surface current density for the case when the incident electric field is parallel to the axis of the cylinder will also be in the z-direction. The surface current density generated by the parallel polarized incident field will be denoted as $K_z(\phi)$, and it is given by[9]

$$K_z(\phi) = H_\phi(a,\phi).$$

Hence, from Eq. (2.9)

$$K_z(\phi) = \frac{i}{\omega\mu} \frac{\partial E_z(\rho,\phi)}{\partial \rho} \Big|_{\rho=a}, \tag{2.45}$$

where $E_z(\rho,\phi)$ is the total electric field.

From Eqs. (2.45), (2.31) and (2.33) we can get

$$K_z(\phi) = \frac{ik}{\omega\mu} \sum_{m-\infty}^{\infty} (i)^m e^{im\phi} [J_m'(ka) - \frac{J_m(ka)}{H_m^{(1)}(ka)} H_m'^{(1)}(ka)].$$

By using Bessel differentation formulas and using the orthogonality relation[10]

$$J_{m+1}(ka)Y_m(ka) - J_m(ka)Y_{m+1}(ka) = \frac{2i}{\pi ka},$$

then,

$$K_z(\phi) = \frac{2}{\omega\mu\pi a} \sum_{m=-\infty}^{\infty} (i)^m \frac{e^{im\phi}}{H_m^{(1)}(ka)}, \tag{2.46}$$

or

$$K_z(\phi) = \frac{2}{\omega\mu\pi a} \left[\frac{1}{H_0^{(1)}(ka)} + 2 \sum_{m=1}^{\infty} \frac{(i)^m}{H_m^{(1)}(ka)} \cos m\phi\right]. \tag{2.47}$$

When the electric field of the incident wave is linearly polarized in the direction normal to the axis of the cylinder, then the magnetic field will be parallel to the axis of the cylinder. At the boundary this magnetic field will induce a surface current density flowing in the ϕ direction, and the surface current, $K_\phi(\phi)$, will be given by[9]

$$K_\phi(\phi) = H_z(\rho,\phi)\Big|_{\rho=a}. \tag{2.48}$$

From Eqs. (2.48), (2.38) and (2.41) we get

$$K_\phi(\phi) = \frac{2i}{\pi ka} \sum_{m=-\infty}^{\infty} (i)^m \frac{e^{im\phi}}{H_m'^{(1)}(ka)}. \tag{2.49}$$

Therefore,

$$K_\phi(\phi) = \frac{2i}{\pi ka} \left\{\frac{1}{H_0'^{(1)}(ka)} + 2 \sum_{m=1}^{\infty} \frac{(i)^m}{H_m'^{(1)}(ka)} \cos m\phi\right\}. \tag{2.50}$$

The surface current densities for both polarizations of the incident field which are given by Eqs. (2.47) and (2.50) have the same format, except for the coefficients of the series, i.e., one of them has the Hankel function and the other has its derivative, and both of them have a period of 2π in ϕ. The surface current $K_z(\phi)$ is plotted in Fig. 2.6(a) for ka = 5, 50 and 500. The surface current is maximum at $\phi = 180°$ which is the center of the illuminating region, then it decreases as we move away towards the shadow region. The surface current will be flowing as travelling waves[9] starting at the shadow boundaries, $\phi = \pi/2$ and $\phi = -\pi/2$. They will travel around the cylinder in the shadow region in opposite directions. Those travelling waves will interfere with each other producing a standing wave at $\phi = 0°$. As ka increases, the current decreases faster as we move towards the shadow region, e.g., for ka = 5, the current drops to 26 dB at $\phi \cong 40°$, while for ka = 50 and 500 the current drops to 26 dB respectively at $\phi \cong 75°$ and 90°. The surface current drops to a negligible value in the shadow region for respectively large values of ka. The surface current density $K_\phi(\phi)$, when the incident electric field is polarized normal to the axis of the cylinder, is plotted in Fig. 2.6(b) for ka = 5, 50 and 500. The surface current flows in the ϕ direction enables it to travel more in the shadow region. As it was for $K_z(\phi)$, $K_\phi(\phi)$ also exists as travelling waves starting from the shadow boundaries and making a standing wave with a maximum at $\phi = 0°$. The surface current density for this case does not drop in its value as rapidly as that for the previous case. We can see that for all values of ka considered the current

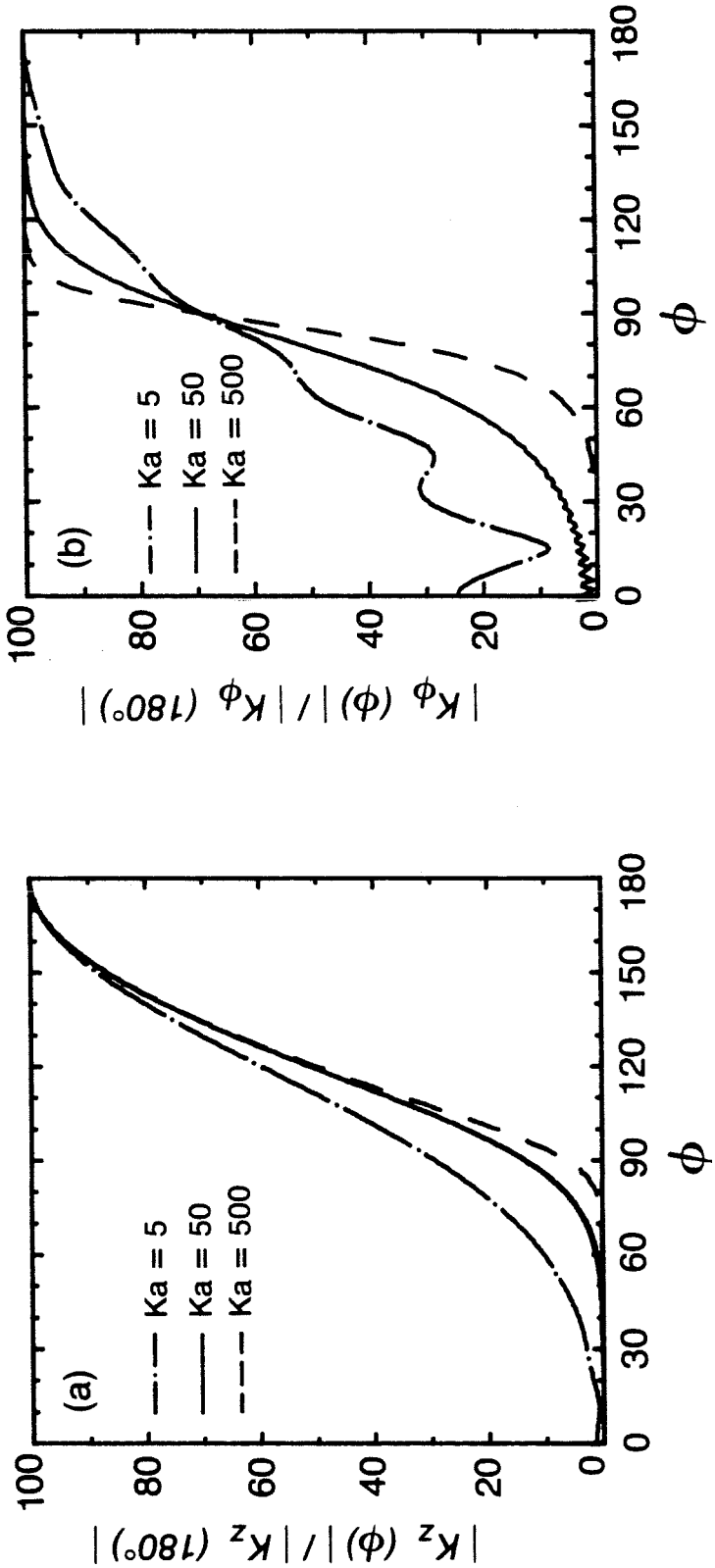

Fig. 2.6 The surface current density (a) $|K_z(\phi)/K_z(180°)|$ and (b) $|K_\phi(\phi)/K_\phi(180°)|$ for parallel and normal polarizations, respectively, in Eqs. (2.46) and (2.48) are plotted vs. the scattering angle for ka = 5, 50, and 500. Note the decrease of surface current in the shadow region by the increase of ka.

drops only by 3 dB at the shadow boundaries ($\phi = \pi/2$ and $-\pi/2$). In Fig. 2.7 the surface currents for both polarization are plotted together for comparison at ka = 5 and ka = 500. The current for the parallel polarization is dropping much faster than that for the normal polarization. If we look at the curves for ka = 500, K_ϕ begins having negligible values around $\phi \cong 40°$; but K_z starts having negligible values around $\phi \cong 80°$. This is the reason there are more nulls in the case of normal polarization than in the parallel polarization case.

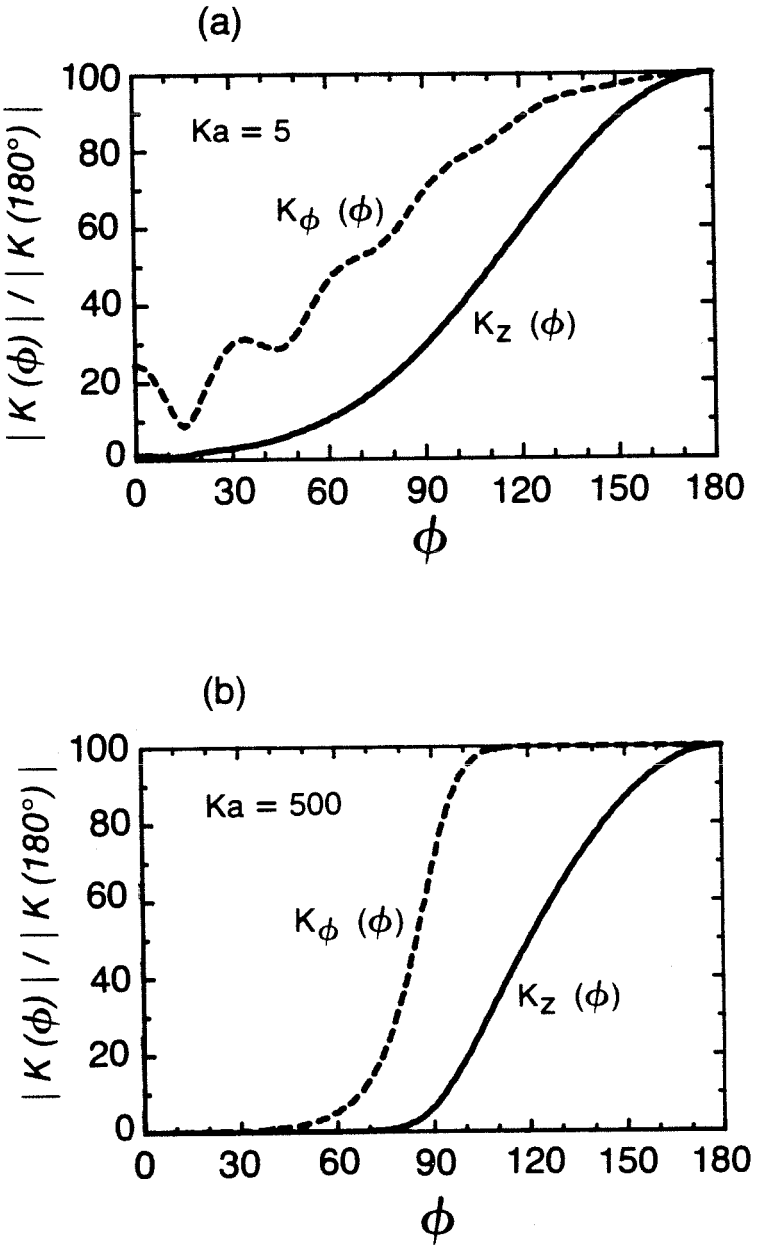

Fig. 2.7 The normalized current densities for both polarizations are plotted for (a) ka = 5, (b) ka = 500. Note that the surface current for the normal polarization is much larger than that for the parallel polarization.

2.5 The Fringe Spacings of the Scattered Field

A main feature of the scattered field amplitude is the fringe pattern and spacings it has. In section 2.3 where we studied the scattered field pattern, and we found that the fringe spacings decrease by the increase of the radius of the cylinder. In this section we would like to study the dependence of these fringe spacings on the scattering angle ϕ and the factor ka for both polarizations.

The fringe spacings $\Delta\phi$ are plotted in Figs. 2.8(a) and (b) for parallel and normal polarizations, respectively, as a function of ϕ for ka = 25, 50 and 100. For the parallel polarization, the fringe spacings have almost the same value over most of the range and they start increasing slightly at the end of the range. The fringes have a cutoff angle of about 40°, and this cutoff is changing with the change of ka. The physical significance of the cutoff angle is explained on the next page. The fringe spacings have a value $\cong (175/ka)°$. For the normal polarization, the fringes exist for a much larger range of ϕ; i.e., they have a much larger cutoff angle than that for the parallel polarization case. The fringe spacing for ka = 25 decreases to a minimum around ϕ = 40°, then increases in the rest of the range. For larger ka, fringe spacing also decreases at the beginning of the range and increasing at the end of it. But they have almost the same value for most of the range, and their minimum value equals that for the parallel polarization case. So the fringe spacings carry the information about the radius of the cylinder and the wavelength of the illuminating wave. The dependence of the cutoff

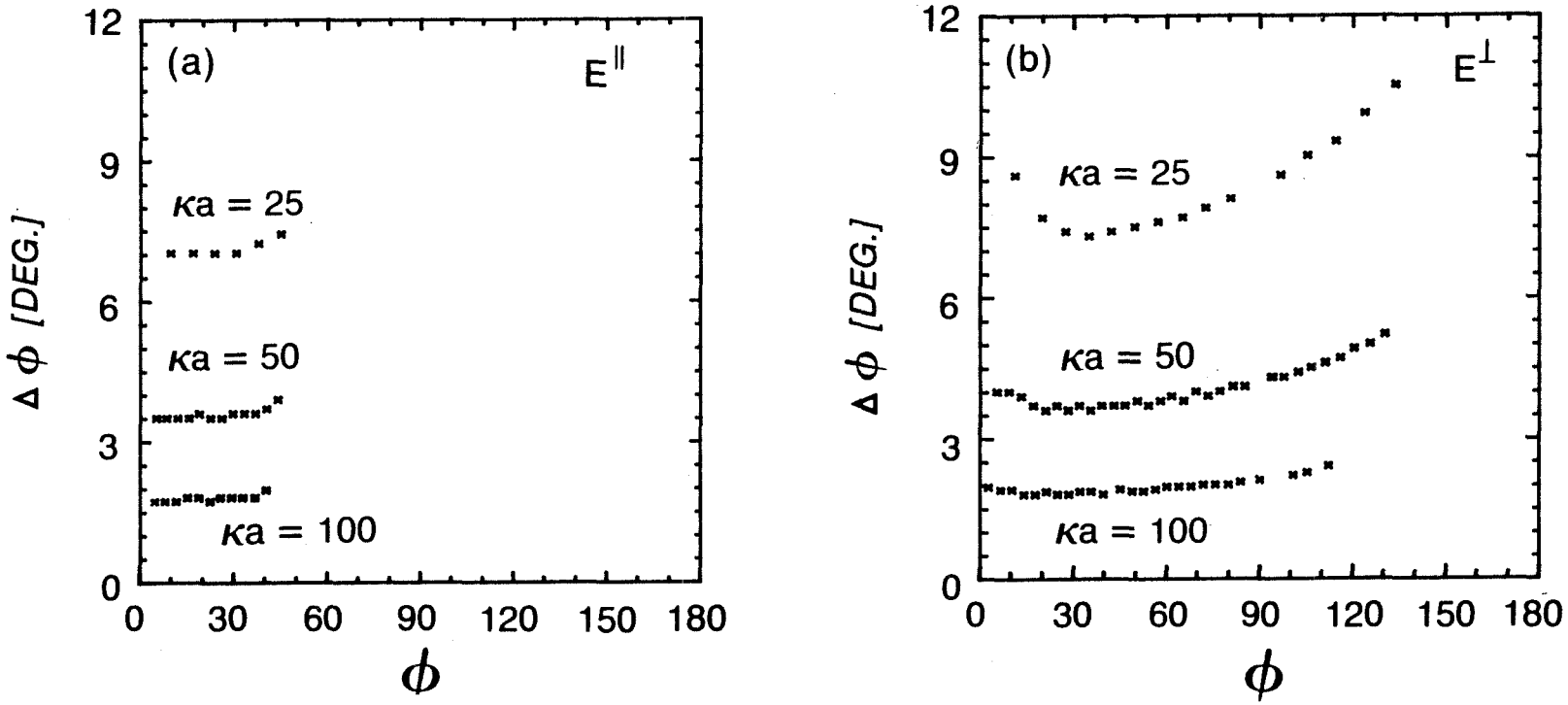

Fig. 2.8 The fringe spacings of the scattered field are plotted for (a) parallel polarization and (b) normal polarization for ka = 25, 50, 100. Note that the spacings decreases with the increase of ka and that they appear for a shorter range of scattering angles for the parallel polarization than for that of the normal incident case.

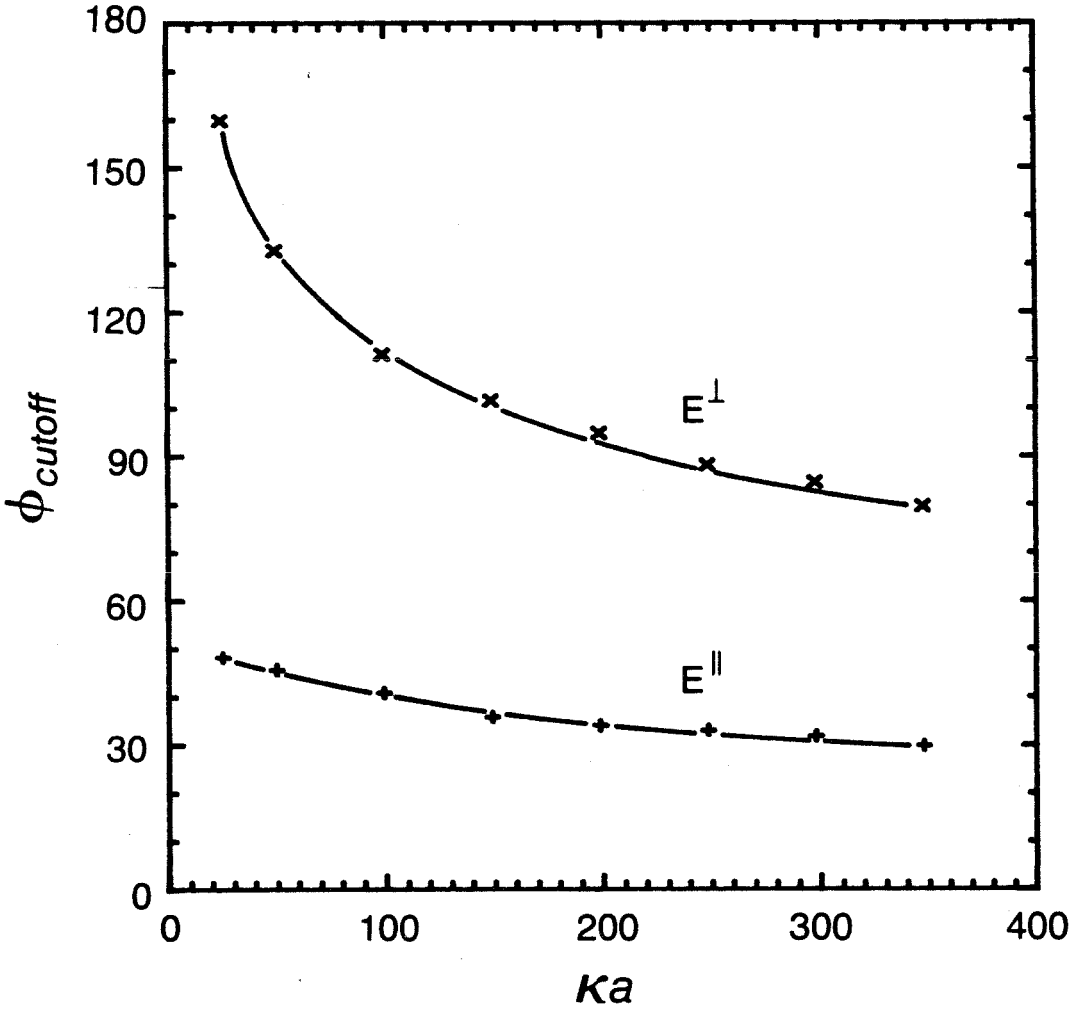

Fig. 2.9 The cutoff angle of the fringes plotted vs. the factor ka for both polarizations of the incident field.

angle of the fringes is plotted in Fig. 2.9 as a function of the factor ka, from ka = 30 to ka = 350 for both polarizations. The cutoff angle decreases by the increase of ka, and it is much less for the parallel polarizations than that for the normal polarization. And also it decreases much more rapidly for the normal polarization case, from 160° to 80°; however, it decreases only from 50° to 30° for the parallel polarization case.

The fringes of the scattered field are generated by interference between the fields that are reflected, diffracted by the edges of the cylinder and fields generated by the surface current travelling waves. When the incident electric field is parallel to the cylinder, the fringes are mainly generated by the diffracted waves because the surface current is very small in the shadow region, which will not allow the current to go around the cylinder. That is the reason there are fringes only in a very small range of the scattering angle and are cutoff beyond this range. When the incident magnetic field is parallel to the axis, the surface current is large in the shadow region which will allow it to go around the cylinder, before it becomes negligible. That will make the field generated by the surface current large and the fringes will extend their region of existence. As the factor ka gets larger, the surface current gets smaller, and in turn the cutoff angle of the fringes also gets smaller.

CHAPTER II

REFERENCES

1. H.C. Van de Hulst, Light Scattering by a Small Particles (Wiley, New York, 1957).
2. M. Kerker, The Scattering of Light and Other Electromagnetic Radiation (Academic, New York, 1969).
3. M. Born, and E. Wolf, Principles of Optics (Pergamon, Oxford, 1975).
4. D.S. Jones, The Theory of Electromagnetism (Macmillan, New York, 1964).
5. J.A. Stratton, Electromagnetic Theory (McGraw-Hill, New York 1941).
6. G.N. Watson, A Treatise on the Theory of Bessel Functions (Cambridge University Press, 1922).
7. I.S. Gradshteyn and I.M. Ryzhik, Tables of Integrals, Series, and Products (Academic Press, New York 1965).
8. C.H. Papas, "Diffraction by a Cylindrical Obstacle," J. Appl. Phys. 21, p. 318 (1950).
9. R.W.P. King and T.T. Wu, The Scattering and Diffraction of Waves (Harvard University Press, Cambridge, 1959).
10. M. Abramowitz, and I.A. Stegun, Handbook of Mathematical Functions (National Bureau of Standards, Washington D.C., 1972).

CHAPTER III

SCATTERING OF LIGHT FROM LARGE DIELECTRIC CIRCULAR CYLINDERS

3.1 Introduction

In this chapter a theory for the scattering of a monochromatic plane wave by a dielectric cylinder is presented. The problem is formulated for dielectric cylinders of circular cross section, constant index of refraction and radius which is larger than the wavelength of the illuminating wave; however, all the formulations are good for the case where the radius is smaller than the wavelength. It is of particular interest to examine how the radius and the refractive index variations map into the scattered field pattern.

Section 3.2 contains a rigorous solution for the Helmholtz wave equation for the scattered field in the two different polarizations of the incident field, parallel and normal to the axis of symmetry of the cylinder.

In Section 3.3 the fringe spacings of the scattered field are studied for a set of cylinders with different radii.

In Section 3.4 the effect of the index of refraction variations on the scattered field pattern are studied, and it is shown that the position of the peak in the backscattered field depends on the index of refraction of the cylinder.

3.2 Rigorous Solution for the Scattered Field

From Maxwell's equations for time harmonic fields Eqs. (2.9) through (2.12), we can derive the following Helmholtz wave equation

$$\nabla^2 \underline{E}(\underline{r}) + n^2 k^2 \underline{E}(\underline{r}) = 0 \tag{3.1}$$

where n is the index of refraction of the material of the cylinder

$$n = \sqrt{\mu_r \varepsilon_r} \tag{3.2}$$

and where μ_r and ε_r are the permeability and permitivity of the medium, respectively.

In the following subsection we will derive the solutions for the Helmholtz wave equation (3.1) for the two different polarizations of the incident wave.

3.2.1 Parallel Polarization Case

When the illuminating wave is a plane wave linearly polarized in the z-direction and parallel to the axis of symmetry of the cylinder then the incident electric field will be given by

$$\underline{E}^{inc}(\rho,\phi) = \underline{e}_z \, e^{ik\rho\cos\phi}$$

which can be expressed in terms of Bessel functions as[1]

$$E_z^{inc}(\rho,\phi) = e^{ik\rho\cos\phi} = \sum_{m=-\infty}^{\infty} (i)^m J_m(k\rho) e^{im\phi} \, . \tag{3.3}$$

To solve the Helmholtz wave equation we will first rewrite it in cylindrical coordinates. Then using the separation of variables

technique following the same procedure outlined in Chapter II we obtain the following solutions for the electric field outside and inside the cylinder

$$E^s(\rho,\phi) = \sum_{m=-\infty}^{\infty} a_m H_m^{(1)}(k\rho)\, e^{im\phi}; \qquad \rho > a \ , \tag{3.4}$$

and

$$E^{inside}(\rho,\phi) = \sum_{m=-\infty}^{\infty} D_m J_m(nk\rho) e^{im\phi}; \qquad \rho < a \ , \tag{3.5}$$

where a_m and D_m are arbitrary constants, which will be determined using the boundary conditions. The boundary conditions for such case are given by[2,3]

$$nE^t \text{ and } n\partial E^t/\partial\rho \text{ are continuous at } \rho = a. \tag{3.6}$$

The total electric field is the superposition of the incident field and the scattered field, i.e.,

$$E^{tot}(\rho,\phi) = E^i(\rho,\phi) + E^s(\rho,\phi) \ . \tag{3.7}$$

The tangential component of the field outside the cylinder from Eqs. (3.3) and (3.4) is given by

$$E^t(\rho,\phi) = \sum_{m=-\infty}^{\infty} [(i)^m J_m(k\rho) + a_m H_m^{(1)}(k\rho)] e^{im\phi} \ . \tag{3.8}$$

By applying the first boundary condition, nE^t is continuous across the boundary $\rho = a$, and using Eqs. (3.5) and (3.8) we get

$$n \sum_{m=-\infty}^{\infty} D_m J_m(nka) e^{im\phi} = \sum_{m=-\infty}^{\infty} [(i)^m J_m(ka) + a_m H_m^{(1)}(ka)] e^{im\phi} \quad . \tag{3.9}$$

From the orthogonality of functions $e^{im\phi}$, we can set the individual terms in Eq. (3.9) to zero, then we obtain

$$D_m = \frac{(i)^m J_m(ka) + a_m H_m(ka)}{n J_m(nka)} \quad . \tag{3.10}$$

And by applying the second boundary condition, $n\partial E^t/\partial\rho$ is continuous across the boundary $\rho = a$, and using Eqs. (3.5) and (3.8) we find

$$n^2 k \sum_{m=-\infty}^{\infty} D_m J_m'(nka) e^{im\phi} = k \sum_{m=-\infty}^{\infty} [(i)^m J_m'(ka) + a_m H_m^{(1)}(ka)] e^{im\phi} \quad .$$

Then,

$$a_m = \frac{n^2 D_m J_m'(nka) - (i)^m J_m'(ka)}{H_m'(ka)} \quad . \tag{3.11}$$

By substituting Eq. (3.10) into (3.11) and by straightforward algebra we find

$$a_m = -(i)^m \frac{n J_m(ka) J_m'(nka) - J_m'(ka) J_m(nka)}{n J_m'(nka) H_m^{(1)}(ka) - J_m(nka) H_m'^{(1)}(ka)} \quad , \tag{3.12}$$

and

$$D_m = -(i)^m \frac{J_n(ka)[H_m'^{(1)}(ka) - H_m(ka)]}{n^2 J_m'(nka) H_m^{(1)}(ka) - n J_m(nka) H_m'^{(1)}(ka)} \quad . \tag{3.13}$$

From Eqs. (3.4) and (3.12) the scattered field will be given by

$$E_z^s(\rho,\phi) = - \sum_{m=-\infty}^{\infty} (i)^m \frac{nJ_m(ka)J_m'(nka) - J_m'(ka)J_m(nka)}{nJ_m'(nka)H_m^{(1)}(ka) - J_m(nka)H_m'^{(1)}(ka)} H_m^{(1)}(k\rho)e^{im\phi}. \tag{3.14}$$

And from Eqs. (3.5) and (3.13) the field inside the cylinder will be given by

$$E_z^{(inside)}(\rho,\phi) = - \sum_{m=-\infty}^{\infty} (i)^m \frac{J_n(ka)[H_m'^{(1)}(ka) - H_m(ka)]}{n^2J_m'(nka)H_m^{(1)}(ka) - nJ_m(nka)H_m'^{(1)}(ka)} \times J_n(nk\rho)e^{im\phi} \tag{3.15}$$

These solutions are the same as those given by van de Hulst.[3]

From Eq. (3.14) we see that the scattered field is expressed in an infinite series of the same form as that for the conducting cylinder case, except for the arbitrary constant a_m which takes a more complex form than that of b_m. So the scattered field will be propagating outside the cylinder in a cylindrical wave, with amplitude and phase depending on the radius, index of refraction, scattering angle, and the distance of observation point from the axis of the cylinder.

To study the scattered field, we need to sum up enough terms of the series until it converges. Then the rest of the terms will have no significant contribution to scattered field. In Appendix A it is shown that the number of terms, which will make the series converge is slightly larger than ka. In Fig. 3.1 the coefficient

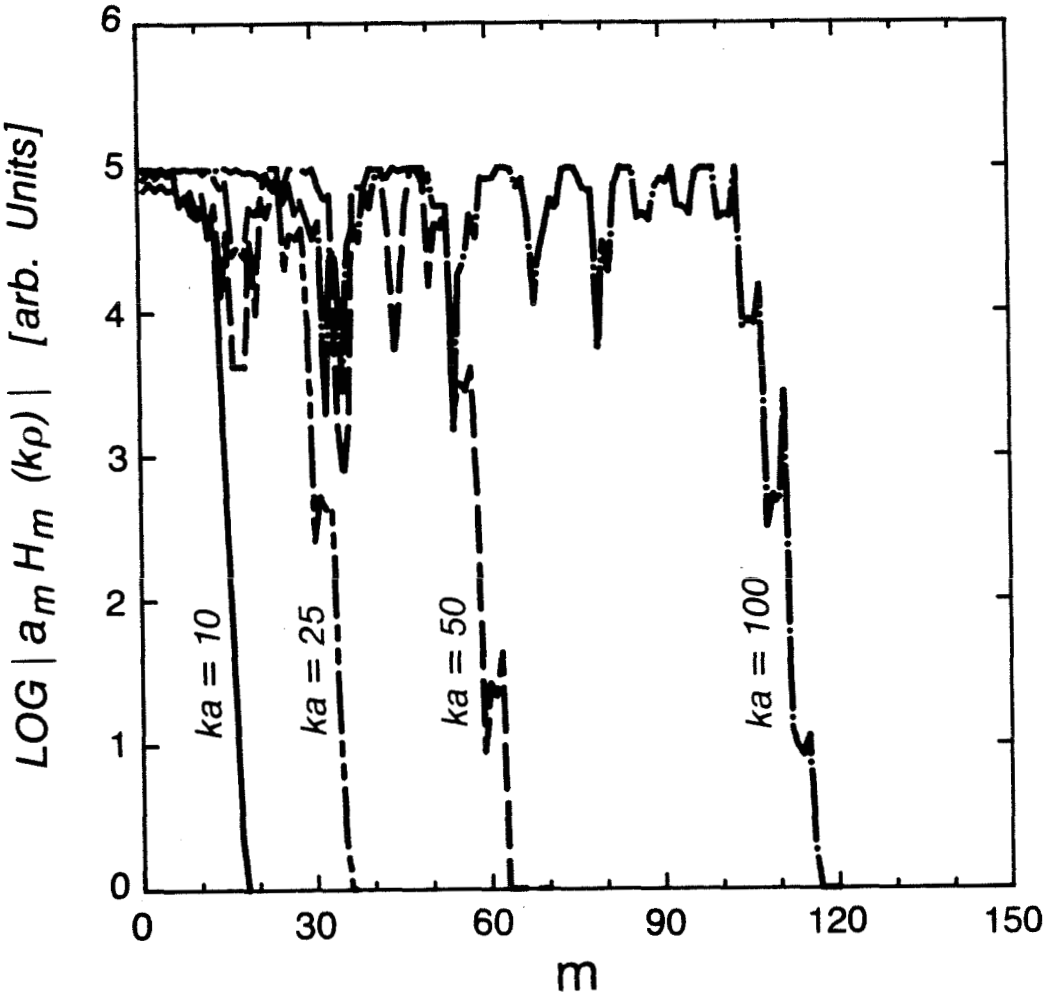

Fig. 3.1 Logarithm of the normalized coefficient $|a_m H_m^{(1)}(k\rho)|$ given by Eq. (3.12) plotted vs. the order m, for ka = 10, 25, 50 and 100. Note that the coefficient reduces to a negligible value at $m \cong ka + 10$.

$\text{Log}\{|a_m H_m^{(1)}(k\rho)|\}$, as a function of the number of terms m at ρ = 10 cm, is plotted. From these curves, the coefficient becomes negligible when $m \cong ka(1+\gamma)$. The value of γ decreases by the increase of ka, e.g., $\gamma = 0.8$ at ka = 10, and $\gamma = 0.17$ at ka = 100.

The normalized scattered electric field $|E_z^s(\rho,\phi)|/|E_z^s(\rho,0)|$ is plotted in Figs. 3.2(a) and (b) in polar coordinates for ka = 5 and 10 respectively. The pattern of the scattered field has a main lobe at $\phi = 0^\circ$, and a number of side lobes with amplitude decreases with the increase of ϕ. In the backscattered field these lobes will increase their amplitude significantly. These backscattered lobes are main features of the dielectric cylinder scattered field and are not present in the case of the conducting cylinder. In Figs. 3.2(c) and (d) the normalized scattered electric field is plotted for ka = 10 and 50, respectively. The width of the main lobe decreases by the increase of ka; the number of lobes increase by the increase of ka; and, hence, the fringe spacings decrease. The backscattered field lobes have a larger amplitude than those before them, so they can be recognized very easily. The other thing we notice about the backscattered lobes, is that they have a peak around $\phi \cong 155^\circ$, and its position does not change significantly by the change of the factor ka.

The fringes of the scattered field pattern are a result of the interference between the refracted rays, which propagate through the cylinder, the reflected rays, which reflects from the surface of the cylinder, and the rays diffracted by the edges of the cylinder. Those are the main sources of the fringes in the forward scattered

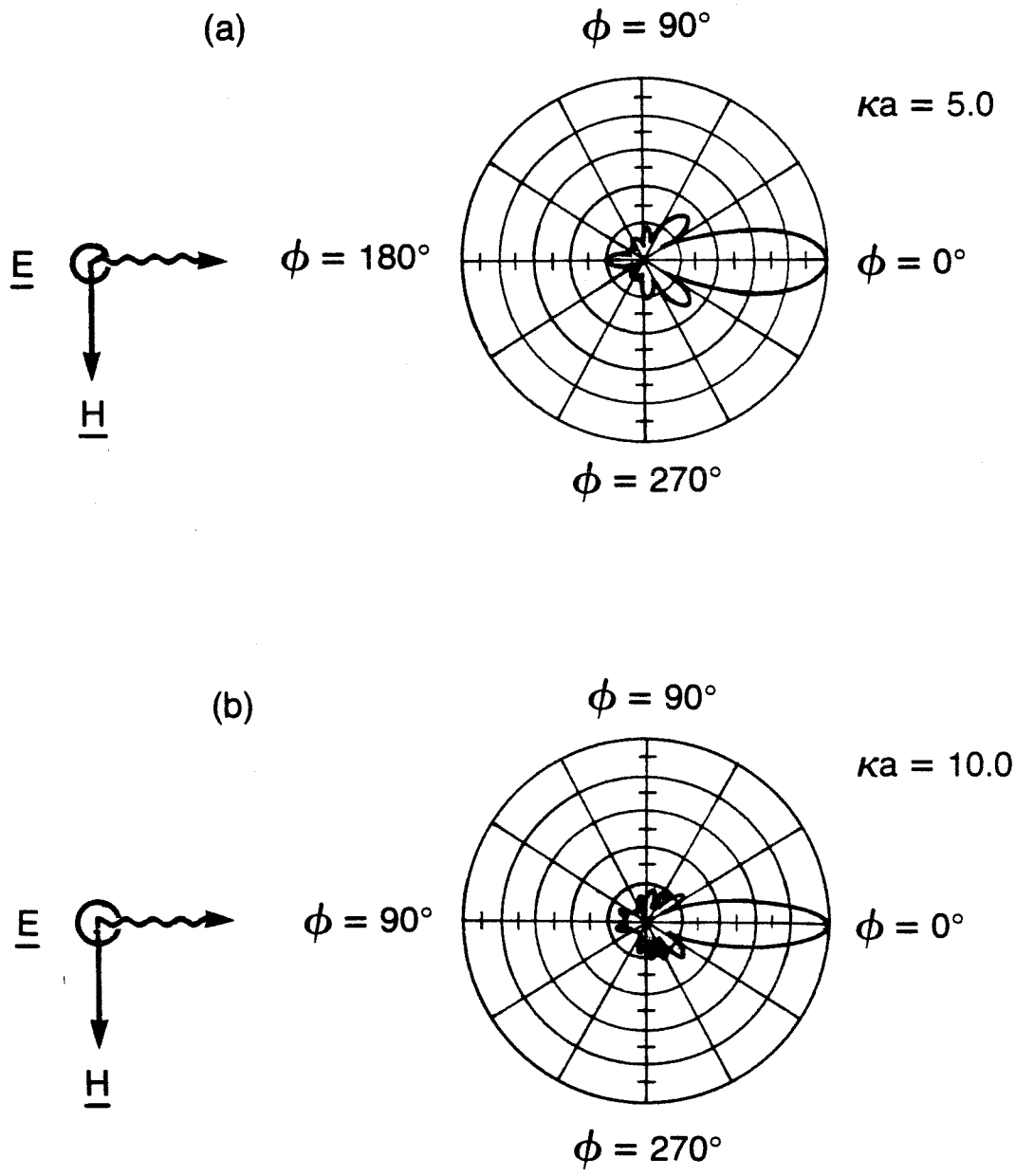

Fig. 3.2 The normalized scattered field $|E^s(\rho,\phi)|/|E^s(\rho,0^\circ)|$ given by Eq. (3.14) plotted vs. the scattering angle ϕ. (a) and (b) are plotted in polar coordinates for ka = 5 and ka = 10, respectively; (continued on next page).

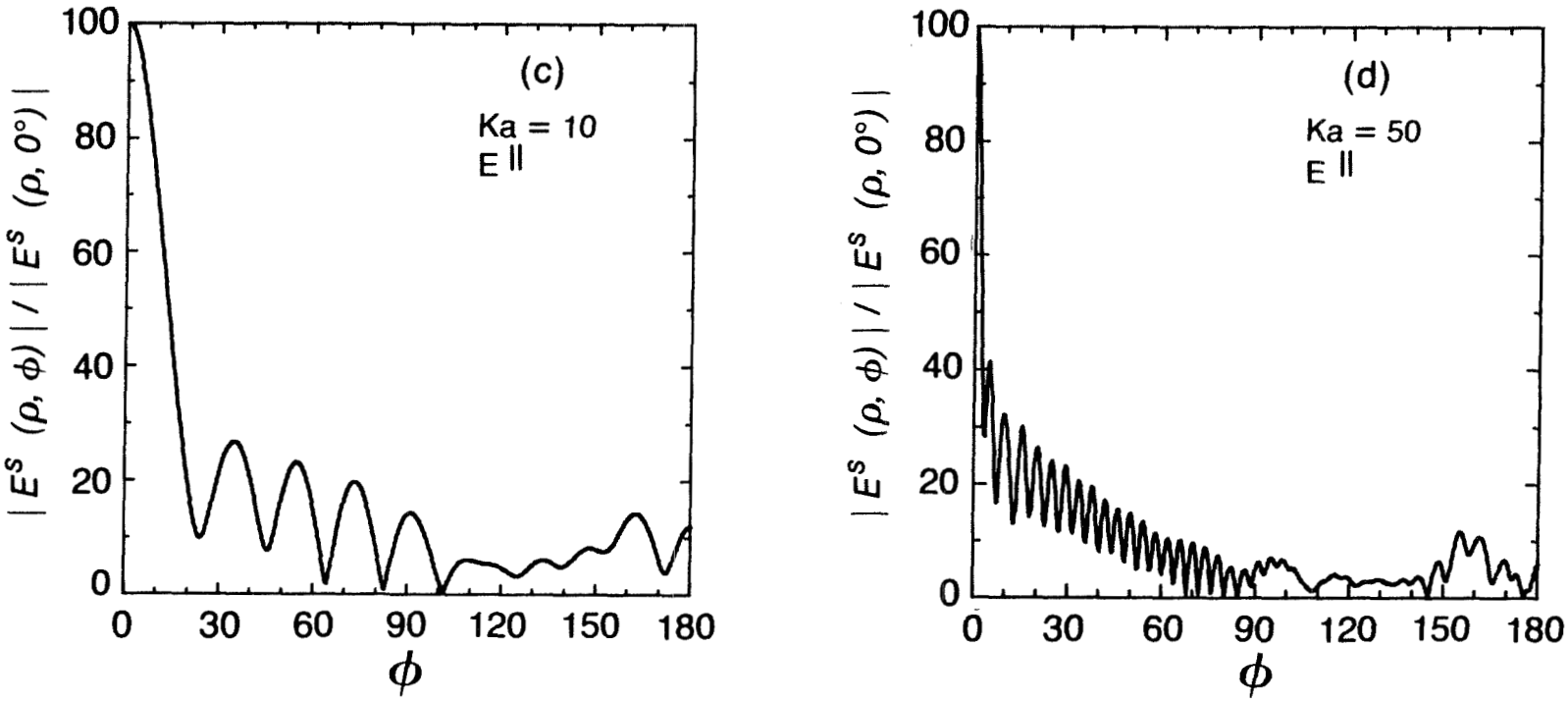

Fig. 3.2 Continued. (c) and (d) the scattered field plotted in linear coordinates for ka = 10 and ka = 50, respectively. Note the width of the main lobe decreases by the increase of ka, and the number of side lobes are more for ka = 50 than those for ka = 10.

field. The rays which will make multiple refractions and reflections inside the cylinder will make contributions to the scattered field especially in the range of $80° \lesssim \phi \lesssim 150°$. The backscattered field fringes are a result of the interference between the reflected rays from the surface of the cylinder, and those which will be refracted through the cylinder once and then are reflected by the inner surface of the cylinder. The range they cover will depend mainly on the index of refraction of the cylinder.

3.2.2 Normal Polarization Case

When the illuminating plane wave is linearly polarized along the direction normal to the axis of symmetry of the cylinder, then the incident magnetic field will be polarized parallel to the axis of the cylinder, i.e.

$$\underline{H}^{inc}(\rho,\phi) = \underline{e}_z e^{ik\rho\cos\phi} ,$$

which can be expressed in terms of Bessel functions as

$$H_z^{inc}(\rho,\phi) = e^{ik\rho\cos\phi} = \sum_{m=-\infty}^{\infty} (i)^m J_m(k\rho) e^{im\phi} .$$

Then we need to solve the Helmholtz wave equation for the scattered magnetic field. Following the same procedure outlined in Chapter II we obtain the following solutions outside and inside the cylinder

$$H_z^s(\rho,\phi) = \sum_{m=-\infty}^{\infty} P_m H_m^{(1)}(k\rho) e^{im\phi}, \qquad \rho > a , \tag{3.16}$$

and the magnetic field inside the cylinder is given by

$$H_z^{inside}(\rho,\phi) = \sum_{m=-\infty}^{\infty} Q_m J_m(nk\rho)e^{im\phi}, \qquad \rho < a \ , \tag{3.17}$$

where P_m and Q_m are arbitrary constants, which will be evaluated using the proper boundary conditions. The boundary conditions for this case are:[1,2]

$$n^2H^t \text{ and } \partial H^t/\partial\rho \text{ are continuous at } \rho = a \ , \tag{3.18}$$

where H^t is the tangential component of the total magnetic field. The tangential component of the total magnetic field outside the cylinder is given by

$$H^t(\rho,\phi) = \sum_{m=-\infty}^{\infty} [(i)^m J_m(k\rho) + P_m H_m^{(1)}(k\rho)]e^{im\phi} \ . \tag{3.19}$$

By applying the first boundary condition, n^2H^t is continuous across the boundary $\rho = a$, and using Eqs. (3.17) and (3.19) we get

$$n^2 \sum_{m=-\infty}^{\infty} Q_m J_m(nka)e^{im\phi} = \sum_{m=-\infty}^{\infty} [(i)^m J_m(ka) + P_m H_m^{(1)}(ka)]e^{im\phi}. \tag{3.20}$$

From the orthogonality of functions $e^{im\phi}$, we can set the individual terms in Eq. (3.20) to zero, then we obtain

$$Q_m = \frac{P_m H_m^{(1)}(ka) + (i)^m J_m(ka)}{n^2 J_m(nka)} \ . \tag{3.21}$$

And by applying the second boundary condition, $\partial H^t/\partial\rho$ is continous across the boundary $\rho = a$, and using Eqs. (3.17) and (3.19) we get

$$nk \sum_{m=-\infty}^{\infty} Q_m J_m'(nka) e^{im\phi} = k \sum_{m=-\infty}^{\infty} [P_m H_m'^{(1)}(ka) + (i)^m J_m'(ka)] e^{im\phi} .$$

Then,

$$P_m = \frac{nQ_m J_m'(nka) - (i)^m J_m'(ka)}{H_m'^{(1)}(ka)} . \tag{3.22}$$

From Eqs. (3.21) and (3.22) it is evident that we get the following expressions for the arbitrary constants P_m and Q_m;

$$P_m = -(i)^m \frac{J_m(ka)J_m'(nka) - nJ_m'(ka)J_m(nka)}{H_m^{(1)}(ka)J_m'(nka) - nH_m'^{(1)}(ka)J_m(nka)} , \tag{3.23}$$

and

$$Q_m = \frac{(i)^m}{n} \frac{H_m^{(1)}(ka)J_m'(ka) - J_m(ka)H_m'^{(1)}(ka)}{H_m^{(1)}(ka)J_m'(nka) - nJ_m(nka)H_m'^{(1)}(ka)} . \tag{3.24}$$

From Eqs. (3.16) and (3.23) the scattered field will be given by

$$H_z^s(\rho,\phi) = - \sum_{m=-\infty}^{\infty} (i)^m \frac{J_m(ka)J_m'(nka) - nJ_m'(ka)J_m(nka)}{H_m^{(1)}(ka)J_m'(nka) - nH_m'^{(1)}(ka)J_m(nka)} H_m^{(1)}(n\rho) e^{im\phi} . \tag{3.25}$$

And from Eqs. (3.17) and (3.24) the field inside the cylinder will be given by

$$H_z^{inside}(\rho,\phi) = - \sum_{m=-\infty}^{\infty} \frac{(i)^m}{n} \frac{H_m^{(1)}(ka)J_m'(ka) - J_m(ka)H_m'^{(1)}(ka)}{H_m^{(1)}(ka)J_m'(nka) - nJ_m(nka)H_m'^{(1)}(ka)} \quad (3.26)$$

The scattered magnetic field is expressed as an infinite series of the same form as that for the parallel polarization case, with minor differences in the coefficient P_m. The scattered field will be propagating as before as a cylindrical wave traveling in the positive ρ-direction, with amplitude and phase dependent on the radius, index of refraction, scattering angle, and ρ.

For plotting the scattered field amplitude we found, as for the previous cases, that we need to take at least $ka(1 + \gamma)$ terms of the series to insure its convergence. The normalized scattered field $|H_z^s(\rho,\phi)|/\ |H_z^s(\rho,0^o)|$ is plotted in Figs. 3.3(a) and (b) in polar coordinates and in Figs. 3.3(c) and (d) in linear coordinates. The main characteristics of the scattered field pattern are the same as those for the parallel polarization case. The pattern has a main lobe, with width decreases by the increase of ka, and a number of side lobes, which increase by the increase of ka.

From the curves of the scattered field of both the parallel and normal incident field polarizations, one sees that the fields have very similar features. The fields of the parallel polarization case have fringes with a large contrast in the range $0^o \leqq \phi \leqq 90^o$, but for the normal polarization case the fringes have very low contrasts.

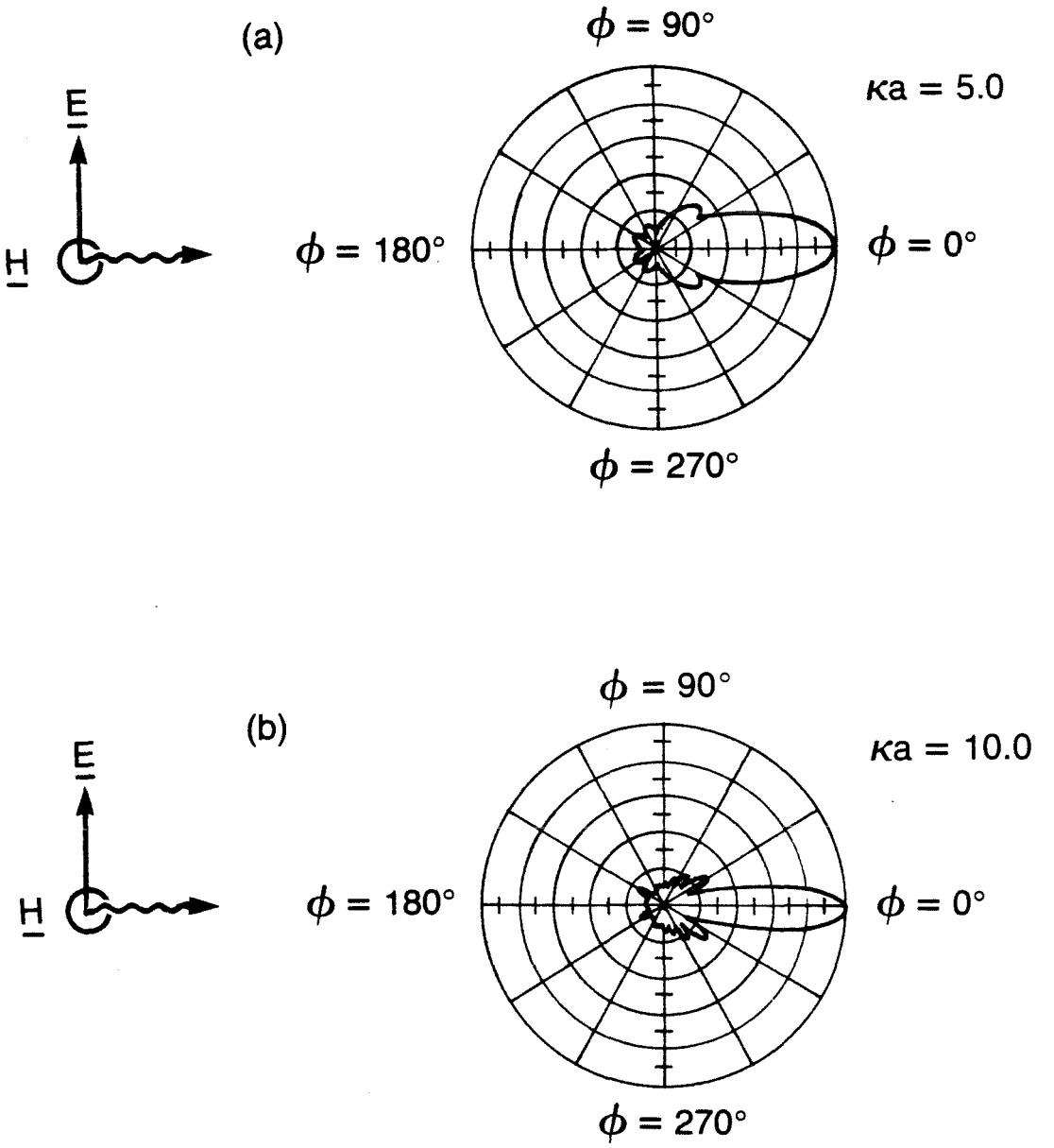

Fig. 3.3 The normalized scattered field $|H^s(\rho,\phi)|/|H^2(\rho,0^\circ)$ for the normal incidence case, in Eq. (3.25), is plotted vs. the scattering angle ϕ. (a) and (b) are plotted in polar coordinates for ka = 5, and 10; (continued on next page)

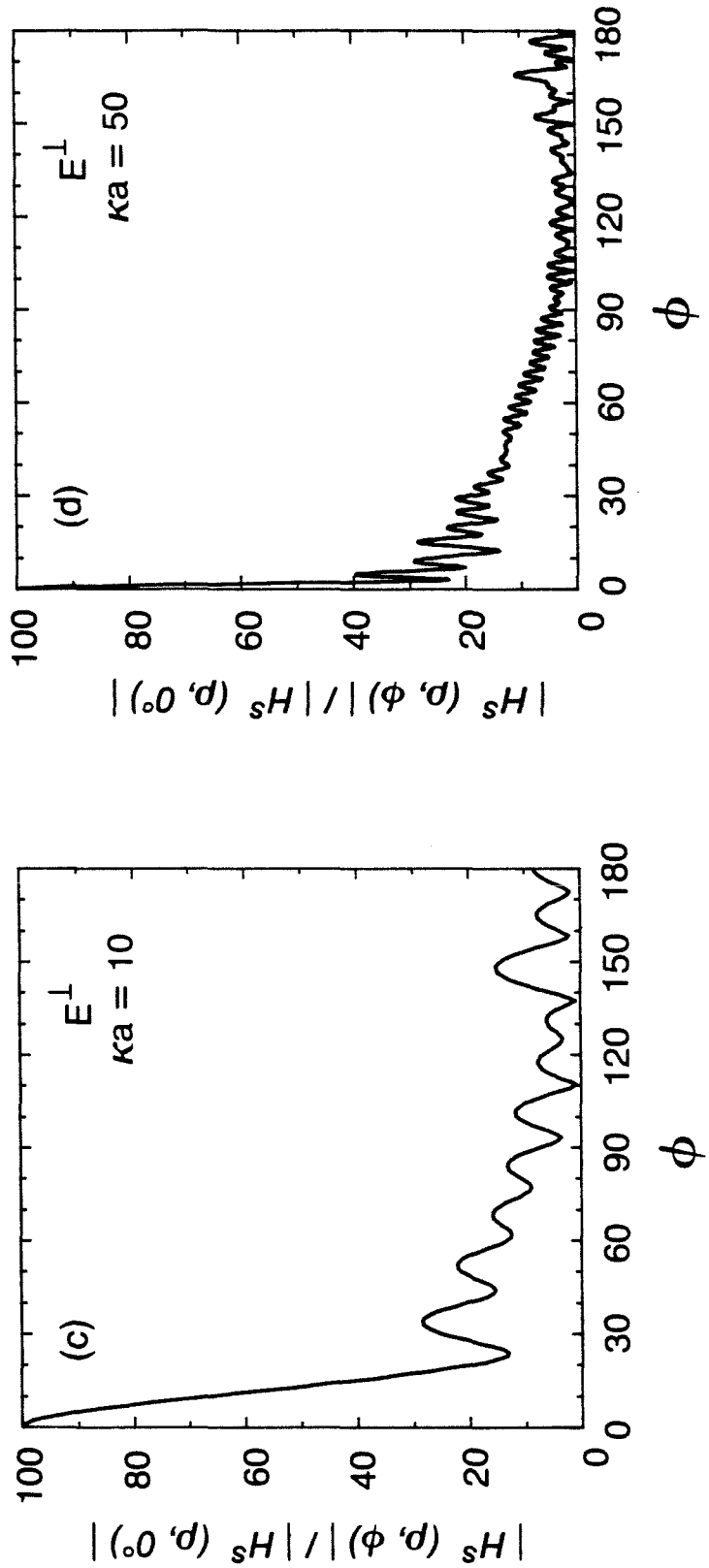

Fig. 3.3 Continued. (c) and (d) shows the normalized scattered field $|H^s(\rho,\phi)|/|H^s(\rho,0^o)|$ plotted for ka = 10 and 50.

3.3 The Fringe Spacings of the Scattered Field

The fringe spacings are one of the main features of the scattered field. In section 3.2 we found that the fringe spacings are functions of the radius of the cylinder and the wavelength. In this section we will study the dependence of the fringe spacings of the scattered field on the scattering angle ϕ and the factor ka for both polarizations of the incident field.

The fringe spacings, $\Delta\phi$, are plotted in Figs. 3.4(a) and (b) for parallel and normal polarizations of the incident field, respectively. In Fig. 3.4(a) the fringe spacings are plotted for ka = 50, 100, and 350 as a function of ϕ. The fringe spacings decrease with the increase of ka, and for large values of ka they have an almost fixed value between $\phi \cong 15°$ and $\phi \cong 90°$. In the range $0° \leqq \phi \leqq 15°$ the fringe spacings start with a larger value than that in the following range of ϕ, and then their values decrease as ϕ increases. In the range from $\phi = 90°$ to 180°, the fringe spacings fluctuate in their value around that of the previous range. So the fringe spacings, especially in the range of $\phi = 15°$ to 90°, carry the information about the value ka. For the normal incident case shown in Fig. 3.4(b) the fringe spacings have similar properties as those for the parallel incident case.

The fringes of the scattered field for the dielectric cylinder is generated by the rays of light transmitted through the cylinder, those reflected from the surface of the cylinder, and by those diffracted by the edges of the cylinder. In the range $0° \leqq \phi \leqq 90°$ the fringes are mainly generated by the interference between the

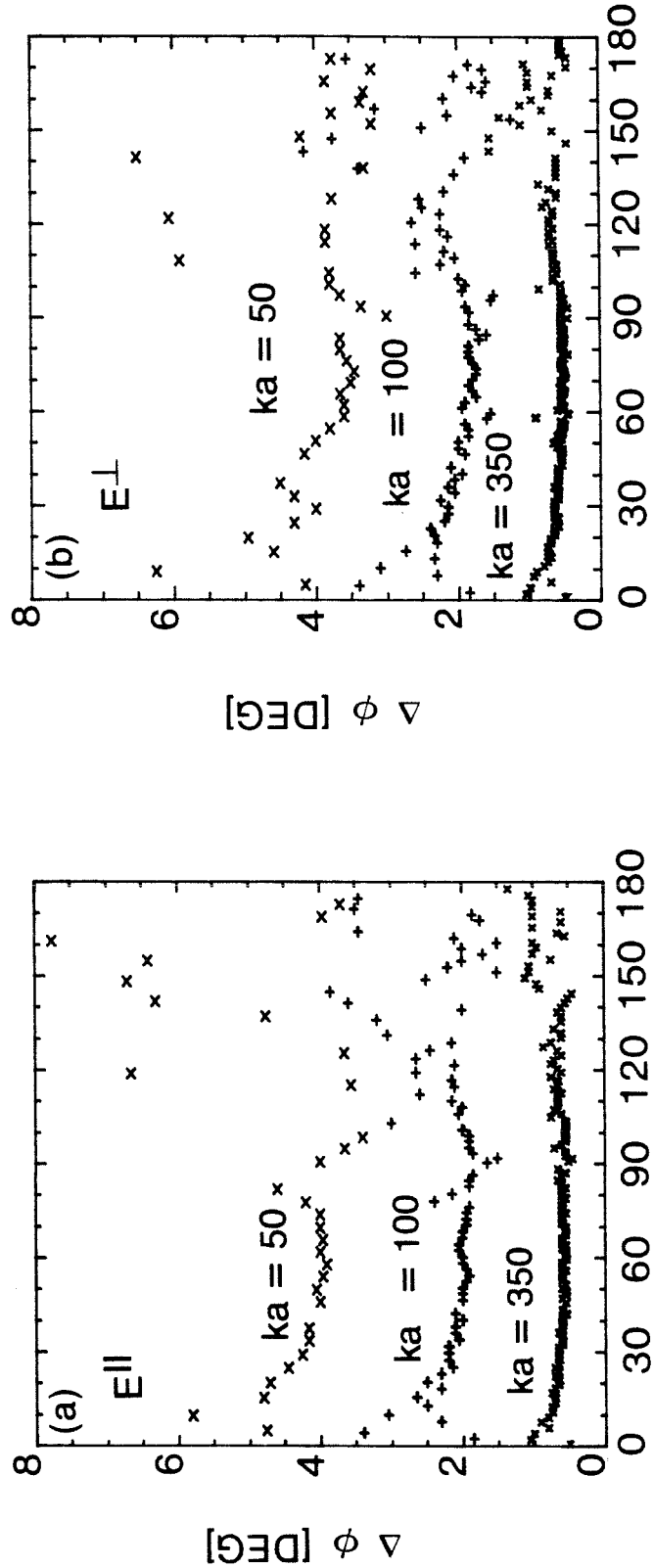

Fig. 3.4 The fringe spacings of the scattered field are plotted for (a) parallel polarization and (b) normal polarization for ka = 50, 100, and 350. Note the spacings decreases by the increase of ka.

reflected, refracted, and diffracted rays. When the rays reflect internally, the more times they reflect before they get transmitted outside the less power they will have, and their contribution to the scattered field will be small. In the range $90° \lesssim \phi \lesssim 150°$ the rays which are transmitted directly through the cylinder will not exist so the field will be produced by the direct reflected rays and the rays which will make multiple reflections inside the cylinder before they emerge outside. That is why the field amplitude and the fringe contrast is generally smaller than those for the previous range of ϕ. In the range $150° \lesssim \phi \leq 180°$ the field is the superposition of the direct reflected rays and the rays get refracted through the cylinder and reflected once by the internal surface, the fields and the fringe contrast are larger in general than those in the previous range of ϕ. The width of this range is mainly controlled by the value of the index of refraction of the cylinder as we will see in the following section.

3.4 The Effect of the Index of Refraction on the Scattered Field

We also study the effect of index of refraction on the scattered field. The index of refraction of the material of the cylinder appears in the coefficient of the series which represents the scattered field as shown in Eqs. (3.11) and (3.22). Since it is present in the numerator and denominator of a_m and P_m in a very similar way, it seems that it has a very small effect on the scattered field. The normalized amplitude of the scattered field is plotted in Figs. 3.5(a)-(d), for ka = 50, and for n = 1.5, 1.457, 1.4 and 1.35, respectively. The patterns of the field look similar in their characteristics especially in the range $0° \leq \phi \leq 90°$. The main differences in this range are in the positions of the side lobes which are not the same for the different refractive-indices. Also if we look at the first side-lobe as we go from n = 1.5 to 1.35 it decreases in its amplitude until it emerges in the main lobe at n = 1.35. Significant changes are seen in the range $90° \leq \phi \leq 180°$ where we can see that the pattern is modulated by a function varying with the index of refraction. In this range the peak of the scattered field moves with the change of the index of refraction, and its position approaches $\phi = 180°$ as n increases. In Fig. 3.6 the portion of the scattered field from $\phi = 90°$ to 180° is plotted for four different values of the index of refraction to demonstrate the movement of the peak of the scattered field with the change of n. It can be seen that the modulation function, which modulates the amplitude of the field, spreads out some of the fringes towards $\phi = 90°$. So the position of this peak is very sensitive to the index of refraction, but is it

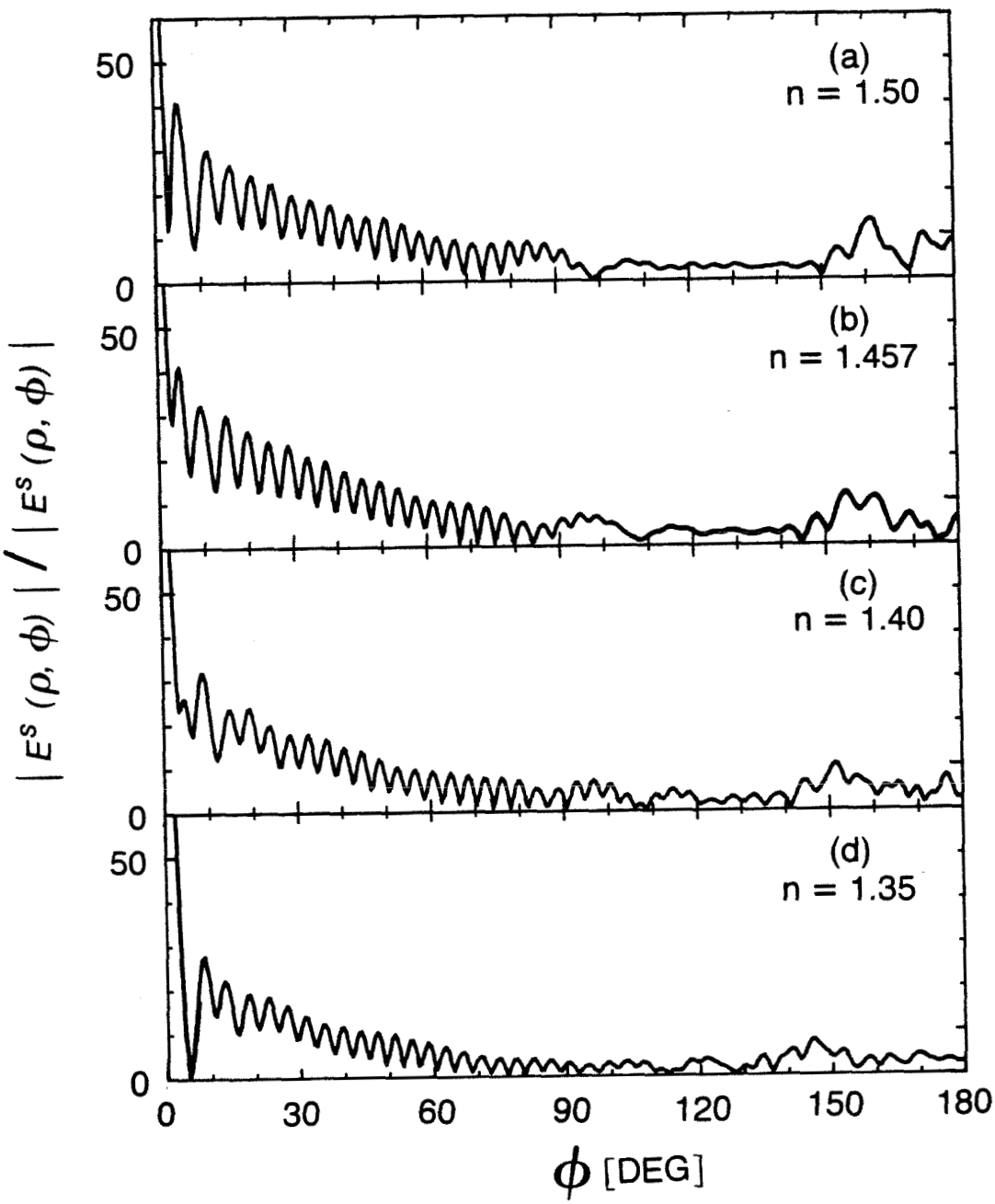

Fig. 3.5 The normalized scattered field $|E^s(\rho,\phi)|/|E^s(\rho,0^\circ)|$ for ka = 50 plotted in, (a) to (d) for n = 1.5, 1.457, 1.4 and 1.35, respectively. Note the similarities of the field pattern in the range $0^\circ \leq \phi \leq 90^\circ$.

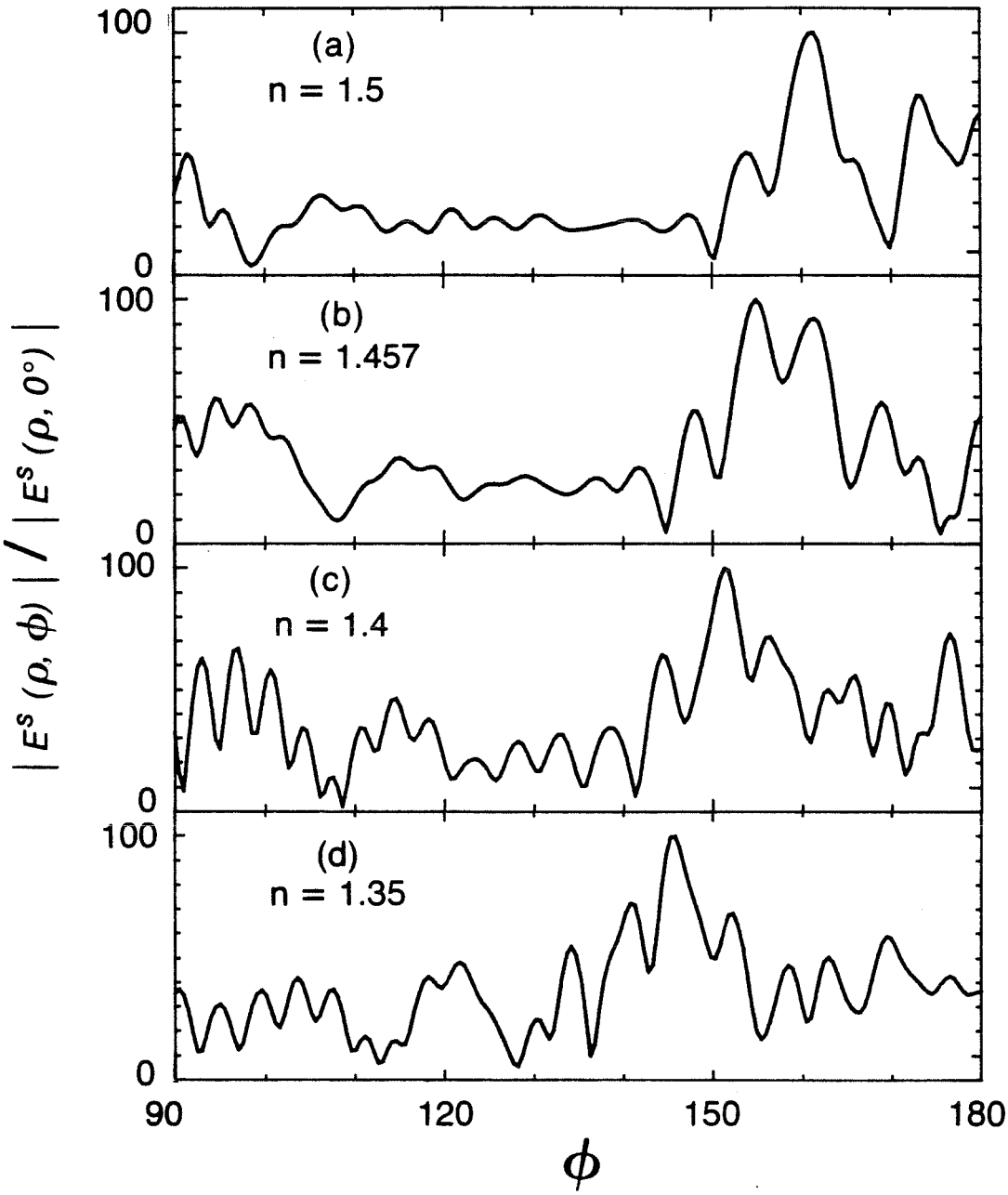

Fig. 3.6 The normalized scattered field plotted for ka = 50 in (a) to (d) for n = 1.5, 1.457, 1.4 and 1.35, respectively. Note the position of the peak as it sweeps towards ϕ = 180° by the increase of n.

sensitive to the index of refraction only? Or is it also sensitive to ka? In Fig. 3.7(a) the position of this peak is plotted as a function of the factor ka for n = 1.45. The position of the peak varies with ka for the values of ka $\leqq$ 100 but after that it varies very little. This leads to the fact that the peak of the back-scattered field is independent of ka for ka very large, but it is very sensitive to the index of refraction. In Fig. 3.7(b) the position of this peak is plotted as a function of the index of refraction from n = 1.3 to 2.0 in 0.025 increments, for ka = 350 and 500. The position of the peak ϕ_{peak} increases with the increase of n in a form very close to a sine function, and also the curves for ka = 350 and ka = 500 coincide with each other having the same values. The position of the peak nears a fixed value at n = 1.85. So the peak position is independent of the radius of the cylinder, and it is very sensitive to the index of refraction, which will make it a good way for measuring the index of refraction for cylinders whose index of refraction is less than the 1.85 limit.

For the normal polarization case, the index of refraction does not vary the peak position as linear as it is in the parallel polarization case. In Fig. 3.8 the peak position is at $\phi \cong 155°$ for n = 1.35, at $\phi = 180°$ for n = 1.4, at $\phi \cong 165°$ for n = 1.457 and at $\phi = 180°$ for n = 1.5. So the peak position is varying with the change of the index of refraction but not in a linear way.

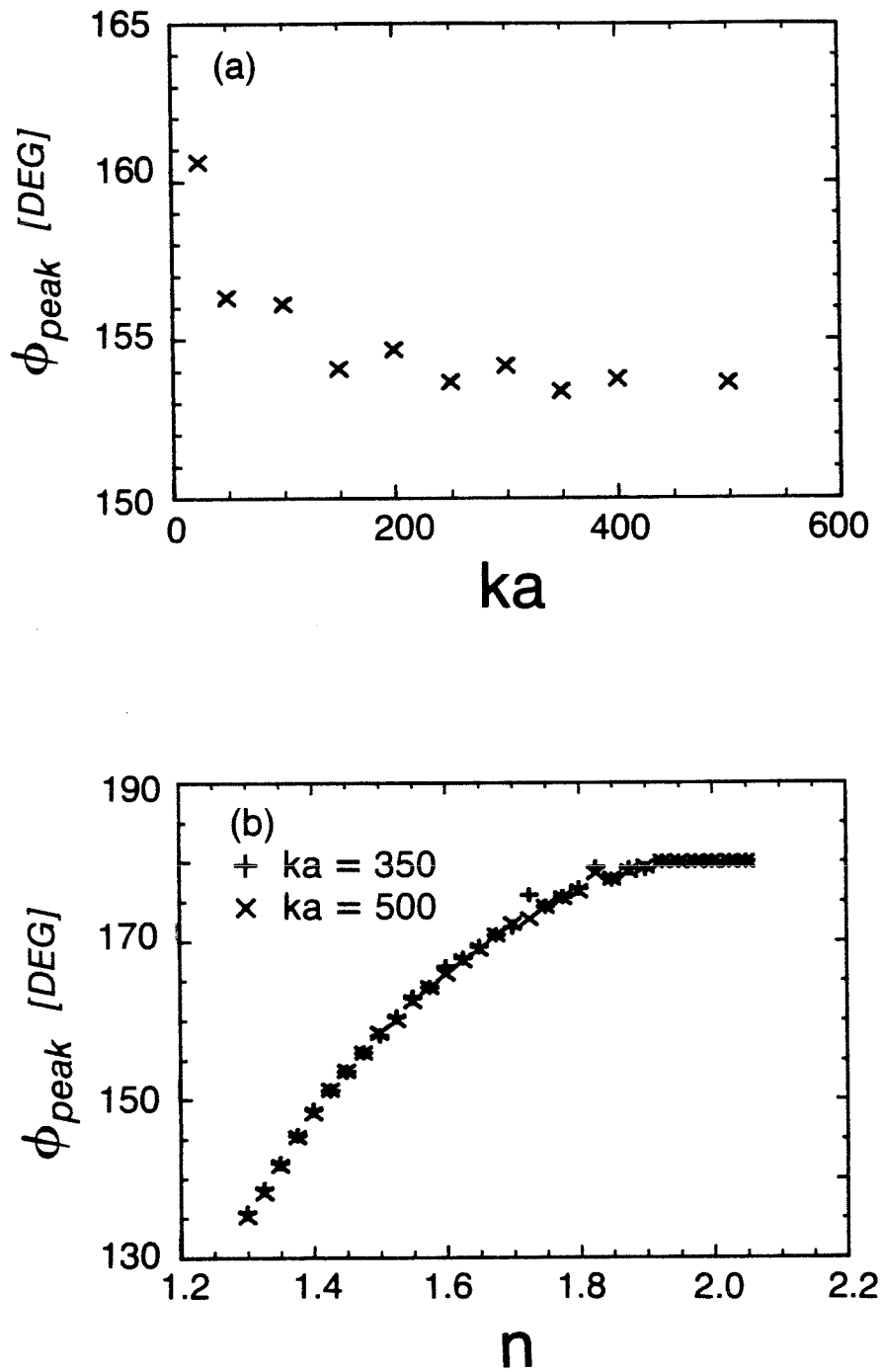

Fig. 3.7 The position of the peak of the back-scattered field is plotted in (a) as a function of ka while n = 1.457 and (b) as a function of n for ka = 350 and ka = 500.

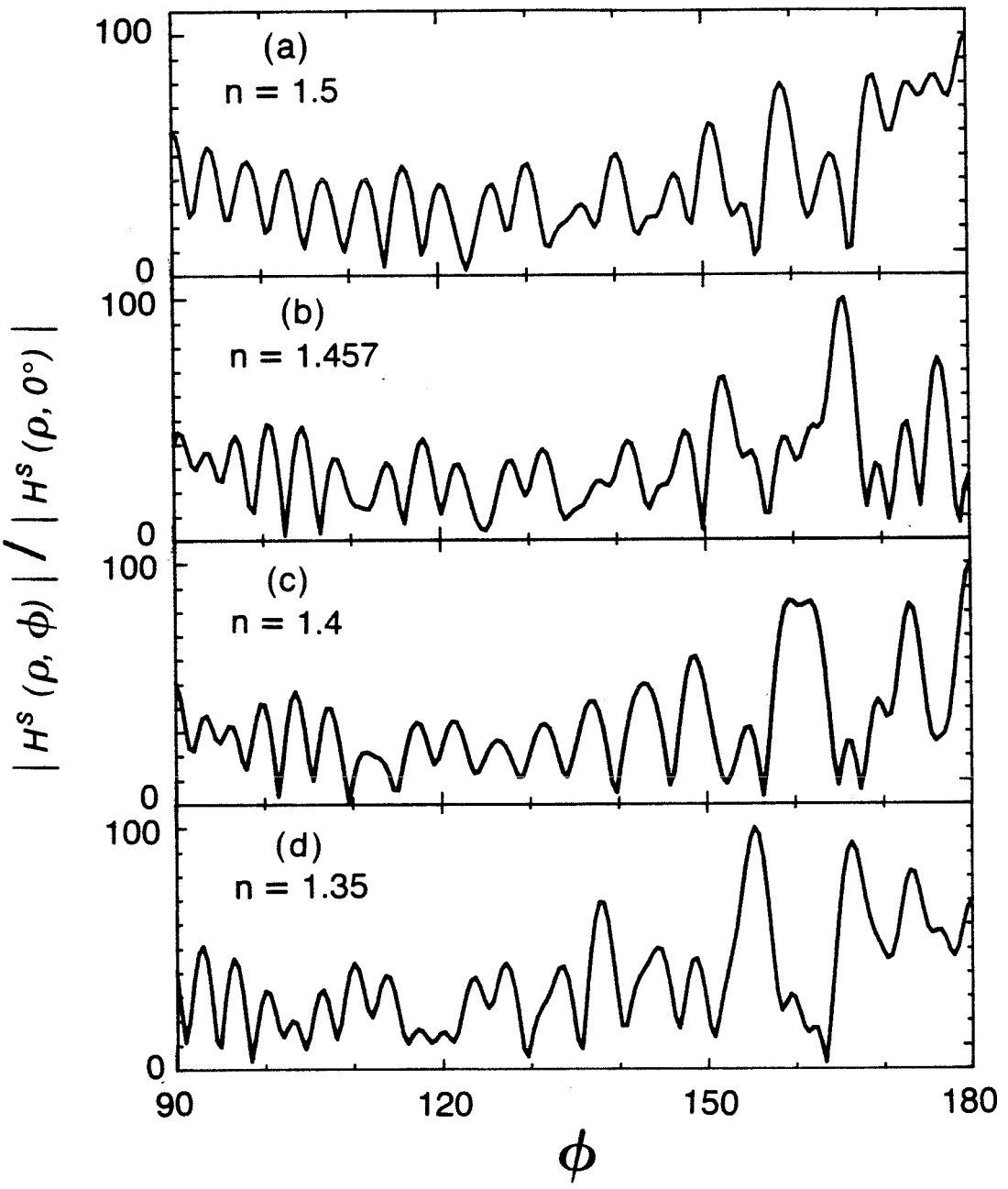

Fig. 3.8 The normalized scattered field for the normal polarization case is plotted in (a) to (d) for n = 1.5, 1.457, 1.4 and 1.35, respectively.

3.5 Comparison between the Scattering from Conducting and Dielectric Cylinders

In the previous sections, and in the previous chapter the scattering field from dielectric and conducting circular cylinders are presented. In this section we make a comparison between the results demonstrated for both kinds of cylinders, and for the two different polarizations of the incident field.

The scattered field from the conducting and the dielectric cylinders represented by infinite series of the same form. The coefficients of the series expressed into two different expressions, the coefficients a_m in Eq. (3.12) and P_m in Eq. (3.23) for the dielectric cylinder will reduce to the coefficients b_m, Eq. (2.33), and d_m, Eq. (2.41), for the conducting cylinder as n the index of refraction tends to infinity. So if the index of refraction of the dielectric cylinder is taken as infinity then its solution for the scattered field outside the cylinder will be the same as that for the conducting cylinder, and the coefficients D_m in Eq. (3.13) and Q_m in Eq. (3.24) for the fields inside the dielectric cylinder will vanish.

The pattern of the scattered field for the two cylinders has a similar form, each has a main lobe that decreases in its width by the increase of ka, and each has a number of side lobes, that increase in number as ka increases. The side lobes of the conducting cylinder scattered field pattern exist in a certain range of the scattering angle and they disappear for the rest of the pattern. This cutoff angle is larger for the normal polarization than that for the paral-

lel polarization case. On the other hand, the side lobes for the dielectric cylinder exist in the full range of the scattered field pattern. The contrast of the fringes of the scattered field as shown in Table 3.1 is much larger in the whole range ϕ for the dielectric cylinder than that of the conducting cylinder, which makes them more visible and detectable especially for $\phi \geq 30°$. Also the contrast of the fringes of the dielectric cylinder is larger for the parallel polarization case than for the normal polarization case. The pattern of the dielectric cylinder has a peak in the backscattered field, its position is moving with the change of the index refraction, but for the conducting cylinder the backscattered field pattern will smoothly increase, reaching a maximum at $\phi = 180°$.

The way the fields are scattered by the two kinds of cylinders is quite different because of the different materials from which the cylinders are made. The conducting cylinder scatters the waves mainly by direct reflection from the surface, by the diffraction from the edges of the cylinder, and by the currents generated on the surface of the cylinder which will generate the fields outside. The scattered field will be the superposition of these different components. The dielectric cylinder scatters the waves by direct reflection from the surface, by diffraction, and by the rays which will refract through it directly or after making one or more internal reflections by the inside surface of the cylinder. The way the fields are generated made all those similarities and differences between the scattered fields from the conducting and the dielectric circular cylinders.

TABLE 3.1

Fringe Contrast for Conducting
and Dielectric Cylinders, ka = 50

Scattering Angle ϕ°	Contrast of the Fringes			
	Conducting		Dielectric	
	$E^{//}$	$E^{\perp}$	$E^{//}$	$E^{\perp}$
5	0.62	0.64	0.42	0.33
30	0.03	0.34	0.34	0.15
60	0.0	0.05	0.61	0.17
90	0.0	0.01	0.19	0.21
120	0.0	0.0006	0.27	0.59
150	0.0	0.0	0.35	0.80

CHAPTER III

REFERENCES

1. I.S. Gradshteyn and I.M. Ryzhik, Tables of Integrals, Series, and Products (Academic Press, New York, 1965).

2. J.A. Stratton, Electromagnetic Theory (McGraw-Hill, New York, 1941).

3. H.C. van de Hulst, Light Scattering by Small Particles (Wiley, New York, 1957).

4. M. Kerker, The Scattering of Light and Other Electromagnetic Radiation (Academic, New York, 1969).

CHAPTER IV

APPROXIMATE SOLUTIONS FOR THE SCATTERING OF LIGHT FROM LARGE CYLINDERS

4.1 Introduction

Approximate solutions for the scattered field from large conducting and dielectric circular cylinders are presented in this chapter. In the previous two chapters we studied rigorous solutions for the scattering of a plane electromagnetic wave by a circular cylinder. The solutions are expressed in terms of an infinite series that converges very slowly. The infinite series solutions are not very practical in plotting the scattered field, especially when the radius of the cylinder is much larger than the wavelength. In this chapter we present approximate solutions using Fourier and geometrical optics approximations. These solutions are simple to calculate, and it is easier to plot the fields from them. The fringe spacings of the scattered field are derived in a closed form. Since the solutions are derived in simple formulas they do not require long computing times as long as those for the rigorous solutions.

In Section 4.2 scattering from a conducting cylinder is considered. The scattered field is represented as the superposition of a diffracted field from a modified strip and a backscattered field which is generated by the surface current density. The scattered

field and fringe spacings are plotted and compared with those introduced in Chapter II.

In Section 4.3 the scattering of light by a dielectric cylinder is presented. The scattered field is derived by geometrical and Fourier optics techniques. A formula is derived for the fringe spacings of the scattered field and this is compared with the rigorous solution. The limit of validity for the fringe spacing formula with the change of ka is tested.

4.2 Scattering from a Conducting Cylinder

In Chapter II we have studied the scattering of a plane electromagnetic wave by a circular conducting cylinder. When the diameter of the cylinder is large compared with the wavelength, we expect that the physical optics solutions for the scattered field will be adequate. In Chapter II we discussed the sources which produced the scattered field, and we found that they are the superposition of the diffracted and the directly reflected fields from the surface. As the radius of the cylinder becomes larger with respect to the wavelength, the diffracted field becomes narrower and more intense[1]. The other fields will be small with respect to it and spread over the whole range of the scattering angle. The diffracted field mainly depends on the size and form of the object rather than its composition or the nature of the surface. So the scattered field in the forward region (near $\phi = 0^{o}$) depends on the diffracted field. And since the diffracted field does not depend on the nature of the surface, the diffracted field of the cylinder will be similar to that of a conducting strip, with a width equal to the diameter of the cylinder.

4.2.1 Diffraction by a Strip

The diffraction by a strip has been studied by many authors.[2] For simplicity we will approach the solution of this problem by means of Fourier optics, which gives a good result for the case we are studying. According to Babinet's principle[3] the intensity distribution possessed by the strip will be equal to that possessed

by a slit because they are complementary screens. So the diffracted field of the slit will have the same amplitude as that for the strip with a phase difference of π.

The diffracted field of a slit can be derived using the Fraunhofer diffraction formula.[4] As shown in Fig. 4.1(a), if we place a slit in the x-z plane then the field at the (u,v) plane will be given by

$$E(u,v) = i \frac{\cos\phi}{\lambda\rho} e^{ik\rho} \int_{-\infty}^{\infty} E_0(y,z)\, e^{-(ik/\rho)(yu+zv)} dydz, \qquad (4.1)$$

where $E_0(y,z)$ is the field distribution at the incident plane. For the case of the slit

$$E_0(y,z) = \text{rect}(y/2a).$$

Since we are interested in the field in the u-v plane and the slit extends infinitely in the z-direction, then Eq. (4.1) will reduce to a one dimensional integral given by

$$E(u) = i \frac{\cos\phi}{\lambda\rho} e^{ik\rho} \int_{-\infty}^{\infty} \text{rect}\left(\frac{y}{2a}\right) e^{-i(k/\rho)yu} dy,$$

and since $u = \rho \sin\phi$ then

$$E(\rho,\phi) = i \frac{\cos\phi}{\lambda\rho} e^{ik\rho} \int_{-a}^{a} e^{-iky\sin\phi} dy. \qquad (4.2)$$

This integral will reduce to

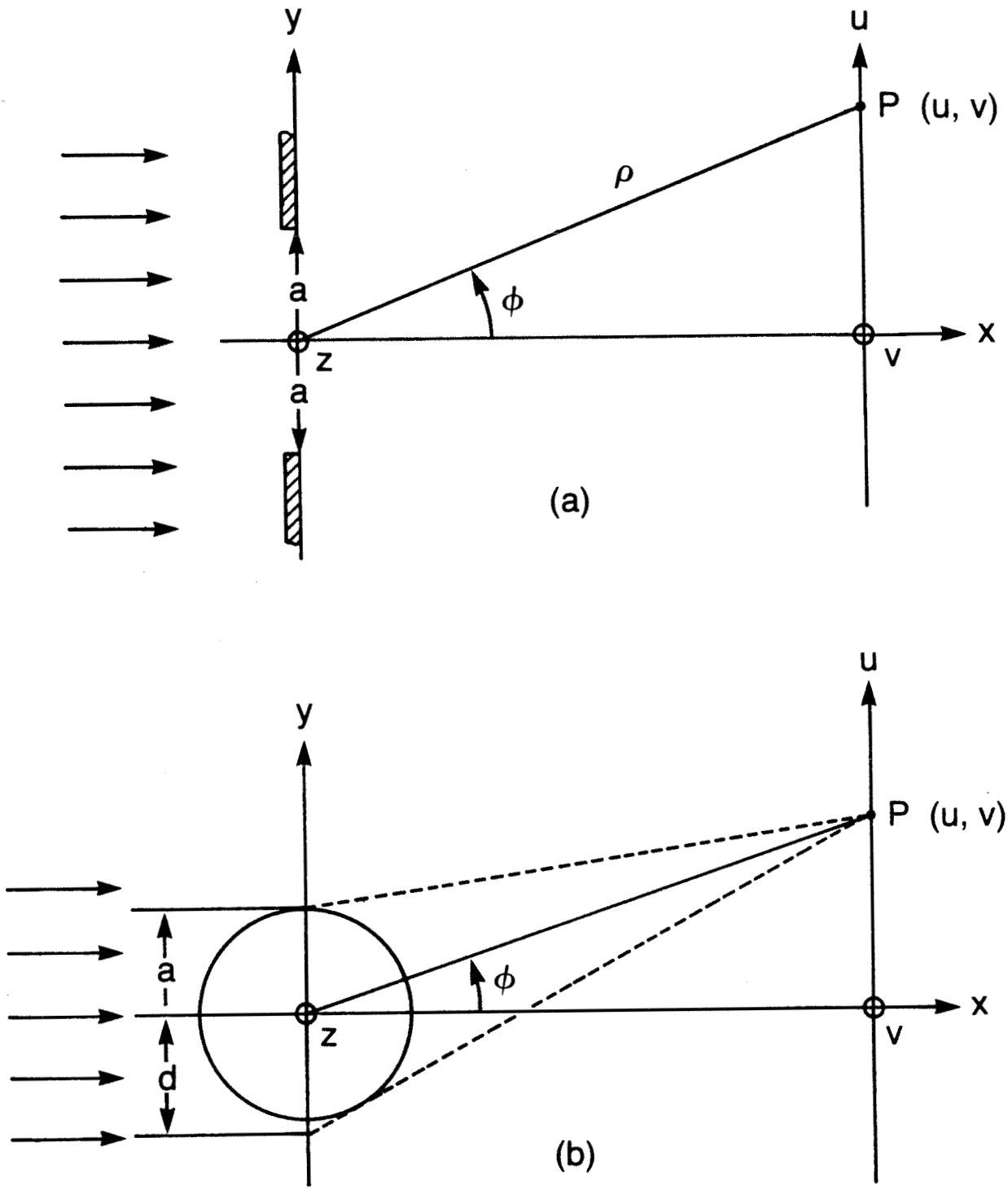

Fig. 4.1 A plane wave illuminates (a) a slit and (b) a conducting cylinder. The diffracted field is observed at point $P(\rho,\phi)$.

$$E(\rho,\phi) = i2 \frac{\cos\phi}{\lambda\rho} e^{ik\rho} \frac{\sin(ka \sin\phi)}{k \sin\phi}.$$

Hence,

$$E(\rho,\phi) = i2 \frac{a \cos\phi}{\lambda\rho} e^{ik\rho} \operatorname{sinc}(\frac{2a}{\lambda} \sin\phi). \tag{4.3}$$

where $\operatorname{sinc}(x) = \sin(\pi x)/\pi x$. According to the Babinet's principle, the field diffracted by the strip will be

$$E_{strip}(\rho,\phi) = -i \frac{ka \cos\phi}{\pi\rho} e^{ik\rho} \operatorname{sinc}(\frac{ka}{\pi} \sin\phi). \tag{4.4}$$

In Fig. 4.2(a) the diffracted field of the strip given by Eq. (4.4) is plotted to be compared with that of the cylinder given by Eq. (2.34) for ka = 50. The diffracted field of the strip has same main lobe width and same amplitude and position of the first three side lobes of the scattered field from the cylinder. For the rest of the pattern the amplitude of the diffracted field decreases with the increase of ϕ, reaching very small values around $\phi \cong 60°$. But the scattered field of the cylinder increases slightly in its amplitude by the increase of ϕ. Also the position of the side lobes of the diffracted field of the strip become further apart with the increase of the angle ϕ, while for the scattered field of the cylinder the position of any two adjacent lobes is almost the same until they terminate at $\phi \cong 30°$ as can be seen in Fig. 4.2(c). The reason for the lobes of the slit pattern to become further apart is that as ϕ increases the width of the strip will become apparently smaller.

So the strip is not a good approximation of the cylinder for scattering angles away from $\phi = 0°$. From Fig. 4.1(b), the width of the wire seems to increase as we increase the angle ϕ. This is because the wire has a depth in the x-axis, so the apparent width will increase. So the cylinder can be modeled as a strip with a varying width. When P is in the far zone, the width of the equivalent strip will be $a+a/\cos\phi$. Therefore, if we rederive the diffracted field for this varying slit, the field will be given by

$$E_{vs}(\rho,\phi) = -i \frac{\cos\phi}{\lambda\rho} e^{ik\rho} \int_{-a/\cos\phi}^{a} e^{-iky \sin\phi} dy.$$

Hence,

$$E_{vs}(\rho,\phi) = - \frac{ka}{2\pi\rho} e^{ik\rho} \{\frac{\cos(ka \tan\phi) - \cos(ka \sin\phi)}{ka \tan\phi}$$

$$+ i[\text{sinc}(\frac{ka}{\pi} \tan\phi) + \cos\phi \text{ sinc}(\frac{ka}{\pi} \sin\phi)]\}. \qquad (4.5)$$

The fields diffracted by the modified strip, given by Eq. (4.5), is plotted in Fig. 4.2(b). In Fig. 4.2(b) we plotted the diffracted field of the modified strip and for the exact solution of the cylinder. The main lobe of the diffracted field has the same width as that for the exact field, and also the amplitude of the first three lobes. The positions of the sidelobes are the same as those for the exact solution till $\phi \cong 30°$, where the exact solution sidelobes terminate. The sidelobes of the diffracted field become closer, and start having small amplitudes for $\phi > 30°$. In Fig. 4.2(c) the fringe spacings of the field amplitude of the strip, the modified

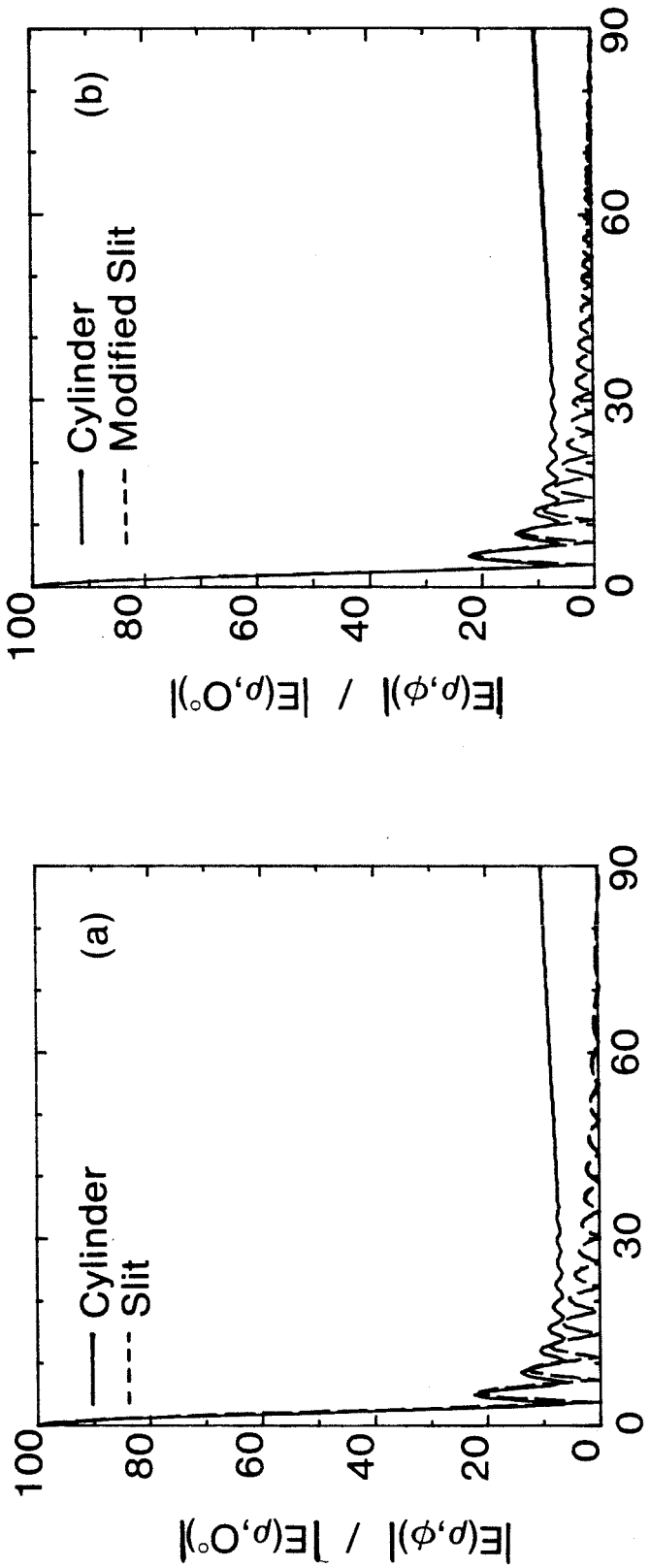

Fig. 4.2 The normalized amplitude of the diffracted field from a slit and a modified slit as given by Eqs. (4.4) and (4.5) are plotted in (a) and (b), respectively. The exact scattered field from a conducting cylinder is plotted for comparison; (continued on next page).

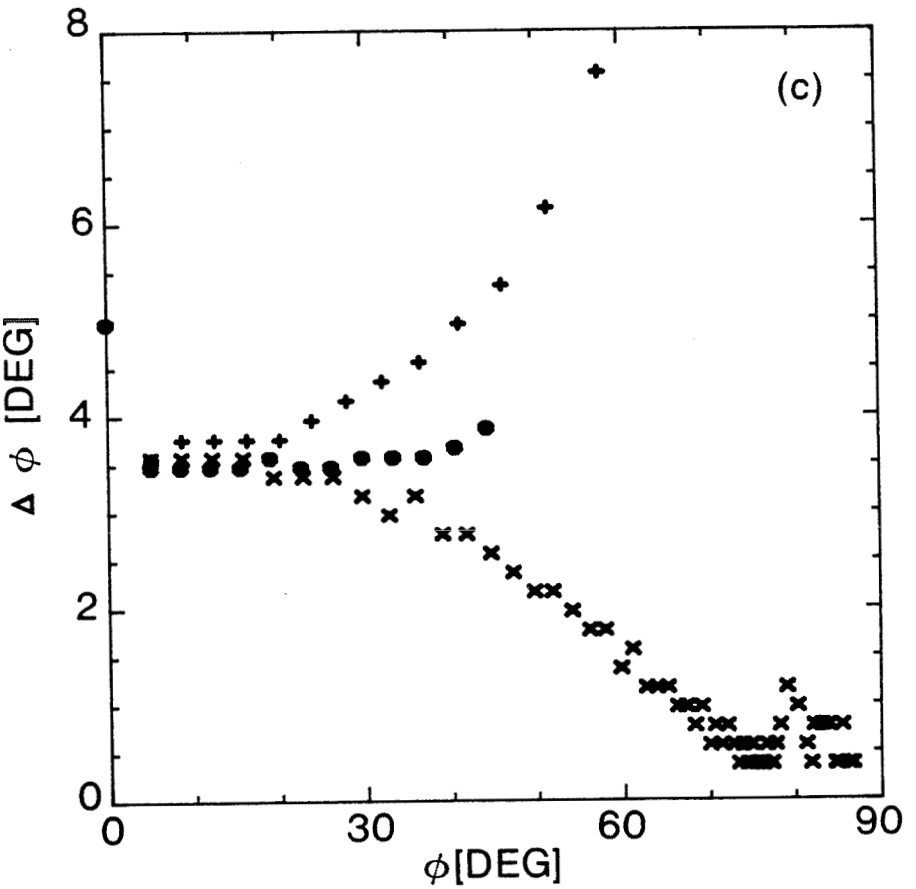

Fig. 4.2 Contined. (c) The fringe spacings of the cylinder (0), the slit (+), and the modified slit (X) are plotted for ka = 50.

strip, and the conducting cylinder (exact solution) are plotted. The fringe spacings of the modified strip have the same value as those for the cylinder but they do not vanish at ϕ_{cut}. The fringes of the strip have comparable values at small angles, and then they depart from the values of the fringes of the cylinder. Thus the modified strip diffracted field is a good approximation for the cylinder in the range of the existence of the fringes. The fields scattered by the cylinder are a superposition of the diffracted fields, reflected fields, and fields generated by the surface current; so we do not expect that the diffracted fields will represent the scattered field of the cylinder in the whole range. In the following subsection the fields generated by the surface current will be derived.

4.2.2 Back-Scattered Field of the Cylinder

The fields generated by the surface current can be derived exactly using Maxwell's equations, and by integrating over the surface of the cylinder. In this section we are interested in an approximate solution for the radiation fields resulting from the scattering of an electromagnetic wave by the surface S of the cylinder, so we will make the usual estimate based on the incident electromagnetic wave.[5] Let the electric field of the incident plane wave be given by

$$\underline{E}^{inc}(\rho,\phi') = E_0 \underline{e}_z e^{ik\rho\cos\phi'}, \tag{4.6}$$

where $\underline{e}_z$ is the z-directed unit vector, and we assumed a unit amplitude. The corresponding magnetic field of the incident plane wave is given by

$$\underline{H}^{inc}(\rho,\phi') = - E_0 \underline{e}_y \sqrt{\frac{\varepsilon}{\mu}}\, e^{ik\rho\, \cos\phi'} . \tag{4.7}$$

Assuming that the cylinder is perfectly conducting, then the surface current density $\underline{K}$ will be given by

$$\underline{K} = 2\, \underline{n}\times\underline{H}^{inc}, \tag{4.8}$$

where $\underline{n}$ is the outward unit normal to the surface. From Eqs. (4.7) and (4.8) we obtain

$$\underline{K} = - \underline{e}_z 2 \sqrt{\frac{\varepsilon}{\mu}}\, e^{ika\, \cos\phi'} \cos\phi', \tag{4.9}$$

and the vector potential produced by $\underline{K}$ is[6]

$$\underline{A}(\rho,\phi) = u \int_S \underline{K}(a,\phi') \frac{e^{ik\rho}}{4\pi\rho}\, ds, \tag{4.10}$$

where the integration is over the illuminated region of the surface of the cylinder, and R is the distance between the observation point (ρ,ϕ) and the integration point (a,ϕ'), as shown in Fig. 4.3. From Eqs. (4.9) and (4.10) we get

$$\underline{A}(\rho,\phi) = -2\sqrt{\mu\varepsilon}\, \underline{e}_z \int_{\pi/2}^{3\pi/2} \cos\phi'\, e^{ika\, \cos\phi'} \frac{e^{ikR}}{4\pi R}\, d\phi'. \tag{4.11}$$

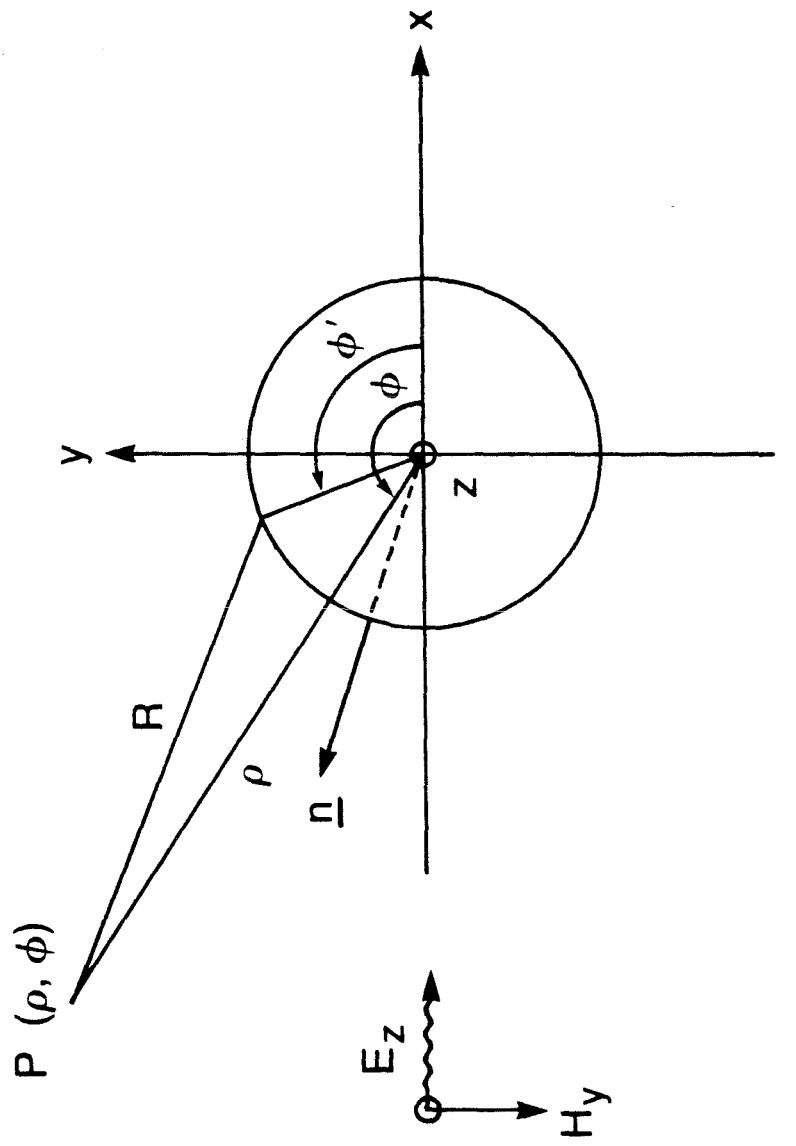

Fig. 4.3 A linearly polarized plane wave illuminates a conducting cylinder of radius a, and the backscattered field is observed at point $P(\rho,\phi)$.

The z-component of the back-scattered electric field is obtained through the relations

$$\underline{B} = \nabla\times\underline{A},\ \nabla\cdot\underline{A} = 0,$$

and

$$\nabla\times\underline{B} = -i\omega\mu\varepsilon\underline{E}.$$

Then,

$$E_z^s(\rho,\phi) = i\omega\underline{e}_z\cdot\underline{A}. \tag{4.12}$$

Therefore

$$E_z^s(\rho,\phi) = -i\,\frac{2k}{4\pi}\int_{\pi/2}^{3\pi/2}\cos\phi'\ e^{ika\cos\phi'}\,\frac{e^{ikR}}{R}\,ds. \tag{4.13}$$

From Fig. 4.3 we get an expression for R at the far zone to be

$$R = \sqrt{\rho^2+a^2-2a\rho\cos(\phi-\phi')} \cong \rho - a\cos(\phi-\phi'). \tag{4.14}$$

If we substitute for R from Eq. (4.14) into the exponential of (4.13) and $R \cong \rho$ in the denominator, we obtain

$$E_z^s(\rho,\phi) = -\frac{ik}{2\pi\rho}\,e^{ik\rho}\int_{\pi/2}^{3\pi k}\cos\phi'\ e^{ika[\cos\phi'-\cos(\phi-\phi')]}d\phi'.$$

Using some trigonometric identities to rewrite the exponent, we get

$$E_z^s(\rho,\phi) = -\frac{i}{\lambda\rho}\,e^{ik\rho}\int_{\pi/2}^{3\pi/2}\cos\phi'\ e^{-i2ka\sin(\phi/2)\sin(\phi'-\phi/2)}d\phi'. \tag{4.15}$$

Using the stationary phase technique to evaluate the integral in Eq. (4.15), since k is very large (for the optical frequencies), then the main contribution of the integral will be from the neighborhood of the stationary points and the end points of the range of integration.[7,8] The stationary points in the range of integration will be at $\phi' = \phi/2 + \pi/2$, so the asymptotic expansion of the scattered field will be given by

$$E_z^s(\rho,\phi) \sim \frac{1}{\lambda\rho} e^{ik\rho} \sqrt{\pi/ka}\ \sqrt{\sin\phi/2}\ e^{-i2ka\ \sin\phi/2 - i\pi/4}. \qquad (4.16)$$

The backscattered field propagates in the positive ρ-direction, i.e. an outgoing wave. The amplitude of the backscattered field, as it is given by Eq. (4.16), will be modulated by the square root of $\sin\phi/2$, reaches a maximum at $\phi = \pi$, and that is the way this field is behaving as we can see it in the rigorous theory plots given in Chapter II. The total scattered field, resulted from the superposition of the diffracted field Eq. (4.5) and the backscattered field Eq. (4.16), is plotted in Fig. 4.4 for ka = 10 and ka = 50. In Fig. 4.4(a) and (b) the curve obtained from the rigorous solution of Eq. (2.34) is plotted to be compared with the approximate scattered field. The approximate scattered field and the exact one both have similar patterns, and the same main lobe width. For ka = 10, the position of the sidelobes are not the same, but the field amplitudes in the range $80° \lesssim \phi \leq 180°$ are very comparable. For ka = 50, the main lobe and first sidelobe have the same width and position, and the position of the sidelobes is also the same till they vanish in

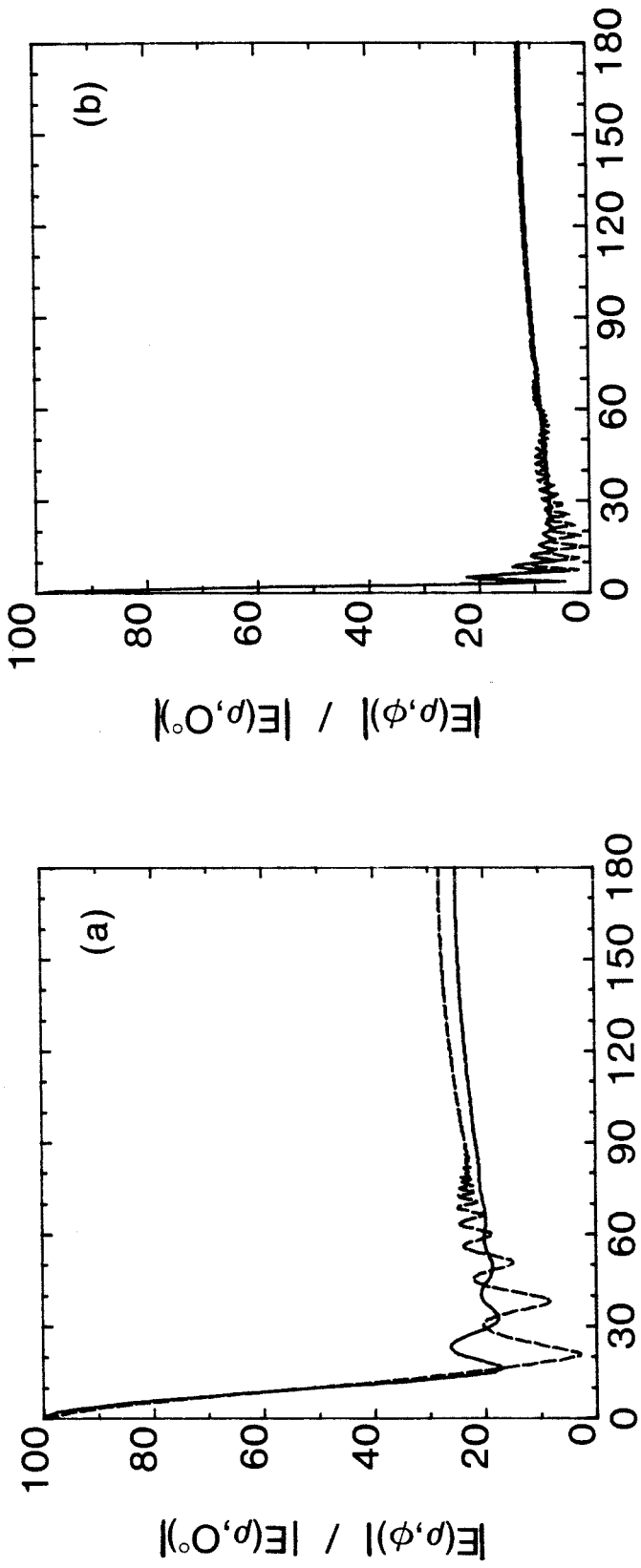

Fig. 4.4 The normalized amplitude of the scattered field from a cylinder plotted from Eqs. (4.5) and (4.16), and the exact solution plotted for comparison in solid line (a) ka = 10, and (b) ka = 50.

the exact scattered field. But the amplitude of the scattered field and the exact one are exactly the same from $\phi \cong 70°$ to 180°. The main difference is that the fringes vanish at a smaller angle for the exact solution but last longer in the approximate solution case. The information carried about the cylinder by the scattered field is contained in the fringe spacings, and this can be detected at small angles where the two fields have the same fringe spacings. The approximate solution has the advantage of being expressed in simple formulas, while the exact theory solution is expressed in an infinite series. The coefficients of the series are functions of the Bessel functions, which are also represented by infinite series. That makes it hard to see directly the effect of the different parameters on the scattered field for the exact theory solution. The exact theory solution takes a lot of computer time to plot it, especially for large ka where the series converges very slowly. But the approximate solution takes very short computing times to plot the scattered field, that makes it more convenient to be used in studying the scattered field even from a very large ka. The advantage of the rigorous solution is that it gives exactly where the fringes terminate.

4.3 Scattering from a Dielectric Cylinder

The rigorous solution for the scattering of a plane electromagnetic wave from a dielectric cylinder was discussed in Chapter III. As has been presented there, the scattered field is the superposition of the diffracted, reflected and refracted fields. The field in the forward region results mainly from the diffraction and refraction of the rays through the cylinder. The refracted and reflected field can be determined by deriving formulas for the phase shift between the observation point and the reference plane. The phase of these two rays and their relative amplitude leads to an expression for the field at the observation point. The superposition of these two fields and the diffracted field gives the total field in the forward scattered pattern. From the phase difference between the refracted and the reflected rays we will derive a formula for the fringe spacings.

4.3.1 The Scattered Field

The scattered field from the dielectric circular cylinder will be considered at the forward zone first. The field in this region results from the interference between the refracting, reflecting and diffracting rays. The way to get a very good approximation of the scattered field is to determine the phase of the refracted and reflected rays at the observation point, $P(\rho,\phi)$, with respect to a plane before the incident wave reaches the cylinder. A cross section of the cylinder is shown in Fig. 4.5. Plane y'-z is the plane of reference for calculating the phase of the fields. Let U and Q be

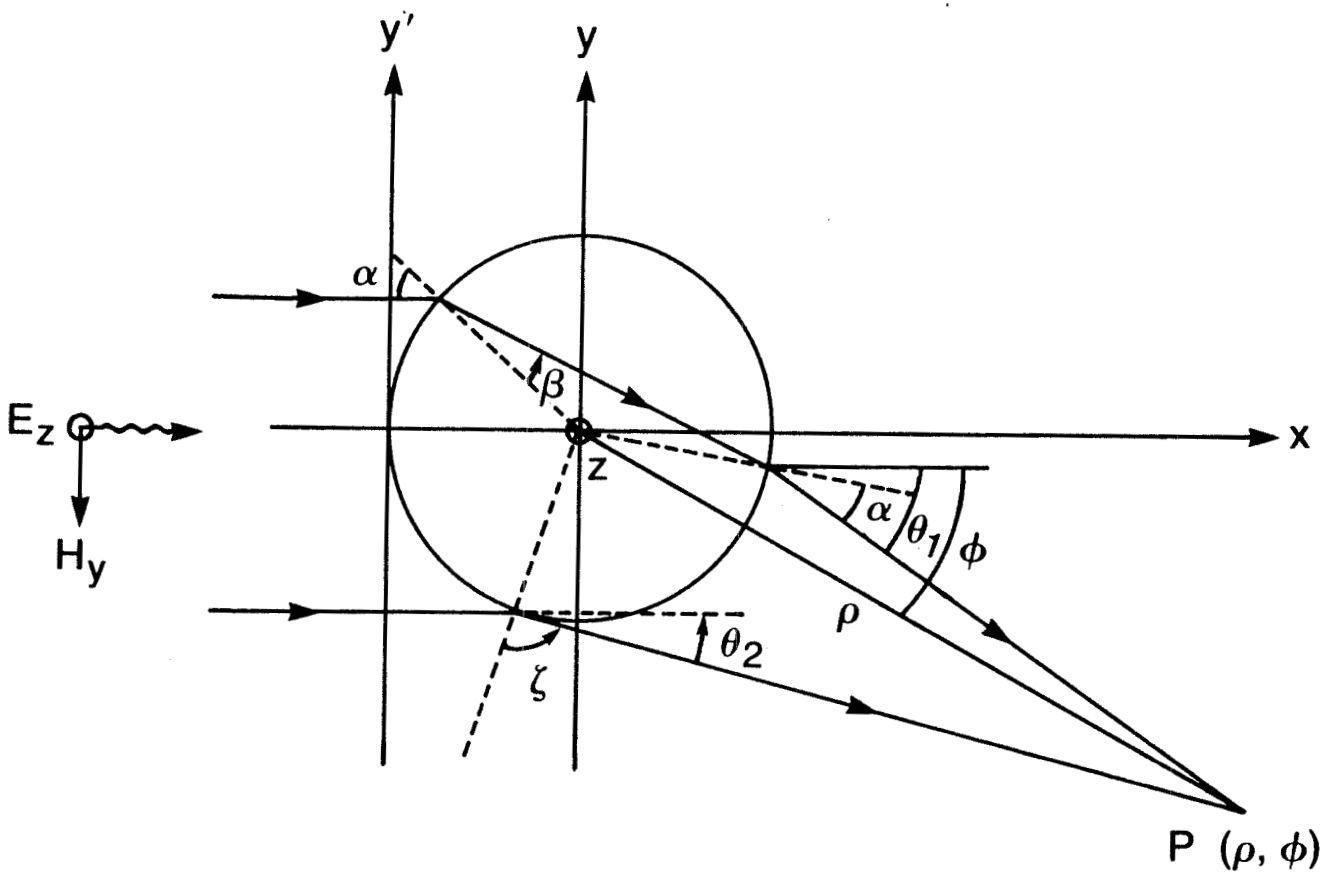

Fig. 4.5 The reflected and refracted rays as they trace through a dielectric cylinder.

the pathlengths of the refracted and reflected waves, respectively, from the plane y'-z to the point $P(\rho,\phi)$. From the geometry of the cylinder, when P is in the far-zone, we obtain $\theta_1 \cong \theta_2 \cong \phi$, and

$$U = AB + BC + CP,$$

$$U \cong a - a\cos\zeta + (\rho - a\cos\alpha);$$

therefore,

$$U = \rho + a - 2a(\cos\alpha - n\cos\beta). \tag{4.17}$$

And similarly

$$Q \cong \rho + a - 2a\sin\phi/2, \tag{4.18}$$

where a is the radius of the cylinder, and n is the index of refraction. The relation between angles α and β are defined by Snell's Law[3]

$$\sin\alpha = n\sin\beta. \tag{4.19}$$

From Fig. 4.6 we can see that

$$\frac{\phi}{2} = \alpha - \beta. \tag{4.20}$$

From Eqs. (4.19) and (4.20) we can derive

$$\cos\alpha = \frac{n\cos\phi/2 - 1}{\sqrt{n^2 - 2n\cos\phi/2 + 1}}, \tag{4.21}$$

and

$$\cos\beta = \frac{n - \cos\phi/2}{\sqrt{n^2-2n\cos\phi/2+1}} \quad . \tag{4.22}$$

From Eqs. (4.17), (4.18), (4.21) and (4.22) we derived formulas for the pathlength and the phase as a function of ρ and ϕ and the parameters of the cylinder. The field scattered by the cylinder due to the reflection and refraction can be given as

$$E(\rho,\phi) = \frac{A_2}{\rho} e^{ik[a+\rho-2a(n-1)(\cos\phi/2-1)]/\Gamma} + \frac{A_1}{\rho} e^{ik(a+\rho-2a\sin\phi/2)}, \tag{4.23}$$

$$\text{where } \Gamma = (n^2-2n\cos\phi/2+1)^{\frac{1}{2}} \tag{4.24}$$

and A_1 and A_2 are the amplitudes of the refracted and reflected waves. The field amplitudes are proportional to the reflection and refraction coefficients, and the reflected ray amplitude will be proportional to the reflection coefficient given by Fresnel formulas.[3] The refracted ray will be transmitted through two boundaries, and its amplitude will be proportional to the product of the refraction coefficients of the two boundaries. Therefore A_1 and A_2 can be represented by

$$A_1 = \frac{E^r}{E^i} = \frac{\sin\phi/2 - \sqrt{n^2-\cos^2\phi/2}}{\sin\phi/2 + \sqrt{n^2-\cos^2\phi/2}}, \tag{4.25}$$

and

$$A_2 = \frac{E^t}{E^i} = \frac{4n\cos\alpha\cos\beta}{(\cos\alpha + \sqrt{n^2-1+\cos^2\alpha})(n\cos\beta+\sqrt{1-n^2+n^2\cos^2\beta})}, \qquad (4.26)$$

where E^i, E^r and E^t are the amplitudes of the incident, the reflected and the refracted fields, respectively. The scattered field in the forward region ($0 < \phi < 90°$) is obtained by adding the diffracted field to the reflected and the refracted fields. The diffracted field from the cylinder will be the same as that for the conducting cylinder, taking into account the phase of the incident field from the y'-z plane to the y-z plane. From Eq. (4.4) we can rewrite the diffracted field as

$$E^d(\rho,\phi) = -i\frac{ka}{\pi\rho}\cos\phi\, e^{ik(\rho+a)}\,\mathrm{sinc}\left(\frac{ka}{\pi}\sin\phi\right). \qquad (4.27)$$

From Eqs. (4.25) to (4.27) we can write the scattered field from the dielectric cylinder in the following form

$$E^s(\rho,\phi) = \frac{e^{ik(\rho+a)}}{\rho}\left\{\frac{\sin\phi/2 - (n^2-\cos^2\phi/2)^{\frac{1}{2}}}{\sin\phi/2 + (n^2-\cos^2\phi/2)^{\frac{1}{2}}}\, e^{-i2ka\sin\phi/2}\right.$$

$$+ \frac{4n\cos\alpha\cos\beta}{[\cos\alpha+(n^2-1+\cos^2\alpha)^{\frac{1}{2}}][n\cos\beta+(1-n^2+n^2\cos^2\beta)^{\frac{1}{2}}]}\, e^{-i\,(2ka/\Gamma)(n-1)(\cos\phi/2-1)}$$

$$\left. -i\frac{ka}{\pi}\cos\phi\,\mathrm{sinc}\left(\frac{ka}{\pi}\sin\phi\right)\right\}, \qquad (4.28)$$

The scattered field depends on the factor ka, the index of refraction, and the scattering angle. The diffracted field, which appears as a sinc function in Eq. (4.28) is the dominating term in the forward region especially for small range of the scattering angle, and

this range gets smaller with the increase of ka. The approximate scattered field given by the first two terms of Eq. (4.28) is plotted in Figs. 4.6(a) and (b), and may be compared with the diffracted field alone. The diffracted field has larger components in the range $0° \leq \phi \lesssim 30°$, for ka = 10, with respect to that of the reflected and refracted fields, which contribute more in the rest of the range. For ka = 50, the diffracted field components dominate in a much narrower range of ϕ than in the previous case. From the study of these curves we conclude that the diffracted field mainly contributes to a narrow range of ϕ for large values of ka, the refracted and reflected fields contribute over the whole range of the scattering angle. The scattered field given by Eq. (4.28), and the field given by the rigorous solution in Eq. (3.14), are plotted in Figs. 4.7(a) and (b), for ka = 10 and 50. For ka = 10 the pattern of the approximate and the exact scattered fields are mainly the same. Both have the same number of sidelobes, but their positions are not exactly the same. For ka = 50, the two curves, the approximate and the exact, have very similar patterns, widths of the main lobe, number of sidelobes, and position of the sidelobes. There are small differences between the amplitudes of the sidelobes because the amplitudes of the approximate fields are not calculated very accurately to simplify the approximate solution. So the approximate solution of the scattered field from a dielectric cylinder derived in this section has the same structure and features of that given by the rigorous solution. It has very similar features to it, and so it is a good approximate solution for large ka. Meanwhile, the approximate

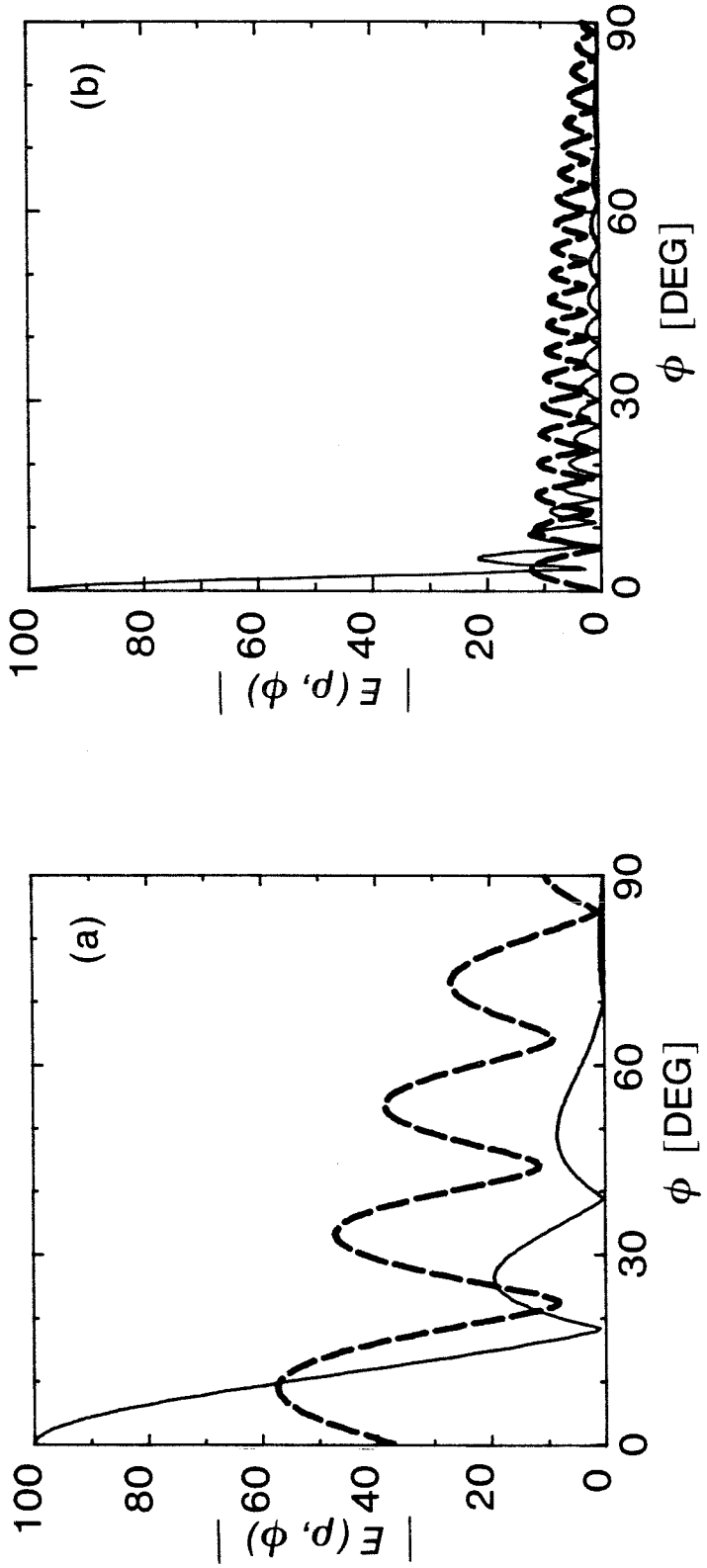

Fig. 4.6 The solid line is the diffracted field amplitude from a strip, and the dashed line is the reflected and refracted resultant field amplitude plotted for: (a) ka = 10, (b) ka = 50.

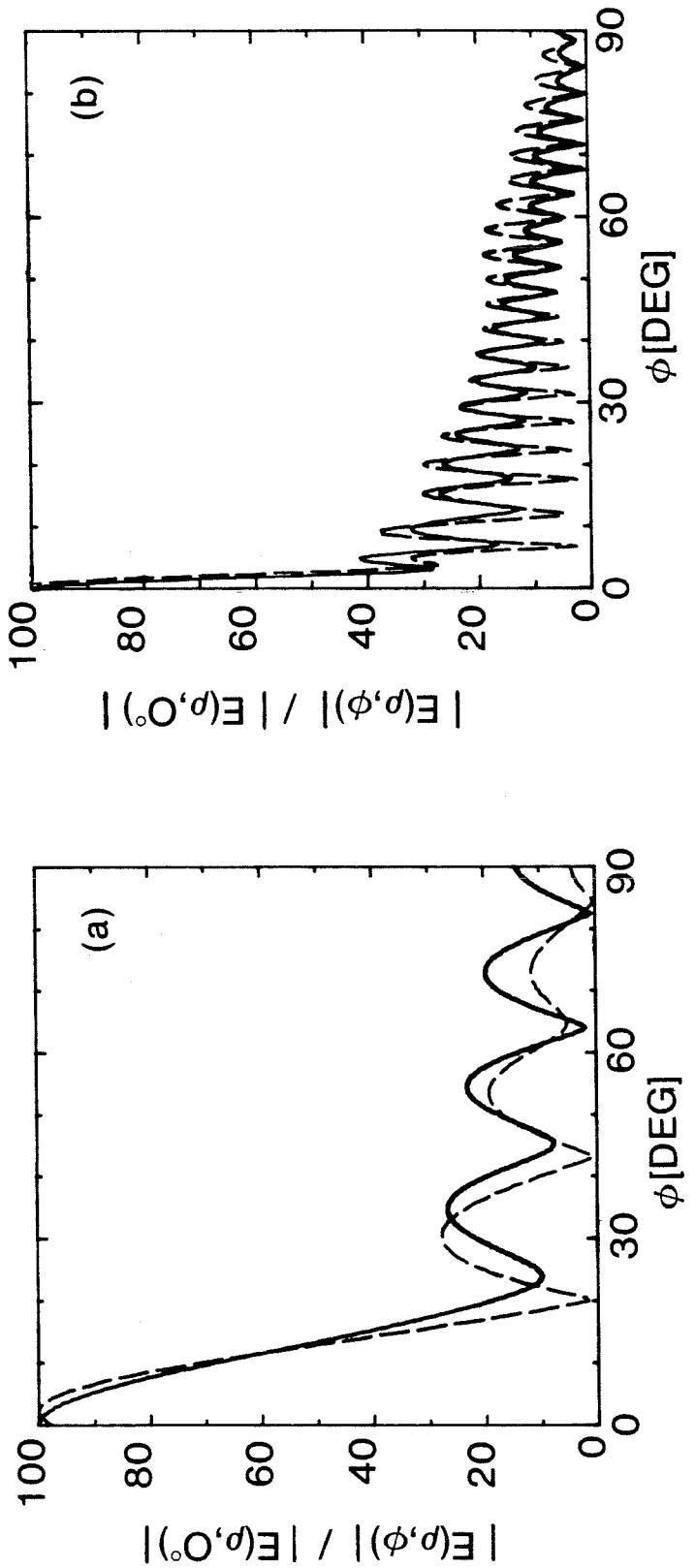

Fig. 4.7 The approximate field amplitude scattered by a dielectric cylinder as given by Eq. (4.28) plotted in the dashed line, and the exact field amplitude plotted in the solid line for (a) ka = 10, and (b) ka = 50.

solution of Eq. (4.28) is expressed in a simple form, from which we can see the effect of the different parameters on the scattered field pattern. Also it does not take as long computing times as that needed by the exact solution which is expressed in an infinite series with coefficients containing Bessel functions. So the approximate solution has the advantage of being expressed in a simple closed form, while it does give a comparable scattering pattern to that of the rigorous solution.

The backscattered field in the range of $150° \lesssim \phi \leq 180°$ is studied by several authors.[9,10] The scattered field in this region results from the interference of the reflected rays and those which make one internal reflection inside the cylinder. It has been reported that this range is governed by the index of reduction of the cylinder.

The scattered field in the range of $90° \lesssim \phi \lesssim 150°$ is a result of the interference between the reflected rays and the refracted rays which make multiple reflections inside the cylinder; and since the field in this range will have very small amplitudes and does not carry any more information about the cylinder, it has not been reported here.

4.3.2 The Fringe Spacings of the Scattered Field

The fringe spacings of the scattered field pattern are studied for the dielectric cylinder in chapter III from the rigorous solutions of the scattered field. There we have not been able to deduce a closed form solution for the fringe spacings. We have seen in the

previous subsection that the field pattern is a result of the interference between the reflected and refracted waves in most of the forward scattered region. So we will derive a formula for the fringe spacings in this subsection.

Let the phase of the refracted ray be P_t, and the phase of the reflected ray be P_r as it propagates from the reference plane y'-z to point $P(\rho,\phi)$. Then from Eqs. (4-17) and (4.18) we obtain

$$P_r = k(\rho+a-2a\ \sin\phi/2) + \pi,$$

and

$$P_t = k(\rho+a-2a\ \cos\alpha+2an\ \cos\beta) - \pi/2,$$

where the π phase in P_r is the phase added when the field is reflected, and $\pi/2$ is the phase subtracted when the ray goes through a focus inside the cylinder.[11] The phase difference between the two rays is

$$P_d = P_t - P_r = 2ka(n\ \cos\beta-\cos\alpha+\sin\phi/2) - \frac{3\pi}{2}, \tag{4.29}$$

where $\cos\alpha$ and $\cos\beta$ are given by Eqs. (4.21) and (4.22). Therefore

$$P_d(\phi) = 2ka(\Gamma+\sin\phi/2) - \frac{3\pi}{2}. \tag{4.30}$$

The spacing between any two adjacent fringes is the change $\Delta\phi$ in the scattering angle, which will change the phase difference $P_d(\phi)$ by 2π. Let ϕ and ϕ_1 be the positions of two adjacent fringes. Then

$$2\pi = P_d(\phi_1) - P_d(\phi) = 2ka(\Gamma_1+\sin\phi_1/2) - 2ka(\Gamma+\sin\phi_1/2), \tag{4.31}$$

where Γ is given by Eq. (4.24), and Γ_1 can be deduced from Eq. (4.24) by changing ϕ to ϕ_1. $\Delta\phi/2$ is a small quantity for the values of $ka \geqq 10$, that allows us to make the following approximations

$$\sin \frac{\Delta\phi}{2} \cong \frac{\Delta\phi}{2}, \text{ and } \cos \frac{\Delta\phi}{2} \cong 1.0 \ . \tag{4.32}$$

From Eqs. (4.31) and (4.32) we derive the following expression

$$\frac{\pi}{ka} = (n^2+1-2n\ \cos\phi/2+n\Delta\phi\ \sin\phi/2)^{\frac{1}{2}}$$

$$- (n^2+1-2n\ \cos\phi_1)^{\frac{1}{2}} + \frac{\Delta\phi}{2}\ \cos\phi/2. \quad (4.33) \ . \tag{4.33}$$

Now we can express the first term in the right hand side of Eq. (4.33) as the following

$$(n^2+1-2n\ \cos\phi/2-n\Delta\phi\ \sin\phi/2)^{\frac{1}{2}} = (n^2+1-2n\ \cos\phi/2)^{\frac{1}{2}}$$

$$\times \left(1 + \frac{n\Delta\phi\ \sin\phi/2}{n^2+1-2n\ \cos\phi/2}\right)^{\frac{1}{2}} \ . \tag{4.34}$$

Using the binomial expansion[12] for the quantity

$$\left(1 + \frac{n\Delta\phi\ \sin\phi/2}{n^2+1-2n\ \cos\phi/2^{\frac{1}{2}}}\right)^{\frac{1}{2}}$$

since $(n\Delta\phi\ \sin\phi/2)/(n^2+1-2n\ \cos\phi) < 1$, then Eq. (4.34) will reduce to

$$(n^2+1-2n\ \cos\phi/2+n\Delta\phi\ \sin\phi/2)^{\frac{1}{2}} = (n^2+1-2n\ \cos\phi/2)^{\frac{1}{2}}$$

$$\times \left[1 + \frac{n\Delta\phi\ \sin\phi/2}{2(n^2+1-2n\ \cos\phi/2)} - \frac{(n\Delta\phi\ \sin\ \phi/2)^2}{8(n^2+1-2n\ \cos\phi/2)^2} + \cdot\ \cdot\ \cdot\right]. \tag{4.35}$$

From Eqs. (4.33) and (4.34) we obtain

$$\frac{\pi}{ka} = \frac{\Delta\phi}{2} \cos \phi/2 + \frac{n\Delta\phi \sin\phi/2}{2\Gamma} - \frac{n^2 \sin^2\phi/2(\Delta\phi)^2}{8\Gamma^3} + \cdots \tag{4.36}$$

From Eq. (4.36) we derive a set of approximate values for the fringe spacings $\Delta\phi$ as

I. Zero Order Approximation

$$(\Delta\phi)_0 = \frac{2\pi}{ka \cos\phi/2}. \tag{4.37}$$

II. First Order Approximation

$$(\Delta\phi)_1 = \frac{2\pi}{ka} \frac{\Gamma}{\Gamma \cos\phi/2 + n \sin\phi/2}, \tag{4.38}$$

which is similar to the expression derived in Appendix B.

III. Second Order Approximation

$$\begin{aligned}(\Delta\phi)_2 = [&2n\Gamma^2 \sin\phi/2 + 2\Gamma^3 \cos\phi/2 - 2\Gamma(n^2 \sin^2\phi/2 \\ &+ \Gamma^4 \cos^2 \phi/2 + 2n\Gamma^3 \sin\phi/2 \cos \phi/2 \\ &- \frac{2n^2\Gamma\pi}{ka} \sin^2\phi/2)^{\frac{1}{2}}]/n^2 \sin^2\phi/2.\end{aligned} \tag{4.39}$$

The fringe spacings $(\Delta\phi)_0$, $(\Delta\phi)_1$, and $(\Delta\phi)_2$ are plotted in Fig. 4.8(a) and (b) for ka = 10 and 50. The zero order fringe spacings continuously increase by the increase of ϕ, and it have a reasonable

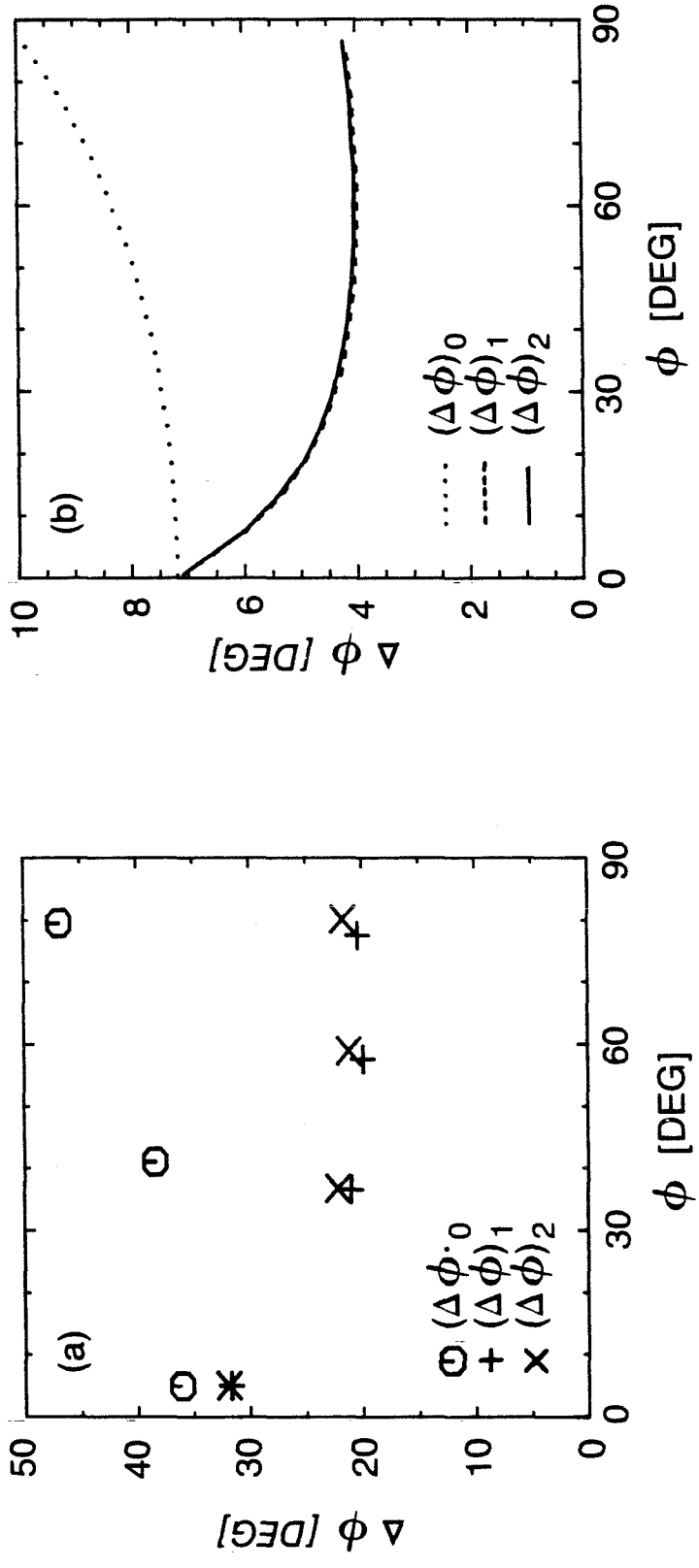

Fig. 4.8 The fringe spacings $(\Delta\phi)_0$, $(\Delta\phi)_1$, and $(\Delta\phi)_2$ as given by Eqs. (4.37) to (4.39) are plotted for (a) ka = 10 and (b) ka = 50.

value only at $\phi \cong 0$. The first and the second order approximations $(\Delta\phi)_1$ and $(\Delta\phi)_2$ have very similar values, especially for ka = 50, and they have a minimum value around $\phi = 60°$. In Fig. 4.9 the first and second order fringe spacings and the fringe spacings of the exact field are plotted for the range $5 \leq ka \leq 500$ for $\phi \cong 60°$. The first and second order fringe spacings have the same values as that of the exact field for ka = 50 or larger. So the fringe spacings derived using ray theory are very accurate for the values of $ka \geq 50$ which will give us the limit of the validity of this solution. This is what we expected from the beginning, because the ray theory is good for large values of ka, i.e., for the high frequency. So the approximate solutions derived using the ray theory for the scattered field and fringe spacings are a very good approximation for $ka \geq 50$, and they have the advantage over the exact solutions because of their simplicity.

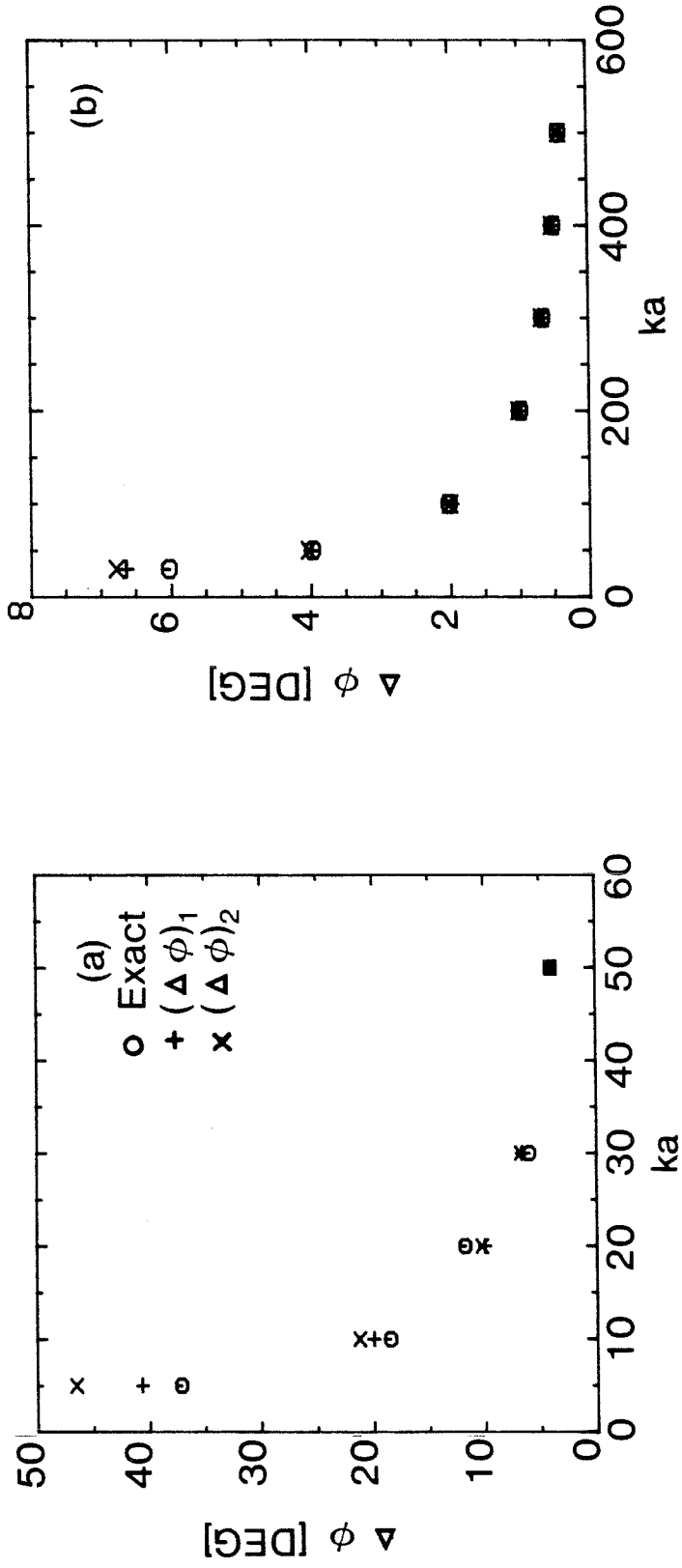

Fig. 4.9 The fringe spacings, exact, $(\Delta\phi)_1$, and $(\Delta\phi)_2$, are plotted vs. ka. Note that all of them have equal values for ka $\geq$ 50.

CHAPTER IV

REFERENCES

1. H.C. Van de Hulst, Light Scattering by Small Particles (Wiley, New York, 1957), Chapt. 15.

2. J.J. Bowman, T.B.A. Senior, and P.L.E. Uslenghi, Electromagnetic and Acoustic Scattering by Simple Shapes (North Holland, Amsterdam, 1969).

3. M. Born, and E. Wolf, Principles of Optics (Pergamon Press, Oxford, 1975).

4. J.W. Goodman, Introduction to Fourier Optics (McGraw-Hill, New York, 1968).

5. N. George, A.C. Livanos, J.A. Roth, and C.H. Papas, "Remote Sensing of Large Roughened Spheres", Optica Acta 23, pp. 367-387 (1976).

6. C.H. Papas, Theory of Electromagnetic Wave Propagation (McGraw-Hill, New York).

7. E.T. Copson, Asymptotic Expansions (Cambridge University Press, Cambridge U.K., 1965).

8. A. Erdélyi, Asymptotic Expansions (New York, Dover Publications, 1956).

9. D. Marcuse, "Light Scattering from Unclad Fibers: Ray Theory", App. Opt. 14, p. 1528 (1975).

10. John W. Lit, "Radius of Uncladded Optical Fiber from Back-Scattered Radiation Pattern", J. Opt. Soc. Am. 65, p. 1311 (1975).

11. L.S. Watkins, "Scattering from Side-Illuminated Clad Glass Fibers for Determination of Fiber Parameters", J. Opt. Soc. Am. 64, p. 767 (1974).

12. M. Abramowitz, and I.A. Stegun, Handbook of Mathematical Functions (National Bureau of Standards, 1964).

CHAPTER V

FINE STRUCTURE OF THE SCATTERING FROM DIELECTRIC CYLINDERS

5.1 Introduction

If a linearly polarized plane electromagnetic wave illuminates a dielectric cylinder, the fields will be scattered all around the cylinder. The fields scattered by a dielectric cylinder are functions of the wavelength (λ) of the illuminating wave. This dependence on the wavelength appears in the formulas derived in Chapter III, implicitly in the factor ka, where $k = 2\pi/\lambda$. Considering the case where the fields reflect internally between the surfaces of the cylinder, when the distance between the two surfaces becomes a multiple of $\lambda/2$ a resonance of the field will occur, and this frequency is called the resonant frequency. The spacings between these resonant frequencies are mainly controlled by the diameter and index of refraction of the cylinder. The study of the resonances of dielectric cylinder is an outgrowth of the study of the resonances of dielectric spheres. The resonant frequencies of the scattering from dielectric spheres are observed by changing the wavelength of the illuminating wave,[1-4] and it was shown that the resonances occur by waves reflecting internally in the sphere and also by surface waves[5]. The resonances of the dielectric cylinders were studied in the microwave region, because of the interest in high-Q microwave

resonators[6,7]. Van Bladel studied the effect of the dielectric constant on the resonances of the scattering cross-section[8]. Some of the studies reported were concerned on using the resonant frequencies to determine the diameter of dielectric cylinders[9,10]. Owen et al. reported a study of the internal field at resonant frequencies[11].

In this chapter we study the resonances of dielectric cylinders and their effects on the scattered field. In Section 5.2 a study of the field at $\phi = 0°$ as a function of the variation of the wavelength is reported to show the resonances of the scattered field. In Section 5.3 the scattered field around the cylinder at-resonance and off-resonance is shown to study the effects of resonances on the scattered field pattern. The incident field polarization considered here is the case when the incident field is polarized parallel to the axis of the cylinder.

5.2 The Resonances of a Dielectric Cylinder

If a linearly polarized plane electromagnetic wave is propagating along the x-axis normal to the axis of symmetry of a dielectric cylinder, then the fields will be scattered all around the cylinder. If we use a cylindrical coordinate system, where the cylinder is lined up such that its axis is parallel to the z-axis, and ρ being the distance away from the center of the cylinder and ϕ being the angle from the x-axis, then the field scattered by the cylinder, as has been derived in Chapter III, is given by

$$E^s(\rho,\phi) = \sum_{m=-\infty}^{\infty} a_m H_m^{(1)}(k\rho)e^{im\phi}, \tag{5.1}$$

where

$$a_m = -(i)^m \frac{nJ_m(ka)J'_m(nka) - J'_m(ka)J_m(nka)}{nJ'_m(nka)H_m^{(1)}(ka) - J_m(nka)H'^{(1)}_m(ka)}, \tag{5.2}$$

and where J_m and $H^{(1)}$ are the Bessel function and Hankel function of the first kind, respectively.

From Eq. (5.1) the scattered intensity is given by

$$I(\rho,\phi) = E^s(\rho,\phi)E^{s*}(\rho,\phi)$$

$$= \sum_{m=-\infty}^{\infty} \sum_{r=-\infty}^{\infty} a_m a_r^* H_m^{(1)}(k\rho)H_r^{(2)}(k\rho)e^{i(m-r)\phi} \tag{5.3}$$

To get the intensity in the far-zone we substitute in Eq. (5.3) the asymptotic expansions for the Hankel functions for large $k\rho$. The asymptotic expansions of the Hankel functions are given by[12]

$$H_m^{(1)}(k\rho) \sim \sqrt{2/\pi k\rho}\; e^{i(k\rho - m\pi/2 - \pi/4)} \tag{5.4}$$

and

$$H_r^{(2)}(k\rho) \sim \sqrt{2/\pi k\rho}\; e^{-i(k\rho - r\pi/2 - \pi/4)} \tag{5.5}$$

From Eqs. (5.3) to (5.5) we obtain the following expression for the intensity at the far-zone:

$$\begin{aligned} I(\rho,\phi) \sim \frac{2}{\pi k\rho} \Big[|a_0|^2 &+ 2 \sum_{r=1}^{\infty} (i)^r a_0 a_r^* \cos r\phi \\ &+ 2 \sum_{m=1}^{\infty} (-i)^m a_0^* a_m \cos m\phi \\ &+ 4 \sum_{m\neq r=1}^{\infty} (i)^{r-m} a_m a_r^* \cos m\phi \cos r\phi \\ &+ 4 \sum_{m=1}^{\infty} |a_m|^2 \cos^2 m\phi . \end{aligned} \tag{5.6}$$

The coefficients a_m are functions of ka, i.e., they are functions of the wavelength, λ, where $k = 2\pi/\lambda$. When the denominator of the coefficient of the series a_m gets to a minimum the field will be at a resonance[10]. Inside the cylinder the fields bounce back and forth between the internal surfaces of the cylinder. When the diameter of the cylinder becomes an integer multiple of halfwavelengths, the field transmission becomes a maximum and there will be a resonance, and the frequency is a resonant frequency[13,14]. If the field at $\phi = 0°$ is plotted from equation (5.6) as a function of the wavelength,

λ, the scattered field will have maxima at the resonant frequencies. In Fig. 5.1 the scattered intensity from a cylinder with a diameter = 66 μm and refractive-index n = 1.45, is plotted for 6327 $\mathring{A} \leq \lambda \leq$ 6552$\mathring{A}$. The scattered intensity has a series of maxima and minima. The maxima occur at the resonant frequencies of the cylinder. The spacings between the resonant frequencies are $\Delta\lambda \cong 13.75\ \mathring{A}$, and depend on the diameter of the cylinder and its refractive-index. The other thing which can be seen in the pattern of the scattered intensity is that it is modulated with a low frequency function which has a period of about 137 $\mathring{A}$. This function also depends on the parameters of the cylinder in its period, and its period decreases with an increase in the diameter of the cylinder.

In the following section the effect of these resonances on the scattered intensity pattern is shown.

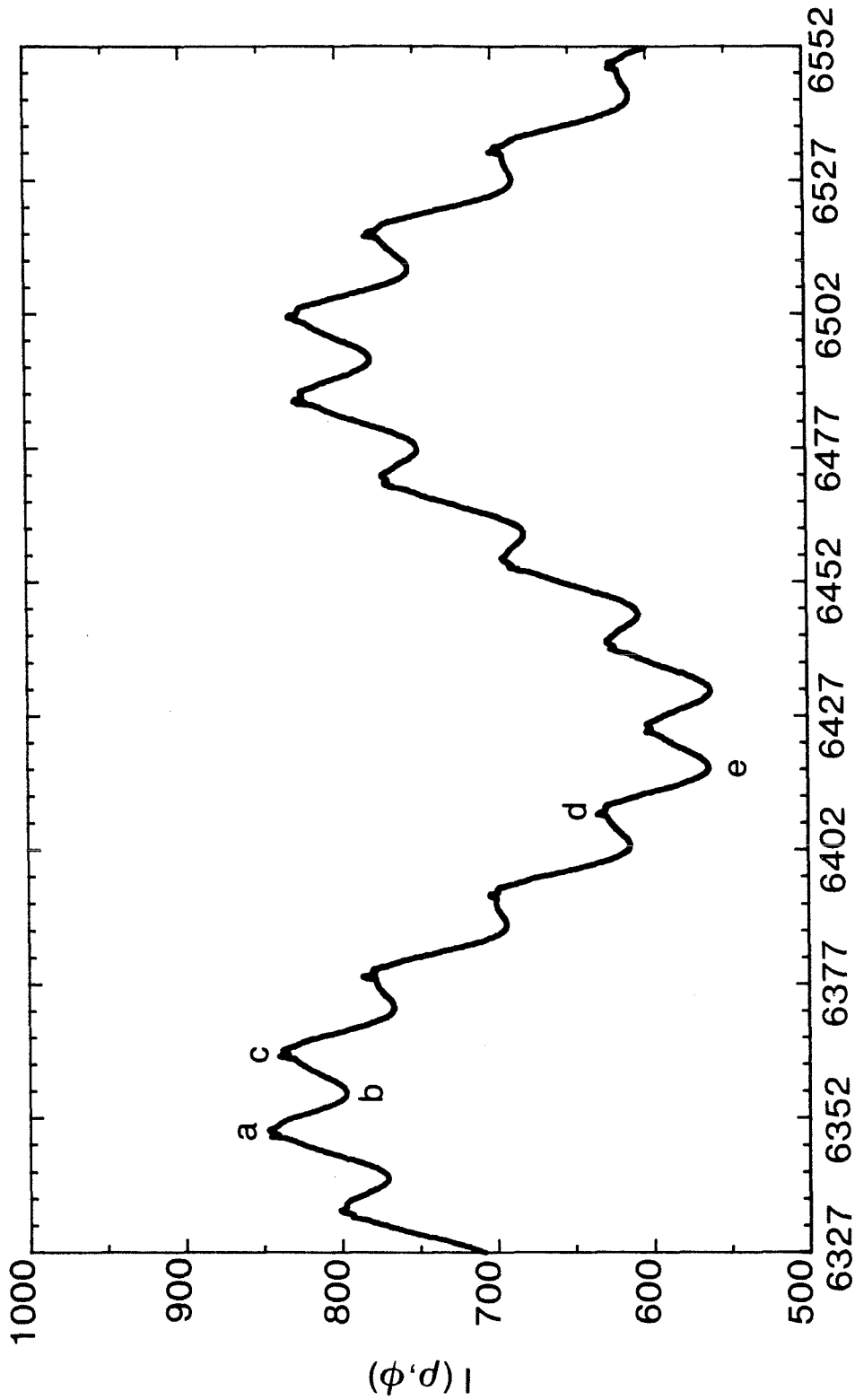

Fig. 5.1 The scattered intensity at $\phi = 0°$ from a dielectric cylinder with $a = 33$ μm and $n = 1.45$, plotted as a function of the wavelength.

5.3 The Effect of the Resonancies on the Scattered Intensity Pattern

In Chapter III we studied the scattered field pattern as a function of the angle ϕ for a different set of diameters and refractive-indices. In the previous section, we found that the fields will have resonances at certain wavelengths, so it is quite important to know what will happen to the pattern of the scattered field as it goes from a resonance to an off-resonance frequency. In Figs. 5.2 to 5.5 the scattered intensity plotted as a function of the angle ϕ at the points a, b, c, d, and e is shown in Fig. 5.1. The points a and c are at-resonance at the peak and d is at-resonance at the trough of the resonance curve, while the point b is at off-resonance at the peak and point e is at off-resonance at the trough of the resonance curve. In Fig. 5.2 the scattered intensity is plotted for $0° \leq \phi \leq 45°$, and the curves (a), (b), (c), (d) and (e) refer to the intensity at wavelengths a, b, c, d and e shown in Fig. 5.1 The patterns at the peak look similar to each other while at-resonance or off-resonance, and the patterns at the trough are also similar. The fields at-resonance have larger amplitude for the main lobe than those off-resonance as shown in Fig. 5.1. The first side lobe located at $\phi \cong 0.8°$ is larger for the fields at-resonance than that off-resonance, e.g., it has the value of 14.68 at a, 11.25 at b and 15.65 at c. The first side-lobe is larger at the trough than that at the peak, it has the value of 14.68 at a, and 59.26 at d. The second side-lobe has also a larger amplitude at-resonance than at off-resonance, and it is very small at the trough while it is very large at the peak. So the main-lobe and the second side-lobe

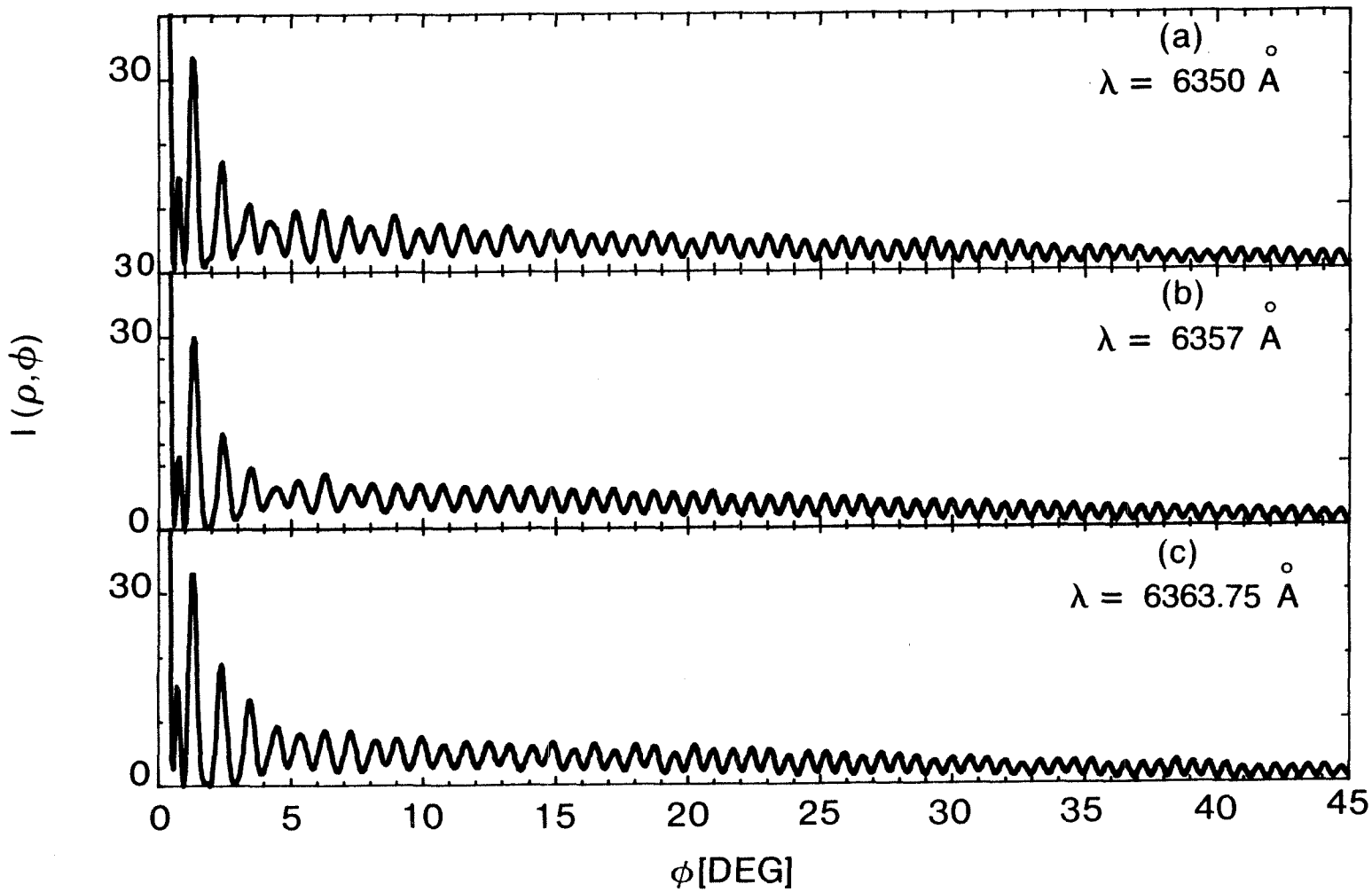

Fig. 5.2 The scattered intensity pattern from a dielectric cylinder plotted for different wavelengths at the peak of the resonance curve; (continued on next page).

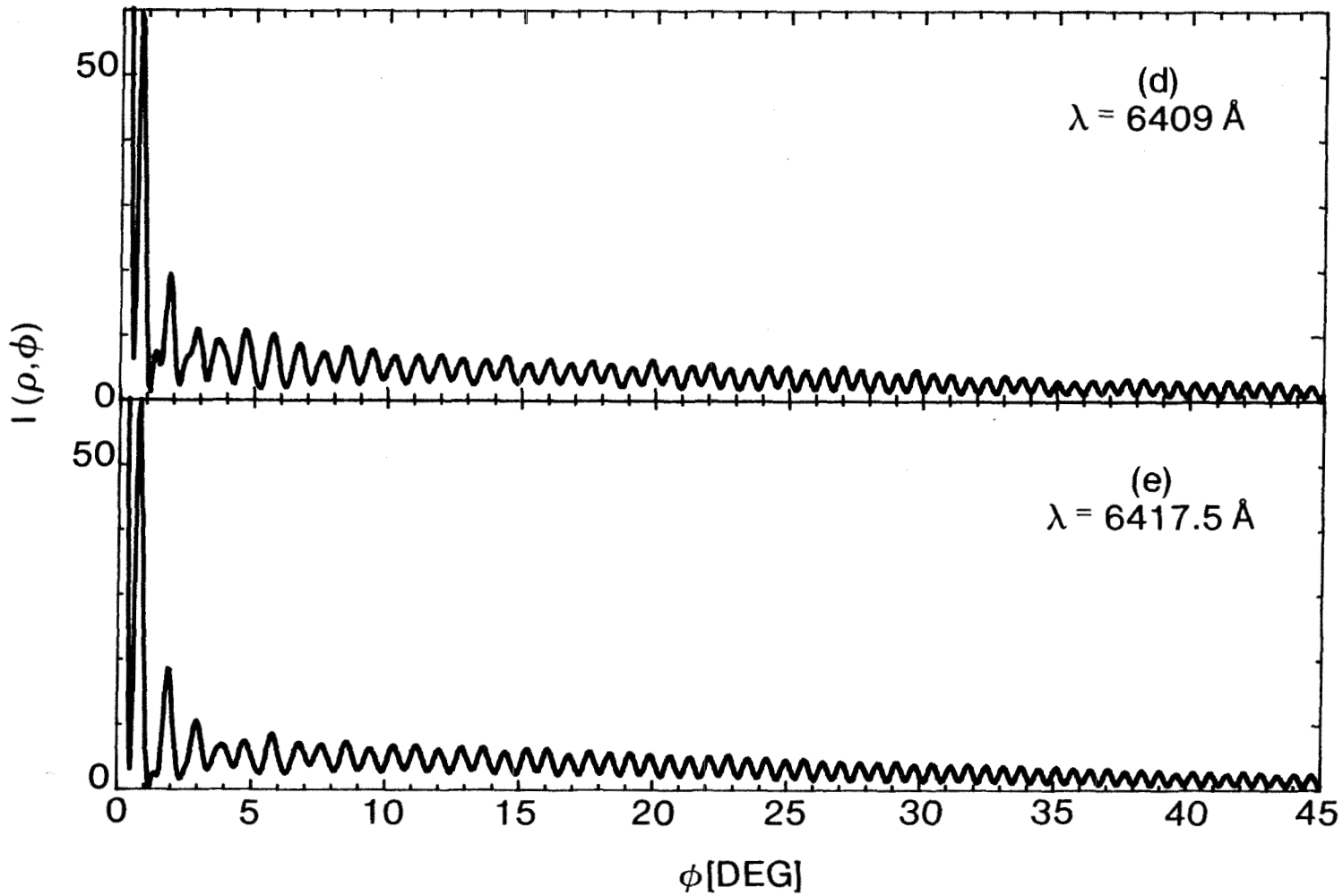

Fig. 5.2 Continued. (d) and (e) the scattered intensity pattern plotted for two different wavelenghts at the trough of the resonance curve.

are large at the peak and they decrease as we go towards the trough, while on the contrary the first side-lobe is small at the peak and very large at the trough. The main lobe and the first and second-side lobes decrease in amplitude as we go from at-resonance to off-resonance at the peak. Also the position of these side-lobes does change as we change the wavelength. The rest of this range $2° \leq \phi \leq 45°$ is about the same in all five curves. Also in the range $0° \leq \phi \leq 45°$ the number of fringes is the same (60 fringes) at all the wavelengths considered. In Fig. 5.3 shows the scattered intensity plotted in the range $45° \leq \phi \leq 90°$, at the five different wavelengths shown in Fig. 5.1. The main difference noticed between the five intensity patterns is in the envelope modulating the patterns. At-resonance the envelope has larger variations in its amplitude than that for the case off-resonance, and it has that behavior at the peak as well as at the trough. The number of fringes in this range are found to be larger for the at-resonance case (72 fringes) than at the off-resonance case (71 fringes). In Fig. 5.4 the scattered intensity patterns are plotted at the five wavelengths considered in Fig. 5.1 in the range $90° \leq \phi \leq 135°$. This region can be divided into two portions: $90° \lesssim \phi \lesssim 110°$ and $110° \lesssim \phi \lesssim 135°$, in the second portion there is a very distinguished difference between the cases at-resonance and off-resonance, in the patterns at-resonance the intensity has a large variation in its amplitude, while at off-resonance the intensity varies very little around its average. The average of the intensity at-resonance and off-resonance is quite the same in this range. In the region $90° \lesssim \phi \lesssim 110°$ the main difference noticed

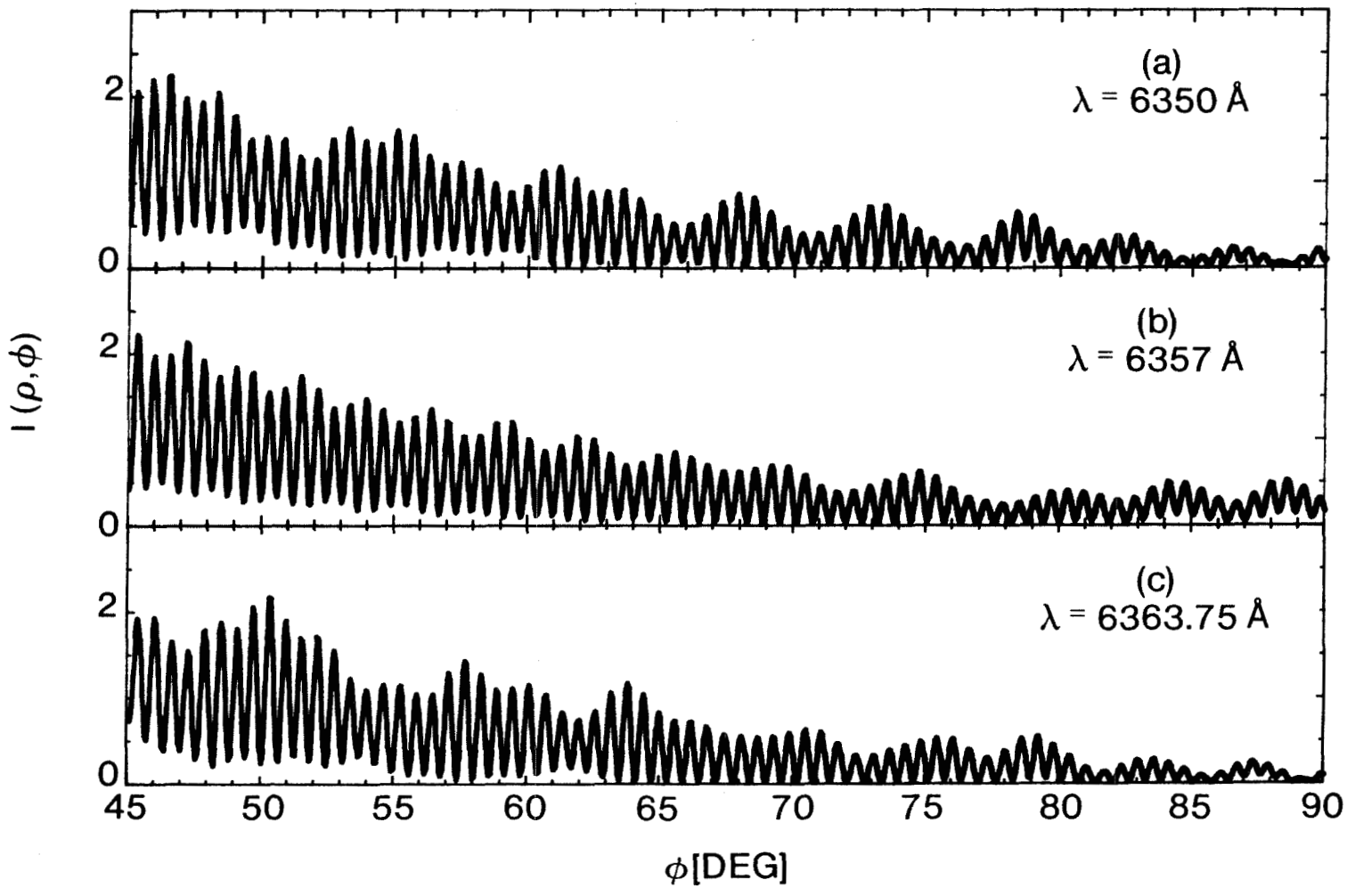

Fig. 5.3 The scattered intensity pattern from a dielectric cylinder plotted for different wavelengths at the peak of the resonance curve; (continued on next page).

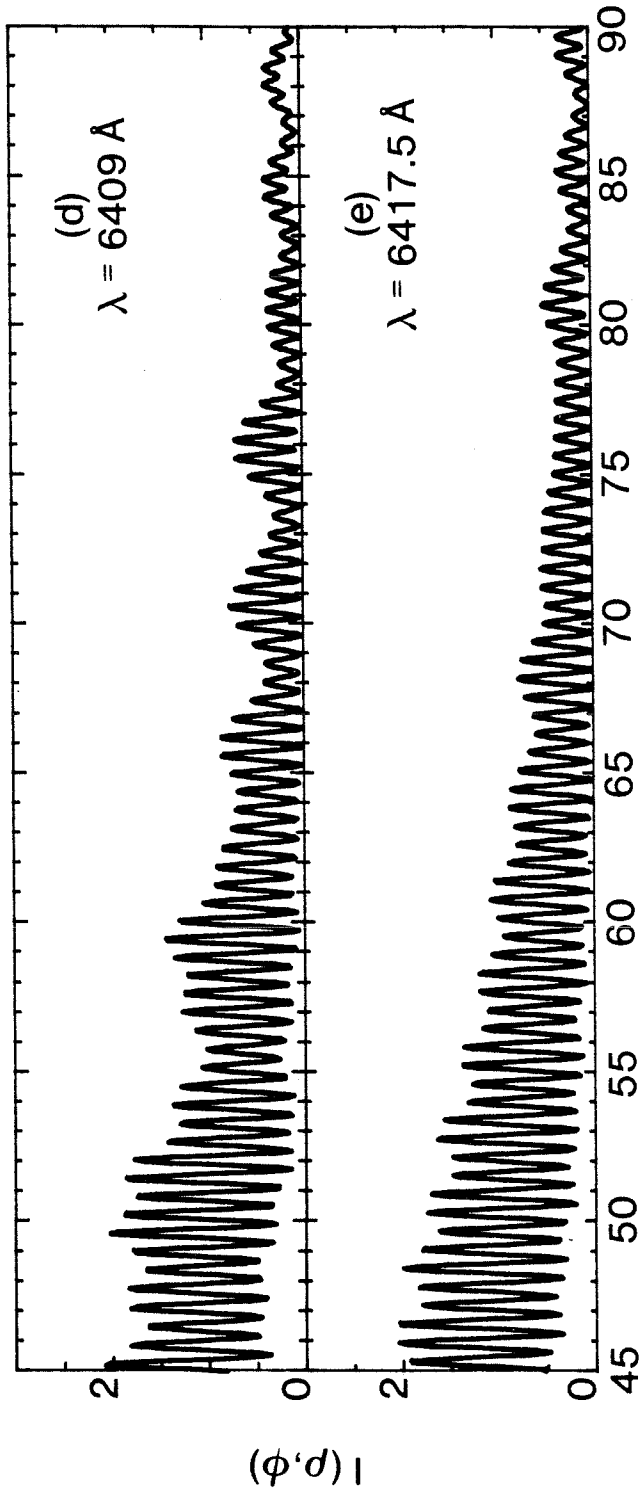

Fig. 5.3 Continued. (d) and (e) the scattered intensity pattern plotted for two different wavelengths at the trough of the resonance curve.

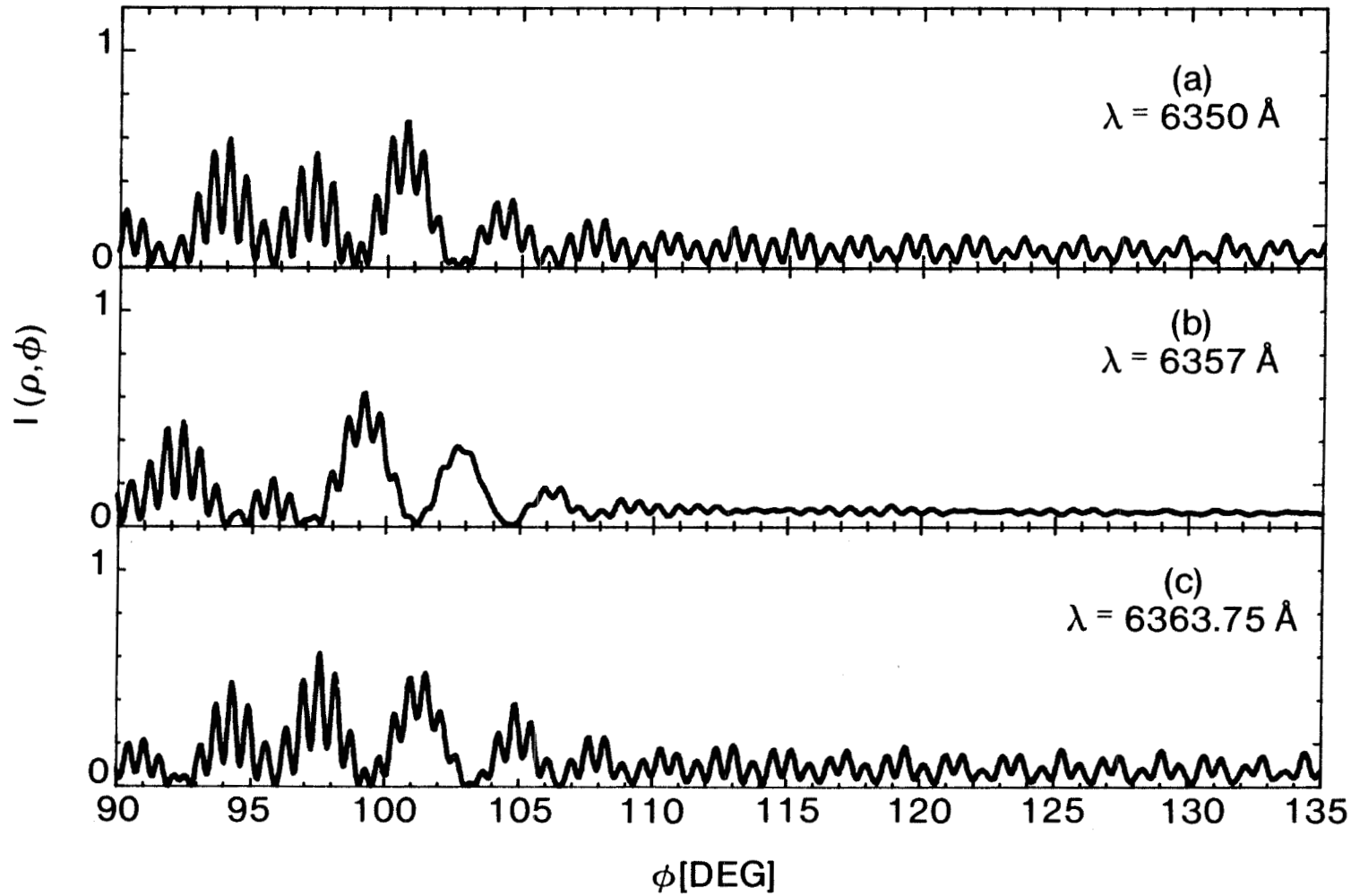

Fig. 5.4 The scattered intensity pattern from a dielectric cylinder plotted for different wavelengths at the peak of the resonance curve; (continued on next page).

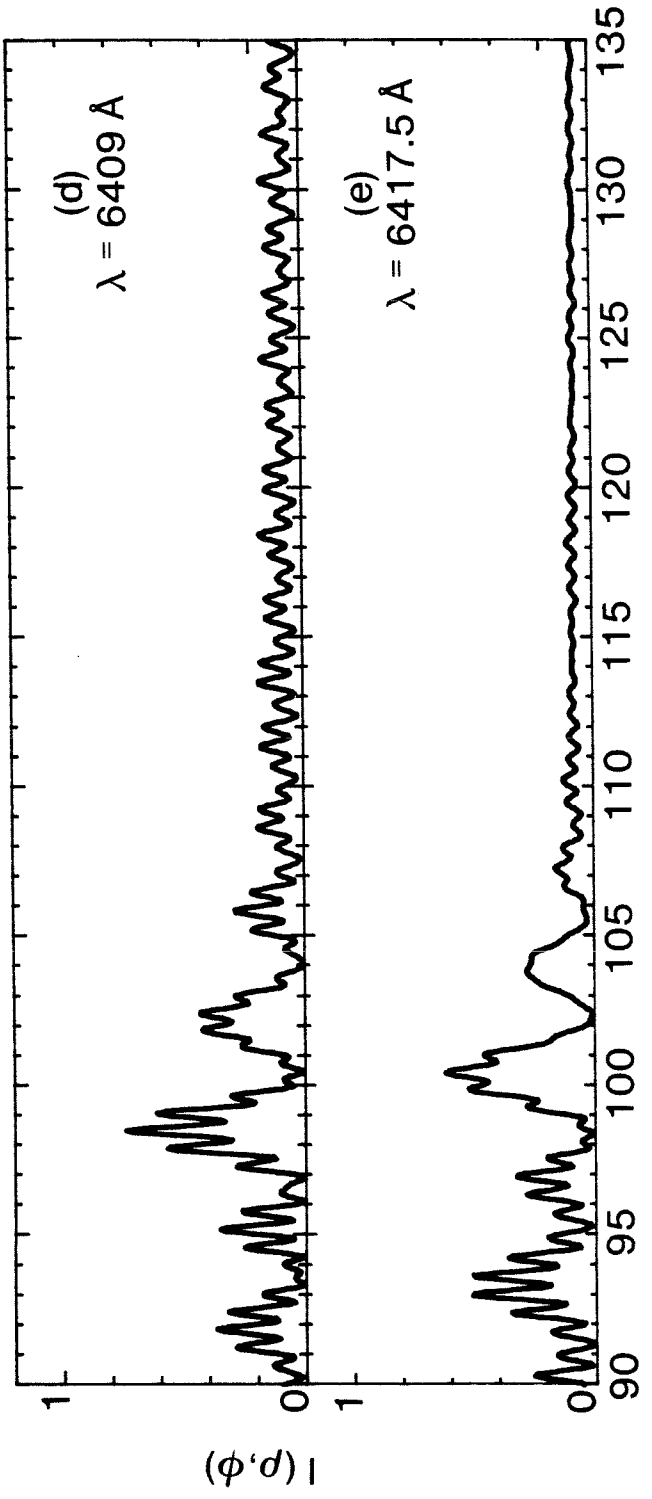

Fig. 5.4 Continued. (d) and (e) the scattered intensity pattern plotted for two different wavelengths at the trough of the resonance curve.

is in the peak at $\phi \cong 103°$ at off-resonance this peak is quite different from the others in the pattern it has a very little structure in it. In Fig. 5.5 the intensity patterns are plotted as a function of the angle ϕ at the five wavelengths considered. In the range $135° \leq \phi \lesssim 150°$ the pattern has the same characteristics as in the range $110 \lesssim \phi \leq 135°$. In the range $150° \leq \phi \leq 180°$, the maximum of the peak is positioned about the same place in all the curves at $\phi \cong 153.5°$, but its value is larger at-resonance than at off-resonance.

The value of the intensity contained in each of these patterns is the same because we illuminate the cylinder with the same unit amplitude incident field. So when the field is at-resonance, the intensity will concentrate around $\phi = 0°$, which will decrease the intensity in the range $45° \lesssim \phi \lesssim 180°$ to balance for the whole value of the intensity. And the main difference between the intensity pattern at the peak and the trough is in the amplitude of the main and the first few side-lobes as shown earlier.

So the resonances of the fields are affecting the pattern of the scattered intensity in the way it shapes up in the different regions of the angle ϕ.

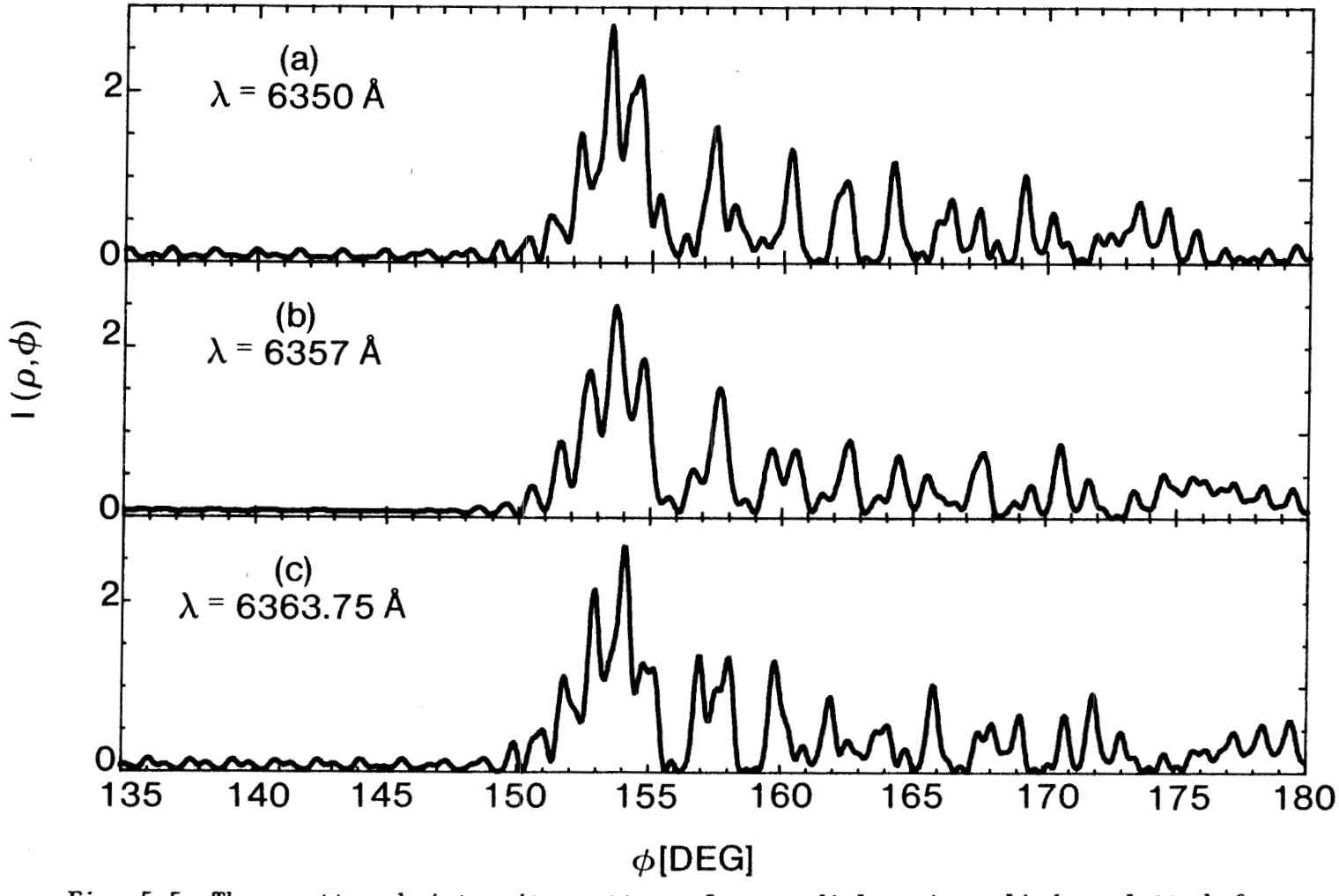

Fig. 5.5 The scattered intensity pattern from a dielectric cylinder plotted for different wavelengths at the peak of the resonance curve; (continued on next page).

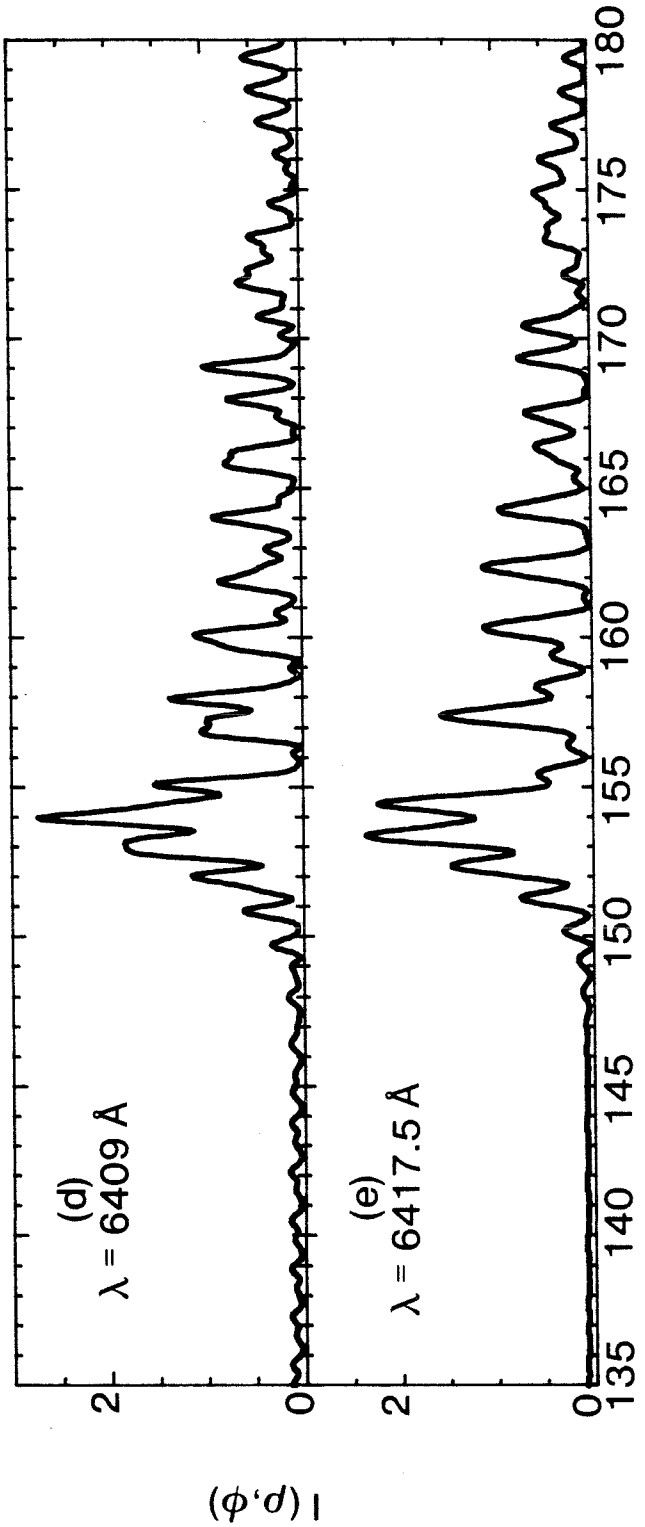

Fig. 5.5 Continued. (d) and (e) the scattered intensity pattern plotted for two different wavelengths at the trough of the resonance curve.

CHAPTER V

REFERENCES

1. M. Gastine, L. Courtois, and J.L. Dorman, "Electromagnetic Resonances of Free Dielectric Spheres," IEEE Trans. Microwave Theory Tech. MTT-15, p. 694 (1967).
2. G.J. Benner, P.W. Barber, J.F. Owen, and R.K. Chang, "Observation of Structure Resonances in the Fluorescence Spectra from Microspheres." Phys. Rev. Lett. 44, p. 475 (1980).
3. A. Ashkin, and J.M. Dziedzic," Observation of Optical Resonances of Dielectric Spheres by Light Scattering," App. Opt. 20, p. 1803 (1981).
4. N. George, "Scattering by Glass Microballoons and Multitone Interferometry", J. Opt. Soc. Am. 66, p. 1135 (1976).
5. J.D. Murphy, P.J. Moser, A. Nagl, and H. Überall, "A Surface Wave Interpretation for the Resonances of a Dielectric Sphere," IEEE Trans., AP-28, p. 924 (1980).
6. M.W. Pospiezalski, "Cylindrical Dielectric Resonators and Their Application in TEM Line Microwave Circuits," IEEE Trans. Microwave Theory Tech., MMT-27, p. 233 (1979).
7. M.W. Pospieszalski, "On the Theory and Application of the Dielectric Post Resonator," IEEE Trans. Microwave Theory Tech., MMT-25, p. 228 (1977).
8. J. Van Bladel, "Resonant Scattering by Dielectric Cylinders," IEEE J. Microwave Opt. and Acoust. (GB), 1, p. 41 (1977).

9. A. Ashkin, J.M. Dziedzic, and R.H. Stolen, "Outer Diameter Measurement of Low Birefringence Optical Fibers by a New Resonant Backscatter Technique," App. Opt. 20, p. 2299 (1981).

10. J.F. Owen, P.W. Barber, B.J. Messinger, and R.K. Chang, "Determination of Optical-Fiber Diameter from Resonances in the Elastic Scattering Spectrum," Opt. Lett. 6, p. 272 (1981).

11. J.F. Owen, R.K. Chang, and P.W. Barber, "Internal Electrical Field Distributions of a Dielectric Cylinder at Resonance Wavelengths," Opt. Lett. 6, p. 540 (1981).

12. M. Abramowitz and I.A. Stegun, Handbook of Mathematical Functions (National Bureau of Standards, Washington D.C., 1972).

13. A.E. Siegman, An Introduction to Lasers and Masers (McGraw-Hill, New York, 1971).

14. Joseph T. Verdeyen, Laser Electronics (Prentice-Hall, Englewood Cliffs, New Jersey, 1981).

CHAPTER VI

EXPERIMENTS

6.1 Introduction

An experimental investigation of the scattering of light from large circular conducting and dielectric cylinders was performed to illustrate the theory reported in Chapters II and III.

In Section 6.2 the experimental scattered intensity pattern from conducting and dielectric cylinders are photographed for the range $0° \leq \phi \lesssim 180°$. These photographs show the overall characteristics of the scattered pattern. The sources responsible for each part of the scattered pattern are discussed. In Section 6.3 the experimental system is described. In Section 6.4 plots of the scattered intensity pattern measured experimentally are compared with the theoretical plots from the formulas of Chapters II and III, for both conducting and dielectric cylinders. Comparisons between the scattering patterns resulting from the different polarizations of the incident field are shown in Section 6.5.

6.2 Photographs of the Scattered Intensity Pattern

In this section photographs of the intensity pattern are shown. Then the fields generating different portions of the intensity pattern are discussed. Unclad optical fibers are used for the dielectric cylinder experiments. An optical fiber coated with aluminum is used for the conducting cylinder experiments.

In Figs. 6.1(a) and 6.1(b) photographs of the whole scattering intensity pattern in the range $0° \leq \phi \lesssim 180°$ are shown for conducting and dielectric cylinders, respectively. For the conducting cylinder, as seen in Fig. 6.1(a), the pattern has a main peak at $\phi = 0°$, a fringe pattern in the range of $0° \leq \phi \lesssim 30°$, and a continuous intensity pattern in the rest of the range of ϕ. The field scattered by the conducting cylinder can be divided into three different regions:

(a) For $0° \leq \phi \lesssim 5°$. The fields are mainly generated by the diffracted fields from the sides of the cylinder.

(b) For $5° \leq \phi \lesssim 90°$. The fields are generated by the interference between the diffracted fields and those reflected from the sides of the cylinder.

(c) For $90° \lesssim \phi \lesssim 180°$. The fields are generated by the surface current.

For the dielectric cylinder, as seen in Fig. 6.1(b), the pattern has fringes in the whole range of ϕ. The pattern has wide variations in intensity for the different ranges of ϕ. The scattered field of the dielectric cylinder can be divided into four different regions:

(a) For $0° < \phi \lesssim 5°$. The fields are mainly generated by diffraction from the edges of the cylinder.

(a)

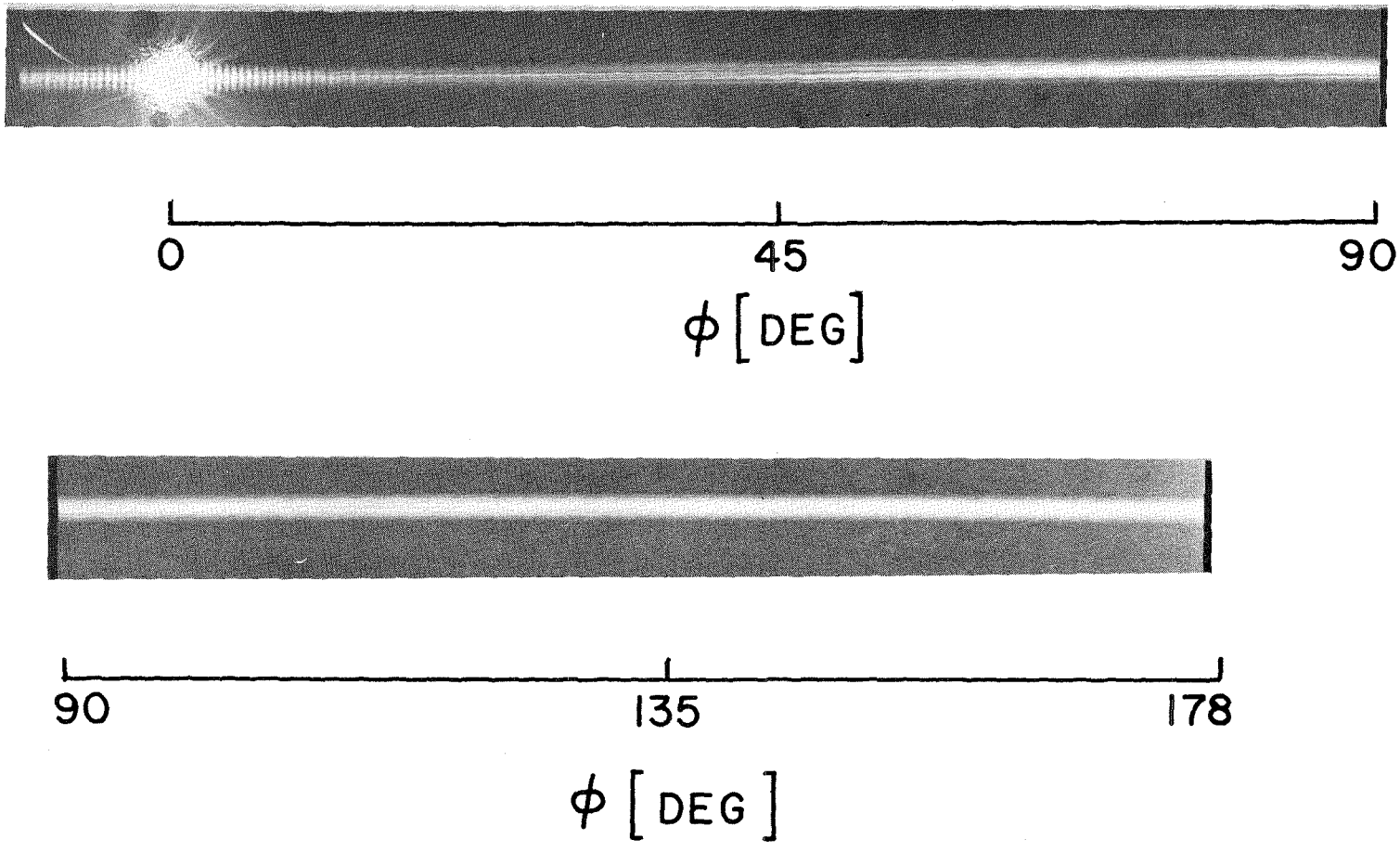

Fig. 6.1 The scattered intensity pattern is photographed for the whole range of ϕ, (a) for a conducting cylinder of ka = 327; (continued on next page).

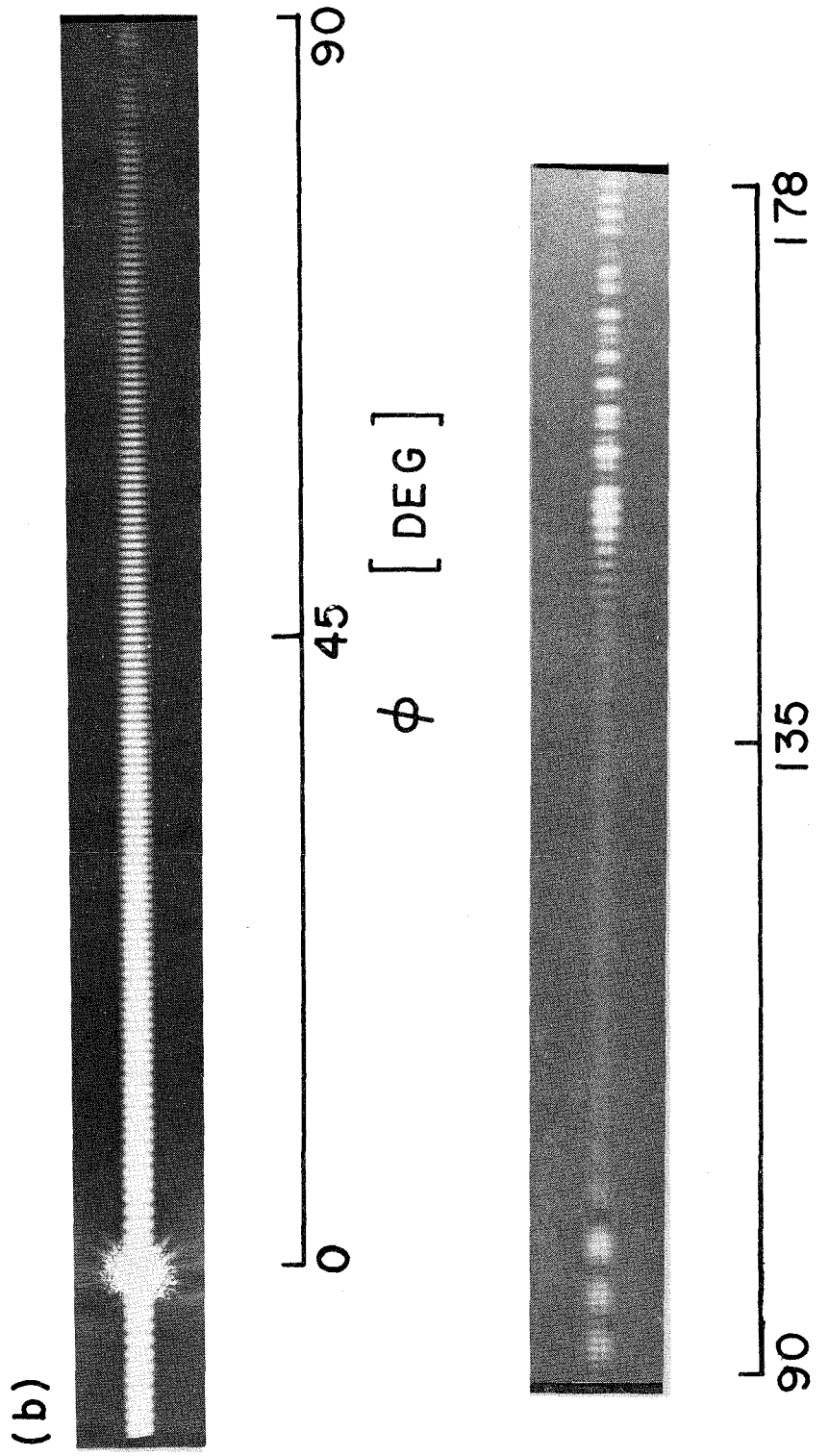

Fig. 6.1 Continued. (b) the scattered intensity pattern for a dielectric cylinder of ka = 327.

(b) For $0° \lesssim \phi \lesssim 90°$. The fields are generated by interference between the refracted and reflected rays.

(c) For $90° \lesssim \phi \lesssim 150°$. The fields are generated by interference between the reflected rays and those refracted rays which have gone through more than one internal reflection.

(d) For $150° \lesssim \phi \lesssim 180°$. The fields are generated by interference between the reflected rays and the refracted rays which have gone through one internal reflection.

These regions are not sharply defined because they overlap each other, but those are the regions where they dominate most. These regions also change when the diameter of the cylinder changes, e.g., the region where the fields are generated by diffraction will increase by the decrease of the diameter.

6.3 System Description

Diagrams of the optical-hybrid systems used in the experiment are shown in Figs. 6.2 and 6.3. The experimental setup shown in Fig. 6.2 consists of a Spectra Physics Model 146P He-Ne laser, operating at $\lambda = 6328\text{Å}$; a Spectra Physics polarizer; a beam expander; and an iris. The cylinder under test is mounted in the center of a cylindrical chamber, which has an open slot of length larger than half the circumference of the chamber. On the top of the chamber a Daedal Inc. Model 20601 rotary stage is mounted. An arm with an avalanche photodiode (RCA C30902E) at its end is mounted on the rotary stage in such a way as to allow the photodiode to rotate in a circle centered on the cylinder under test. The light emitted by the laser is a linearly polarized plane wave, and its plane of polarization can be changed using the polarizer. The beam expander enlarged the plane wave emitted by the laser to a diameter of about 5 mm. The expanded plane wave illuminates the cylinder under test, and the resulting scattered wave propagates in all directions around the cylinder. A portion of this scattered wave will propagate through the slot of the chamber for $-10^\circ \lesssim \phi \lesssim 190^\circ$. The avalanche photodetector was rotated in steps in the range $-10^\circ \lesssim \phi \lesssim 178^\circ$, to locate exactly the position of the main peak at $\phi = 0^\circ$ using the symmetry of the pattern around $\phi = 0^\circ$. The electric signal generated by the photodiode, corresponding to the intensity of the light illuminating it, was amplified and digitized by the A/D convertor. The Cromemco Z-2 microcomputer triggers the stepping motor control, which in turn drives the stepping motor of the rotary stage. At each step, the

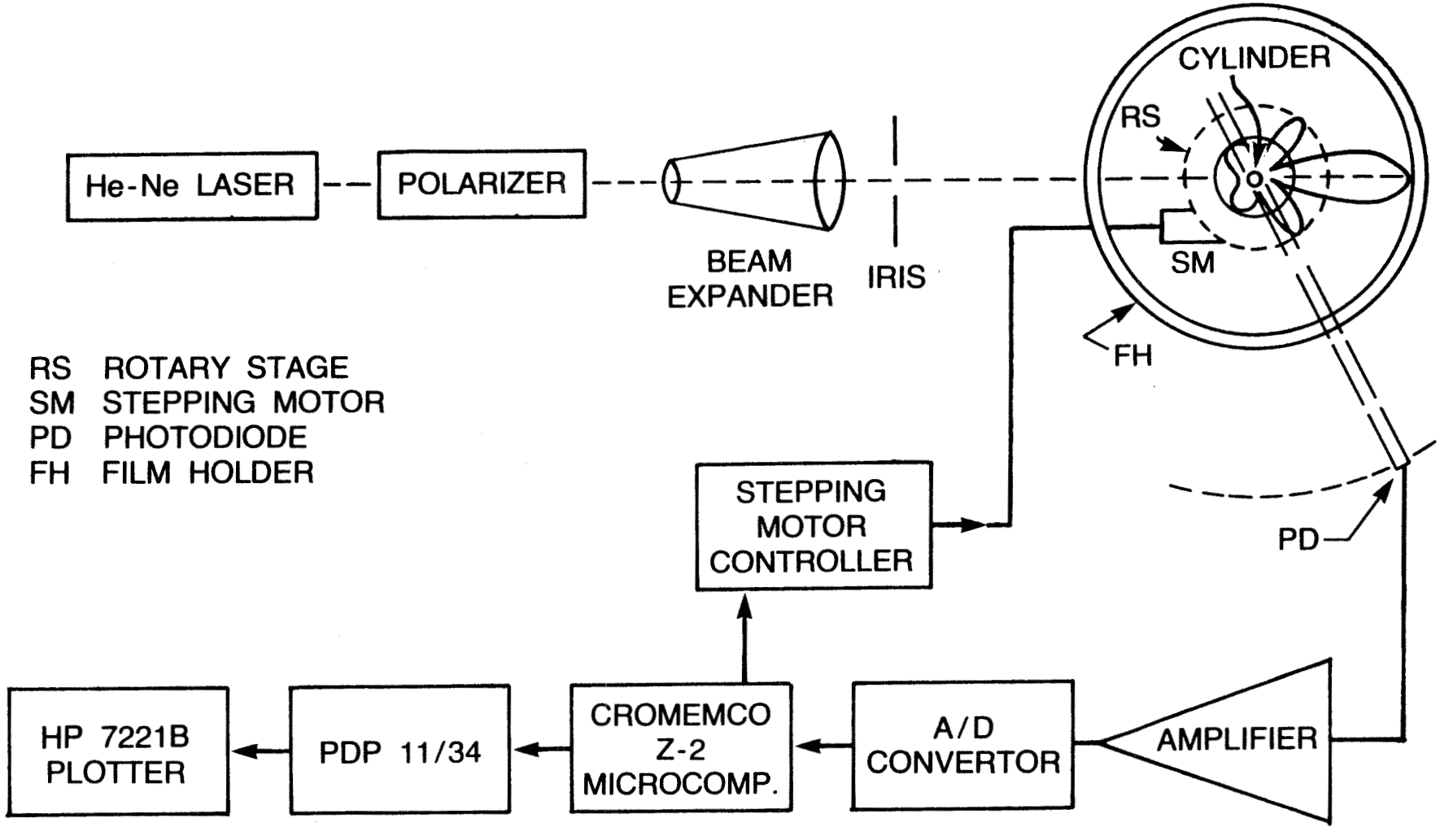

Fig. 6.2 The photodiode optical-hybrid system used in the experimental investigations.

rotary stage drove the photodiode a specified distance around the sample. After a specific time interval, controlled by the user, the microcomputer triggers the A/D convertor to sample the existing signal from the photodiode. This time interval between the movement of the photodiode and the start of signal conversion is to insure that the photodiode vibrations caused by its movement from one position to the next were completely damped. The intensity data converted by the A/D convertor are then stored on a floppy disk. When all the data points are collected, the information is transferred to the PDP 11/34 minimcomputer, which has more capabilities. The minicomputer will perform the necessary data processing and will plot the intensity patterns.

The resolution of the rotary stage is $\Delta\phi = 0.01°$/step while the diameter of the active area of the photodiode is ~ 0.5 mm. Since the photodetector is mounted 50 cm from the center of the chamber, it limits the resolution to ~0.06°. The resolution of the system can be increased by putting a pinhole in front of the detector, but that in turn will reduce the signal-to-noise ratio.

In Fig. 6.3 an alternative setup of the experiment is shown. In this system the scattered light is recorded on a photographic film mounted on the slotted chamber, and its position is registered by 6 pins which are mounted on the cylindrical chamber. After processing, the film was scanned by a Joyce-Loebl Model III-CS double beam recording microdensitometer to obtain a plot of the density of the film. The density curves are then digitized by an HP-7221B digitzer controlled by a mini-computer PDP 11/34, and the data are stored on

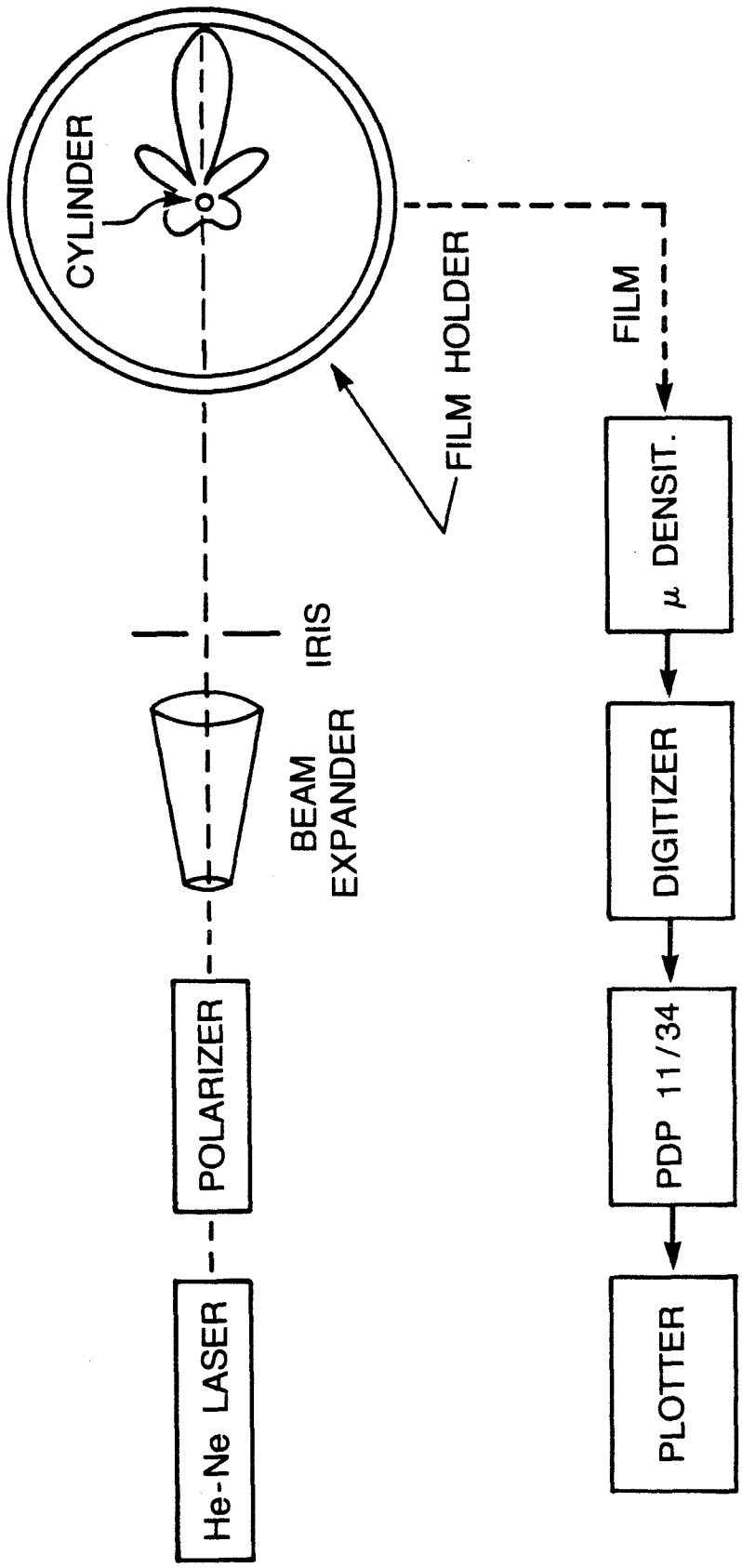

Fig. 6.3 The film/microdensitometer system used in the experiments.

a disk. The density data is then converted to intensity data using the method shown in Appendix C. The H-D curve of the film is fitted using a polynomial, which is used in converting density to intensity data. The intensity data are stored in the minicomputer for further processing and plotting.

In Table 6.1 a comparison between the two experimental systems is shown. The photodetector system has the advantage of collecting intensity data directly, and of giving an almost real time record. While the film/microdensitometer combination system has the advantage of providing a continuous record of the density and of having a high angular resolution, which is higher than that of the photodiode. But we preferred to use the photodiode system for the overall advantages such as its reliability and ability to obtain a direct record of the intensity. To show the value of using the film/microdensitometer system, and to illustrate that it gives a very comparable result to that obtained using the photodetector system, some of these results are shown in Figs. 6.4(a), (b) and (c). In Fig. 6.4(a) the density curve of the film recorded for the intensity pattern of a dielectric cylinder in the range $45° \leqq \phi \leqq 90°$ is plotted. In 6.4(b) the corresponding intensity pattern converted from the density data, using the method demonstrated in Appendix C, is shown, and it is very comparable with the intensity plot using the photodiode system which is plotted in Fig. 6.4(c). The intensity pattern measured using both systems is the same for all characteristics of the pattern. This shows us that this method of measurement is very valuable, and also proves that it is a very compatible alternative system of measure-

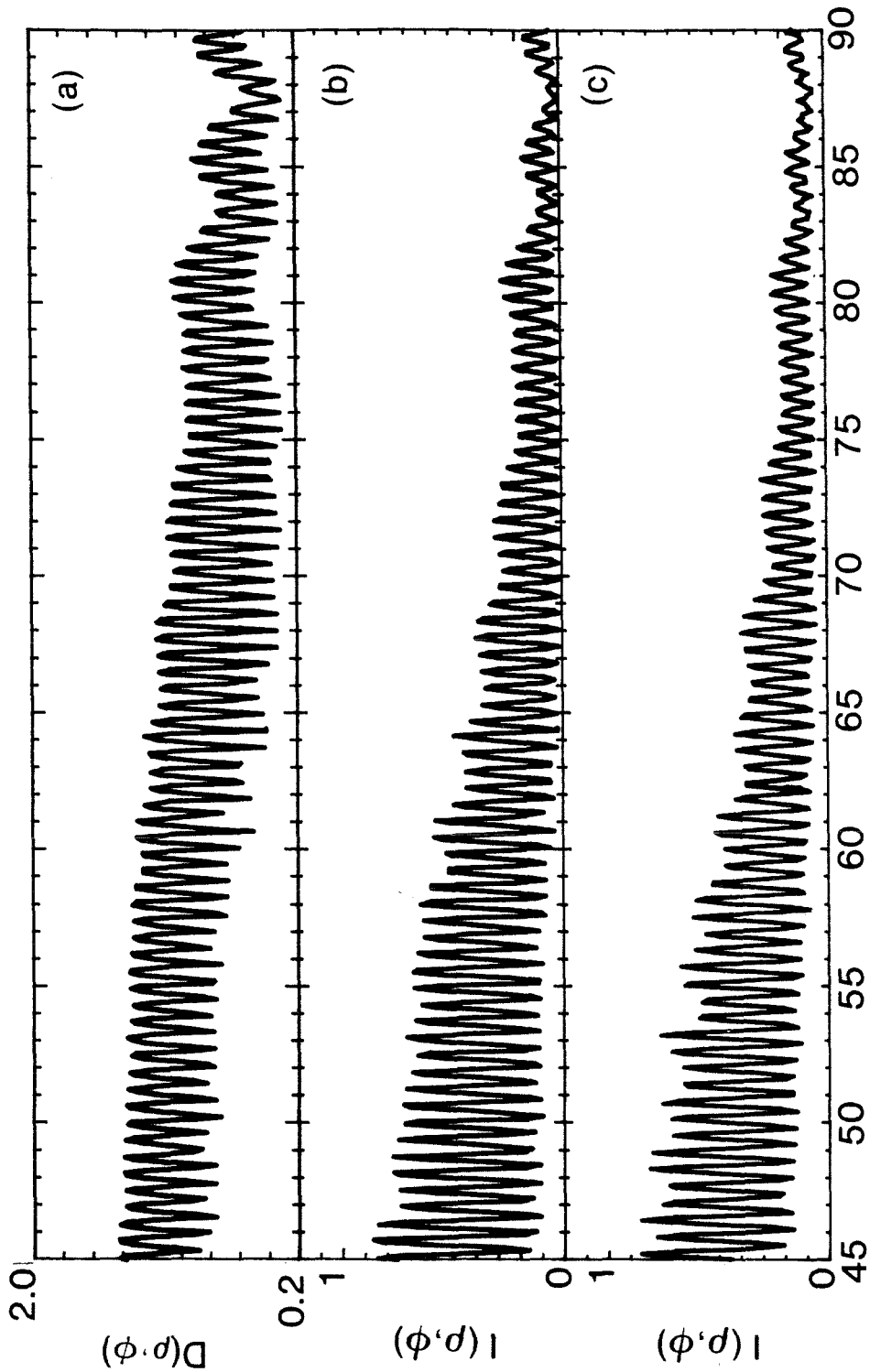

Fig. 6.4 The scattered pattern from a dielectric cylinder of ka = 327, (a) density plot of the film whicoh has a record of the intensity, (b) intensity converted from density plot, and (c) intensity plot measured by the photo-diode system.

Table 6.1

Comparison Between the Photodiode and the Film/Microdensitometer Systems

Photodiode-System	Film/Microdensitometer System
1. Collect intensity data directly.	1. Collect the intensity data as a density of the film.
2. Almost a real time system.	2. To obtain intensity data, the film will be developed and then the density plot is provided by the micro-densitometer, the density curves are digitized and finally converted to intensity.
3. Produces a discrete record for the data.	3. A continuous record is stored on the film.
4. The accuracy of the angular position of the photodiode depends on the accuracy of the rotary stage and the centering of the cylinder undertest.	4. The accuracy of the angular data depends only on the centering of the cylinder with respect to the chamber.
5. The angular resolution is limited by the area of the photodiode and the resolution of the rotary stage.	5. The angular resolution is limited by the resolution of the film.
6. The accuracy of the intensity data is limited by the nonlinearity of the photodiode.	6. The accuracy of the intensity data is limited by: a) the nonlinearity of the film (exposure times, development time, ...), b) the reading of the microdensitometer, (c) the digitization and conversion process.

ment. The results using this system for the experiments discussed in this chapter are presented in Appendix D.

6.4 Plots of the Scattered Intensity Pattern

In this section we present the experimental results collected using the photo-detector system for the conducting and the dielectric cylinders, and to compare them with the exact theoretical results. Parallel polarization is considered in this section. A comparison of polarizations is described in Section 6.5 below.

The main characteristic of the intensity pattern of the light scattered from a conducting cylinder, as shown in the photographs of Fig. 6.1, is its fringe pattern which extends only to $\phi \cong 30°$ after which the pattern will be just a continuous intensity pattern with no structure. In Fig. 6.5(a) the scattered intensity pattern is plotted for $0° \leq \phi \leq 45°$ using the data collected with the photodiode system. The pattern has a main lobe centered at $\phi = 0°$ and a number of side-lobes, which extend to $\phi \cong 30°$. For angles greater than $\phi \cong 15°$ the contrast of the fringes becomes very small, which makes them hard to see in the scale used. In Fig. 6.5(b) the theoretical plot is presented for the scattered intensity from a conducting cylinder using the formulas obtained in Chapter II. The diameter of the conducting wire used in the experiment is measured using a micrometer ($ka \cong 327$), then this value is used for ka in the calculations. From Figs. 6.5(a) and (b) the agreement between the theory and experiment is evident. A comparison between the theoretical and experimental results for the range $45° \leq \phi \leq 180°$ will be shown in Appendix D.

In Figs. 6.6(a) and (b) the intensity pattern scattered by a dielectric cylinder is plotted. The experimental and theoretical

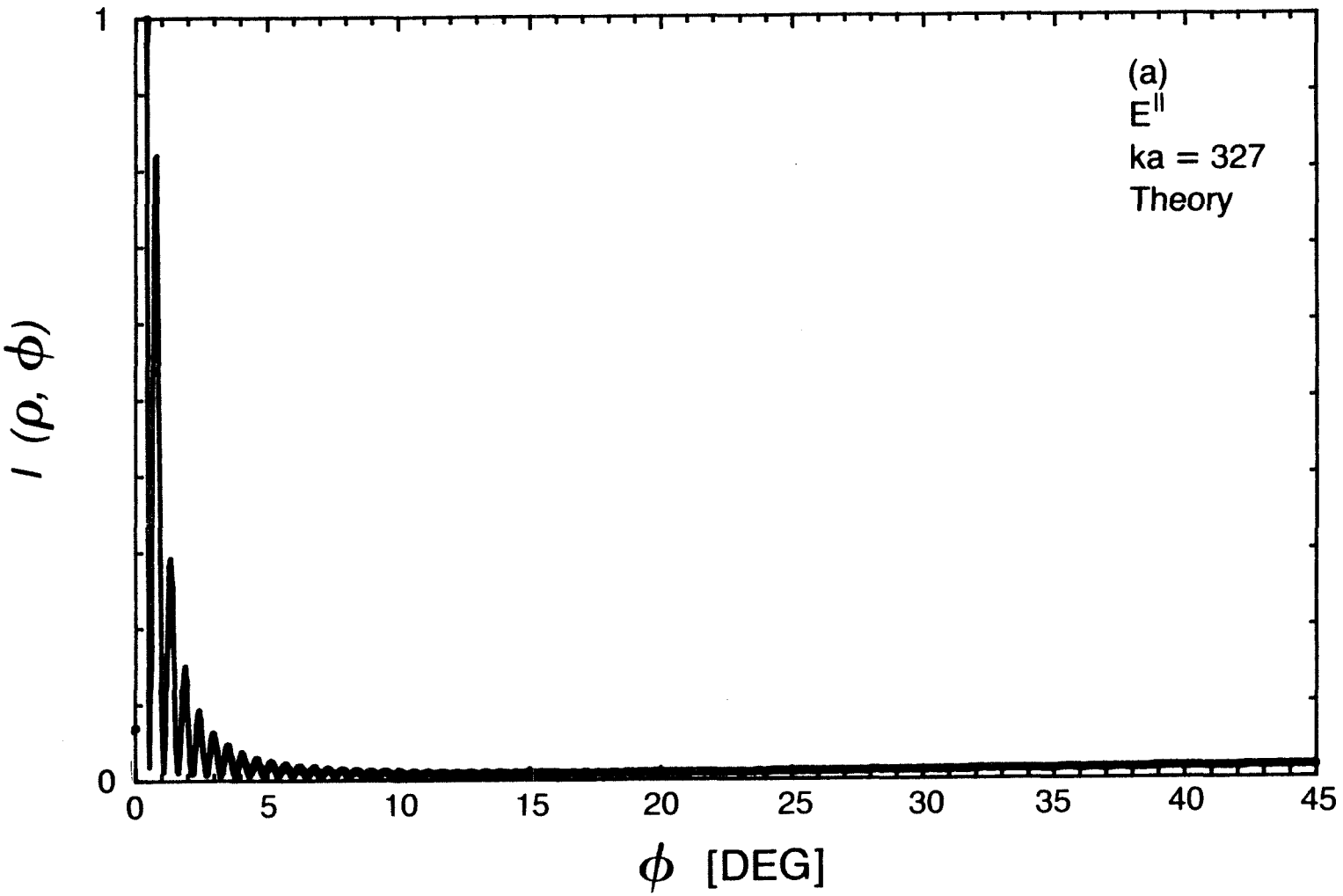

Fig. 6.5 The scattered intensity pattern is plotted using the exact solution given by Eq. (2.34) for a parallel polarized field for a conducting cylinder with ka = 327; (continued on next page).

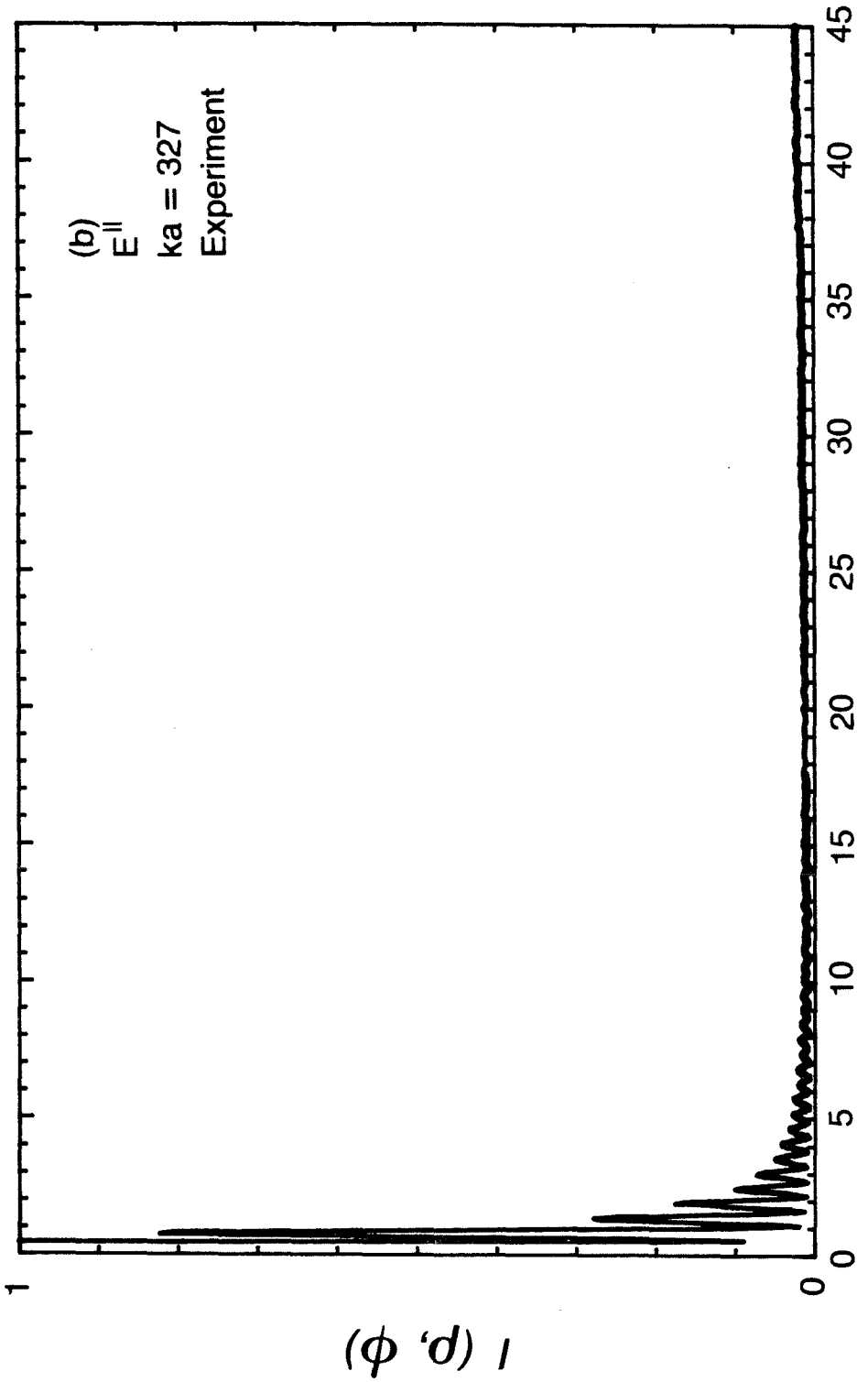

Fig. 6.5 Continued. (b) the scattered intensity pattern is measured using the system in Fig. 6.1 for a conducting cylinder with ka = 327.

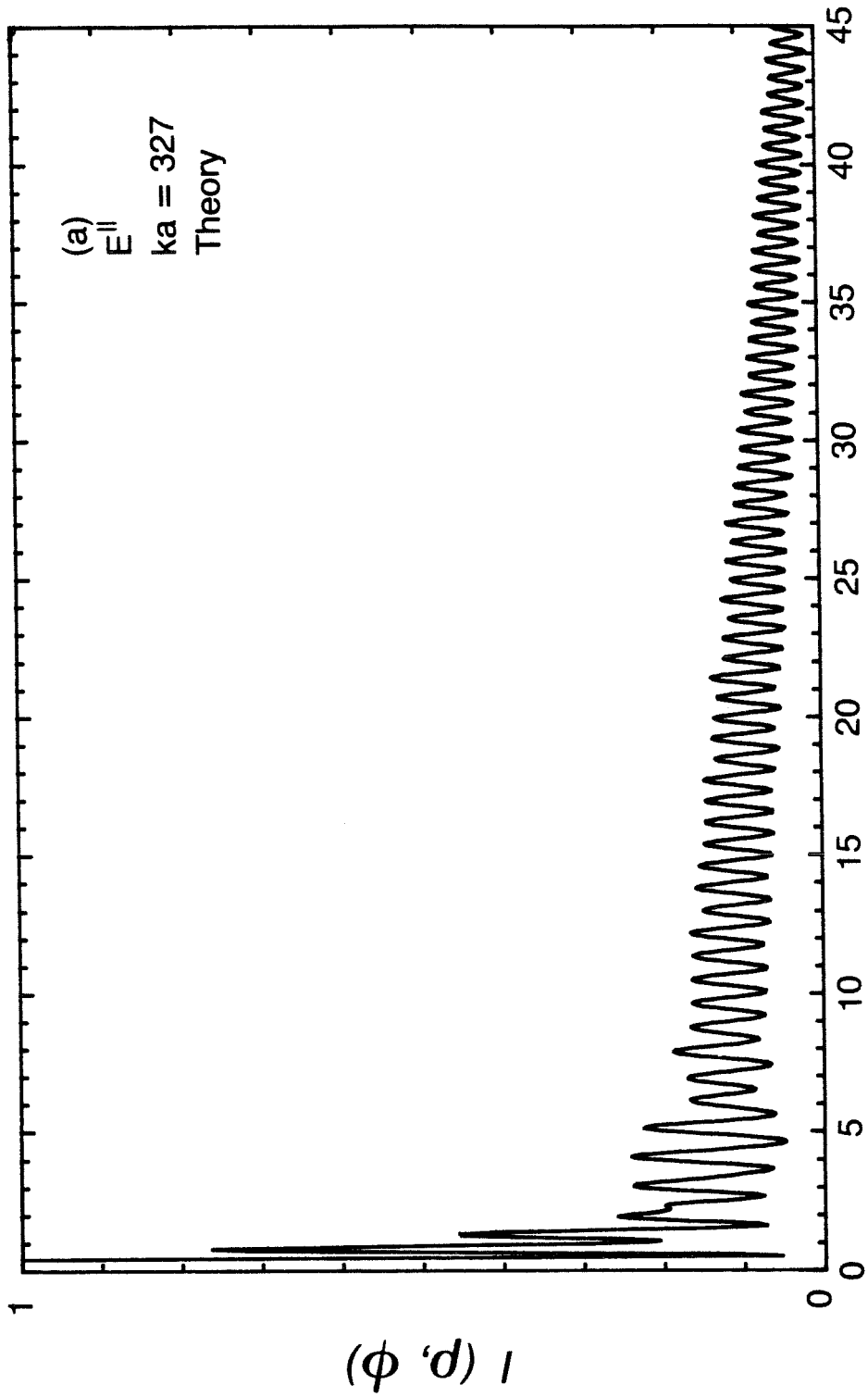

Fig. 6.6 The intensity scattered by a dielectric cylinder with ka = 327 is plotted using the rigorous solution given by Eq. (3.14) for a parallel polarized field; (continued on next page).

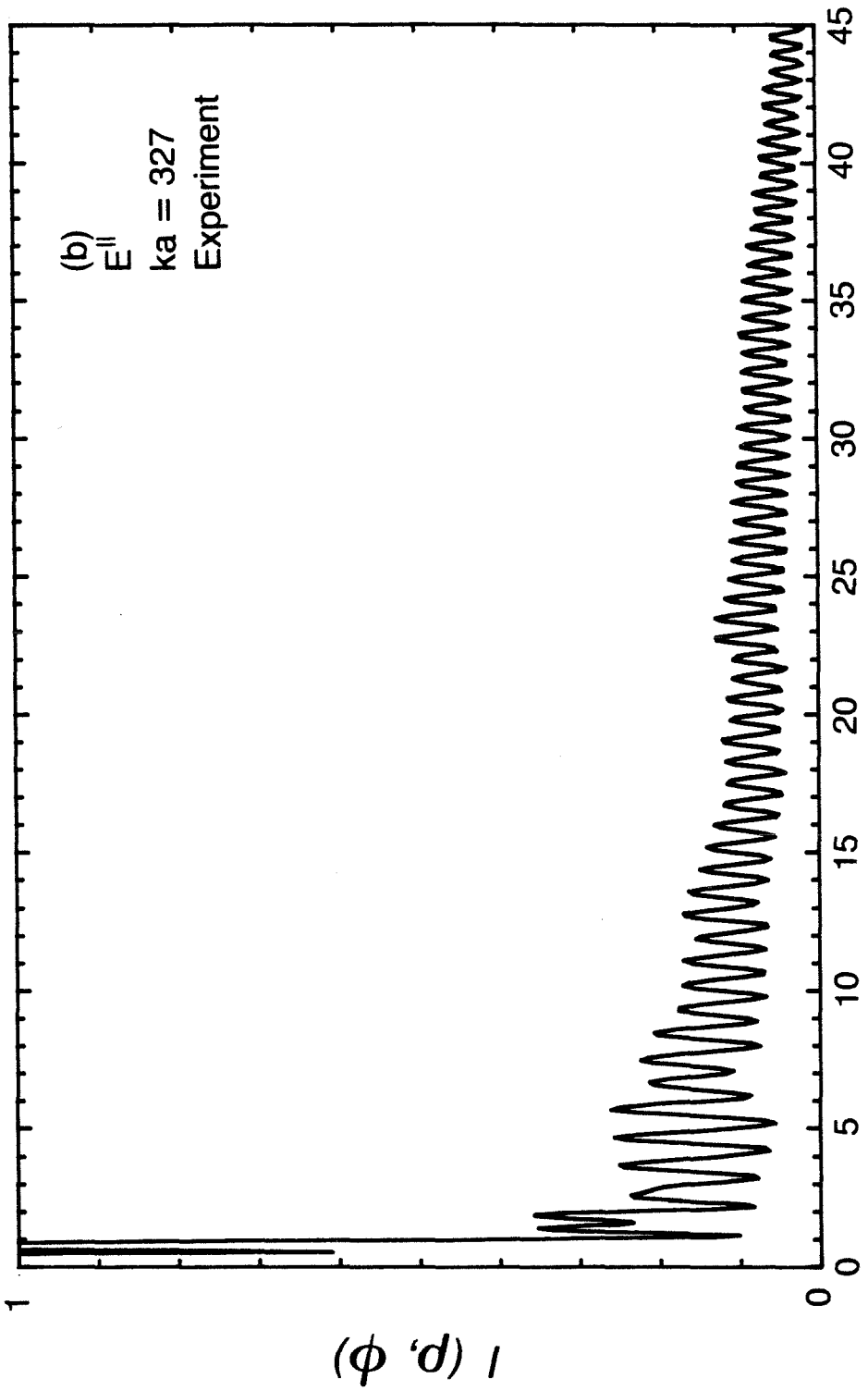

Fig. 6.6 Continued. (b) the scattered intensity pattern measured using the photodiode system for a dielectric cylinder with ka = 327.

plots have similar patterns and the number of fringes for $0° \leq \phi \leq 45°$ is 61 for both plots. The positions of the fringes are slightly different between the theoretical and experimental plots and that is because there might be a slight difference in either or both the wavelength and refractive index as explained in Chapters III and V. The number of fringes for $0° \leq \phi \leq 90°$ is 134 for the theoretical plot and only 133 for the experimental plot. The difference in the number of fringes might be caused by three factors:

(1) an error in measuring the diameter of the cylinder using the micrometer where the accuracy of ka will be $\cong \pm 6$.

(2) an error in positioning the cylinder in the center of the cylindrical chamber where a 1 mm deviation in the position of cylinder along the x-axis will result in a deviation of 0.32% of the value of the angle ϕ.

(3) An error in the wavelength used in the calculations because as shown in Chapter V the number fringes is different at-resonance and at off-resonance wavelengths.

So these factors will contribute to the inaccuracy of the experimental results which produces the main differences between the theoretical and experimental results.

In Figs. 6.7(a) and (b) the scattered intensity by a dielectric cylinder of ka $\cong$ 950 is plotted from experimental and theoretical results, respectively, for $0° \leqq \phi \leqq 30°$. The two patterns are very similar in their character, amplitude, and the position of the fringes. The number of fringes of the experimental plot is 110, while the theoretical plot has 108 fringes. These differences might

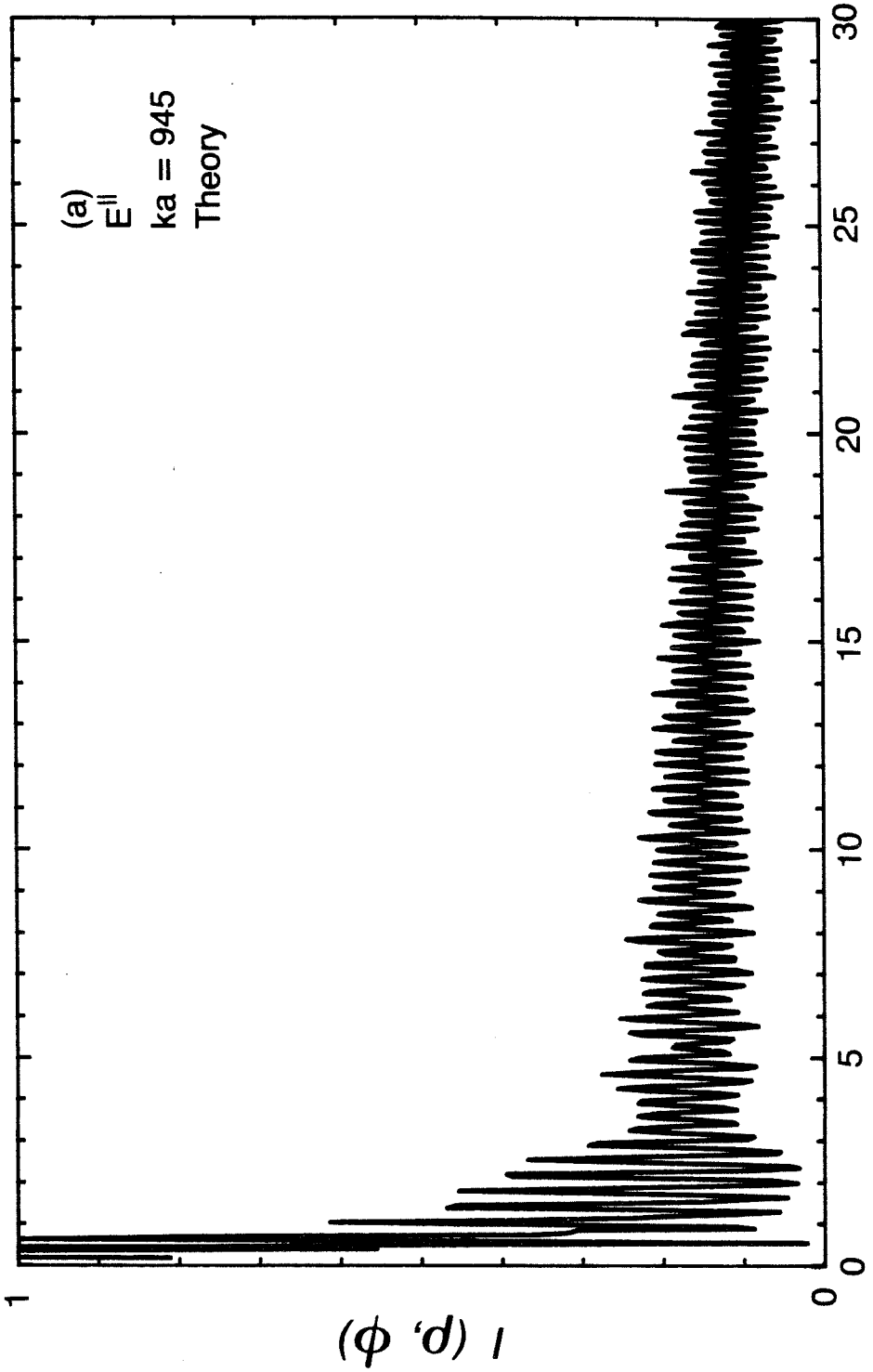

Fig. 6.7 The scattered intensity pattern for a dielectric cylinder with ka = 945 is plotted using Eq. (3.14) for a parallel polarized wave; and for (continued on next page).

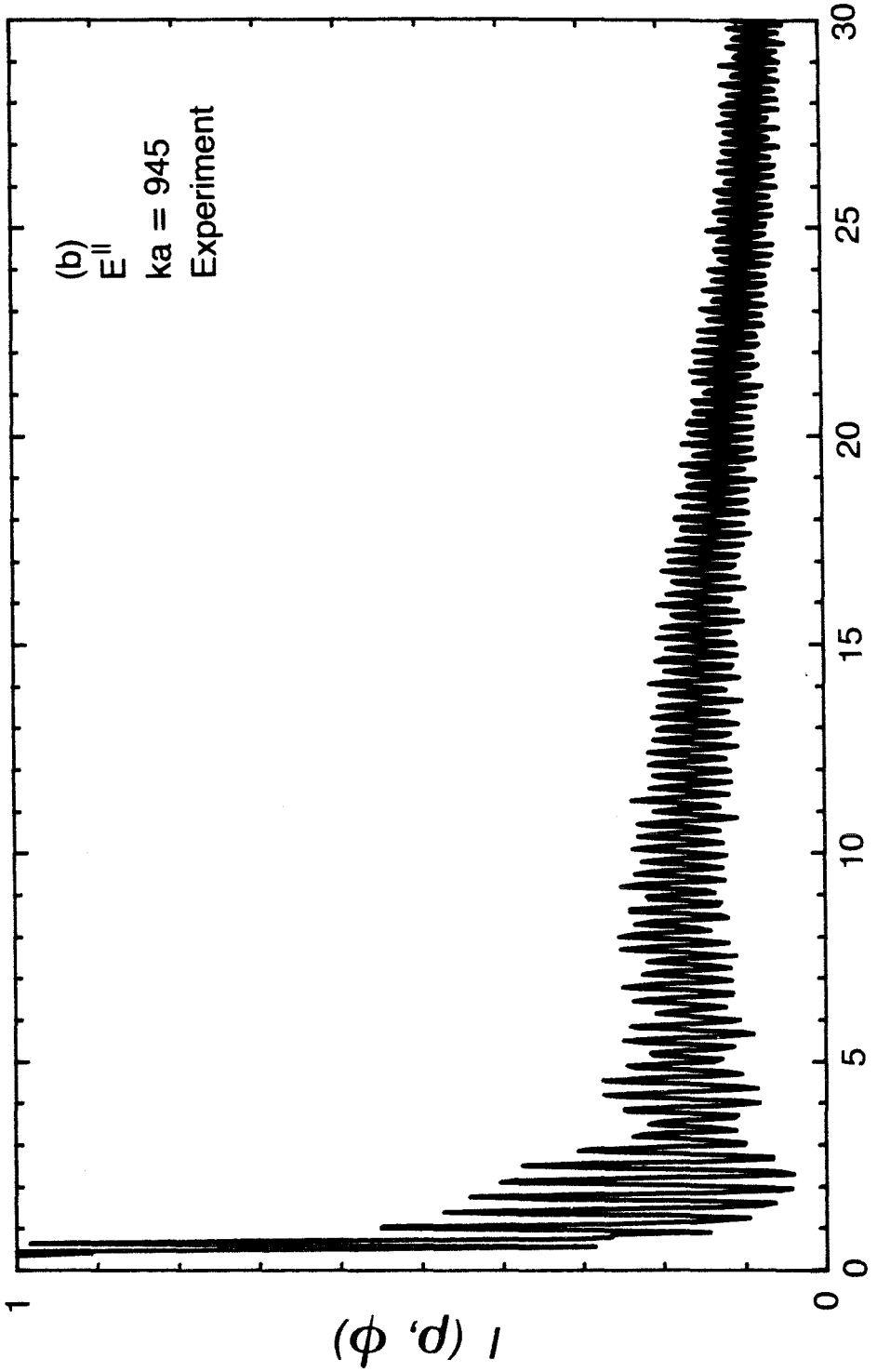

Fig. 6.7 Continued. (b) the scattered intensity pattern measured by the photodiode system for a dielectric cylinder with ka = 945; and for (continued on next page).

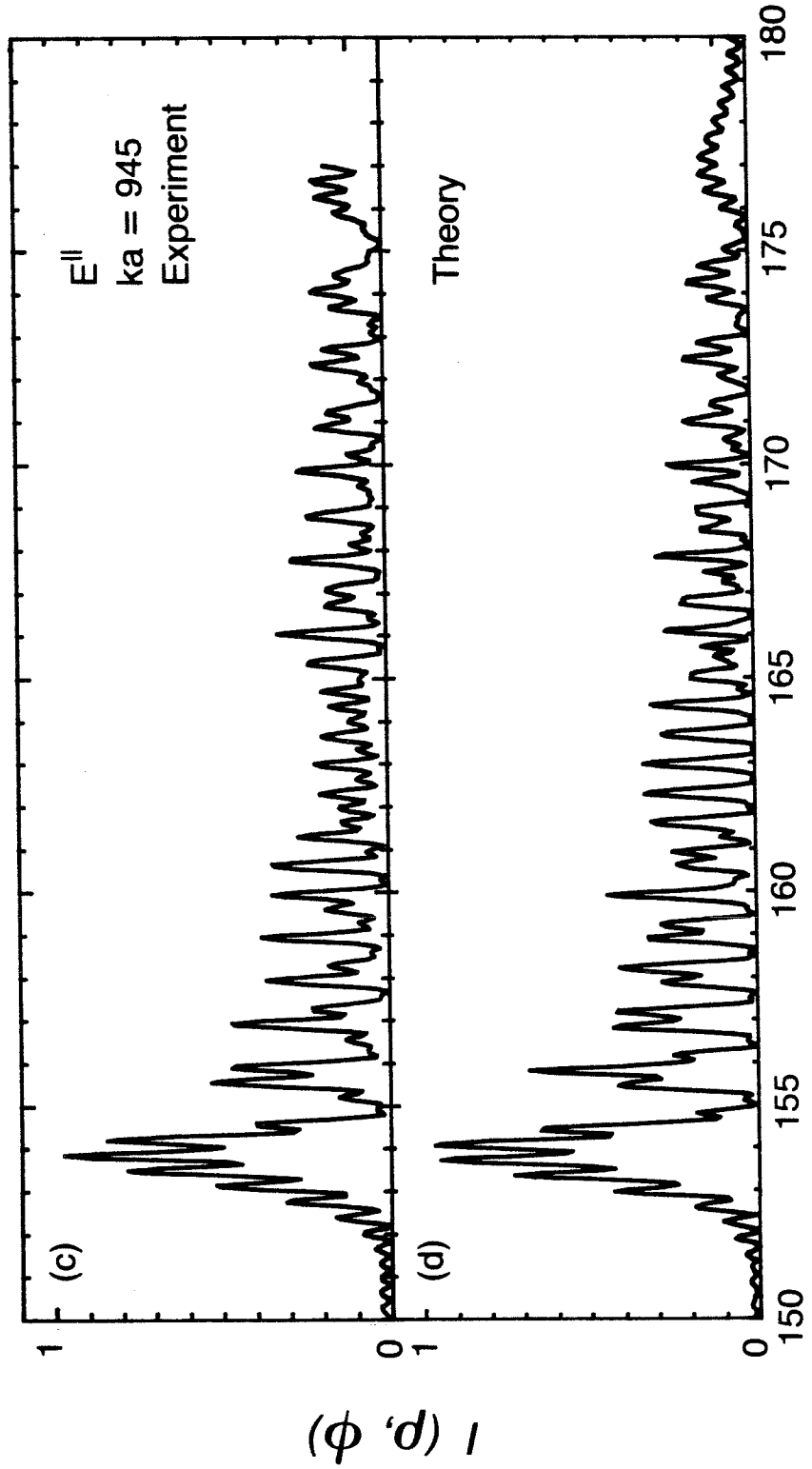

Fig. 6.7 Continued. (c) the scattered intensity pattern measured by the photodiode system for a dielectric cylinder with ka = 945; and (d) for the corresponding pattern plotted using Eq. (3.14) for a parallel polarized field.

be explained by the same factors introduced in the previous paragraph. In Fig. 6.7(c) the intensity is plotted for $150° \leqq \phi \leqq 180°$, which is the backscattered field. The two curves are quite similar, and they peak at the same position, which indicates that both the theoretical and experimental plots have the same index of refraction, $n = 1.45$.

These plots of the experimental and theoretical data illustrate the agreement between the two results, except for minor differences which are expected because of the inaccuracy of the experimental measurements. A comparison between the theoretical and experimental results for the rest of the range of the scattering angle ϕ are reported in Appendix D.

6.5 The Effect of the Different Polarizations on the Scattered Intensity Pattern

The scattered intensity pattern from a cylinder depends on the polarization of the incident field. For the conducting cylinder case the amplitude of the surface current density depends on the polarization of the incident field, as shown in Chapter II. When the incident field is linearly polarized parallel to the axis of symmetry of the cylinder, the surface current density generated will flow also in a direction parallel to the axis of the cylinder, and it will decrease to a negligible amplitude near the boundary of the shadow region. When the incident field is linearly polarized normal to the axis of the cylinder, the surface current density generated flows around the axis of the cylinder; and it has a large amplitude beyond the boundary of the shadow region, which allows it to circulate around the cylinder before it becomes negligible. The surface current density is the main source which generates the scattered field; and since it has different values for the different polarizations, the scattered field for the two different polarizations will be different. In Figs. 6.8(a) and (b) the scattered intensity is plotted from the exact solution for the normal and parallel polarizations, respectively, for a perfectly conducting cylinder with $ka = 327$ in the range $5° \leqq \phi \leqq 60°$. The amplitude of the intensity, for the parallel incident case, is larger than that for the normal incidence case in the range $0° \leqq \phi \leqq 20°$; for larger angles they both tend to have the same peak values. The two patterns have the same number of fringes in the range $0 \leqq \phi \leqq 20°$. The main differences

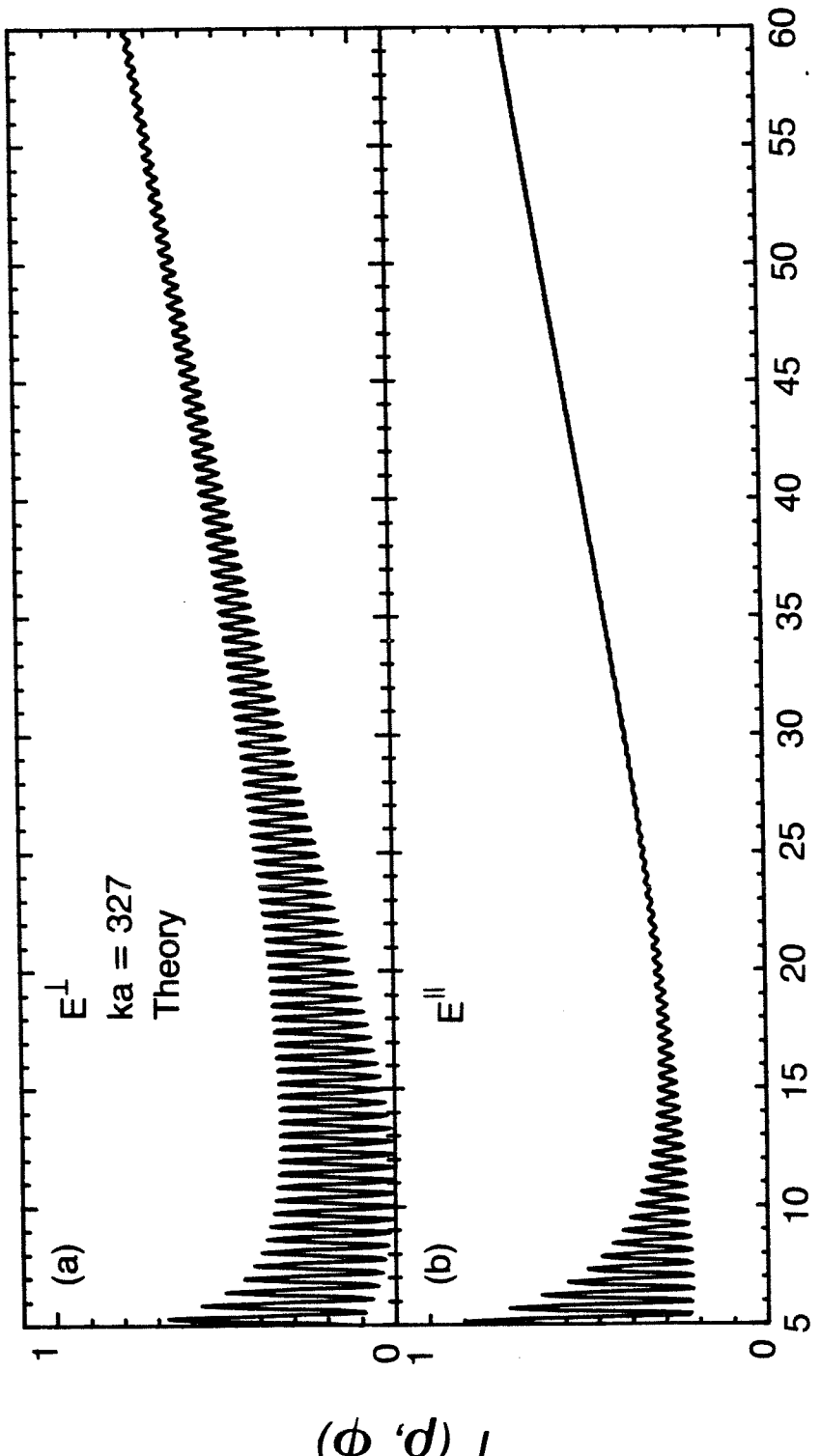

Fig. 6.8 The scattered intensity pattern for a conducting cylinder with ka = 327 plotted from the exact solution formulas; (continued on next page).

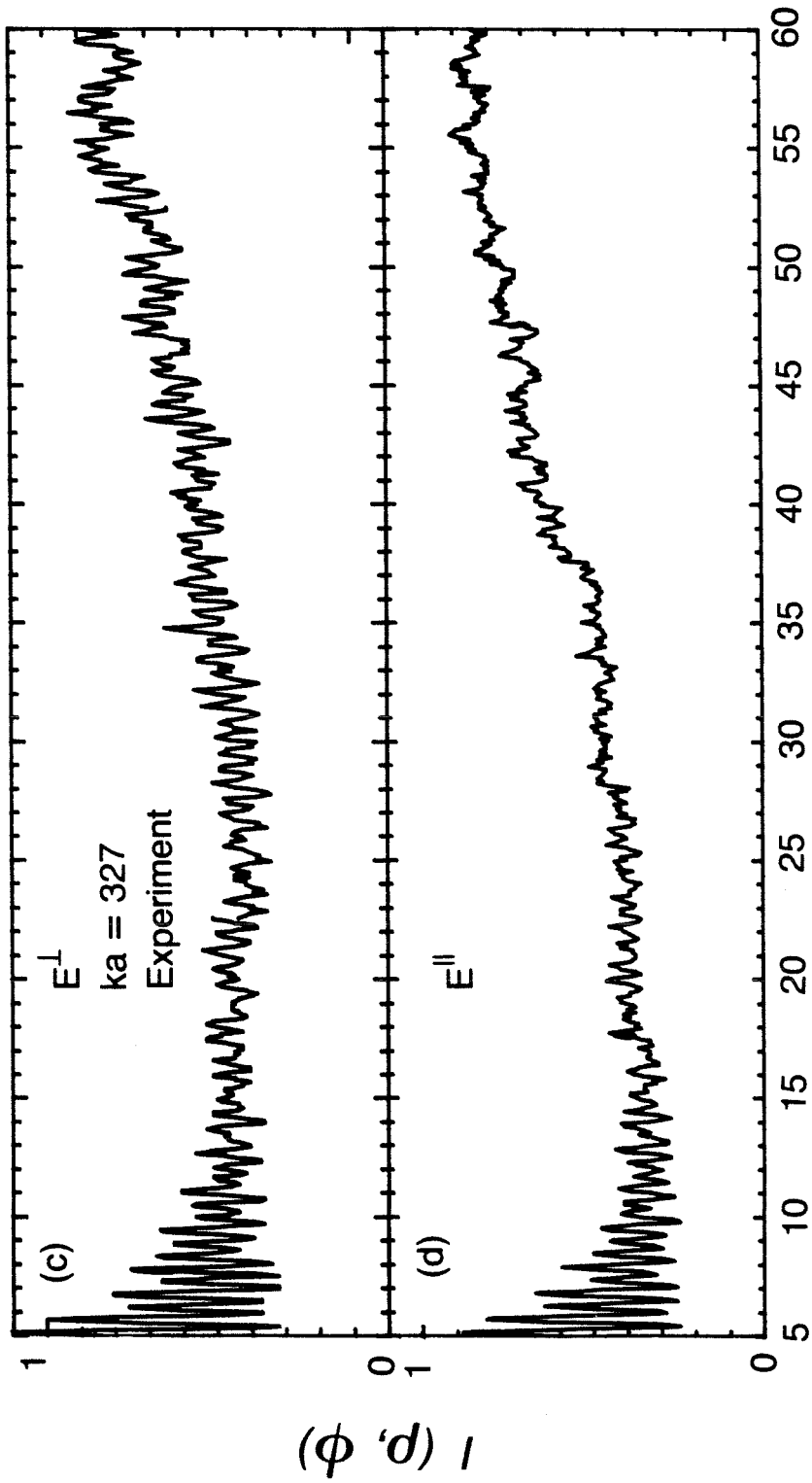

Fig. 6.8 Continued. (c) and (d) the scattered intensity pattern for a conducting cylinder with ka = 327, measured using the photodiode system.

between the two patterns are that the contrast of the fringes is larger for the normal incidence case beyond $\phi = 20°$; and that the sidelobes, for the parallel incidence case, vanish around $\phi \cong 30°$, while they still exist even beyond 60° in the other case of polarization. In Figs. 6.8(c) and (d) the corresponding experimental plots to those in Figs. 6.8(a) and (b) are plotted. The main difference between the two patterns is that the fringes vanish around 30° for the parallel incidence case while they exist in the whole range shown for the normal incident case. The experimental and theoretical plots are in good agreement for $E^{//}$, while the fringe contrast is much smaller for the experimental plot than for that of the theoretical one, for $E^{\perp}$ case. The main reason for this difference in patterns is that aluminum has a finite conductivity ($\sigma \cong 4.88 \times 10^5$ at $\lambda \cong 0.65$ μm), while the theoretical plots are for a perfectly conducting cylinder.

For the dielectric cylinder, the intensity pattern is plotted in Figs. 6.9(a) and (b) for $E^{\perp}$ and $E^{//}$, respectively, using exact theory, and in Figs. 6.9(c) and (d) using experimental data. The theoretical and experimental data are in good agreement for both cases of polarization. The number of sidelobes is the same for both polarization in the range $0 \leqq \phi \leqq 60°$ (86 sidelobes); but for the range $60° \leqq \phi \leqq 90°$ the intensity pattern for $E^{//}$ has 48 sidelobes, while the intensity pattern for $E^{\perp}$ has 52 sidelobes. Another significant difference between the two patterns is that the fringe contrast for $E^{//}$ is much larger than that for $E^{\perp}$. For $E^{//}$ the intensity amplitude has an envelope function, which starts at $\phi \gtrsim 65°$. For $E^{\perp}$ the intensity

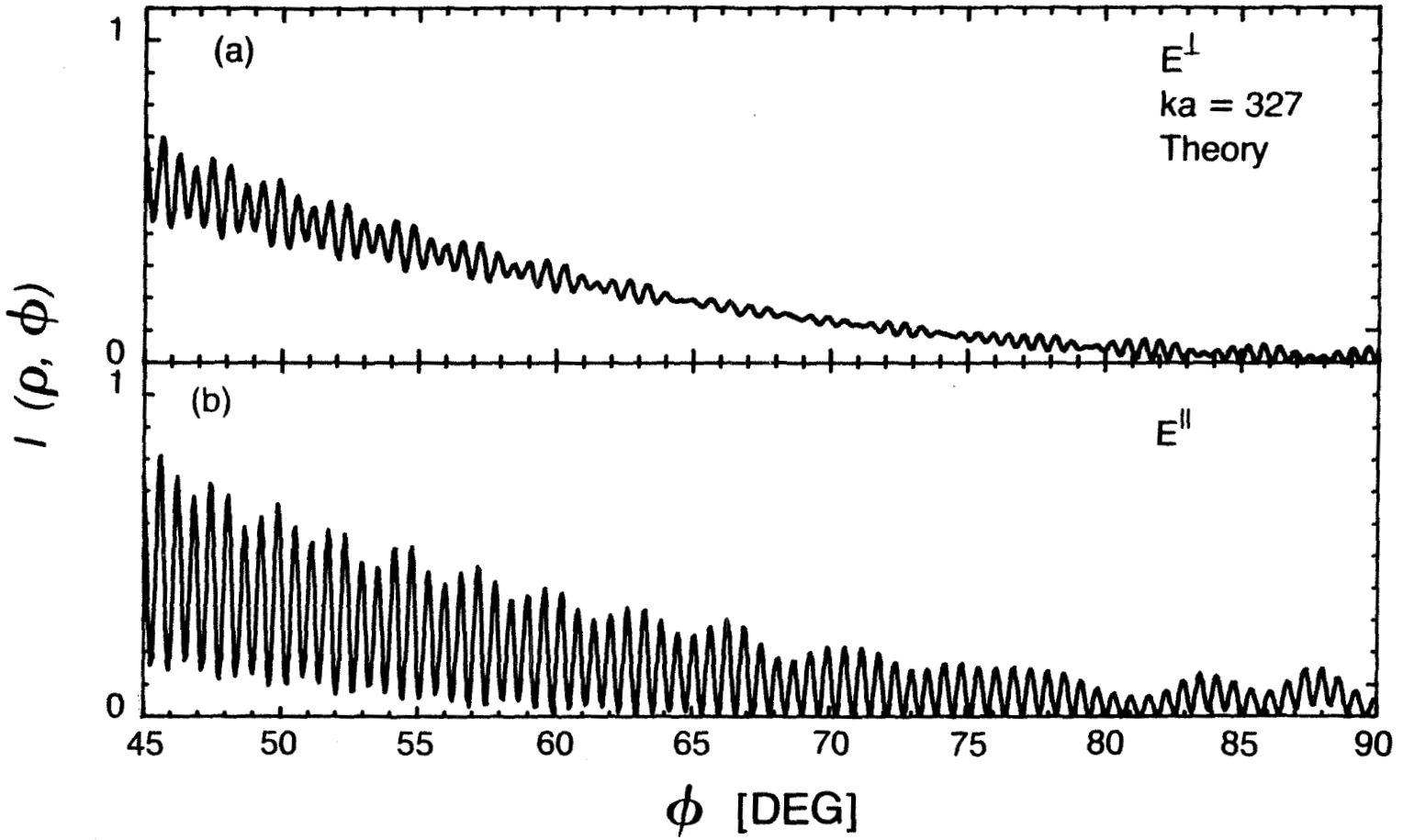

Fig. 6.9 The scattered intensity pattern for a dielectric cylinder with ka = 327 plotted from the exact solution formulas; (continued on next page).

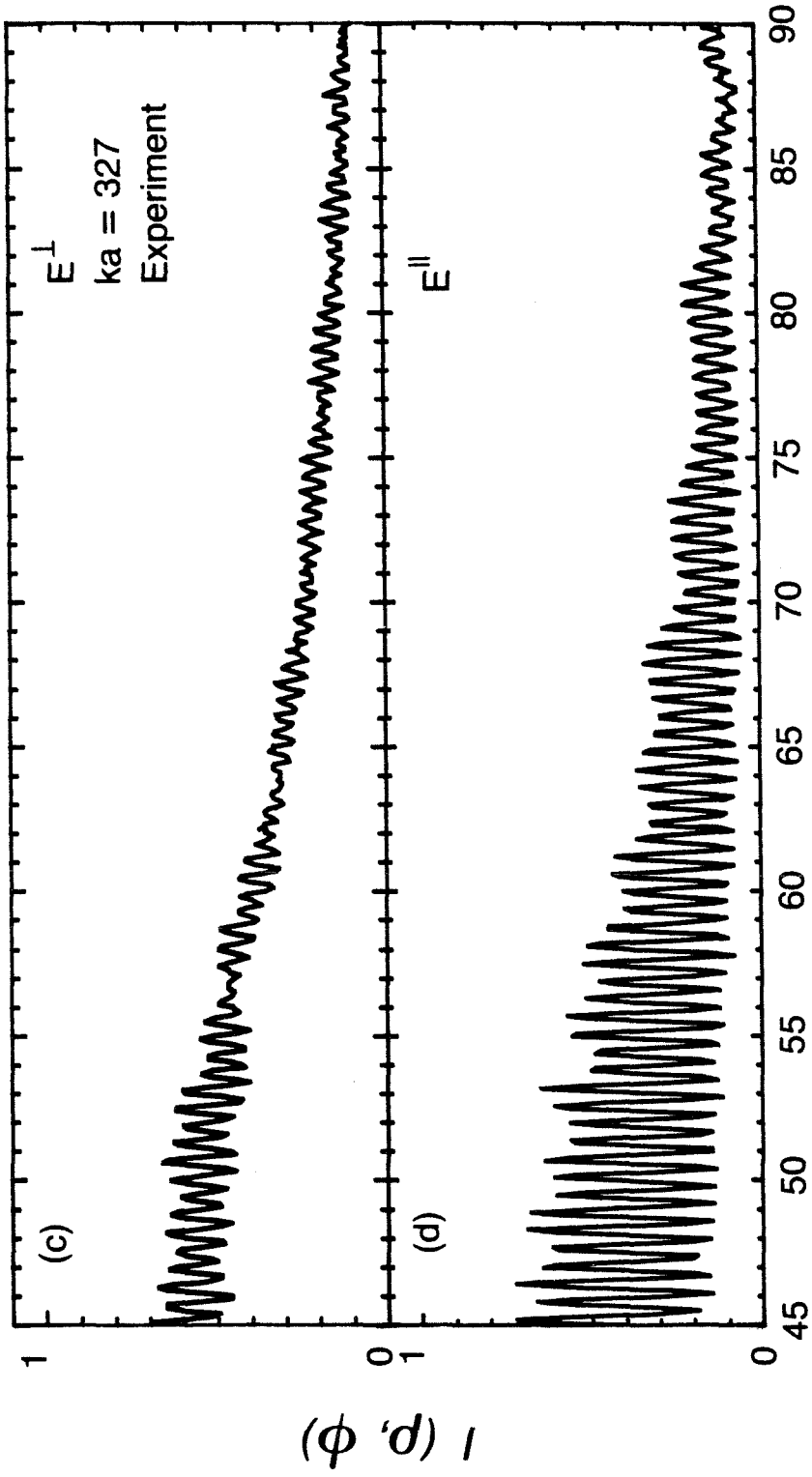

Fig. 6.9 Continued. (c) and (d) the scattered intensity pattern for a dielectric cylinder with ka = 327, measured using the photodiode system.

amplitude is modulated with a quite low frequency function, the notches of the modulating signal can be seen, e.g., at $\phi = 61°$, $67°$, $70°$, . . . So there are a few notable differences between the two different polarizations.

The experimental intensity pattern for a very large dielectric circular cylinder (ka = 945) is plotted for the two different polarizations in Figs. 6.10(a) and (b). There are 247 sidelobes in the range $0° \leqq \phi \leqq 60°$ for both polarizations. In the range shown ($60° \leqq \phi \leqq 90°$), the intensity pattern for $E^{//}$ has 139 sidelobes, while the intensity pattern for $E^{\perp}$ has 157 sidelobes. Also the fringe contrast for $E^{//}$ is much larger than those for $E^{\perp}$, e.g. contrast at $\phi = 60°$ is almost three times larger for the $E^{//}$ pattern than that for $E^{\perp}$.

The discussions in the previous sections show that the scattered intensity pattern depend on the material of the cylinder, the polarization of the incident field, and the factor ka. The scattered intensity pattern in all circumstances has a main lobe and a number of sidelobes, and the width of the main lobe and the spacing between the sidelobes both are inversely proportional to the factor ka. The dielectric cylinder has sidelobes over all ϕ, while the conducting cylinder has sidelobes only in limited range of ϕ which decreases with increasing of ka. The sidelobes of the intensity pattern have spacings which decrease with increasing ϕ to a minimum around $\phi \cong 60°$, while the spacings of the sidelobes of the conducting cylinder have constant values as function of ϕ. The intensity pattern of the dielectric cylinder has the same number of sidelobes in

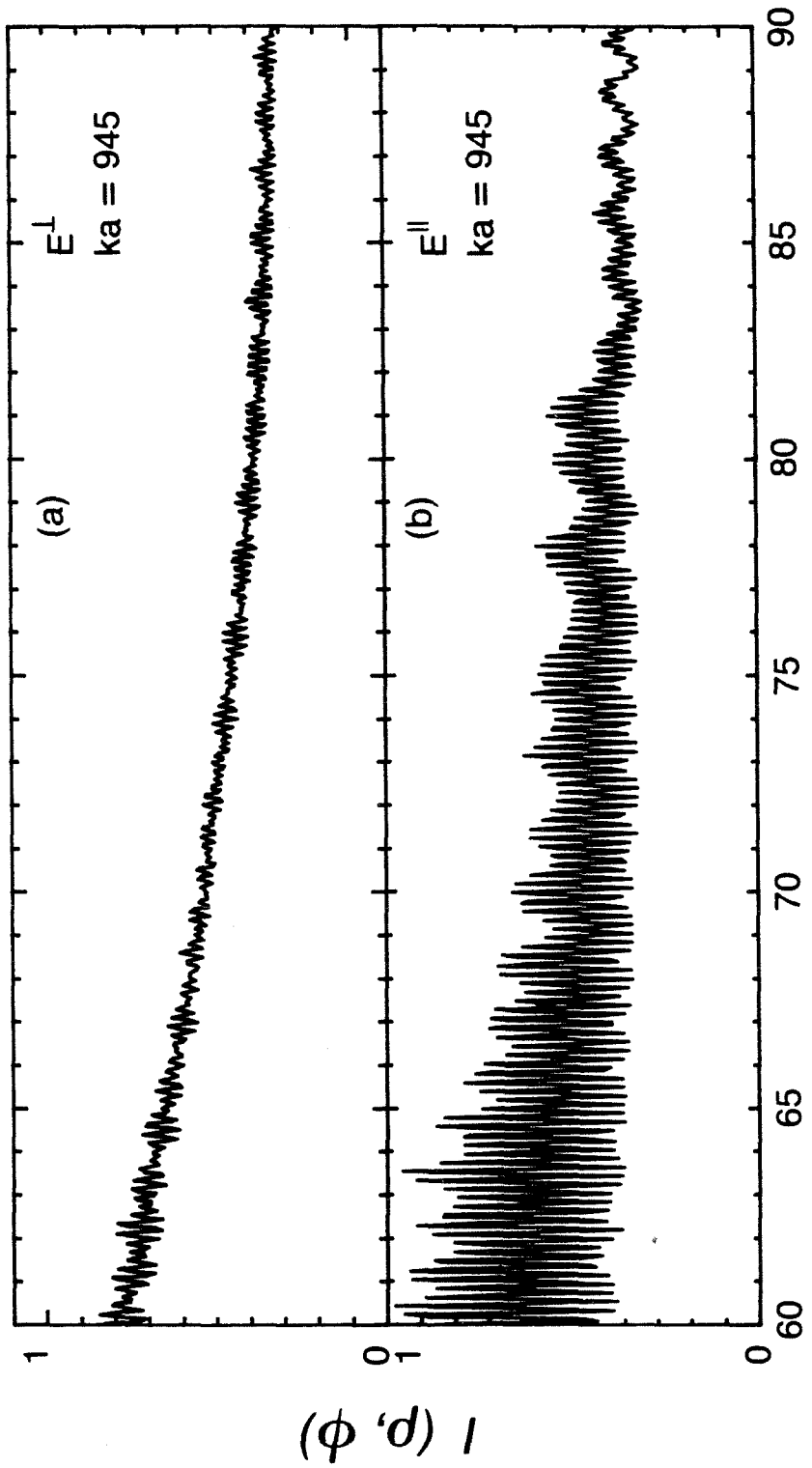

Fig. 6.10 The intensity pattern for a dielectric cylinder with ka = 945, measured using the photodiode system.

the range $0 \leqq \phi \lesssim 60°$ for both polarizations of the scattered field, while for the normal polarization case the number of sidelobes are larger in the range $60 \lesssim \phi \lesssim 90°$ than those for the parallel polarization case. On the other hand the fringe contrast is much larger for the parallel polarization case than that for the normal polarization case. For the conducting cylinder the sidelobes extend over a larger range of ϕ for the normal polarization case than that for the parallel polarization case.

CHAPTER VII

SUMMARY AND CONCLUSIONS

In summary we have studied the rigorous solutions of the scattered field from cylinders in order to develop a better understanding of the detailed characteristics of this scattering and the effects of the different parameters of the cylinder, the polarization of the incident field and the change in the wavelength of the illuminating wave.

In this thesis we also consider approximate methods of solution. Workers in modern optics use the simpler methods of ray optics and Fourier optics; these techniques lead to direct results, although of course they are approximate. In our research, we developed an adequate approximate solution for dielectric and conducting cylinders, after first showing that the zero-order Fourier optics solution is not very good. Our approximate solution is shown to be in good accord with the exact calculations with regard to forward scattering amplitudes and fringe spacings.

The scattered field from a conducting cylinder when the incident field is linearly polarized parallel to the axis of the cylinder is given by Eq. (2.34). The scattered field patterns are plotted in Fig. 2.3 for the parallel polarization case. When the incident field is polarized normal to the axis of the cylinder the scattered field is given by Eq. (2.42) and it is plotted in Fig. 2.5. The surface

current density is given by Eqs. (2.46) and (2.48) for the parallel and normal polarizations, respectively. The surface current density is plotted in Figs. 2.6 and 2.7. The fringe spacings of the scattered field are plotted in Fig. 2.8, and it is found that their value decreases with the increase of ka. The scattering angle at which the fringes terminate is smaller for the parallel polarization case than for the normal polarization case, and it also decreases by the increase of ka as it can be seen in Fig. 2.9.

In Chapter III the field scattered by a dielectric cylinder with the incident field polarized parallel and normal to the axis of the cylinder is given by Eqs. (3.14) and (3.25), respectively. In Fig. 3.2 the scattered field pattern is plotted for the case when the incident field is linearly polarized parallel to the axis of the cylinder, while it is plotted in Fig. 3.3 for the normal polarization case. The dependence of the scattered pattern on the refractive-index of the cylinder is demonstrated on Fig. 3.5. It is shown in Figs. 3.6 and 3.7 that the position of the peak of the backscattered field depends mainly on the refractive-index of the cylinder. A comparison between the scattered field patterns of the conducting and dielectric cylinders is given in Section 3.5 and Table 3.1.

In Chapter IV approximate solutions for the conducting cylinder are given by Eqs. (4.5) and (4.16). The scattered field pattern is plotted in Fig. 4.4. The approximate solution for the field scattered by a dielectric cylinder is given by Eq. (4.28) and it is plotted in Fig. 4.7. An approximate solution for the fringe spacings

of the dielectric cylinder is given by Eqs. (4.37) to (4.39) and is plotted in Figs. 4.9 and 4.10.

In Chapter V the fine structure of the scattering from dielectric cylinders is studied and a plot for the intensity at $\phi = 0°$ as a function of the wavelength is given in Fig. 5.1. The intensity patterns for a 5 different wavelengths at-resonance and off-resonance at the peak and the trough of the resonance curve are plotted in Figs. 5.2 to 5.5. The effects of the resonances on the shape of the patterns are discussed.

In Chapter VI photographs of the scattered intensity patterns for conducting and dielectric cylinders are shown in Figs. 6.1(a) and (b), respectively. The two different systems used in the experiments are shown in Figs. 6.2 and 6.3 and a comparison between them is given in Table 6.1. The intensity patterns for conducting and dielectric cylinders measured experimentally are plotted in Figs. 6.5 to 6.7. A comparison between the scattered patterns for the different polarizations of the incident field is shown in Figs. 6.8 to 6.10. In all the plots in Chapter VI the theoretical curves are plotted with the experimental ones to show their agreement.

APPENDIX A

NUMBER OF TERMS OF THE SERIES NEEDED FOR THE SUMMATION

In the preceding chapters we have found that the solutions for the scattered field from a circular cylinder are represented by an infinite series. To plot these fields we can sum only a finite number of terms, so it is important to know how many terms (approximately) of the series are needed to get an accurate value for the series. It has been mentioned by King and Wu[1] that the number of terms needed are around the value of ka. In this appendix an analytical derivation of the approximate number of terms of the series needed to get an accurate result for both conducting and dielectric cylinders are presented.

A.1 Conducting cylinders

To get an accurate value for the summation of the series, we need to sum enough terms until the coefficient of the series becomes negligible. The coefficient of the series in Eq. (2.36) is

$$C_m = \frac{J_m(ka)}{H_m^{(1)}(ka)} H_m(k\rho) \quad . \tag{A1}$$

The asymptotic expansions for the Bessel and Hankel functions for large values of m are given by[2]

$$J_m(ka) \sim \frac{1}{\sqrt{2\pi m}} \left(\frac{e}{2} \frac{ka}{m}\right)^m, \tag{A2}$$

and

$$H_m^{(1)} \sim \frac{1}{\sqrt{2\pi m}} \left(\frac{e}{2} \frac{ka}{m}\right)^m \left[1 - 2i \left(\frac{e}{2} \frac{ka}{m}\right)^{-2m}\right]. \tag{A3}$$

The Hankel function with argument $k\rho$, which is very large, will be given by the following asymptotic expansion[2]

$$H_m^{(1)}(k\rho) \sim \frac{2}{\rho k \rho} e^{i(k\rho - m\rho/2 - \rho/4)}. \tag{A4}$$

By substituting Eqs. (A2) to (A4) into Eq. (A1) we get the following

$$C_m \sim \frac{1}{1 - 2i \left(\frac{e}{2} \frac{ka}{m}\right)^{-2m}} \sqrt{\frac{2}{\pi k \rho}} e^{i(k\rho - m\pi/2 - \pi/4)},$$

$$|C_m| \sim \frac{1}{\sqrt{1 - 4 \left(\frac{e}{2} \frac{ka}{m}\right)^{-4m}}} \sqrt{\frac{2}{\rho k \rho}} \tag{A5}$$

$$= \sqrt{\frac{2}{k\pi\rho}} \frac{1}{\sqrt{1 - 4 \left(\frac{2}{e} \frac{m}{ka}\right)^{4m}}},$$

therefore $|C_m|$ will have a negligible value when

$$\left(\frac{2}{e} \frac{m}{ka}\right) > 1 \tag{A6}$$

which will lead to

$$m > \frac{e}{2} ka. \tag{A7}$$

From (A7) we can see that the number of terms necessary to give an accurate result of the sum of the series is slightly larger than the value of ka, which has been shown from the plots of the Log of the coefficient in Chapter II. And it will take the same value also for the normal polarization case.

A.2 Dielectric Cylinders

From Chapter III we can write the coefficient of the series as it is given by Eq. (3.10)

$$a_m = -(i)^m \frac{N}{D} \tag{A8}$$

where

$$N = n\, J_m(x)\dot{J}_m(y) - \dot{J}_m(x)J_m(y), \tag{A9}$$

$$D = n\, \dot{J}_m(y)\, H_m^{(1)}(x) - J_m(y)\dot{H}_m^{(1)}(x), \tag{A10}$$

and

$$x = ka,\ y = nka.$$

Substituting in Eqs. (A9) and (A10) from Eqs. (A2) and (A3) for the asymptotic expansions of the Bessel and Hankel functions for a large order m, we get

$$N \sim n \frac{1}{\sqrt{2\pi m}} \left(\frac{ex}{2m}\right)^m \left[\frac{m}{y} \frac{1}{\sqrt{2\pi m}} \left(\frac{ey}{2m}\right)^m - \frac{1}{\sqrt{2\pi(m+1)}} \left(\frac{ey}{2m+2}\right)^{m+1}\right]$$

$$- \left[\frac{m}{x} \frac{1}{\sqrt{x\pi m}} \left(\frac{ex}{2m}\right)^m - \frac{1}{\sqrt{2\pi(m+1)}} \left(\frac{ex}{2m+2}\right)^{m+1}\right] \frac{1}{\sqrt{2\pi m}} \left(\frac{ey}{2m}\right)^m$$

$$= \frac{1}{2\pi m} \left(\frac{ex}{2m}\right)^m \left(\frac{ey}{2m}\right)^m \left\{n\left[\frac{m}{y} - \sqrt{\frac{m}{m+1}} \left(\frac{ey}{2m+2}\right)^{m+1} \left(\frac{2m}{ey}\right)^m\right]\right.$$

$$\left. - \left[\frac{m}{x} - \sqrt{\frac{m}{m+1}} \left(\frac{ex}{2m+2}\right)^{m+1} \left(\frac{2m}{ex}\right)^m\right]\right\} .$$

Hence;

$$N \sim \frac{1}{2\pi m} \left(\frac{ex}{2m}\right)^m \left(\frac{ey}{2m}\right)^m \left\{n\left[\frac{m}{y} - \frac{ey}{2m} \left(\frac{m}{m+1}\right)^{m+3/2}\right] - \left[\frac{m}{x} - \frac{ex}{2m} \left(\frac{m}{m+1}\right)^{m+3/2}\right]\right\}. \tag{A11}$$

$$D \sim \frac{n}{\sqrt{2\pi m}} \left(\frac{ex}{2m}\right)^m \left[\frac{m}{y} \frac{1}{\sqrt{2\pi m}} \left(\frac{ey}{2m}\right)^m - \frac{1}{\sqrt{2\pi(m+1)}} \left(\frac{ey}{2m+2}\right)^{m+1}\right]$$

$$\times \left[1 - i2 \left(\frac{ex}{2m}\right)^{-2m}\right] - \frac{1}{\sqrt{2\pi m}} \left(\frac{ey}{2m}\right)^m \left\{\frac{m}{x} \frac{1}{\sqrt{2\pi m}} \left(\frac{ex}{2m}\right)^m\right.$$

$$\left. \times \left[1 - 2i \left(\frac{ex}{2m}\right)^{-2m}\right] - \frac{1}{\sqrt{2\pi(m+1)}} \left(\frac{ex}{2m+2}\right)^{m+1} \left[1 - 2i \left(\frac{ex}{2m+2}\right)^{-2m-2}\right]\right\},$$

$$D \gtrsim \frac{1}{2\pi m} \left(\frac{ex}{2m}\right) \left(\frac{ey}{2m}\right)^m \left\{n\left[\frac{m}{y} - \frac{ey}{2m} \left(\frac{m}{m+1}\right)^{m+3/2}\right]\right.$$

$$\left. - \frac{m}{x} - \frac{ex}{2m} \left(\frac{m}{m+1}\right)^{m+3/2}\right\} \left[1 - 2i \left(\frac{2m}{ex}\right)^{2m}\right]. \tag{A13}$$

From Eqs. (A11) and (A13) we can get

$$\frac{N}{D} < \frac{1}{1 - 2i \left(\frac{2m}{ex}\right)^{2m}} \quad ,$$

$$\text{then} \qquad |a_m| < \frac{1}{\sqrt{1 - 4 \left(2m/ex\right)^{4m}}} \quad . \tag{A14}$$

From Eq. (A14) the amplitude of the coefficient $|a_m|$ will have a negligible value when

$$\frac{2m}{ex} > 1 \ ,$$

i.e., when $m > \frac{e}{2} ka$. (A15)

So if m is slightly larger than ka, the summation of the series will give an accurate value for the field. From Eqs. (A7) and (A15), the same number of terms needs to be summed for both kinds of cylinders.

APPENDIX A

REFERENCES

1. R.W.P. King, and T.T. Wu, The Scattering and Diffraction of Waves (Harvard University Press, Cambridge, 1959).

2. M. Abramowitz, and I.A. Stegun, Handbook of Mathematical Functions (National Bureau of Standards, Washington D.C., 1972).

APPENDIX B

MEASUREMENT OF OPTICAL FIBER DIAMETER USING

THE FAST FOURIER TRANSFORM

Measurement of optical fiber diameter using the fast Fourier transform

Mustafa A. G. Abushagur and Nicholas George

The variation of the fringe spacing of the far zone scattered intensity of an illuminated optical fiber has been plotted vs the scattering angle, theoretically and experimentally. A method for measuring fiber diameters by taking the Fourier transform of the scattering intensity is described. Theoretical and experimental results have been compared at various angles for different fiber diameters.

I. Introduction

The scattering of electromagnetic waves by dielectric and conducting cylinders has been treated by several authors[1-4] and summarized by Kerker[5] and Bowman *et al.*[6] Interest in fiber optics has led to the study of methods for making remote measurements of fiber parameters. Presby presented a method for measuring fiber diameter from the backscattered intensity.[7] Watkins described diameter measurements that consisted of counting the number of fringes in a certain range of the scattering angle in the forward scattering field.[8]

In this paper we report some careful measurements of the variation in fringe spacing as a function of the cylindrical angle. An optimum angle for the remotely sensing fiber diameter is established, and we describe a fast Fourier transform (FFT) processing method that efficiently senses fiber diameter and minimizes the effect of diode-to-diode random noise.

When the optical fiber is illuminated with a monochromatic plane wave, energy is scattered all around the fiber. The scattering intensity displays the fringe pattern shown in Fig. 1. An approximate theory for the forwardscatter case has been published.[9] The number of fringes N between scattering angles ϕ_1 and ϕ_2 is

$$N = \frac{2a}{\lambda}\left(\left|\sin(\phi_2/2) + [n^2 + 1 - 2n\cos(\phi_2/2)]^{1/2}\right| - \left|\sin(\phi_1/2) + [n^2 + 1 - 2n\cos(\phi_1/2)]^{1/2}\right|\right), \quad (1)$$

where a = radius of the optical fiber,
λ = wavelength of the electromagnetic wave, and
n = index of refraction of the fiber.

Fringe spacing $\Delta\phi$ between two adjacent fringes can be found by substituting $N = 1$ into Eq. (1), letting $\phi_2 = \phi_1 + \Delta\phi$ and solving for $\Delta\phi$ using well-known trigonometric approximations for small $\Delta\phi$. The resulting equation for the fringe spacing of the scattered intensity as a function of angle is given by

$$\Delta\phi = \frac{\lambda}{a}\left\{\left[1 - \frac{2n}{1+n^2}\cos(\phi/2)\right]^{1/2} \Big/ \left\{\cos(\phi/2)\left[1 - \frac{2n}{1+n^2}\cos(\phi/2)\right]^{1/2} + \frac{n}{(1+n^2)^{1/2}}\sin(\phi/2)\right\}\right\}. \quad (2)$$

To study the dependence of $\Delta\phi$ on ϕ, Eq. (2) is plotted in Fig. 2. Notice that the fringe spacing decreases as scattering angle ϕ increases, reaching a minimum at $\sim 60°$ (for $n = 1.457$).

The expression for $\Delta\phi$ is valid for scattering angle $0 < \phi \leq \phi_F$, where ϕ_F is given by[8] $\phi_F = 2\cos^{-1}(1/n)$, but at larger angles, $\phi > \phi_F$, there is no refracted ray.

Detailed comparison of the approximate theory with the exact expression for $\Delta\phi$ is beyond the scope of this paper. From Eq. (2) it is seen that $\Delta\phi$ is inversely proportional to the radius of the fiber; thus the remote method for measuring the diameter is feasible.

II. Experiment

In the experiment a He–Ne laser is used to illuminate the optical fiber. The scattered intensity is detected in the far zone using a photodiode array of 1024 elements manufactured by Reticon Corporation. The far-zone intensity is coupled into a PDP 11/34 for processing. Simply reading null-to-null spacing on the

The authors are with University of Rochester, Institute of Optics, Rochester, New York 14627.

Received 26 November 1979.
0003-6935/80/122031-03$00.50/0.

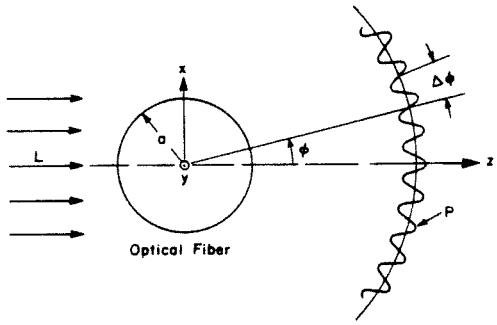

Fig. 1. Schematic diagram of experimental setup: L, monochromatic EM plane wave; P, far zone scattered pattern.

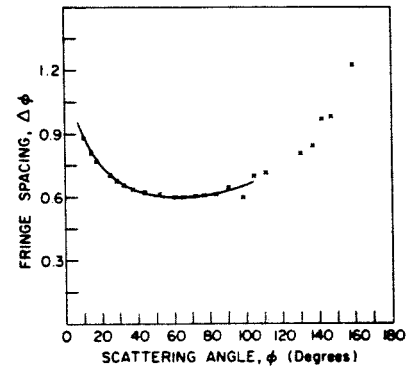

Fig. 2. Fringe spacing variations. Continuous curve, Eq. (2). ×—experimental data for 66.7-μm fiber diam.

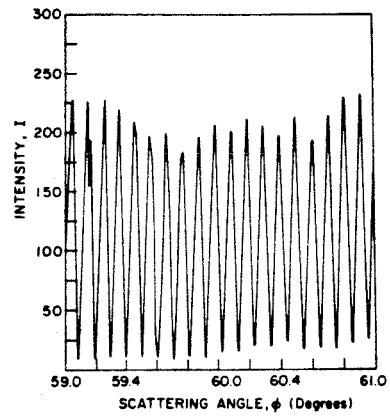

Fig. 3. Far zone scattered intensity plotted vs scattering angle.

pattern (as shown in Fig. 3) is not an efficient process, especially if diode noise is a limiting factor.

Since the detected intensity is in the far zone, the scattered field is roughly the Fourier transform of the field at the fiber. The angle factors and the nonplanar nature of the scatterer prevent this from being a precise relationship. Nevertheless, as in other remote sensing problems, it does give a rationale for using a FFT. Noting that the recorded intensity is approximately a sinusoid in the presence of noise, it follows that an efficient filter is a bandpass adjustable to the anticipated frequency. Reading the frequency of fringe spacing is greatly simplified if one uses the FFT of the recorded intensity as shown in Fig. 4.

Denote the intensity in the far zone by $I(f)$ in which f is given by

$$f = x/\lambda z = \tan(\phi)/\lambda. \tag{3}$$

Let $E(x_N)$ be the FFT of the intensity, i.e.,

$$\text{FFT}|I[\tan(\phi)/\lambda]| = E(x_N), \tag{4}$$

where $x_N = N\lambda/[\tan(\phi + \phi_0) - \tan\phi]$,
N = number of data points used in the FFT process, and
ϕ_0 = angle subtended at the fiber by an array of length d and distance R from the fiber. ϕ_0 is given by $\phi_0 = 2\tan^{-1}d/2R$.

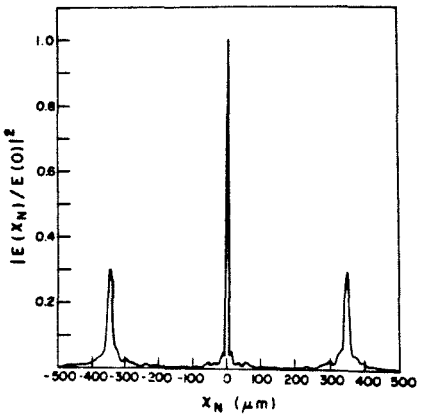

Fig. 4. Normalized FFT$|E(x_N)/E(0)|^2$ plotted vs x_N.

In Fig. 4 $|E(x_N)/E(0)|^2$ is plotted vs x_N, and the curve consists of three spikes: the middle is the dc component, and the other two spikes give the fundamental frequency of the scattering intensity. If we model the intensity as

$$I(f) = \sin^2(Kf), \tag{5}$$

where K is the local radian frequency of the intensity. One can readily show that $K = \pi\lambda \cos(\phi) \cos(\phi + \Delta\phi)/\sin \Delta\phi$, where $\Delta\phi$ is given by Eq. (2). Then by taking the Fourier transform of $I(f)$, we find the following expression for spacing D_c between the outer two spikes:

$$D_c = \frac{2K}{\pi} \simeq \frac{2\lambda \cos^2\phi}{\Delta\phi}. \tag{6}$$

Hence, D_c depends upon fringe spacing $\Delta\phi$ and implicitly the diameter of the fiber ($2a$). Substituting Eq. (6) for $\Delta\phi$ into Eq. (2) and solving for the diameter ($2a$) yield the following result:

$$2a = D_c \left\{\left[1 - \frac{2n}{1+n^2}\cos(\phi/2)\right]^{1/2} \Big/ \left\{\cos^2\phi \times \left\{\cos(\phi/2)\left[1 - \frac{2n}{1+n^2}\cos(\phi/2)\right]^{1/2} + \frac{n}{(1+n^2)^{1/2}}\sin(\phi/2)\right\}\right\}\right\}. \tag{7}$$

So by measuring D_c at a known angle ϕ, we can compute the diameter of the fiber. This method has been used to determine the diameter of two different fibers, namely, 66.7 and 400 μm. Measurements have been made over a wide range of angles from 15° to 75°. Better results are obtained for ϕ in the range of 25° to 40°. A consistency of 0.6% is obtained in these measurements using the FFT method.

In making the determination of fiber diameter from the FFT of the diffracted intensity, one needs $2N \log_2 N$ operations on a digital computer for N data points.[10] For the 1024 array used, this is 20480 operations. In our research experiments, we used an IBM 3032 that required 1.1 μsec/operation. Hence, the FFT is computed in ~23 msec. However, one may be much more interested in a stand-alone system. With special purpose chips such as Reticon's R5601, one can obtain an FFT in times of the order of 5 msec without difficulty.

Thus, it is possible to measure the fiber diameter in line while pulling it out of the furnace. The method requires only low light levels since the detection of the almost periodic fringe pattern, first transforming, gives in effect a very narrowband filter for measuring the diameter.

This research was supported in part by the U. S. Air Force Office of Scientific Research.

References

1. H. C. van de Hulst, *Light Scattering by Small Particles* (Wiley, New York, 1957), Chap. 15.
2. M. Kerker and E. Matijevic, J. Opt. Soc. Am. **51**, 506 (1961).
3. D. Marcuse and H. M. Presby, J. Opt. Soc. Am. **65**, 367 (1975).
4. C. H. Papas, J. Appl. Phys. **21**, 318 (1950).
5. M. Kerker, *The Scattering of Light and Other Electromagnetic Radiation* (Academic, New York, 1969), Chap. 6.
6. J. J. Bowman, T. B. A. Senior, and P. L. E. Uslenghi, *Electromagnetic and Acoustic Scattering by Simple Shapes* (North-Holland, Amsterdam, 1969).
7. H. M. Presby, J. Opt. Soc. Am. **64**, 280 (1974).
8. D. H. Smithgal, L. S. Watkins, and R. E. Frazee, Jr., Appl. Opt. **16**, 2395 (1977).
9. L. S. Watkins, J. Opt. Soc. Am. **64**, 767 (1974).
10. W. T. Cochran *et al.*, IEEE Trans. Audio Electroacoust. **AU-15**, 45 (1967).

APPENDIX C

CONVERSION OF THE DENSITY TO INTENSITY DATA

In this appendix we show the H-D curve of the film as it is measured experimentally, and how it was curve fitted to enable us to convert the density data, collected on the film from the scattered intensity pattern, back to intensity data. The film used in the experiments is a Kodak Panatomic-X film. This film was chosen because it has an extremely fine grain which gives a very high resolution, and it has a moderate value of γ which allows us to record the very large diversity of the intensity which exists in the scattered pattern.

The H-D curve of the film is measured experimentally using the He-Ne laser light for exposing it, using the exposure time used in collecting the intensity data, and developing it following the same procedure followed in developing the film used to collect data, to minimize the effect of the nonlinearities of the film. These depend primarily on: exposure time, the wavelength of light, the kind of developer, and the development time. In developing the film we followed the following procedure:

1. Develop in Microdol X for 5 minutes at 70°F.
2. Stop the process by a Kodak Stop Bath for 30 seconds.
3. Fix using Kodak Rapid Fix for 2 minutes.
4. Clean in running water for about 10 minutes.

To plot the characteristic curve of the film, the film is exposed using a uniform plane wave of laser light; and by changing the neutral density filters we can change the intensity of the field exposing the film. Then the density recorded on the film is measured by the microdensitometer. The characteristic curve of the film as it was measured using the previous method is plotted in Fig. C.1.

To use this curve to convert density data recorded on this kind of film to intensity data, we need to fit this H-D curve with a polynomial which will allow us to substitute density data in it to get intensity data corresponding to the given density values.

The density can be represented using the following expression

$$D = D_S + \gamma \log \left(\frac{\varepsilon}{\varepsilon_1} + 1\right) - \gamma \log \left(\frac{\varepsilon}{\varepsilon_2} + 1\right) \quad , \qquad (C.1)$$

where D = density of the film

ε = exposure corresponding to D

and ε_1, γ and ε_2 are as defined in Fig. C.1, where we fitted the H-D curve by a straight line as a first approximation.

From Eq. (C.1) we can write

$$D = D_S + \gamma \log \left[\left(\frac{\varepsilon + \varepsilon_1}{\varepsilon + \varepsilon_2}\right) \left(\frac{\varepsilon_2}{\varepsilon_1}\right)\right],$$

$$D = D_S + \log \left[\left(\frac{\varepsilon_2}{\varepsilon_1}\right)^{\gamma} \left(\frac{\varepsilon + \varepsilon_1}{\varepsilon + \varepsilon_2}\right)^{\gamma}\right] \quad .$$

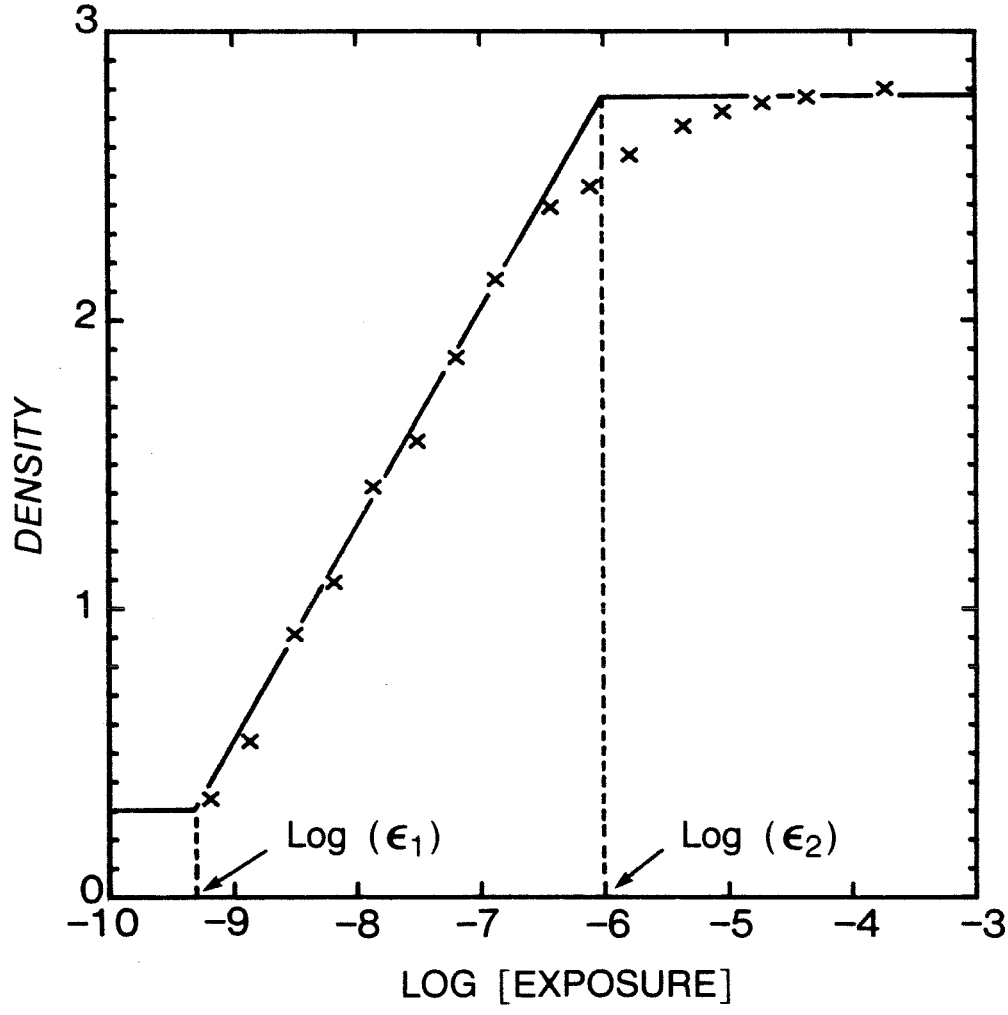

Fig. C.1 The characteristic curve of the Panatomic-X film used in the experiments.

Then

$$10^{D-D_S} = \left(\frac{\varepsilon_2}{\varepsilon_1}\right)^{\gamma} \left(\frac{\varepsilon + \varepsilon_1}{\varepsilon + \varepsilon_2}\right)^{\gamma} \quad . \tag{C.2}$$

Now let

$$B = 10^{D-D_S} \quad ,$$

and

$$A = \left(\frac{\varepsilon_2}{\varepsilon_1}\right)^{\gamma} \quad .$$

Therefore,

$$B = A \left(\frac{\varepsilon + \varepsilon_1}{\varepsilon + \varepsilon_2}\right)^{\gamma} + C \tag{C.3}$$

where C is a correction factor, then

$$\left(\frac{B}{A} - C\right)^{1/\gamma} = \frac{\varepsilon + \varepsilon_1}{\varepsilon + \varepsilon_2} \quad .$$

Let

$$\alpha = \left(\frac{B}{A} - C\right)^{1/\gamma},$$

then

$$\varepsilon = \frac{\alpha\varepsilon_2 - \varepsilon_1}{1 - \alpha} \quad , \tag{C.5}$$

$$\text{where } \alpha = \left(\frac{10^{D-D_S}}{(\varepsilon_2 - \varepsilon_1)^{\gamma}} - C\right)^{\gamma}, \tag{C.6}$$

ε = exposure = It,

I = intensity,

and t = exposure time.

So from Eq. (C.5) we can determine the exposure by knowing the density and ε_1, ε_2 and α of the film. To demonstrate this, Eq. (C.5) is plotted in Fig. C.2 as the solid line, and the experimental data plotted in Fig. C.1 are replotted here again showing that Eq. (C.5) gave a very good fit for most of the range of the characteristic curve. So it will be used to convert density to intensity data in the experiments done.

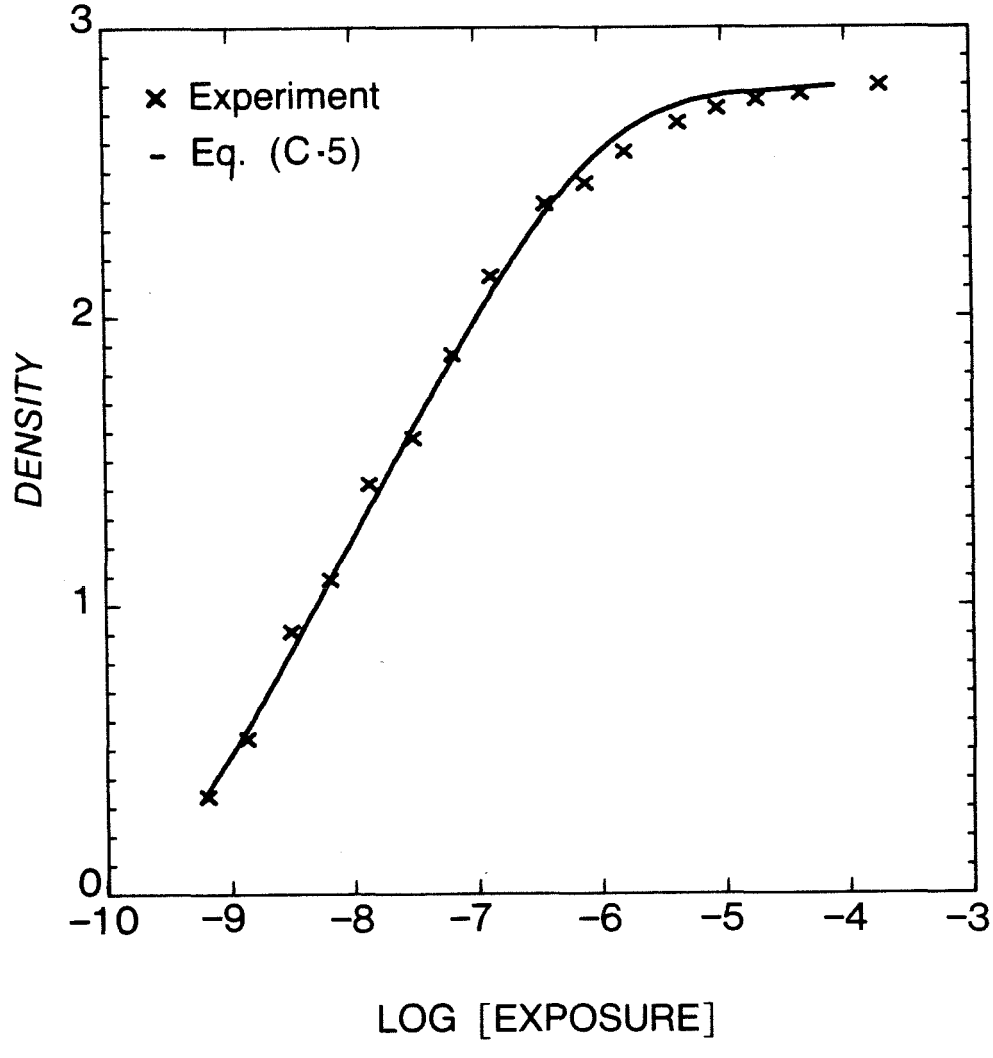

Fig. C.2 The characteristic curve of the film plotted using the curve fitting Eq. (C.5) and the experimental data.

APPENDIX D

PLOTS OF THE INTENSITY PATTERNS FROM EXPERIMENTAL DATA

In Chapter VI we presented the experimental results obtained for the scattered intensity patterns from dielectric and conducting cylinders. The results are obtained for the two different polarizations of the incident field parallel and normal to the axis of the cylinder. In Chapter VI we presented only portions of the scattered intensity patterns to demonstrate the experimental results and to compare them with the theory. In this appendix we present the rest of the scattered intensity patterns in all the range of the angle ϕ. The results presented here are obtained using both experimental methods discussed in Chapter VI. In each figure in this appendix there are three different curves (except for dielectric cylinders with ka = 945): (a) is a plot of the intensity pattern obtained using film/microdensitometer combination system following the same procedure outlined in Chapter VI, (b) is a plot of the intensity pattern using the photodetector system, and (c) is a plot of the comparable theoretical results derived in either Chapter II or III.

Intensity Patterns of the Conducting Cylinder

In Figs. D.1 to D.6 show the scattered intensity patterns from conducting cylinders with ka = 327 plotted as a function of the angle ϕ. In Figs. D.1 to D.3 the polarization of the incident field is parallel to the axis of symetry of the cylinder. In Figs. D.4 to D.6 the polarization of the incident field is normal to the axis of symmetry of the cylinder. In Fig. D.1 the intensity pattern is plotted for $0° \leq \phi \leq 45°$. The pattern has main lobe and a number of side lobes. The three different patterns have the same features. The number of fringes are the same and they terminate at $\phi \cong 30°$. The amplitude of the side-lobes are quite the same. The intensity pattern plotted using the film/microdensitometer system has larger amplitude in the range $15° \lesssim \phi \lesssim 45°$ and that is due to the non-linearity of the photographic film. In Figs. D.2 and D.3 the pattern does not have any structure. The small ripples which might be seen in the experimental data curve are mainly due to the noise in the background. In Fig. D.4 the scattered intensity pattern is plotted for the case when the incident wave is polarized normal to the axis of the cylinder. The pattern plotted using the experimental data is very comparable to the theoretical plot. The curves have comparable amplitudes of the side lobes and the spacings of the fringes. In Fig. D.5 the patterns still have fringes till $\phi \cong 80°$. In Fig. D.6 the theoretical curve does not have any structure while the experimental curves have ripples which are mainly generated because of the noise, and the speckle pattern produced by the surface of the cylinder which might not be perfectly smooth. So in all the results shown

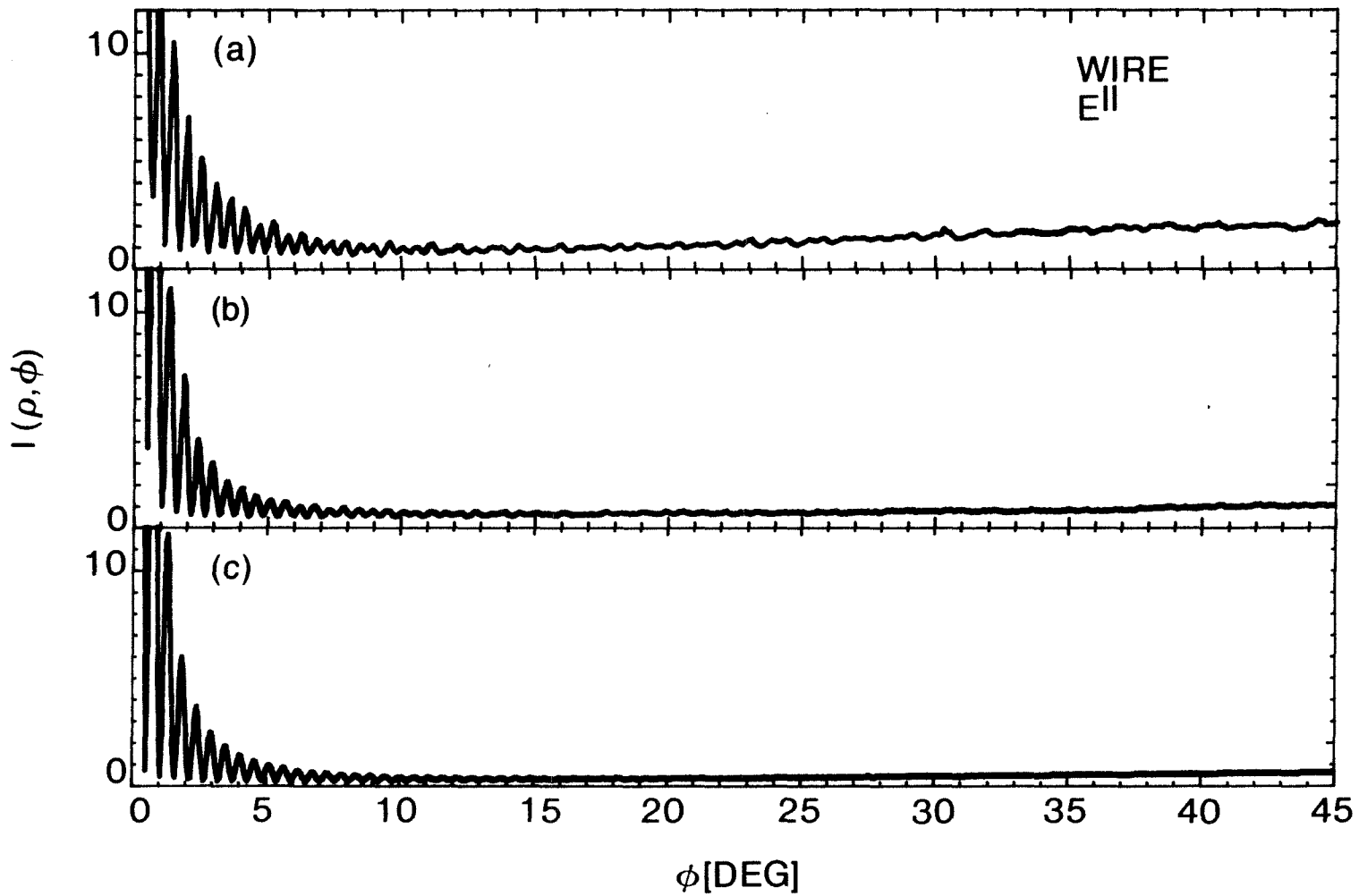

Fig. D.1 The scattered intensity pattern plotted for a conducting cylinder with ka = 327 using (a) film/microdensitometer system, (b) photodetector system and (c) Eq. (2.34).

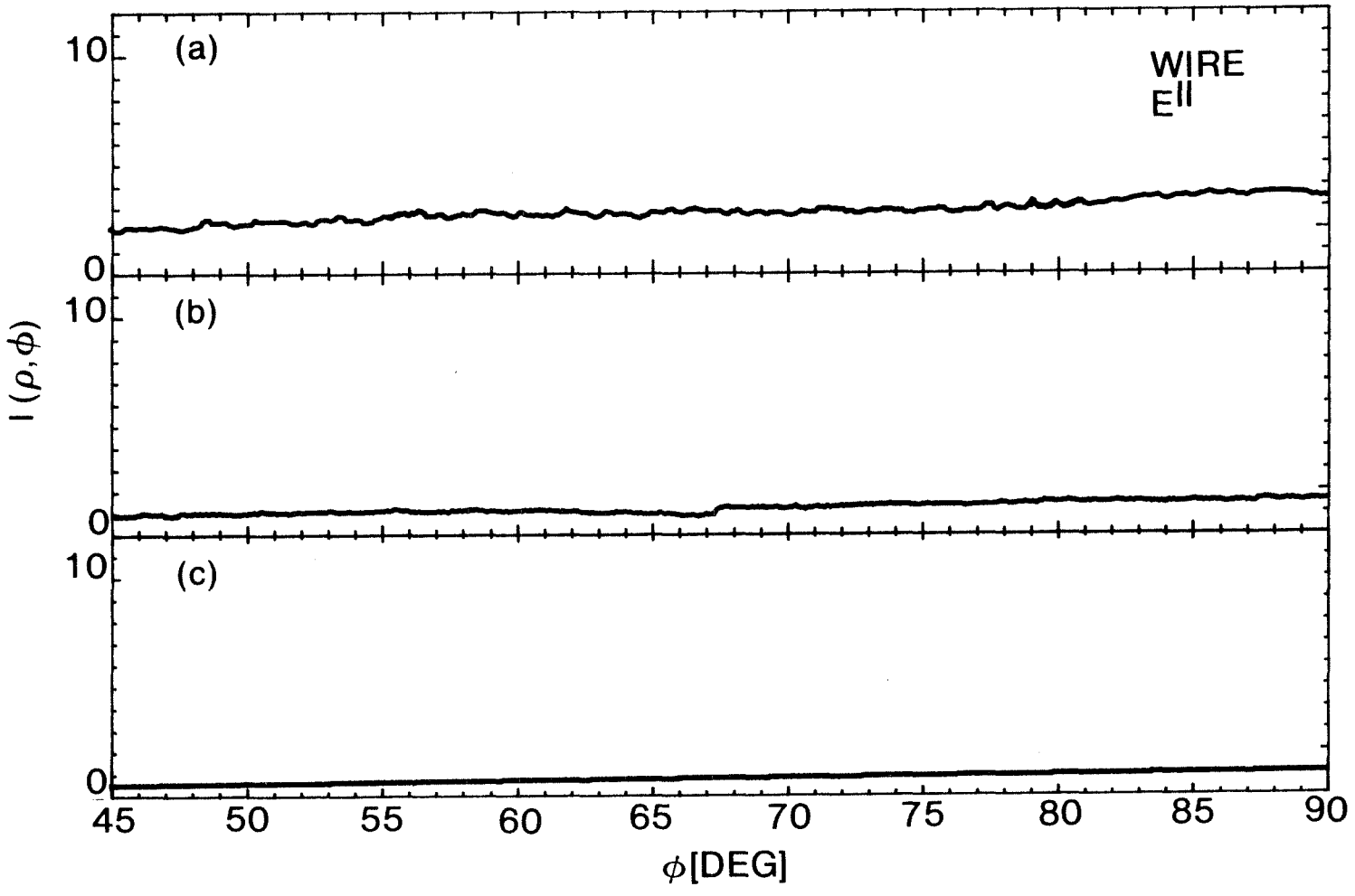

Fig. D.2 The scattered intensity pattern plotted for a conducting cylinder with ka = 327 using (a) film/microdensitometer system, (b) photodetector system and (c) Eq. (2.34).

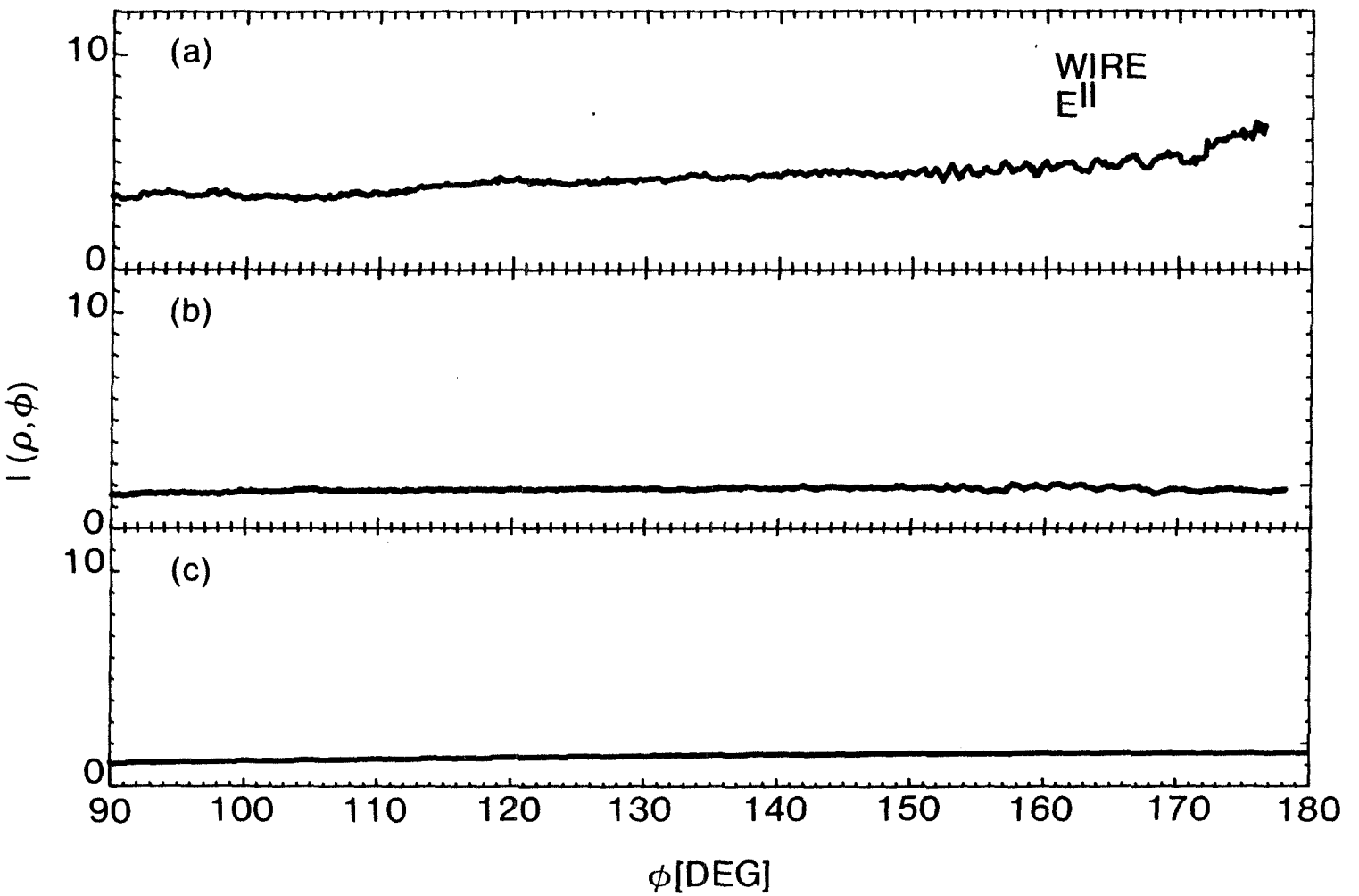

Fig. D.3 The scattered intensity pattern plotted for a conducting cylinder with ka = 327 using (a) film/microdensitometer system, (b) photodetector system and (c) Eq. (2.34).

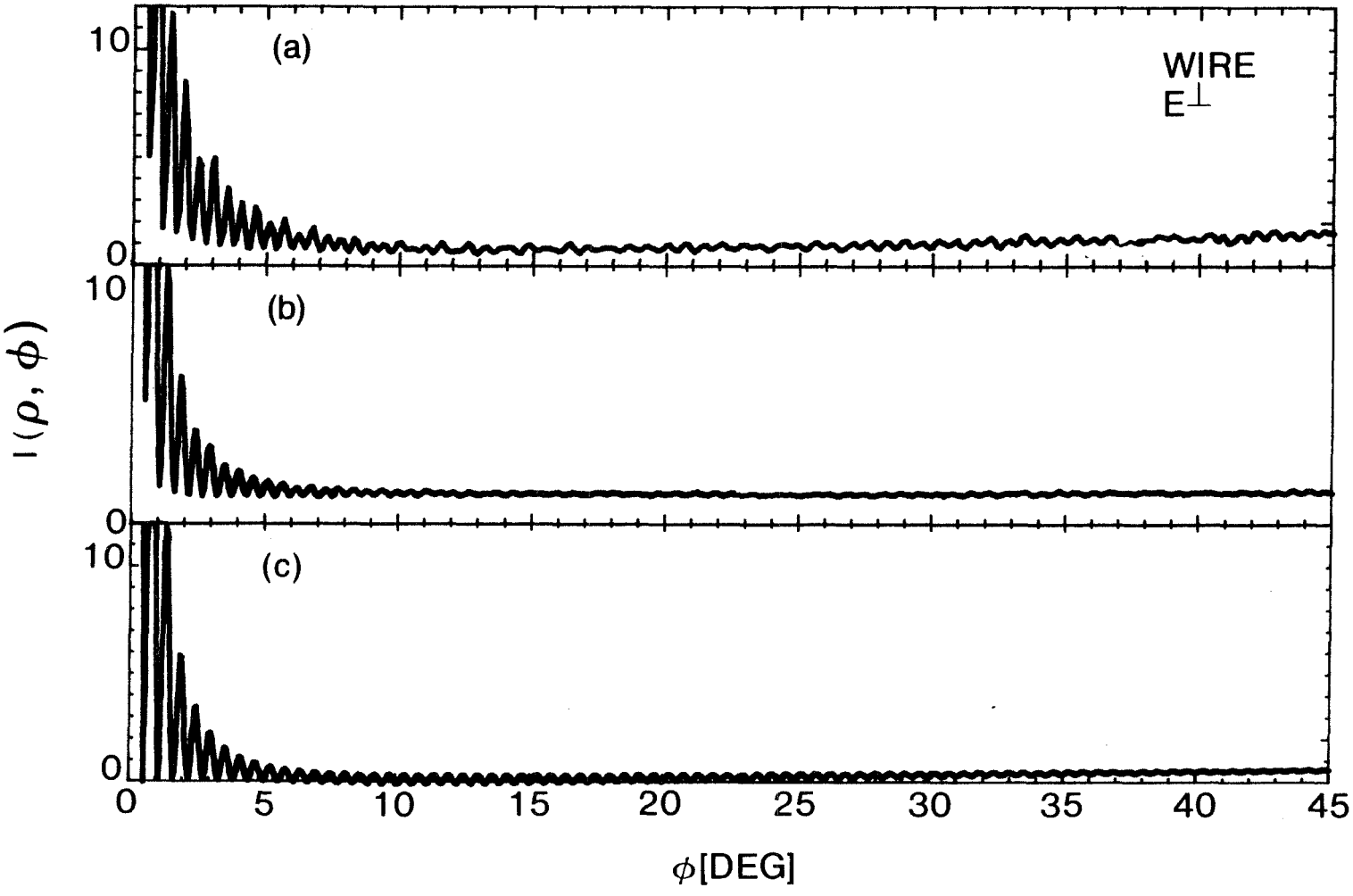

Fig. D.4 The scattered intensity pattern plotted for a conducting cylinder with ka = 327 using (a) film/microdensitometer system, (b) photodetector system and (c) Eq. (2.42).

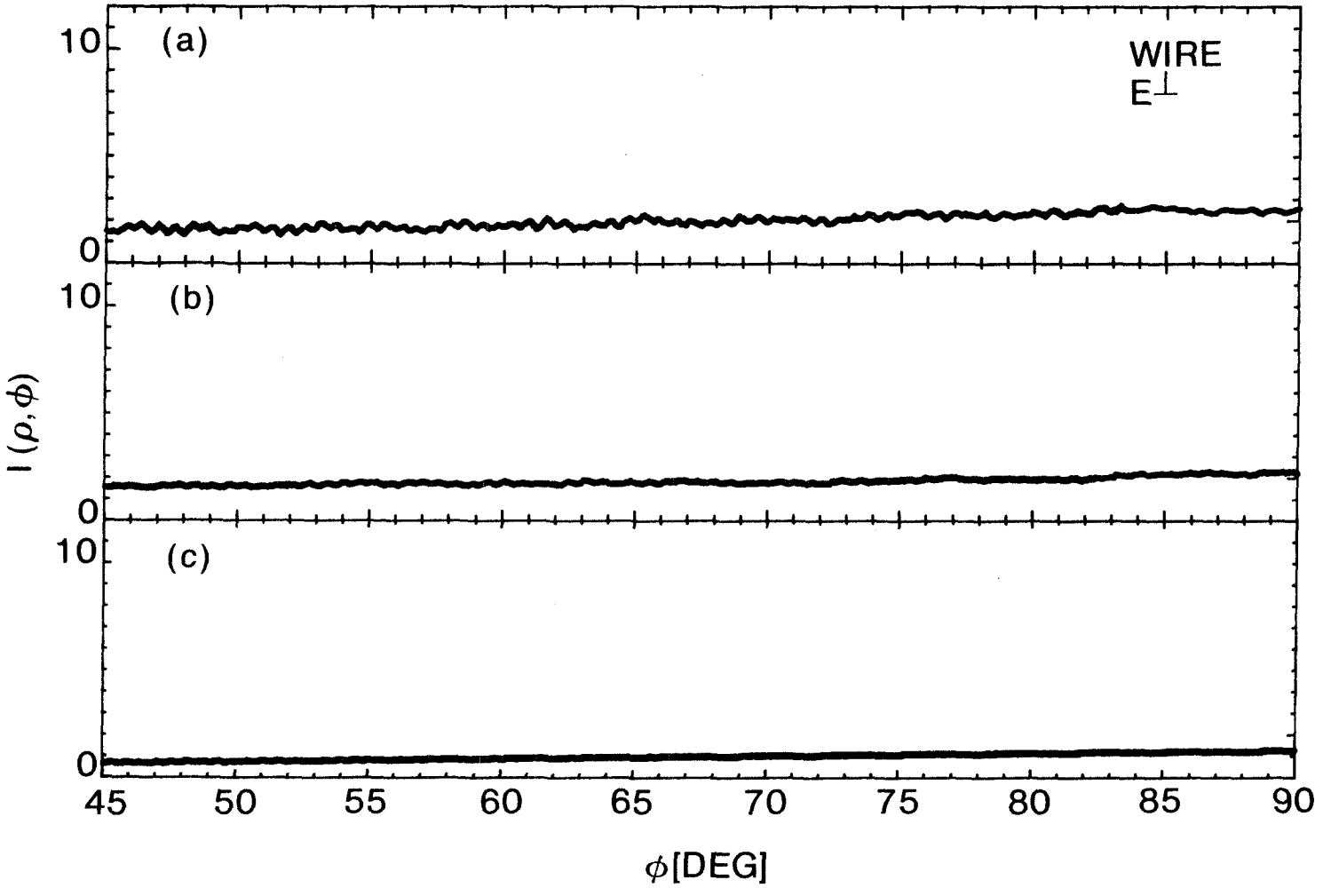

Fig. D.5 The scattered intensity pattern plotted for a conducting cylinder with ka = 327 using (a) film/microdensitometer system, (b) photodetector system and (c) Eq. (2.42).

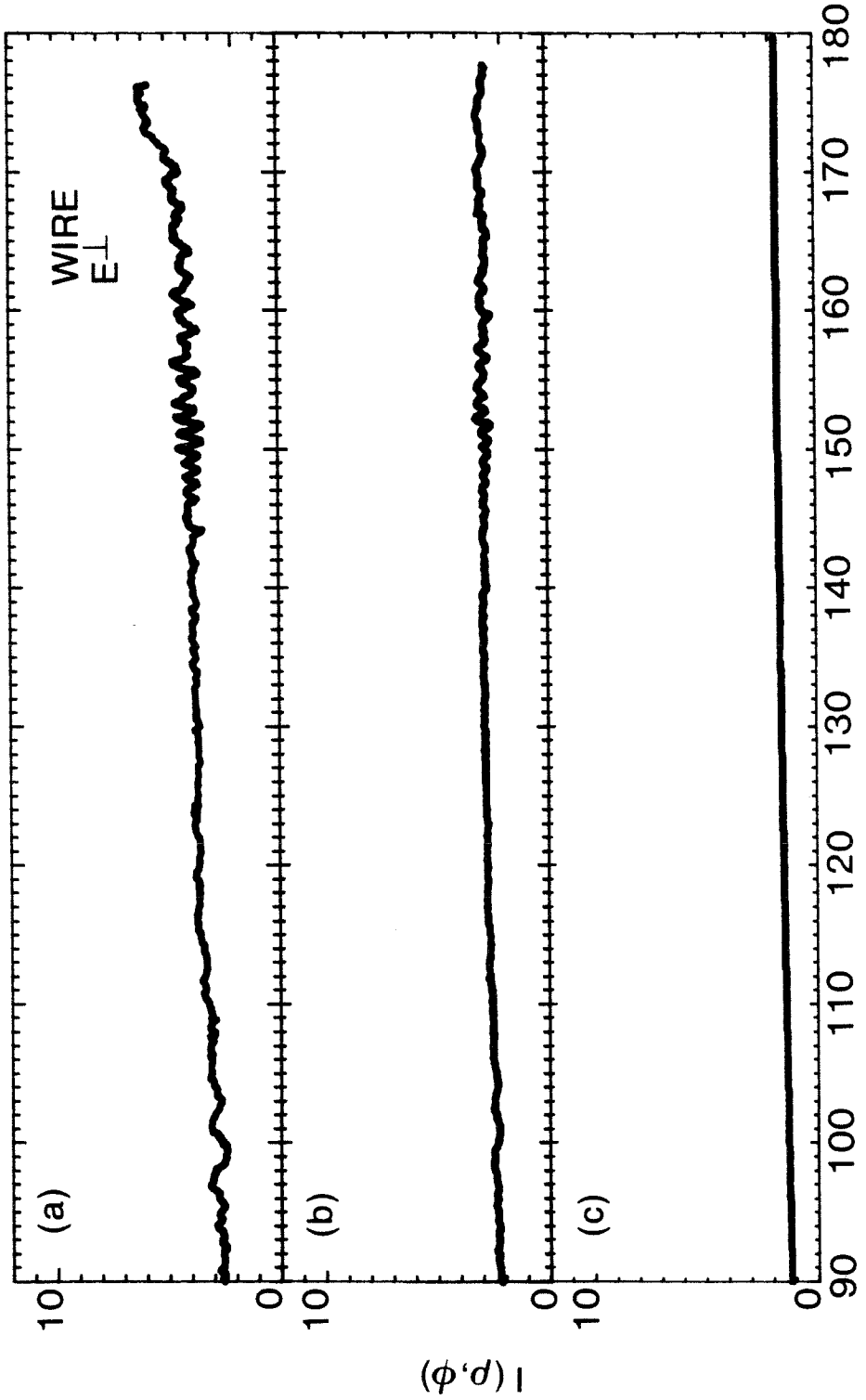

Fig. D.6 The scattered intensity pattern plotted for a conducting cylinder with ka = 327 using (a) film/microdensitometer system, (b) photodetector system and (c) Eq. (2.42).

in Figs. D.1 to D.6 the experimental and theoretical curves are in good agreement, and the two experimental methods agree well.

Intensity Patterns of the Dielectric Cylinder (ka = 327)

In Figs. D.7 to D.12 show the scattered intensity patterns from a dielectric cylinder with ka = 327 and n = 1.45 plotted as a function of the scattering angle ϕ. In Figs. D.7 to D.9 the polarization of the incident wave is parallel to the axis of the cylinder. In Figs. D.10 to D.12 the polarization of the incident wave is normal to the axis of the cylinder. In Fig. D.7 the intensity pattern is plotted for $45° \leq \phi \leq 90°$. The patterns plotted using the two experimental methods are the same. The experimental plots agree well with theoretical plot particularly in the range $45° \leq \phi \lesssim 70°$, in the range $70° \lesssim \phi \leq 90°$ the modulating function which modulates the pattern is a little different, and that is mainly because there might be a slight difference in the wavelength between the one we used in the theoretical plot ($\lambda = 0.6328$ μm) and the wavelength of the laser used, as we discussed that in Chapter V. By looking at the experimental curves in the range $45° \lesssim \phi \lesssim 100°$ we can tell that the fields are close to a resonance. In Figs. D.8 and D.9 the experimental curve plotted using the photodetector system has a lot of background noise in the range $110° \lesssim \phi \lesssim 150°$, while the curve plotted using the film/ microdensitometer does not have that much noise. The peak of the field in the range of $90° \leq \phi \leq 180°$ is located at $\phi \equiv 154°$ in all the three curves. The number of fringes is the same for the three curves in the range $45° \leq \phi \leq 90°$. In Figs. D.10 to

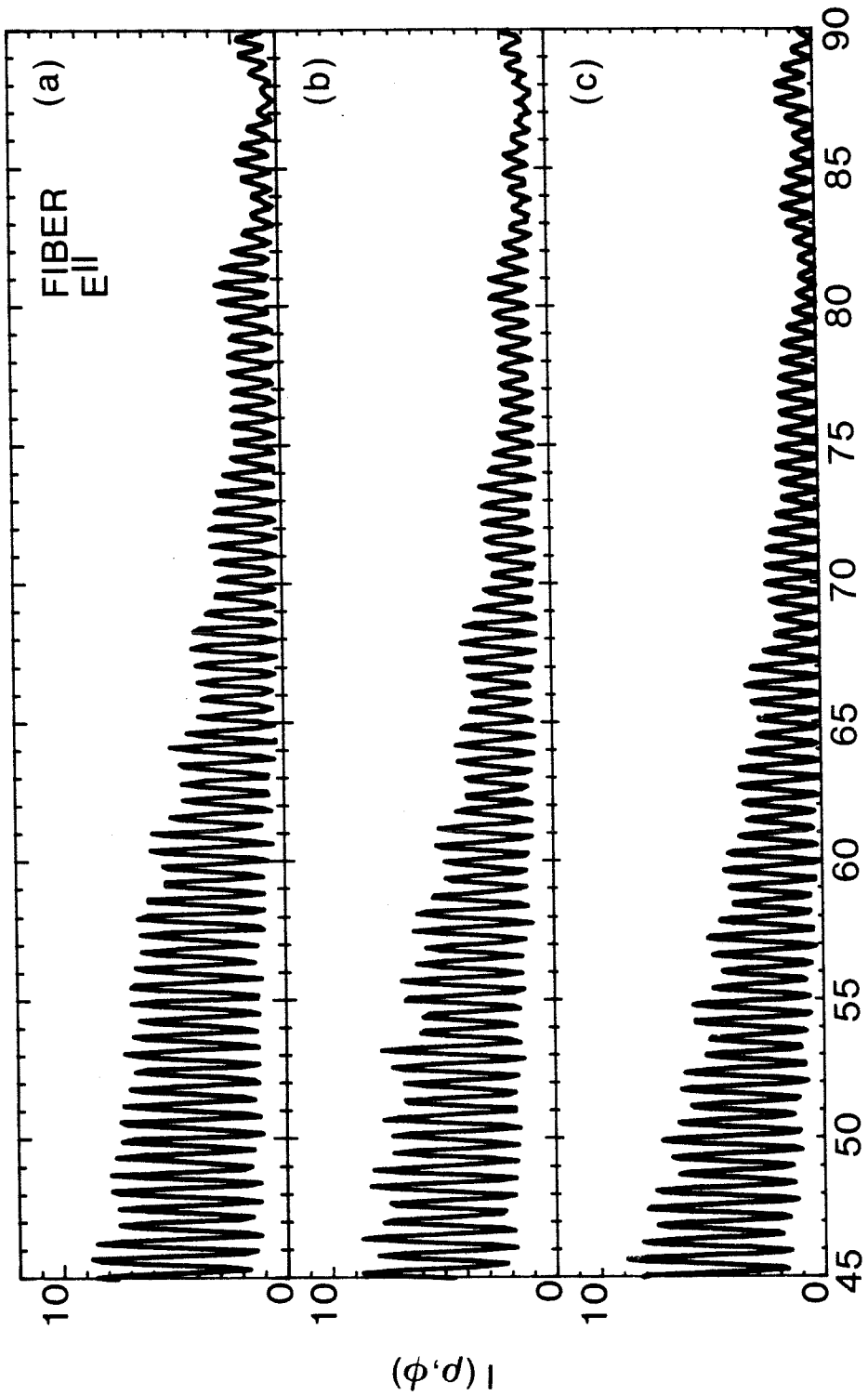

Fig. D.7 The scattered intensity pattern plotted for a dielectric cylinder with ka = 327 using (a) film/microdensitometer system, (b) photodetector system and (c) Eq. (3.14).

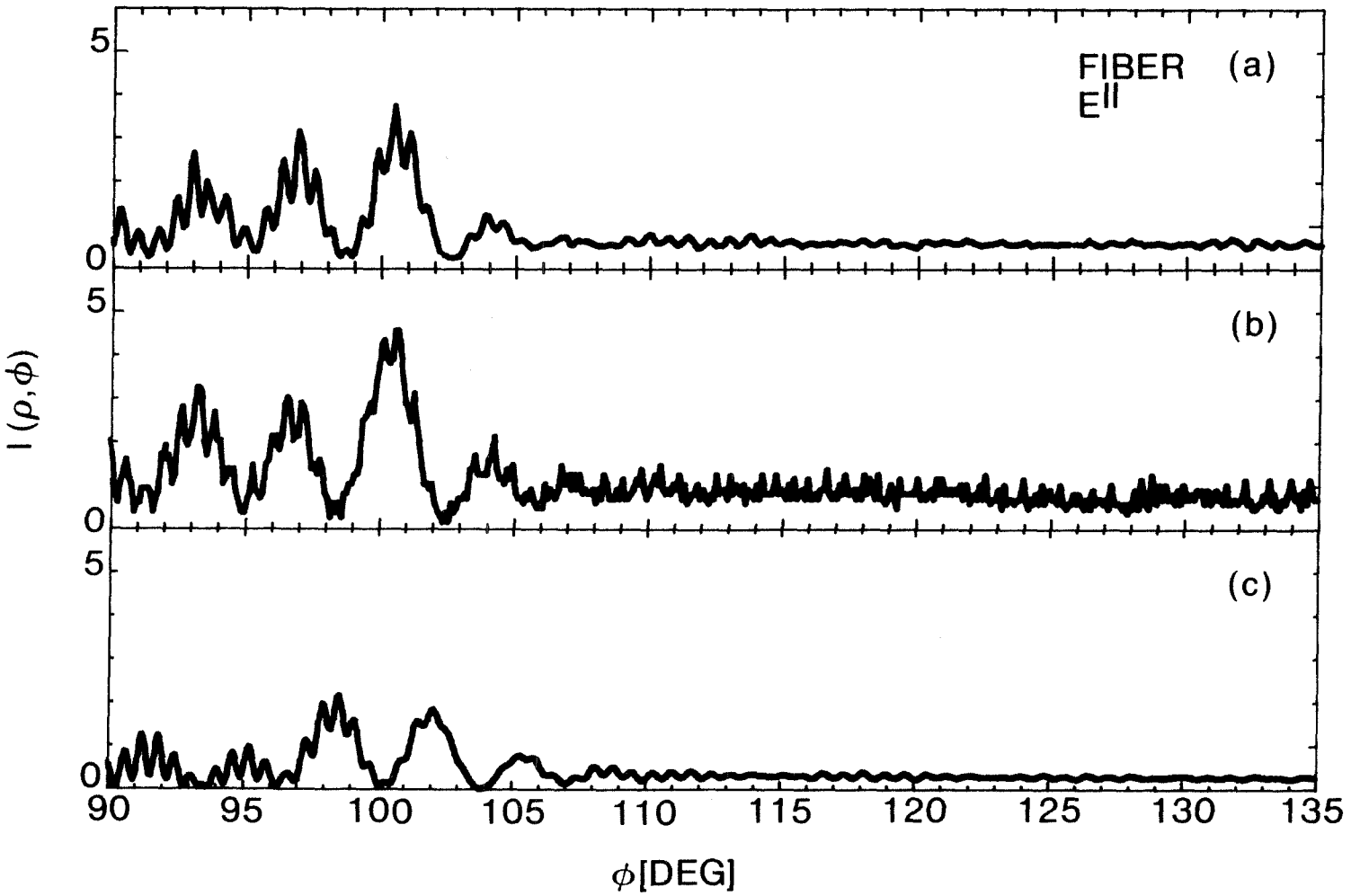

Fig. D.8 The scattered intensity pattern plotted for a dielectric cylinder with ka = 327 using (a) film/microdensitometer system, (b) photodetector system and (c) Eq. (3.14).

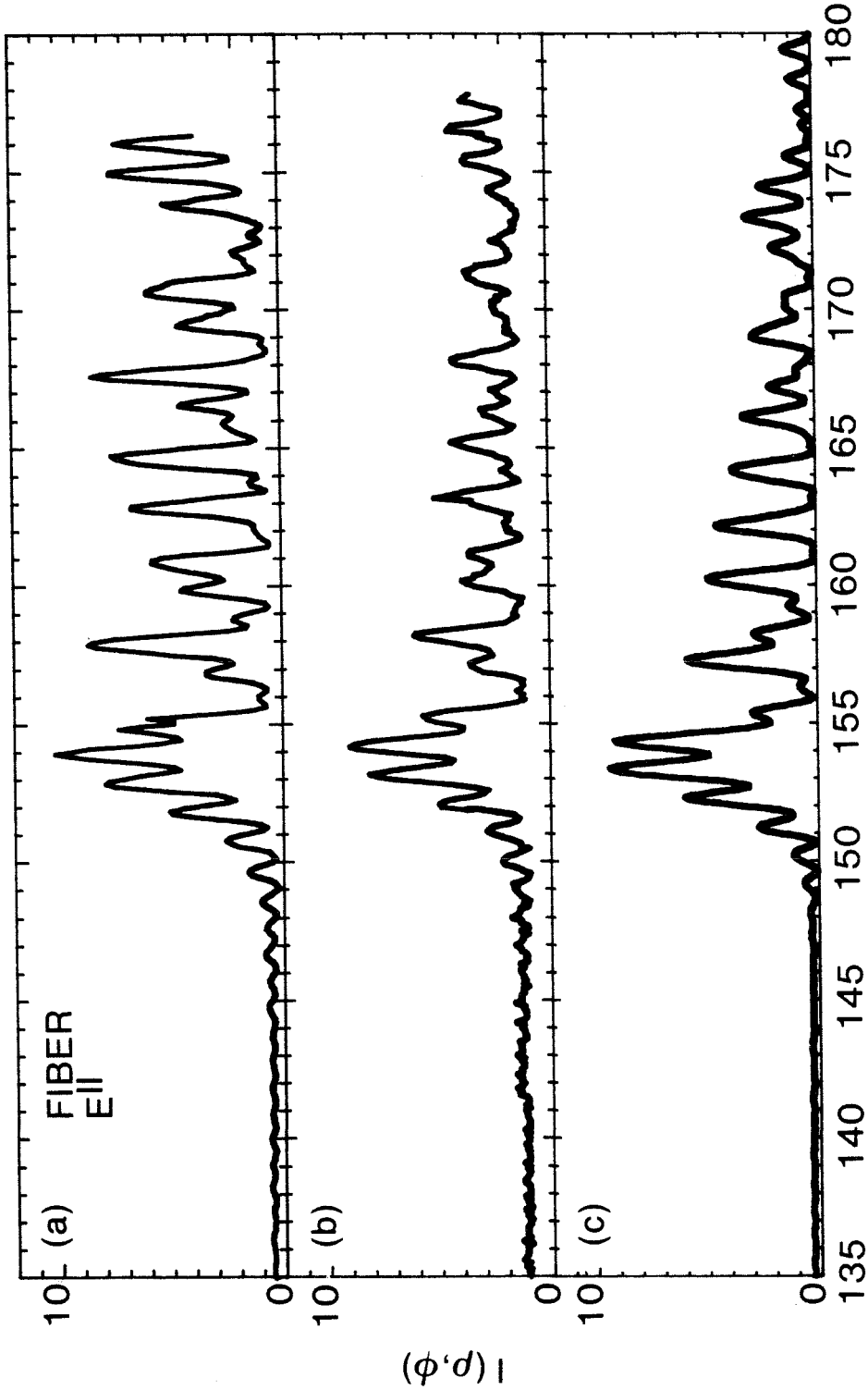

Fig. D.9 The scattered intensity pattern plotted for a dielectric cylinder with ka = 327 using (a) film/microdensitometer system, (b) photodetector system and (c) Eq. (3.14).

D.12 the scattered intensity pattern is plotted for the case when the incident field is polarized normal to the axis of the cylinder. In Fig. D.10 the patterns are comparable in all the three curves. The fringes have a smaller contrast with respect to that in the parallel-polarization case, and there are the same number of fringes in the experimental and theoretical curves. In Figs. D.11 and D.12 the patterns are very similar to each other. The photodiode system results have more background noise in the range $105° \lesssim \phi \leq 150°$ than that obtained using the film/microdensitometer system.

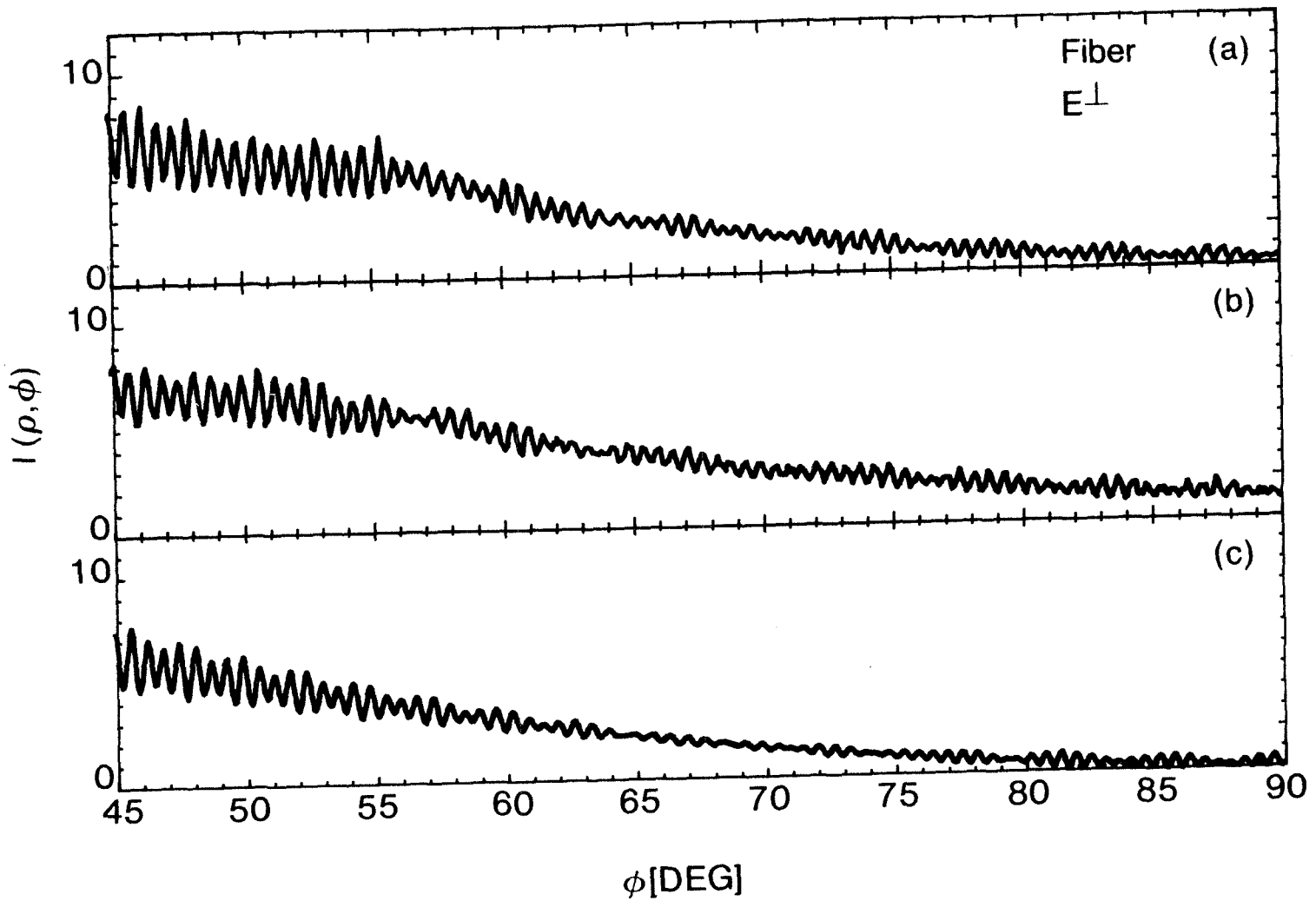

Fig. D.10 The scattered intensity pattern plotted for a dielectric cylinder with ka = 327 using (a) film/microdensitometer system, (b) photodetector system and (c) Eq. (3.25).

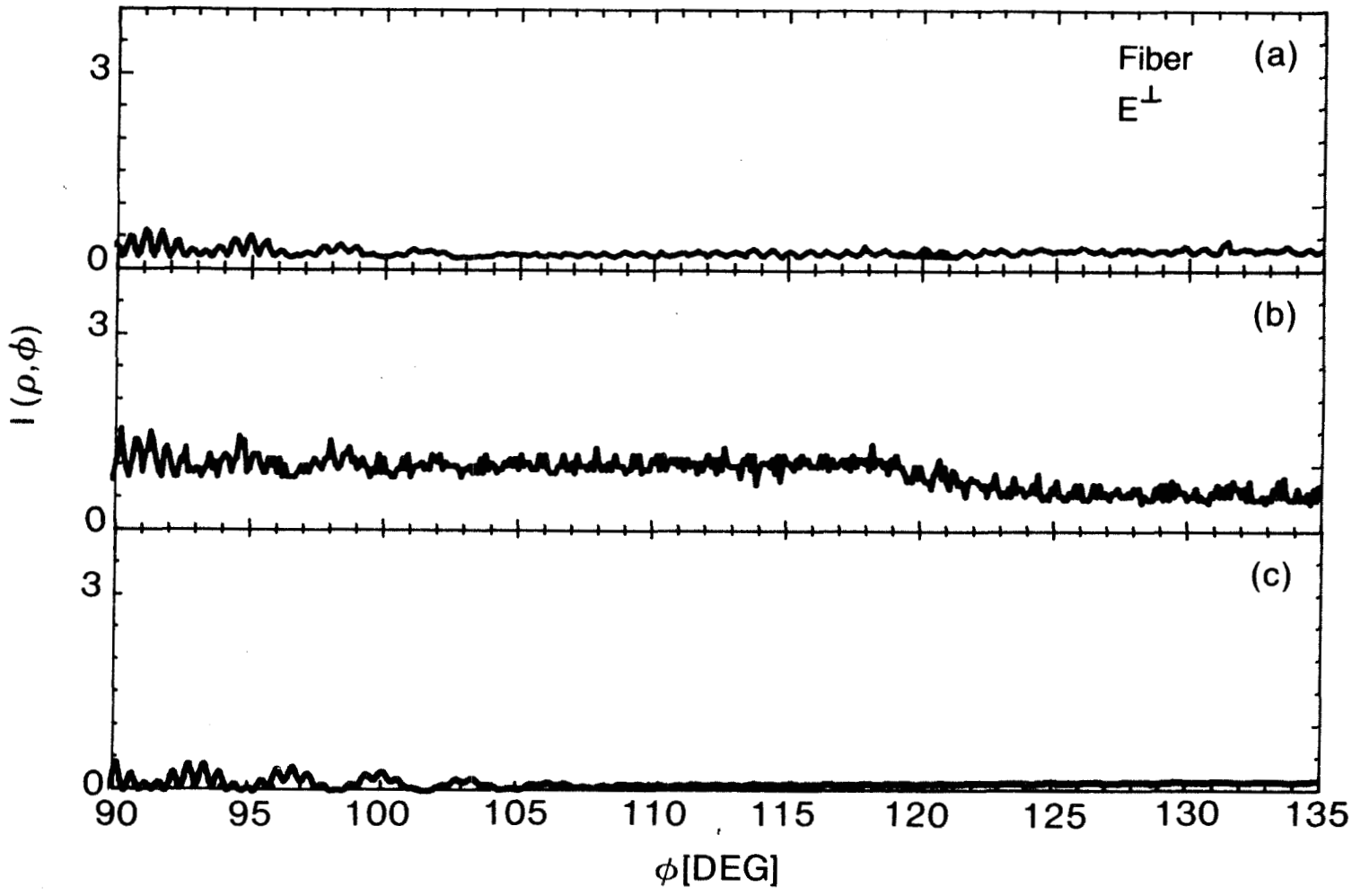

Fig. D.11 The scattered intensity pattern plotted for a dielectric cylinder with ka = 327 using (a) film/microdensitometer system, (b) photodetector system and (c) Eq. (3.25).

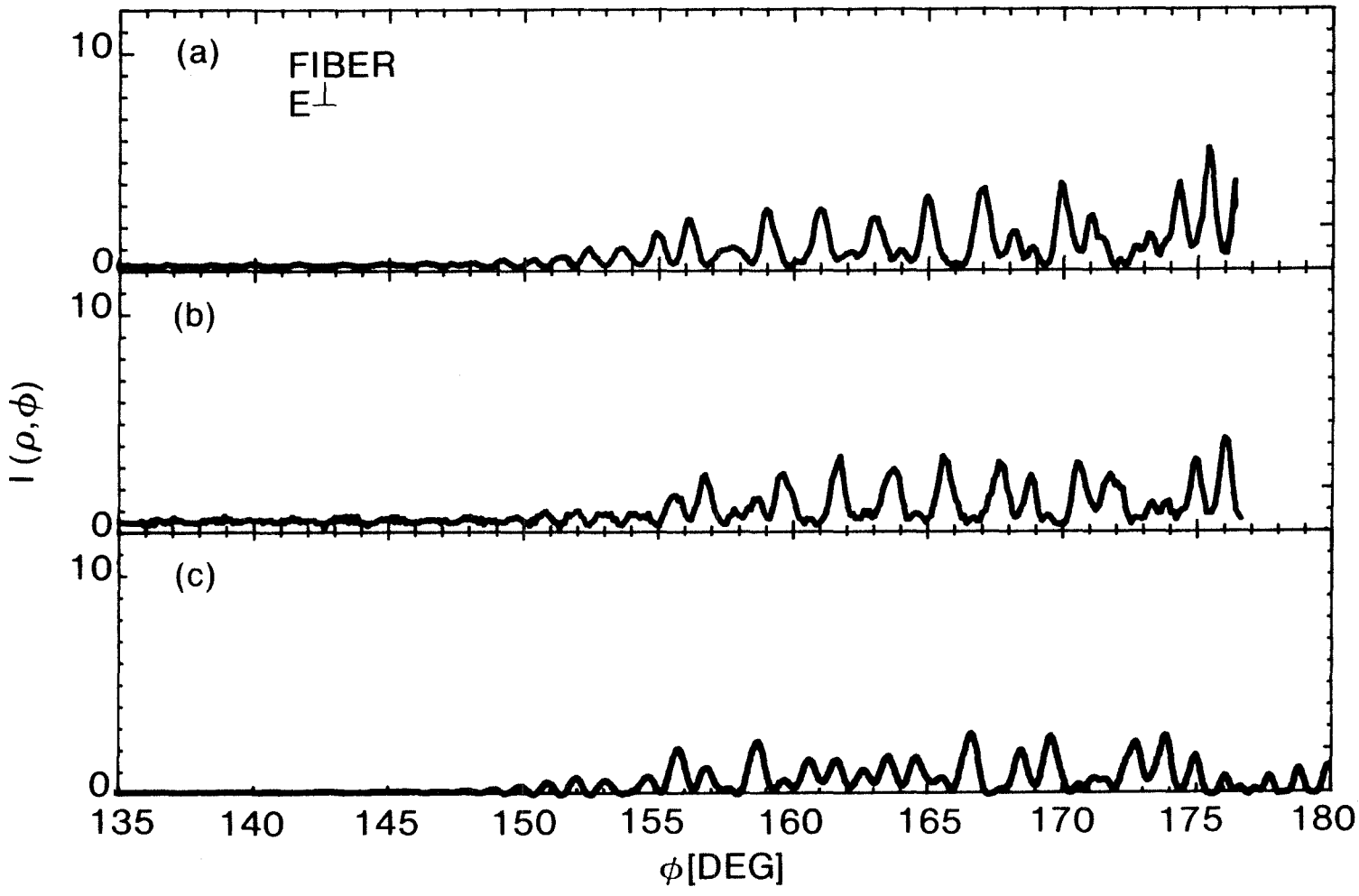

Fig. D.12 The scattered intensity pattern plotted for a dielectric cylinder with ka = 327 using (a) film/microdensitometer system, (b) photodetector system and (c) Eq. (3.25).

Intensity Patterns of the Dielectric Cylinder (ka = 945)

In Figs. D.13 to D.22 the scattered intensity patterns from a dielectric cylinder with ka = 945 and n = 1.45 are plotted as a function of the angle ϕ. In Figs. D.13 to D.17 the polarization of the incident field is parallel to the axis of the cylinder, while in Figs. D.18 to D.22 the polarization of the incident field is normal to the axis of symetry of the cylinder. In Fig. D.13 the pattern obtained experimentally using the photodiode system is plotted in (a), while the theoretical curve using formulas of Chapter III is plotted in (b). The two curves have the same characteristics and same number of fringes. In Fig. D.14 the two curves have the same number of fringes, and both have the same shape until $\phi \cong 70°$, then in $70° \lesssim \phi \leq 90°$ the curve modulating the pattern has a large variation in the theoretical curve than that for the experimental curve. This difference can be explained using the results of Chapter V, which indicate that the possible reason is that there is a slight difference in the wavelength used in the calculations and that of the laser used in the experiment. The theoretical and experimental curves in Figs. D.15 to D.17 are the same, in their shape and the position of the fringes. In Figs. D.18 to D.22 the patterns are plotted for the case when the incident field is polarized normal to the axis of the cylinder. The experimental curves obtained using the photodiode system plotted in (a) and the theoretical curves are plotted in (b). The experimental and theoretical curves are the same in all the different characteristics.

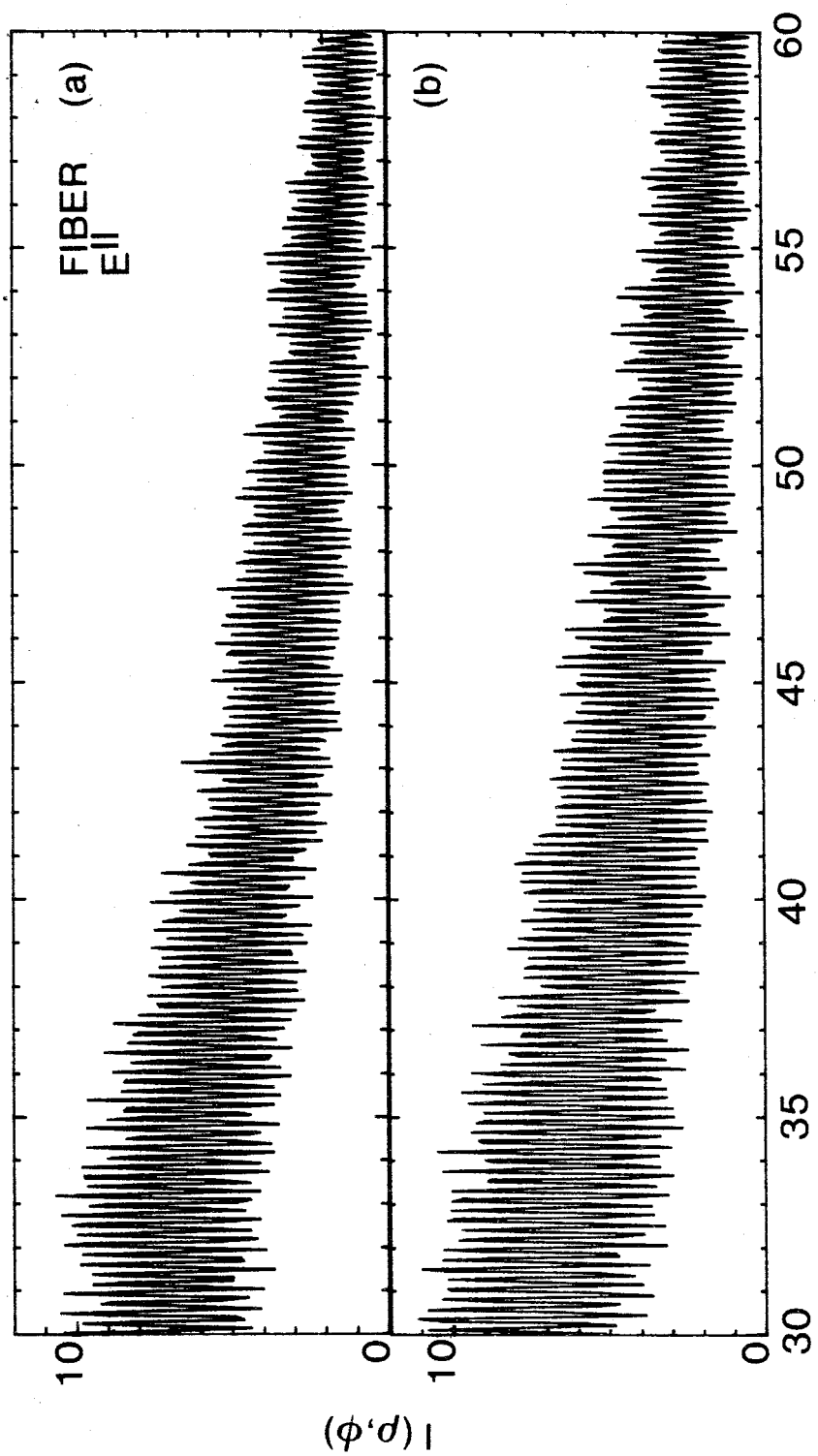

Fig. D.13 The scattered intensity pattern plotted for a dielectric cylinder with ka = 945 using (a) photodetector system and (b) Eq. (3.14).

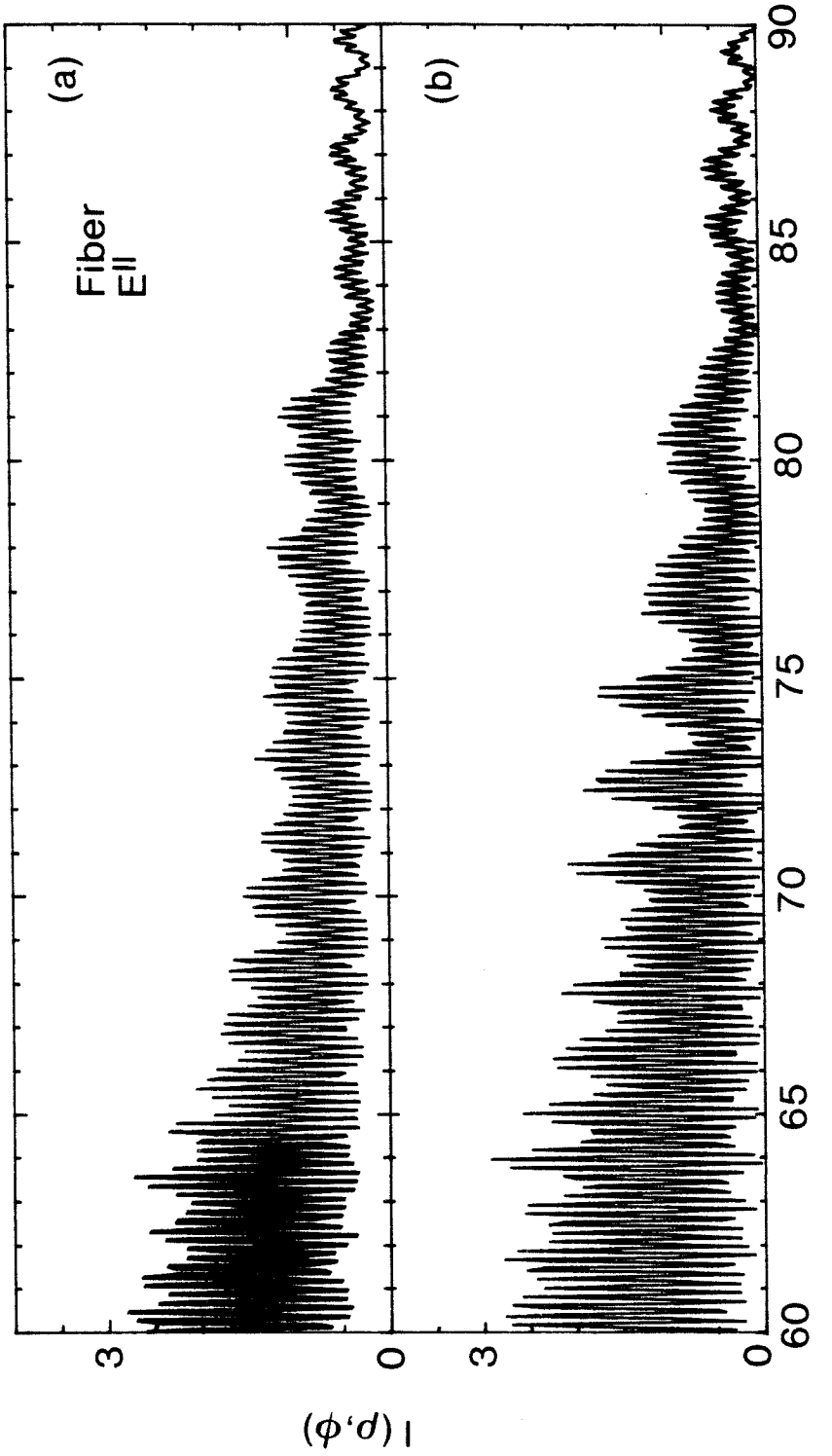

Fig. D.14 The scattered intensity pattern plotted for a dielectric cylinder with ka = 945 using (a) photodetector system and (b) Eq. (3.14).

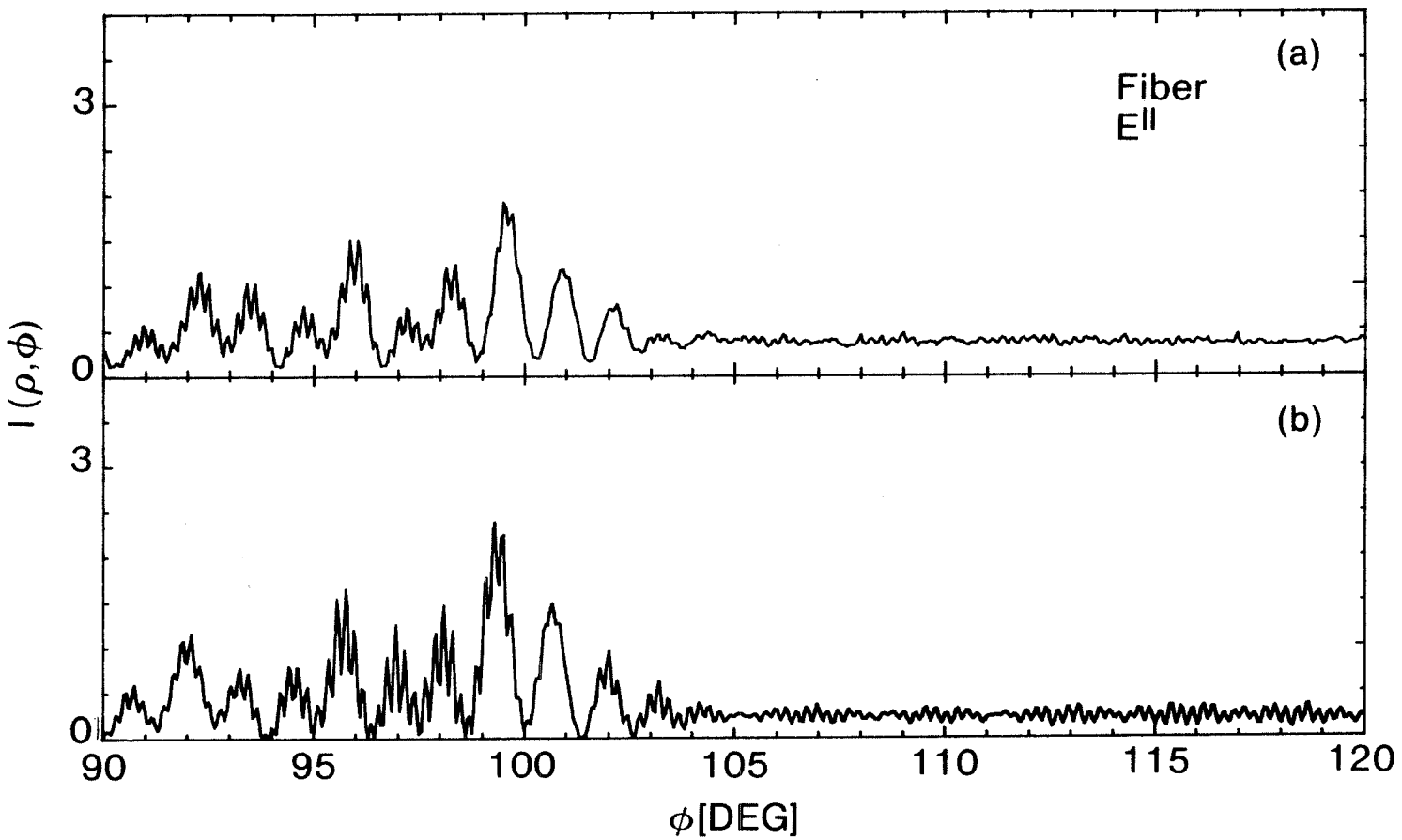

Fig. D.15 The scattered intensity pattern plotted for a dielectric cylinder with ka = 945 using (a) photodetector system and (b) Eq. (3.14).

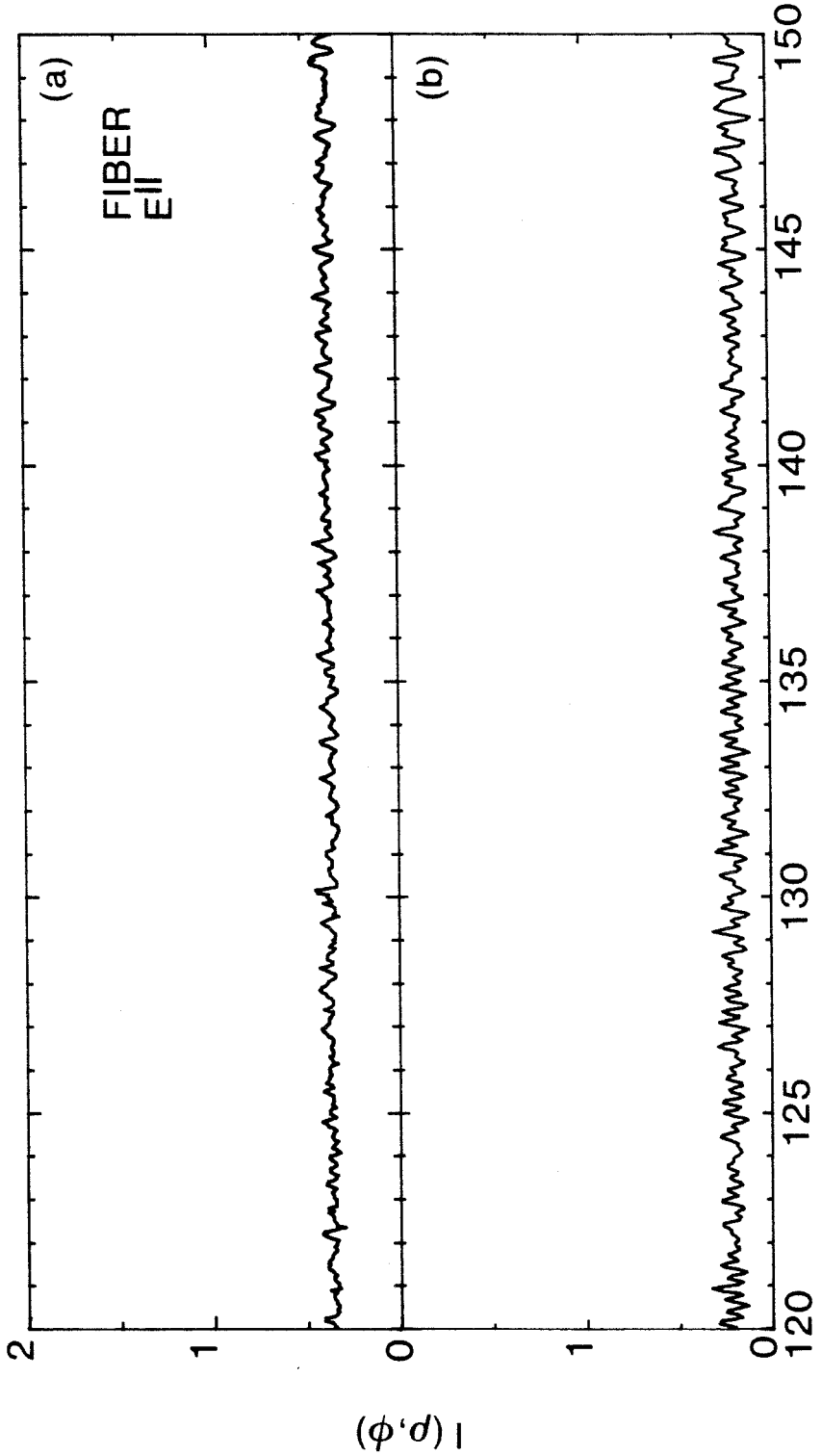

Fig. D.16 The scattered intensity pattern plotted for a dielectric cylinder with ka = 945 using (a) photodetector system and (b) Eq. (3.14).

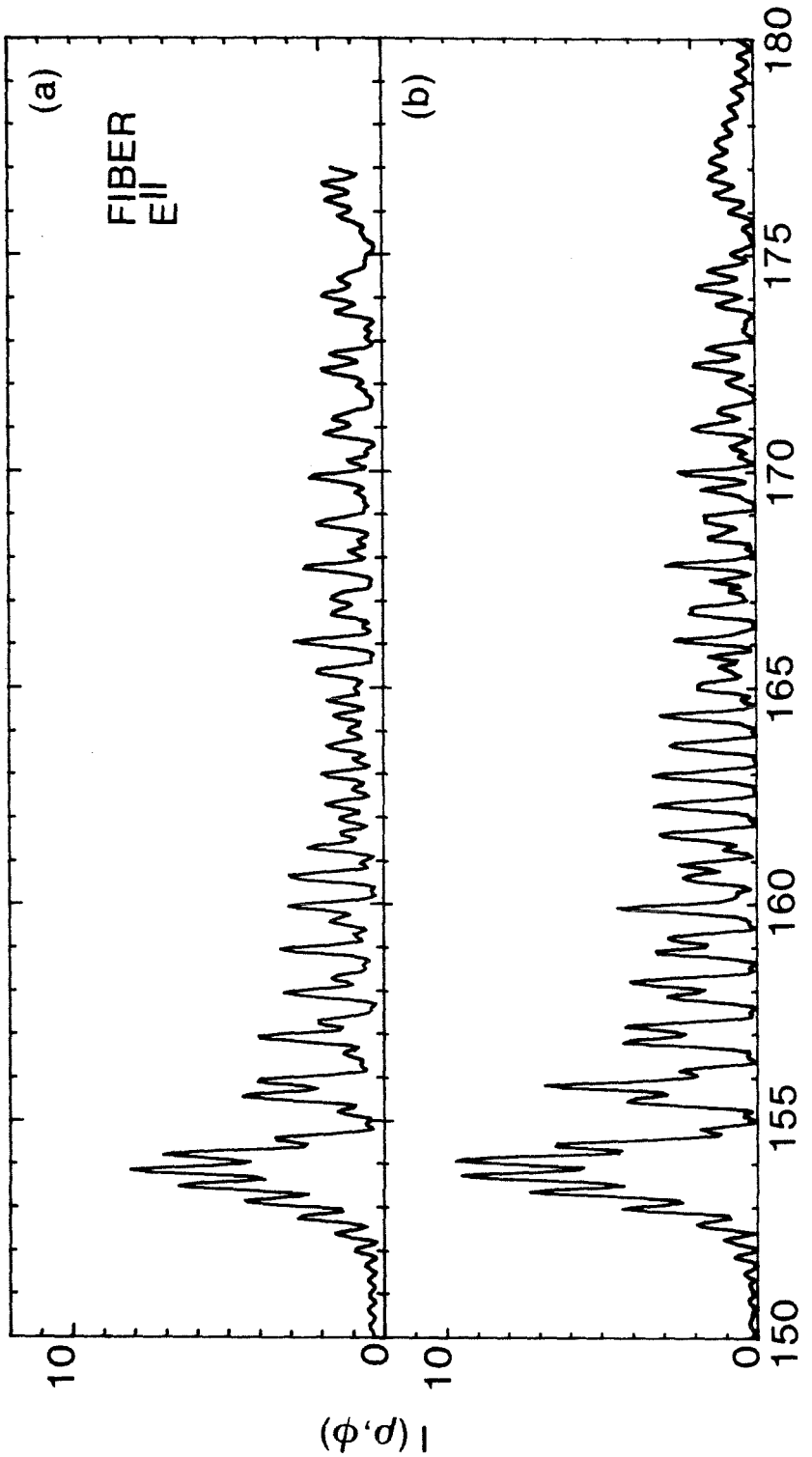

Fig. D.17 The scattered intensity pattern plotted for a dielectric cylinder with ka = 945 using (a) photodetector system and (b) Eq. (3.14).

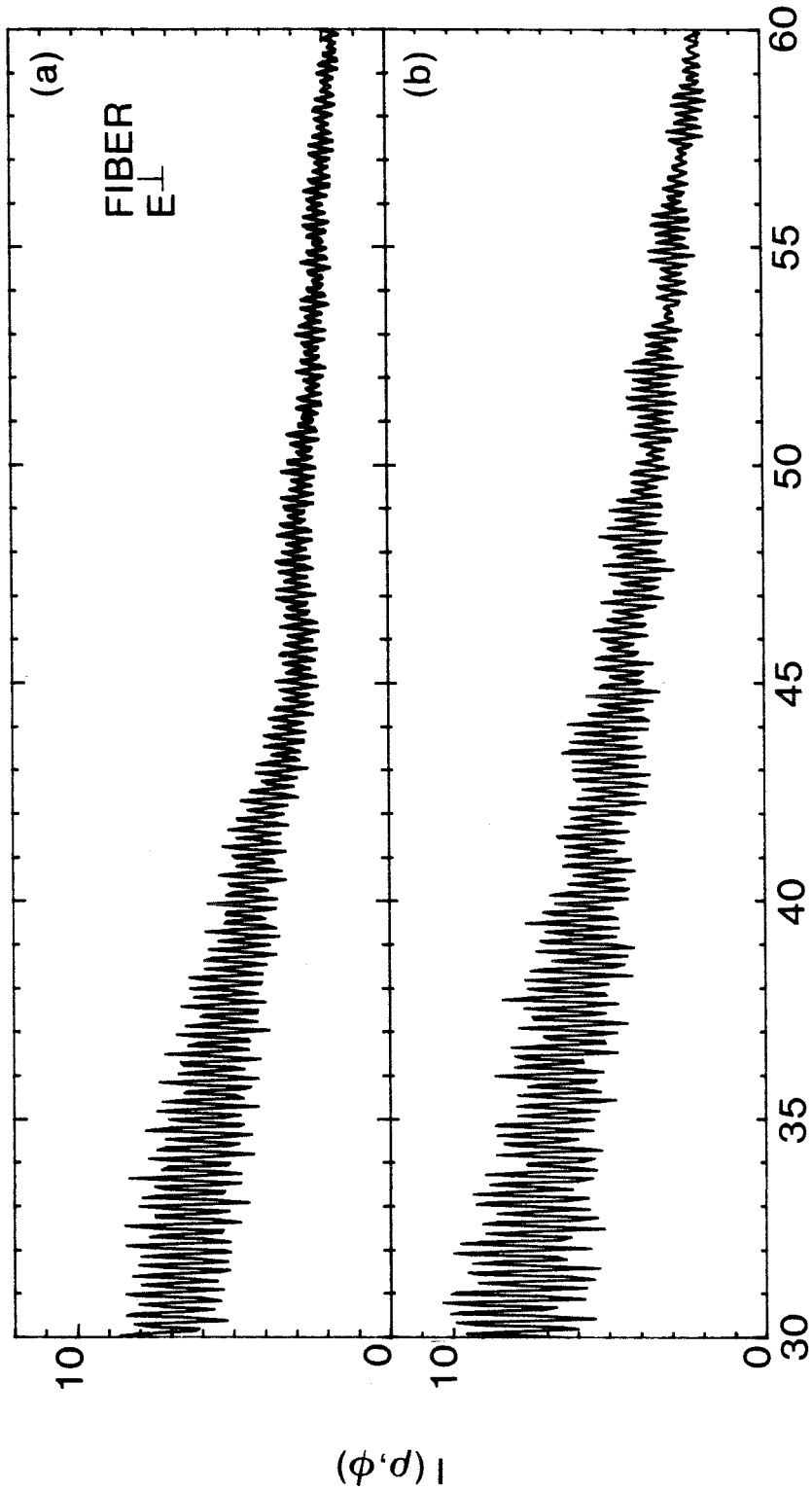

Fig. D.18 The scattered intensity pattern plotted for a dielectric cylinder with ka = 945 using (a) photodetector system and (b) Eq. (3.25).

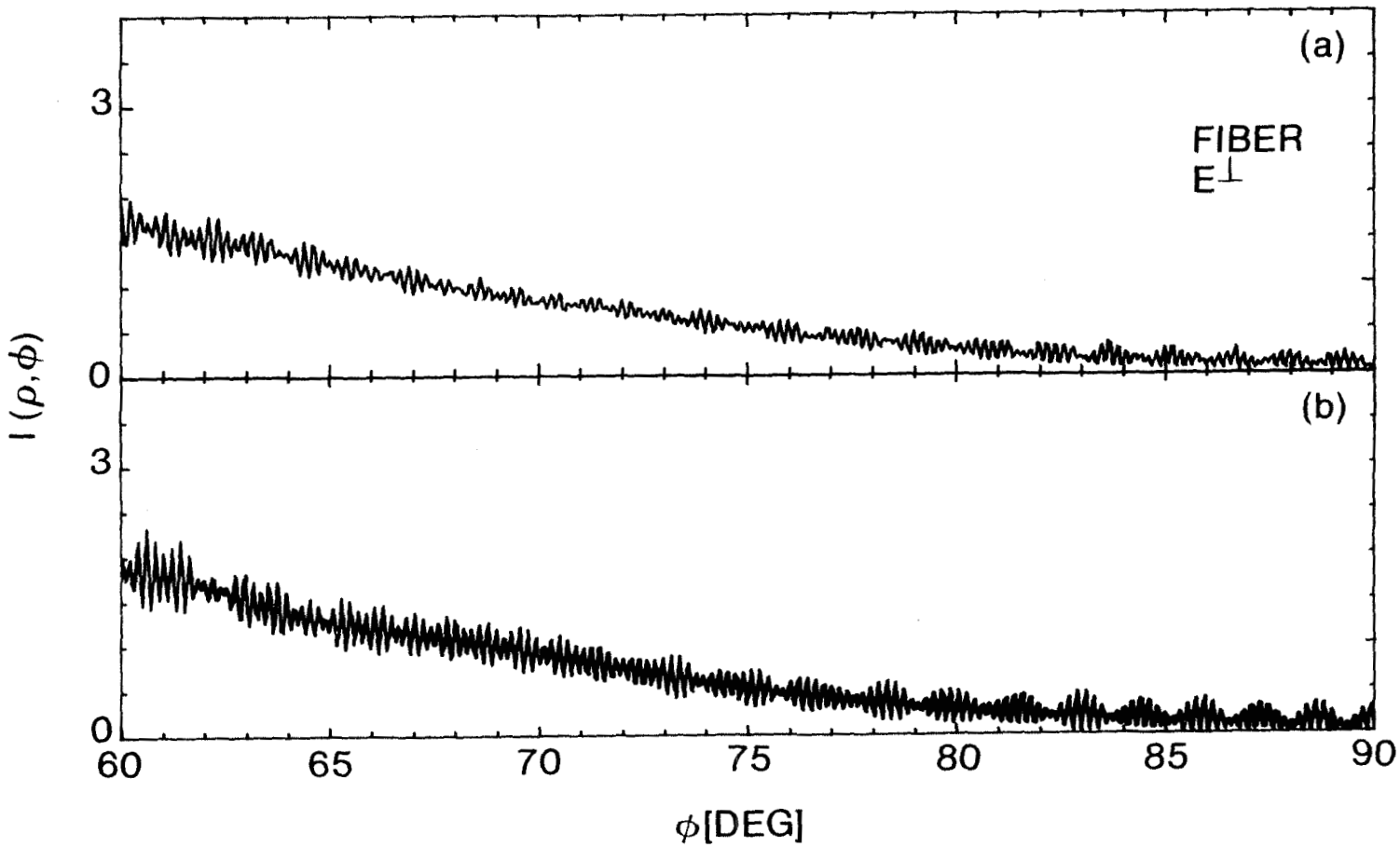

Fig. D.19 The scattered intensity pattern plotted for a dielectric cylinder with ka = 945 using (a) photodetector system and (b) Eq. (3.25).

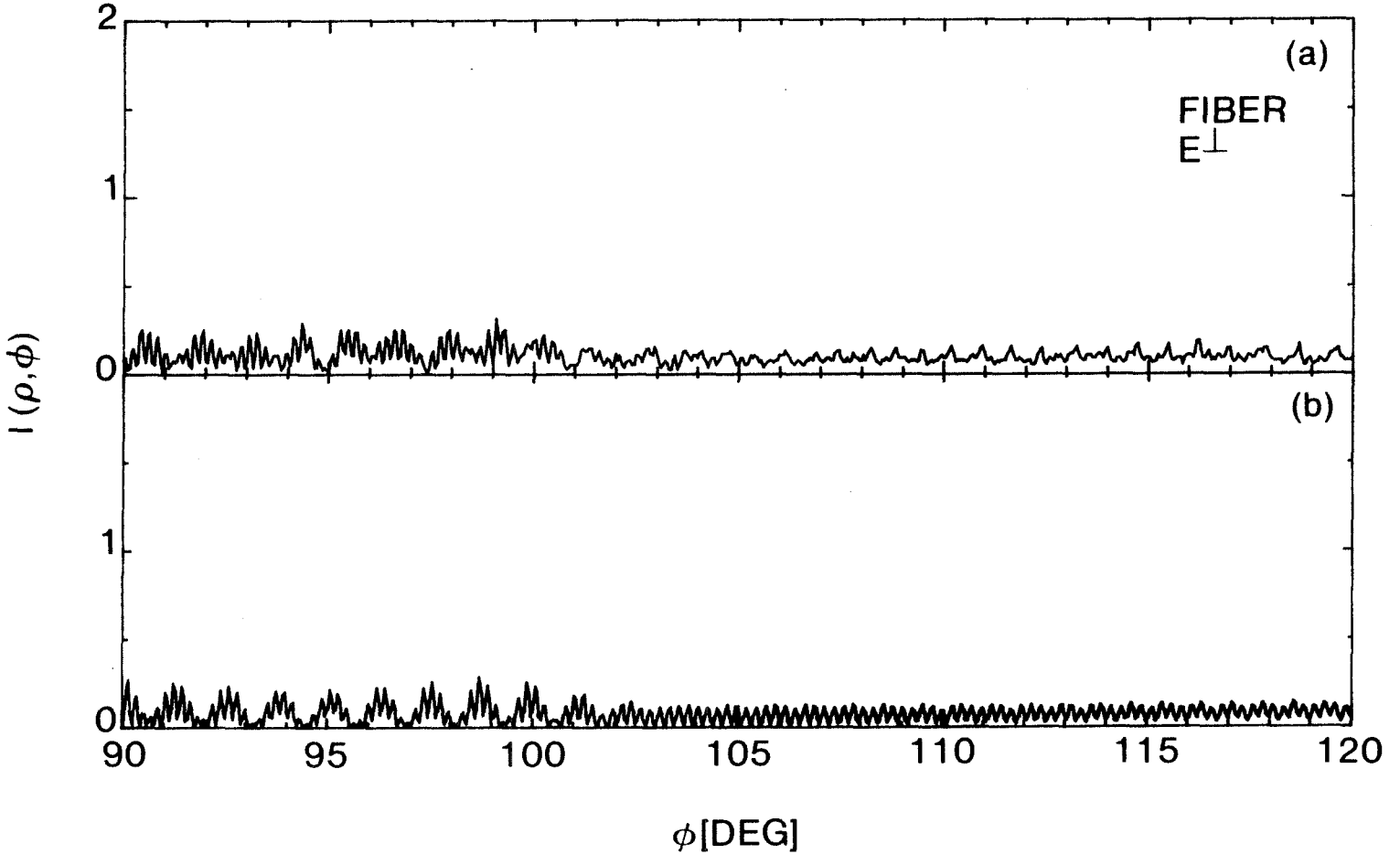

Fig. D.20 The scattered intensity pattern plotted for a dielectric cylinder with ka = 945 using (a) photodetector system and (b) Eq. (3.25).

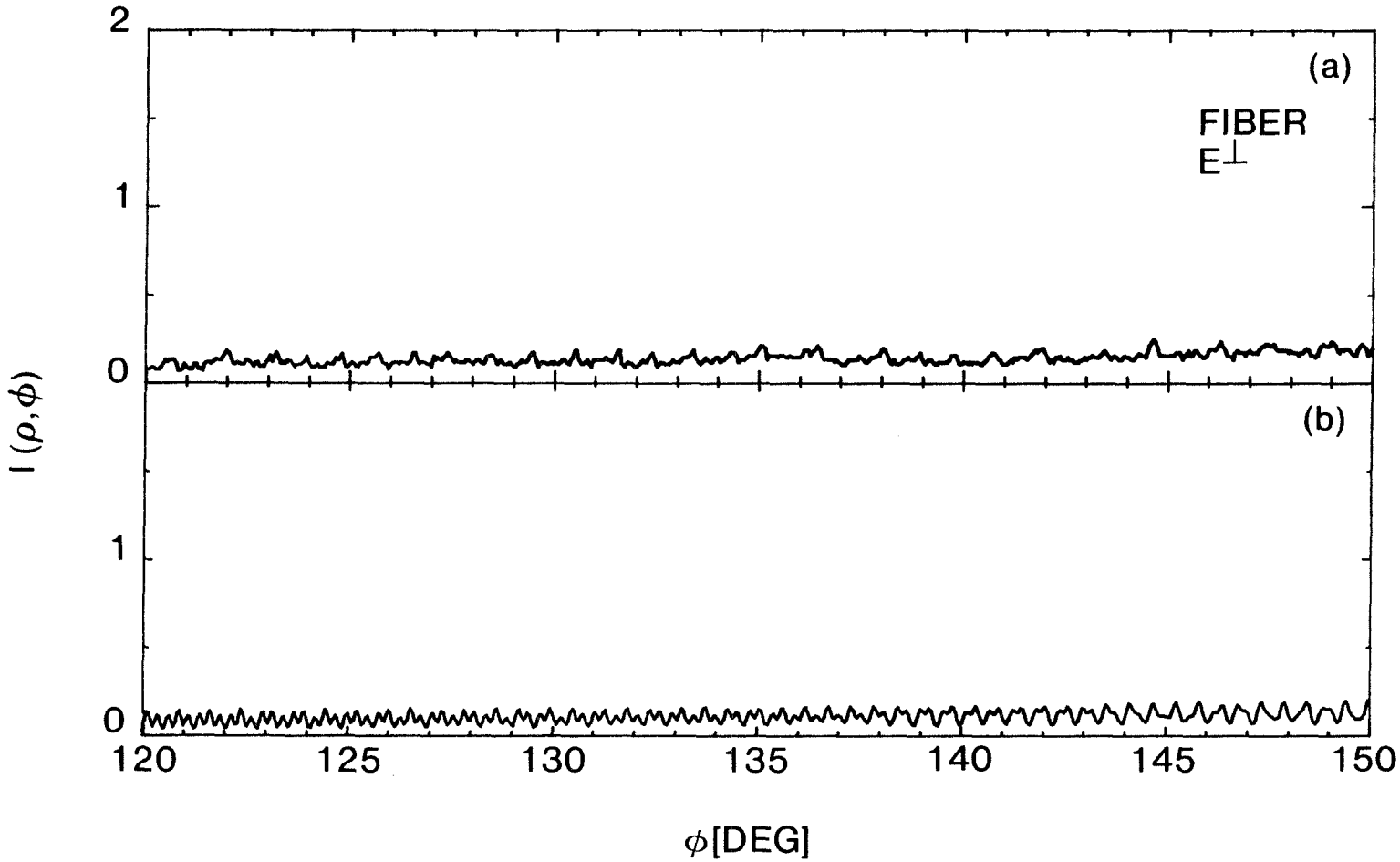

Fig. D.21 The scattered intensity pattern plotted for a dielectric cylinder with ka = 945 using (a) photodetector system and (b) Eq. (3.25).

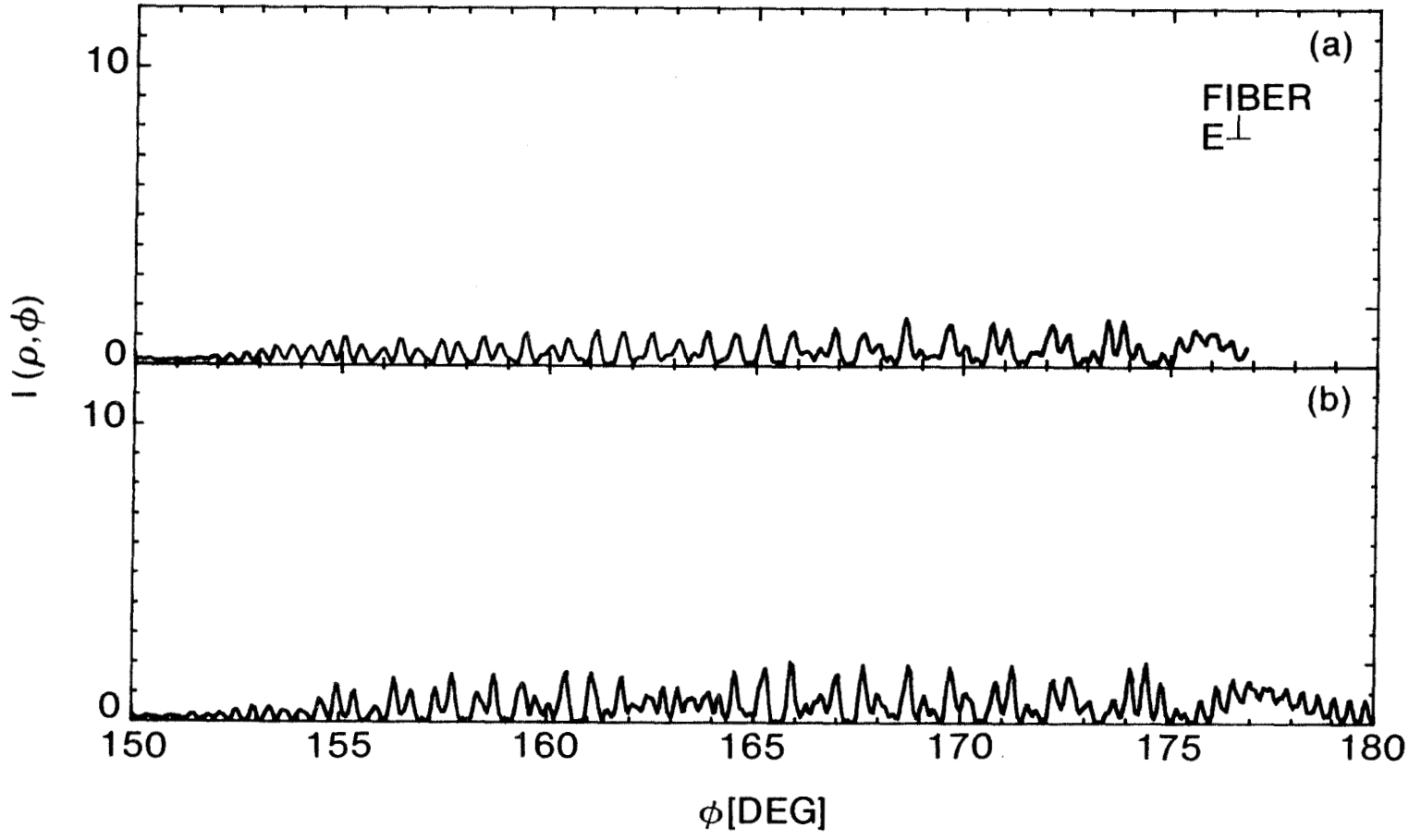

Fig. D.22 The scattered intensity pattern plotted for a dielectric cylinder with ka = 945 using (a) photodetector system and (b) Eq. (3.25).